# Developing a Toolkit for Experimental Studies of Two-Dimensional Quantum Turbulence in Bose-Einstein Condensates

by

Kali Elena Wilson

Copyright © Kali Elena Wilson 2015

A Dissertation Submitted to the Faculty of the

College of Optical Sciences

In Partial Fulfillment of the Requirements
For the Degree of

Doctor of Philosophy

In the Graduate College

The University of Arizona

2 0 1 5

# The University of Arizona
# Graduate College

As members of the Dissertation Committee, we certify that we have read the dissertation prepared by **Kali Elena Wilson** entitled **Developing a Toolkit for Experimental Studies of Two-Dimensional Quantum Turbulence in Bose-Einstein Condensates** and recommend that it be accepted as fulfilling the dissertation requirement for the Degree of Doctor of Philosophy.

_____ Date: April 17, 2015
Brian P. Anderson

_____ Date: April 17, 2015
Alexander D. Cronin

_____ Date: April 17, 2015
Ewan M. Wright

Final approval and acceptance of this dissertation is contingent upon the candidate's submission of the final copies of the dissertation to the Graduate College.

I hereby certify that I have read this dissertation prepared under my direction and recommend that it be accepted as fulfilling the dissertation requirement.

_____ Date: April 17, 2015
Dissertation Director: **Brian P. Anderson**

## Statement by Author

This dissertation has been submitted in partial fulfillment of requirements for an advanced degree at The University of Arizona and is deposited in the University Library to be made available to borrowers under rules of the Library.

Brief quotations from this dissertation are allowable without special permission, provided that accurate acknowledgment of source is made. Requests for permission for extended quotation from or reproduction of this manuscript in whole or in part may be granted by the copyright holder.

Signed: _____ Kali Elena Wilson_____

# Acknowledgments

First and foremost, thanks are due to my advisor, Brian Anderson, for his endless encouragement and mentorship, and for introducing me to Canyonlands with an amazing week-long backpacking trip. I think there are few lab groups that would have survived that trip intact, much less have a blast together. I have perhaps abused Brian's open-door policy, but I have greatly appreciated his availability, keen physical insight, creativity, enthusiasm, and eclectic book recommendations.

In addition to Brian, a number of professors in both the College of Optical Sciences and the Physics Department contributed to my development as a scientist, and I have greatly appreciated their mentorship. In particular I would like to thank Alex Cronin, Masud Masuripur, and Ewan Wright for their open doors, sound advice, and willingness to contemplate my questions.

Over the course of my Phd, I have been extremely lucky to work with talented experimentalists and all around good people. The elusive Carlo Samson taught me how to run the apparatus and accepted my failings as a minion. Zach Newman joined the lab shortly after I did, and has been a wonderful friend throughout. He is particularly skilled at designing and building lab equipment with attention to both form and function, and he helped me bring my machine shop skills back up to speed when it came time to build the custom parts for the QVM2. Sam Nerenberg kindly copied and emailed me lab notebook pages. Joe Lowney worked closely with me throughout the long QVM2 optimization process, and applied his considerable computer skills to develop the current Pixis imaging software. I am leaving the experiment in Joe's capable hands, and I look forward to seeing what he and the ducks choose to investigate.

I would like to thank all of those who went adventuring with me in the beautiful Southwest and reminded me that life exists beyond the lab. In particular, thanks to Amber Young for accompanying me on some amazing (and occasionally terrifying) backpacking adventures; to Will Holmgren and Alex Brummer for climbing, hiking and general ranting over beer; to the garden crew for providing laughter, conversation and some much needed time with a mattock; and to Kate McClain for lending a supportive ear on a weekly basis.

Last but not least, thanks to my parents for giving me the support and freedom to follow my curiosity, for trusting me with power tools, and for teaching me to ask questions, to debate passionately, to try my hand at anything, and to read the dictionary for entertainment.

# Dedication

To my fellow Wilson chickens: Amalia, Andrea, and Bill

# Table of Contents

Table of Contents—*Continued*

Table of Contents—*Continued*

# List of Figures

List of Figures—*Continued*

List of Figures—*Continued*

List of Figures—*Continued*

# List of Tables

# Abstract

Bose-Einstein condensates (BECs), with their superfluid behavior, quantized vortices, and high-level of control over trap geometry and other system parameters provide a compelling environment for studies of quantum fluid dynamics. Recently there has been an influx of theoretical and numerical progress in understanding the superfluid dynamics associated with two-dimensional quantum turbulence, with expectations that complementary experiments will soon be realized. In this dissertation I present progress in the development of an experimental toolkit that will enable such experimental studies of two-dimensional quantum turbulence. My approach to developing this toolkit has been twofold: first, efforts aimed at the development of experimental techniques for generating large disordered vortex distributions within a BEC; and second, efforts directed towards the design, implementation, and characterization of a quantum vortex microscope.

Quantum turbulence in a superfluid is generally regarded as a disordered tangle of quantized vortices in three dimensions, or a disordered planar distribution of quantized vortices in two dimensions. However, not all vortex distributions, even large disordered ones, are expected to exhibit robust signatures of quantum turbulence. Identification and development of techniques for controlled forcing or initialization of turbulent vortex distributions is now underway. In this dissertation, I will discuss experimental techniques that were examined during the course of my dissertation research, namely generation of large disordered distributions of vortices, and progress towards injecting clusters of vortices into a BEC.

Complimentary to vortex generation is the need to image these vortex distributions. The nondeterministic nature of quantum turbulence and other far-from-equilibrium superfluid dynamics requires the development of new imaging techniques that allow one to obtain information about vortex dynamics from a single BEC. To this end, the first vortex microscope constructed as part of my dissertation research enabled the first *in situ* images of quantized vortices in a single-component BEC, obtained without prior expansion. I have further developed and characterized a second vortex microscope, which has enabled the acquisition of multiple *in situ* images of a lattice of vortex cores, as well as the acquisition of single *in situ* images of vortex cores in a BEC confined in a weak hybrid trap. In this dissertation, I will discuss the state-of-the-art of imaging vortices and other superfluid phenomena in the University of Arizona BEC lab, as indicated by the examined performance of the quantum vortex microscope.

# Chapter 1
# Introduction

Dilute-gas Bose-Einstein condensates (BECs) offer a compelling environment for studies of quantum fluid dynamics. Experimentally, we have a high-level of control over trapping geometry and other system parameters, with access to both two-dimensional (2D) and three-dimensional (3D) fluid regimes. The superfluid nature of BECs allows them to support such superfluid hallmarks as quantized vortices and persistent currents [1, 2]; these vortices can be readily generated with swiping beams or modulations of the trapping potential [3, 4]. Vortex cores are on the order of 1 $\mu$m in diameter, easily resolved after ballistic expansion, and in some scenarios observable *in situ*.

Complementary numerics based on the evolution of the non-linear Schrödinger equation, or Gross-Pitaevski equation, [5] allow for highly accurate simulations based on a microscopic model of BEC behavior. The combined power of numerics and experiment make BECs a seductive environment for studies of two-dimensional quantum turbulence (2DQT) and other far-from equilibrium phenomena.

## 1.1 Format of this dissertation

In this dissertation I present progress towards the development of an experimental toolkit that will enable studies of 2DQT in dilute-gas BECs. My approach to developing this toolkit has been twofold: first, efforts aimed at the development of experimental techniques for generating large, disordered vortex distributions within a BEC, with varying degrees of control over vortex placement, charge, and clustering; and second, efforts directed towards observation of these vortex distributions, in particular, the design, implementation, and characterization of a quantum vortex microscope.

In the remainder of the current chapter, I give an introduction to 2D turbulence in

the context of dilute-gas BECs, followed by a discussion of the state of numerical and experimental studies of 2DQT. Chapter 2 gives a brief overview of aspects of the apparatus relevant to the experiments described in this dissertation. Chapter 3 gives an introduction to the four imaging techniques, phase-contrast, bright-field absorption, dark-field, and Faraday imaging, commonly used to acquire information about BECs. I provide representative images and discuss the relative merits of each technique.

Chapter 4 describes four methods for vortex generation that provide a representative sample of recent experimental efforts towards forcing vortex cores into a BEC, and demonstrate the breadth of vortex distributions that may be generated in a compressible quantum fluid. Two of these techniques were included in the article *Experimental Methods for Generating Two-Dimensional Quantum Turbulence in Bose-Einstein Condensates* [4] reproduced in Appendix A. Excerpts from this article are included in Chapter 4. In addition, I describe more recent work aimed at generating vortex clusters, which shows promise for generating vortex distributions with positive point-vortex energy while minimizing acoustic energy. These efforts were motivated by the need to identify vortex states that demonstrate robust phenomenological and statistical signatures of turbulence. In particular, we are interested in identifying forcing mechanisms and initial vortex distributions that will enable observation of Onsager-Kraichnan condensation [6], turbulent states in BECs with both the large-scale clustering of like-signed vortices indicative of Onsager's negative-temperature vortex distributions [7], and the spectral condensation at the system scale predicted by Kraichan [8].

Much of the latter half of this dissertation research was directed towards improving vortex detection capabilities. The complex and nondeterministic vortex distributions that arise when a BEC is driven far from equilibrium require the development of new imaging techniques beyond the current standard of absorption imaging after a period of ballistic expansion. In particular, the nondeterministic nature of quantum turbulence and other far-from-equilibrium superfluid dynamics requires techniques that allow one to obtain in-

formation about vortex dynamics from a single BEC. While my efforts have largely focused on imaging 2D vortex distributions, Chapter 5 describes my initial foray into tomographic imaging of three-dimensional (3D) vortex distributions.

Chapter 6 describes the first *in situ* observation of a 2D distribution of bare vortex cores in a single-component BEC. This result has far reaching implications ranging from enabling vortex studies in trapping geometries that are not conducive to self-similar expansion, to ultimately enabling direct observations of the dynamics of vortex cores and other superfluid density features. While our ultimate goal is the acquisition of tens of images of a vortex distribution taken from a single BEC in order to study vortex dynamics, even two such vortex images would allow us to begin to correlate initial and final vortex distributions, reducing dependency on vortex number statistics, and enabling direct measurement of vortex lifetimes. The paper, *In situ observation of two-dimensional vortex distributions in Bose-Einstein condensation*, describing this work was published in Physical Review A [9], and Chapter 6 is largely excerpts from this paper.

The remainder of this dissertation focuses on our efforts towards *in situ* imaging of 2D vortex distributions, beyond the proof-of-principle results presented in Chapter 6. In Chapter 7, I present further treatment of the dark-field imaging numerics, with the goal of understanding the effect of mask size, detuning and other imaging parameters on vortex core signal. Chapter 8 covers the initial design, offline testing, and implementation of the second phase of the quantum vortex microscope, dubbed QVM2. Chapter 9 contains a summary and preliminary analysis of the QVM2 images to date, a discussion of the limitations of the QVM2 with suggestions for improvements to be considered when designing a QVM3, and a discussion of the unexpected observation of *in situ* vortex cores with both bright-field absorption, and Faraday imaging techniques. Finally, in Chapter 10, I present my conclusions and outlook for further development of this toolkit and its application to 2DQT experiments in dilute-gas BECs.

## 1.2 Introduction to turbulence

### 1.2.1 Key ideas in 2D turbulence

From a phenomenological standpoint, Lesieur [10] and Sommeria [11] define classical turbulence as fluid flow that is disordered in space and time, is unpredictable, exhibits rapid mixing (compared to diffusion timescales), and exhibits interactions between a wide range of length scales. A classical two-dimensional turbulent flow is represented by its velocity field $\vec{v}(x, y, t)$ confined in the $x$-$y$ plane and the corresponding vorticity field,

$$\vec{\omega}(x, y, t) = [\nabla \times \vec{v}(x, y, t)], \tag{1.1}$$

which gives a measure of the rotation in the fluid. For the case of strictly 2D fluid flow, $\vec{\omega}$ is oriented along the $z$-direction. For fluid flow to be considered 2D, the velocity vector must be confined to two dimensions such that $\vec{v}(x, y, t)$ of Eqn. 1.1 has no $z$ component. However, the fluid itself can extend in the third dimension; thus a thin atmospheric layer can exhibit 2D flow. In an inviscid fluid, kinetic energy

$$E = \frac{1}{2} \int \rho v^2 dx dy \tag{1.2}$$

is conserved, regardless of the dimensionality of the fluid. Here $\rho(x, y)$ is the 2D mass density. In two-dimensions, vortex-stretching in the $\hat{z}$ direction is prohibited resulting in a second conserved entity, namely enstrophy, defined by integrating over the square of vorticity,

$$\Omega = \frac{1}{2} \int \omega^2 dx dy. \tag{1.3}$$

Given their disordered and unpredictable nature, turbulent flows are often characterized by statistical properties of the system such as kinetic energy spectra $E(k)$, which specifies the distribution of kinetic energy among the various length scales $\ell$ of the system. Here the wavenumber $k = 2\pi/\ell$ corresponds to a spatial frequency, or inverse length. Kraichnan [8] identified the existence of two inertial ranges in forced 2D classical turbulence, associated

with distinct kinetic energy and enstrophy spectra and both energy and enstrophy flux between length scales. The first range extends from a mid-range forcing length scale to larger length scales, with kinetic energy spectra $E(k) \propto k^{-5/3}$, and is characterized by an inverse energy cascade where energy flows from the forcing length scale to larger length scales. This inverse energy cascade may result in spectral condensation, or a build up of kinetic energy, at low wavenumbers, on the order of the size of the system. The second range extends from the forcing length scale to smaller length scales and is characterized by an direct enstrophy cascade giving the kinetic energy spectrum $E(k) \propto k^{-3}$ behavior. This dual cascade of entropy and enstrophy is a conspicuous feature of two-dimensional classical turbulence and has been observed experimentally in soap films [12].

Onsager [7, 13] gives a complementary statistical mechanics argument for the emergence of large-scale vorticity in a system of point vortices confined to two dimensions. In the point-vortex model, the configuration-space variables $x_i$ and $y_i$ for a given vortex are canonical conjugate variables following the equations of motion,

$$\kappa_i \frac{dx_i}{dt} = \frac{\partial H}{\partial y_i} \tag{1.4}$$

$$\kappa_i \frac{dy_i}{dt} = \frac{\partial H}{\partial x_i} \tag{1.5}$$

where $\kappa_i$ is the circulation of the $i$th vortex, and the Hamiltonian describing the inter-vortex energy in an unbounded system is

$$H = -\frac{1}{2\pi} \sum_{i>j} \kappa_i \kappa_j \ln(r_{i,j}/L) \tag{1.6}$$

where $r_{i,j}$ is the separation between any two vortices $i$ and $j$, and L is an arbitrary length scale. Tightly packed ($r_{i,j} << L$) clusters of like-signed vortices thus contribute large point-vortex energy to a vortex distribution.

Given that $x$ and $y$ are canonical conjugate variables, the phase space of the system is the same as the configuration space accessible to the vortex cores. In other words, a vortex has just two degrees of freedom, $x$ and $y$, such that placing a set of vortices in

space completely defines the state of the vortex distribution. This means that imposing a physical boundary on the system also imposes a boundary on the accessible phase space. If we consider the statistical mechanics definition of temperature $T = dE/dS$, with entropy $S$ corresponding to the natural log of the number of accessible vortex distributions with a given point-vortex energy $E$, bounding phase space results in the possibility of negative-temperature states, in that, above some threshold point-vortex energy, states with higher point-vortex energy have fewer accessible vortex distributions, and therefore lower entropy, than lower energy states since the vortices cannot just push apart indefinitely. For distributions with sufficiently high point-vortex energies, the configurations corresponding to maximum entropy contain large coherent groups of like-signed vortices, such that order seems to emerge from chaos. In other words, a vortex distribution containing higher energy clusters of closely packed like-signed vortices gives more space for the rest of the vortex cores to distribute themselves more freely, with fewer constraints and thus higher entropy.

Onsager's statistical approach has yet to be tested experimentally in classical fluids, in part because turbulent classical velocity fields cannot be easily described as systems of point vortices. In contrast, a 2D quantum fluid, with quantized vortices localized in space may provide an excellent testing ground for Onsager's playful vortices [14].

### 1.2.2 2DQT: turbulence in BECs

From a hydrodynamic perspective, a dilute-gas BEC is a tiny droplet of superfluid with a velocity,

$$\vec{v}(\vec{r},t) = \frac{\hbar}{m}\nabla\phi(\vec{r},t), \tag{1.7}$$

proportional to the gradient of the phase $\phi(\vec{r},t)$ of the BEC wavefunction

$$\psi(\vec{r},t) = \sqrt{n(\vec{r},t)}e^{i\phi(\vec{r},t)} \tag{1.8}$$

where $n(\vec{r},t)$ is the density profile of the BEC.

While superfluids are by definition irrotational with $\nabla \times \vec{v} = 0$, BECs support circular fluid flow in the form of vortices of quantized circulation located at singularities in the quantum phase profile. At each phase singularity, $\nabla \times \vec{v}$ is formally infinite, but the density at the location of the singularity is zero. These vortices are associated with either clockwise or counter-clockwise fluid flow [7, 15, 16] and are observed to group into metastable structures such as vortex dipoles and clusters [3]. See Ref. [2] for a discussion of BEC vortex experiments up to 2010.

In a system with quantized vortices, the vorticity field consists of discrete points of vorticity coincident with each vortex, and enstrophy is proportional to the total number of vortices. Adapting Lesieur's phenomeological definition of classical turbulence [10], we identify 2DQT as a highly disordered configuration of vortices with a wide range of intervortex separations, unpredictable vortex dynamics, and rapid mixing such that vortices disperse rapidly throughout the BEC as compared to other system timescales. When considering 2DQT in BECs, the fluid flow is restricted to two dimensions, meaning that 3D phenomena such as Kelvin waves, and vortex crossings and reconnections are eliminated as mechanisms for dissipating energy and enstrophy [17], leaving vortex-antivortex annihilation as the predominate decay mechanism. While we generally work with highly oblate BECs to achieve this 2D fluid flow, our BECs are clearly three-dimensional with a chemical potential $\mu_0 \sim 8\hbar\omega_z$, where $\omega_z$ is the axial trapping frequency of our harmonic trap.

## 1.3 State of 2DQT studies in BECs

While 3D quantum turbulence has been studied experimentally in superfluid $^4$He for many years [18, 19] and more recently in dilute-gas BECs [20, 21], the field of 2DQT in dilute-gas BECs is relatively new, and at present predominately restricted to theory and numerics. In this section I present an overview of a selection of recent, primarily numerical, advances in 2DQT in an effort to motivate the experimental efforts presented in this dissertation.

Much of this work addresses the potential for observation of Onsager-Kraichnan conden-

sation, the emergence of large-scale vortex clusters associated with negative-temperature point-vortex distributions linked with spectral condensation at the system scale [6], in a compressible 2D fluid, and explores questions such as the role of forcing and dissipation. In dilute-gas BECs, vortex-antivortex annihilation allows for transfer of energy between the incompressible kinetic energy associated with vortex cores, and the compressible kinetic energy associated with phonons and acoustic energy. In addition to allowing energy exchange, vortex-antivortex annihilation removes a pair of oppositely charged vortices from the system with the result that enstrophy is no longer conserved. At present it is unclear to what degree this decay mechanism prohibits Onsager-Kraichnan condensation in dilute-gas BEC experiments, leading to open questions involving the role of vortex clustering, and whether we can we seed an initial vortex distribution with sufficiently high point-vortex energy, or sufficiently large vortex cluster fraction, to suppress the vortex-annhilation decay mechanism and observe Onsager's negative-temperature states. More broadly, the goal is to link statistical measurements of turbulence such as kinetic energy spectra to vortex distributions and vortex dynamics.

To date there have been just a handful of experimental studies of 2DQT in BECs. In 2013, Neely *et al.* [22] observed the formation of large-scale persistent currents due to small-scale forcing. A small-scale stir with a blue-detuned laser beam resulted in an initially disordered vortex distribution which then evolved into a large-scale persistent current pinned to the beam. Complementary numerics, using the experimental parameters, predicted the formation of coherent vortex structures, and an incompressible kinetic energy spectrum $E_i \propto k^{-5/3}$ for $k < k_{\text{force}}$, where $k_{\text{force}}$ is associated with the inverse of the stirring length scale. Rooney *et al.* [23] used the observations of this experiment, namely the number of free vortices and the winding number of the persistent current, as a test of classical-field theory, and report that both damping and noise must be taken into account in order to give a quantitatively accurate model of the experimentally observed time-dependent vortex statistics.

More recently, Kwon *et al.* [24], generated a large disordered vortex distribution by moving a repulsive obstacle rapidly through a BEC. They measured the vortex decay rate, primarily attributed to vortex-antivortex pair annihilation, and suggest this measurement as an additional test of classical-field theory. Their study was motivated in part by the controversy over whether vortex-pair annihilation prohibits the inverse energy cascade in a compressible fluid.

Numerical studies of 2DQT are more prevalent and here I summarize a selection of the recent studies. In 2012, Bradley and Anderson [25] provided an analytical method for obtaining the approximate incompressible kinetic energy spectra associated with vortices, and identify the role of the vortex core in the large-$k$ region of the incompressible kinetic energy spectrum. While the energy decomposition ignores the role of the quantum phase and is not directly physically measurable, the incompressible kinetic energy spectrum provides a direct analog to the hydrodynamic kinetic energy spectrum in a classical fluid. Reeves *et al.* [26] further explore the role of the BEC's quantum phase in the quantum kinetic energy spectrum and identify a link between the quantum hydrodynamic kinetic energy spectrum and the experimentally measurable momentum distribution, in the limit of low acoustic energy.

In an effort to explore potential forcing mechanisms and to link vortex distributions with kinetic energy spectra, Reeves *et al.* [27], consider forcing regimes that may yield signatures of turbulence. They simulate a circular stir with a repulsive potential in a BEC confined in a harmonic trapping potential and link the resulting vortex dynamics to kinetic energy spectra for a range of stirring parameters. More recently, Billam *et al.* [6] developed a first-principles treatment of Onsager's point-vortex model for 2D BECs, and provided a link between the emergence of large-scale vortex clusters and spectral condensation at the system scale as end states of decaying 2DQT in a homogenous compressible 2D superfluid.

Lastly, Reeves *et al.* consider the development of a von Kârmân vortex street, another example of large-scale vorticity commonly observed in classical fluids, and link the

resulting vortex distribution in the flow behind an obstacle to quantum analogs of the Reynolds number used to classify fluid flow in classical systems, and an effective viscosity that emerges from the nucleation of quantum vortices [28].

While the current state of numerics seems promising in terms of identifying regimes where vortex clustering occurs and methods to statistically characterize said clustering, these numerics generally treat large homogenous systems and the extension of their results to the smaller, inhomogenous systems that are currently experimentally accessible is unclear. This results in an experimental wishlist of sorts, where I imagine an experimentally realizable system containing a large number of vortices within a homogenous BEC confined within a flat-bottomed hardwall potential [29]. In this ideal system I would be able to nucleate vortex distributions with high point-vortex energy and minimal acoustic energy, or in other words to nucleate a large number of clusters of vortex cores with control over placement and circulation of these clusters. Lastly, I would be able to observe the vortex distribution in real time and link the subsequent dynamics with measurements of kinetic energy spectra. While some of the experimental techniques comprising my dream experiment, such as direct measurements of kinetic energy spectra, may be a long way from realization, the vortex generation and *in situ* imaging techniques described in this dissertation represent a significant, concrete step towards developing the experimental toolkit necessary to enable experimental studies of 2DQT in BECs.

# Chapter 2
# Experimental Apparatus

Our $^{87}$Rb BEC apparatus is optimized for large BECs with $N \sim 2\times10^6$ atoms and lifetimes on the order of 60 s, and allows for a versatile range of trapping geometries including, but not limited to, an $R_\mathrm{r} : R_\mathrm{z} \sim 2 : 1$ magnetic time-averaged orbiting potential (TOP) trap [30], an $R_\mathrm{r} : R_\mathrm{z} \sim 10 : 1$ hybrid optical and magnetic trap, and a toroidal trap formed with the hybrid trap and an additional axial repulsive potential. Here $R_\mathrm{r}$ and $R_\mathrm{z}$ are the radial and axial Thomas-Fermi radii. A number of our experiments begin by nucleating vortices with an obstacle formed by a blue-detuned laser beam, and we control the motion of this beam with respect to the center of the BEC either through a set of piezoelectric transducer (PZT)-controlled steering mirrors to move the beam directly, or through a set of magnetic field coils, referred to as 'push coils,' used to push the BEC past a stationary beam.

In this chapter we give a brief overview of experimental details relevant to the research discussed in this dissertation and refer the reader to previous dissertations from the University of Arizona BEC lab for a more in depth description of the experimental components. In particular, the design and construction of the experimental apparatus is primarily described in David Scherer's dissertation [31]. This includes the Labview-controlled timing system, the lasers used for trapping and imaging, the magneto-optical trap (MOT) used for preliminary cooling, the transfer system used to move atoms from the MOT to the science cell, and the evaporation sequence used to reach the BEC transition. Chad Weiler's dissertation [32] adds information regarding phase-contrast imaging and the design of the phase mask. Tyler Neely's dissertation [33] discusses the design and implementation of the 1090-nm laser and various configurations of the hybrid trap employing this laser, as well as toroidal trap configurations and the push coils used to move the BEC past a repulsive barrier. Lastly, Carlo Samson's dissertation [34] discusses the PZT-controlled steering mirrors

used to vary the 660-nm stirring beam position in the horizontal plane at the BEC.

## 2.1 Trapping potentials

We used three different traps to achieve the BEC geometries desired for this dissertation. The first is a standard magnetic TOP trap [30], the second is a variation on the standard TOP trap that employs a 1D field oscillation rather than a 2D rotating field (our '1D TOP trap'), and the third is a hybrid trap with a 1090-nm red-detuned cylindrical laser beam providing additional tight confinement along the $z$-direction of the TOP trap.

Regardless of trapping geometry, BEC formation begins with preliminary cooling in a 3D MOT. A set of magnetic field coils, referred to as the 'transfer coils', are used to transfer approximately a third of the pre-cooled atoms about a meter through the vacuum chamber to the BEC cell where evaporative cooling through the BEC transition occurs. The evaporative cooling is achieved with an RF transition between the trapped $|F = 1, m_{\rm F} = -1\rangle$ and untrapped $|F = 1, m_{\rm F} = 0\rangle$ and $|F = 1, m_{\rm F} = 1\rangle$ Zeeman sublevels, resulting in a typical BEC of about $2 \times 10^6$ $^{87}$Rb atoms in the $5^2{\rm S}_{1/2}$ $|F = 1, m_{\rm F} = -1\rangle$ ground state.

### 2.1.1 TOP trap

Our TOP trap combines a DC quadrupole magnetic field of variable axial gradient $B'_{\rm z}$, with an AC bias field of magnitude $\rm B_0$ rotating in the $x$-$y$ plane with frequency $\omega_{\rm TOP} = 2\pi \times 4$ kHz. The time-dependent bias field with $x$ and $y$ components

$$B_{\rm x}(t) = B_0 \cos(\omega_{\rm TOP} t) \tag{2.1}$$

$$B_{\rm y}(t) = B_0 \sin(\omega_{\rm TOP} t) \tag{2.2}$$

results in the minimum of the quadrupole field orbiting in a circle within the $x$-$y$ plane. For an atom with magnetic dipole moment $\mu$ and mass $m$, the time average of the combined

magnetic fields results in a harmonic potential with trap frequencies determined by

$$\omega_{\rm x} = \omega_{\rm y} = \left[\frac{\mu B_{\rm z}'^2}{8mB_0}(1+\eta^2)\sqrt{1-\eta^2}\right]^{1/2} \tag{2.3}$$

$$\omega_{\rm z} = \left[\frac{\mu B_{\rm z}'^2}{mB_0}(1-\eta^2)^{3/2}\right]^{1/2} \tag{2.4}$$

where the factors involving $\eta = mg/\mu B_{\rm z}'$ account for the vertical sag due to gravity (with acceleration $g$) of the TOP trap minimum from that of a static quadrupole field. Such traps are now in common use; see Refs. [30, 35] for a detailed description of TOP traps.

In a typical two-stage evaporation sequence, atoms are loaded into the quadrupole trap with the quadrupole magnetic field gradient set to $B_{\rm z}' = 160$ G/cm and held for 10 s, after which point the rotating bias field, the quadrupole field, and the RF frequency jump to $B_0 = 43$ G, $B_{\rm z}' = 266$ G/cm, and $\nu_{\rm RF} \sim 60.3$ MHz respectively. $B_{\rm z}'$ is held constant while $B_0$ and $\nu_{\rm RF}$ ramp to $B_0 = 5$ G and $\nu_{\rm RF} \sim 7$ MHz respectively over a period of about 60 s. We refer to the magnetic field configuration at the end of this bias field ramp as the 'tight trap.' To complete the initial stage of evaporation, the BEC is held in the tight trap and the RF frequency is ramped down to $\nu_{\rm RF} \sim 5.1$ MHz over 12 s. After this 'tight cut', $\nu_{\rm RF}$ jumps to 5.3 MHz, and $B_{\rm z}'$ is ramped from 266 G/cm to approximately $50 - 55$ G/cm over 2 s. We refer to this final magnetic field configuration as the 'sag trap' since the equilibrium trapping position is about 0.6 mm below the center of the quadrupole field due to gravity, and we adjust the final value of $B_{\rm z}'$ to maintain a consistent vertical position for the BEC from day to day. We suspect that the day-to-day fluctuations in the BEC sag trap position are due to MOSFET calibration issues so tweaking the value of $B_{\rm z}'$ in the Labview timing program is effectively adjusting the calibration rather than the actual field gradient associated with a given sag position. All of the magnetic field values reported here are the values entered into the timing program and the actual field values may differ slightly. The atoms are held in the sag trap for 6 s to allow for thermal damping of any excitations that may have occurred during the quadrupole ramp; at this point the

distribution is still mostly thermal. Lastly, we ramp the RF frequency to $\nu_{\mathrm{RF}} \sim 4.8$ MHz to cool below the BEC transition. This final evaporation stage is referred to as the 'sag cut.' The two-stage evaporation process results in BECs of $5\,^2S_{1/2}\ |\mathrm{F}=1, m_{\mathrm{F}}=-1\rangle\ ^{87}\mathrm{Rb}$ atoms, with radial and axial trap frequencies of $(\omega_{\mathrm{r}},\ \omega_{\mathrm{z}}) \sim 2\pi \times (8, 16)$ Hz, BEC atom numbers of $N \sim 1.8 \times 10^6$, and BEC Thomas-Fermi radii of $(R_{\mathrm{r}}, R_{\mathrm{z}}) \sim (35, 19)\ \mu$m.

### 2.1.2 1D TOP trap

As we will discuss in Chapter 3, the rotating bias field inherent in the TOP trap means that the net magnetic field vector never points directly along the vertical imaging axis ($\hat{z}$), resulting in suboptimal imaging conditions. At the same time, the rotating bias field is necessary to avoid Majorana spin flip loses near the $B = 0$ point of the quadrupole field [30]. One way around this difficulty is to work with a bias field that oscillates in 1D, in our case oscillating along the $y$-axis, rather than rotating in a circle in the $x - y$ plane. Reducing the time-averaged rotating bias field to a 1D oscillation does mean that the net bias field passes through zero twice every 4 kHz cycle, however at the sagged BEC position $B_{\mathrm{z}} \sim 3$ G resulting in a net magnetic field that is greater than zero.

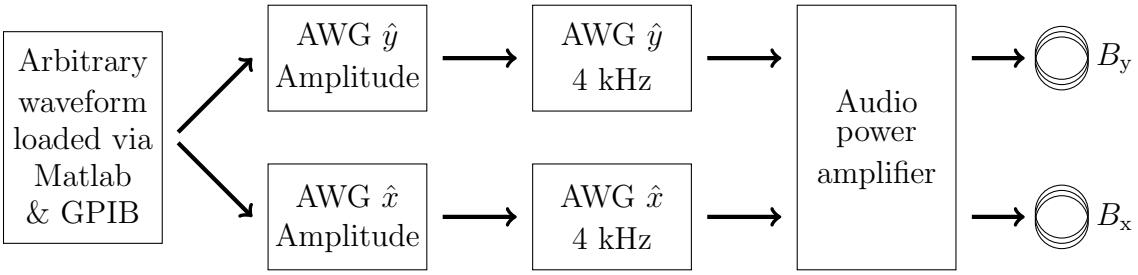


Figure 2.1: Schematic showing the AWG control for a 1D TOP trap.

The 1D TOP trap requires independent control of the amplitudes of $B_{\mathrm{x}}(t)$ and $B_{\mathrm{y}}(t)$ in Eqns. 2.1 and 2.2. To achieve this we used four SRS arbitrary waveform generators (AWGs) configured as shown in Fig. 2.1. As with the standard TOP trap, the desired amplitudes $B_{0,\mathrm{x}}$ and $B_{0,\mathrm{y}}$ are loaded as arbitrary waveforms onto the appropriate amplitude AWG.

Each amplitude AWG is used to externally modulate the amplitude of the 4 kHz sine wave generated by the corresponding 4 kHz AWG. The output of each 4 kHz AWG provides the input to one channel of a two-channel audio power amplifier, which provides the necessary power to the bias field coils. Both 4 kHz AWGs reference the same timebase and their relative phase can be adjusted to round out the trap. The amplitudes and the relative phase of the bias field coils are monitored with a pair of pickup coils mounted in line with each bias coil, and we note that the sinusoidal voltage signal read off from a pickup coil is out of phase from the actual current, and the corresponding bias field value, by approximately 90°.

For more efficient evaporation we start each run in the TOP trap and run through the normal evaporation sequence up to and including the $B'_{\rm z}$ ramp to the sag trap configuration. At this point we jump the RF frequency out to $\nu_{\rm RF} \sim 6.5$ MHz, and transition to the 1D TOP trap by ramping $B_{0,{\rm x}}$ to zero while simultaneously ramping $B_{0,{\rm y}}$ to $1.65 \times 5$ G over $t_{\rm ramp} = 2$ s. The ramp follows the form of $\cos^2(\Delta t/2t_{\rm ramp})$ where $\Delta t$ is the time from the start of the ramp. We found that increasing $B_{0,{\rm y}}$ was necessary to keep the vertical position of the BEC constant. After the bias field ramps, we hold for 4 s and then perform the sag cut to a final RF frequency of $\nu_{\rm RF} \sim 6.35$ MHz. The BECs formed in the 1D TOP trap are now asymmetric in the $x$-$y$ plane, with $R_{\rm x}/R_{\rm y} \sim 3/4$.

### 2.1.3 Hybrid optical and magnetic trap

To obtain a highly oblate BEC geometry conducive to studies of 2D superfluid dynamics, we work in a hybrid trap consisting of the TOP trap, in either the 1D or the 2D bias field configuration, with additional axial confinement provided by a red-detuned 1090-nm laser beam. As shown in Fig. 2.2, the 1090-nm beam propagates along the $y$-axis. An $f = 100$ mm cylindrical lens focuses the beam in the $z$ direction such that the $1/e^2$ beam radii at the BEC location are $w_{\rm x} \sim 2$ mm and $w_{\rm z} \sim 20$ $\mu$m. We use a 1090-nm beam power $P_{1090} \sim$ 200-400 mW, resulting in a measured axial trap frequency of $\omega_{\rm z} \sim 2\pi \times 70$ Hz

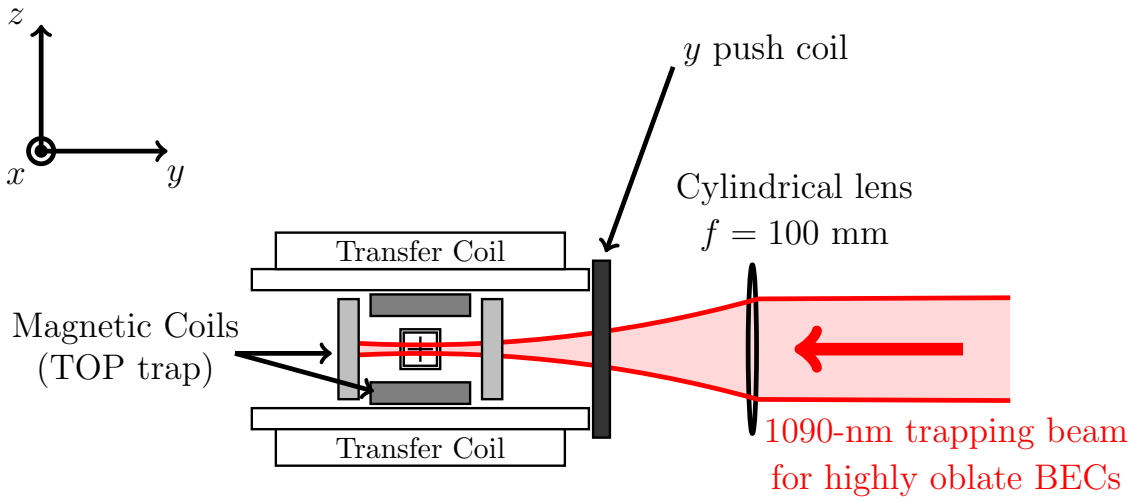


Figure 2.2: Layout of the hybrid optical and magnetic trap

(for $P_{1090} = 200$ mW). The radial trap frequency should be similar to the TOP trap radial frequency, $\omega_x \sim 2\pi \times 8$ Hz. Typical BEC atom numbers are $N \sim 2 \times 10^6$. We note that the 1090-nm beam power used is considerably less than the power reported for the experiments in Refs. [3, 22, 33]. Our primary reason for lowering the power was observed heating and overall poorer BEC quality at higher powers.

At this point we should note a few changes regarding the operation of the 1090-nm laser used for the hybrid trap, from that described in Refs. [33, 34]. First, we removed the polarizing beamsplitter cube (PBSC) in the 1090-nm beam path between the shutter and the AOM. This allows us to operate the 1090-nm laser at a lower power, which was necessary given that the laser now undergoes power fluctuations when we run it above about 7 W. Second, we replaced the quadrant photodiode located in the 1090-nm beam path after the beam passes through the BEC cell with a photodiode located in the 1090-nm laser box, placed in the beam path directly after the AOM and 1090-nm beam focusing optics. This photodiode is used to provide the signal for the 1090-nm power servo loop.

## 2.2 Spin up of a vortex lattice

For the various imaging techniques presented in this dissertation, our trusty test vortex distribution was a vortex lattice. The lattice provides a reproducible vortex distribution with a regular arrangement of cores, making it easier to pick out vortex core signal above a noisy background. In addition, the angular momentum added through rotating the BEC results in the vortices aligning with the axis of rotation and imaging, giving good vortex core contrast and approximating the 2D vortex distributions that we ultimately want to image. Our approach to spinning up a lattice is implemented by squeezing and rotating the magnetic trapping field as first implemented by Hodby *et al.* [36].

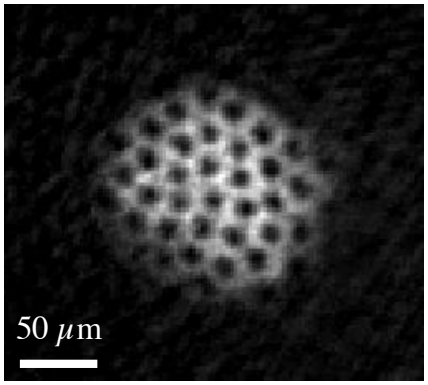


Figure 2.3: An image of a slightly irregular vortex lattice in a rotating BEC released from our TOP trap. The image was taken after a period of expansion, using bright-field absorption imaging with standard image processing and contrast inversion such that bright pixel values indicate higher atom column density. Vortices are observed as dark regions associated with zero atom column density.

In order to rotate and add angular momentum to the atomic cloud it is necessary to break the symmetry of the trapping potential. In our case this is done by adding an additional bias field to the rotating bias field for the symmetric TOP trap described in

Sec. 2.1.1 so that now

$$B_{\rm x} = B_0 \cos(\omega_{\rm TOP} t) + B_\epsilon \cos(\omega_{\rm mod} t) \tag{2.5}$$

$$B_{\rm y} = B_0 \sin(\omega_{\rm TOP} t) - B_\epsilon \sin(\omega_{\rm mod} t) \tag{2.6}$$

where $B_0 = 5$ G is the magnitude of the TOP trap rotating bias field, $B_\epsilon \sim 0.1\, B_0$ determines the magnitude of squeezing, $\omega_{\rm TOP} = 2\pi \times 4$ kHz is the frequency of the TOP trap, and $\omega_{\rm mod}$ is the frequency of the modulating bias field. If $\omega_{\rm mod} = \omega_{\rm TOP}$ the asymmetric bias field causes the time-averaged trap to have stationary ellipsoidal potential energy surfaces in the $x$-$y$ plane with the ratio of the minor and major axes determined by $B_\epsilon$ and $B_0$. Increasing $B_\epsilon$ with respect to $B_0$ increases the ellipticity. If $\omega_{\rm mod} \neq \omega_{\rm TOP}$ the ellipse rotates in the $x$-$y$ plane with frequency $\omega_{\rm s} = |\omega_{\rm mod} - \omega_{\rm TOP}|/2$. The direction of rotation of the ellipse can be switched between clockwise and counter-clockwise by flipping the sign of $\omega_{\rm mod} - \omega_{\rm TOP}$. In the TOP trap, choosing $\omega_{\rm s} \sim 0.7\omega_{\rm r}$ excites the quadrupole mode which decays to a collection of quantized vortex cores of the same circulation. The minimum energy configuration of the rotating BEC consists of a large regular lattice of vortices [37]. A representative vortex lattice formed by spinning the BEC in our purely magnetic TOP trap (i.e., without the red-detuned trapping potential) is shown in Fig. 2.3.

## 2.3 660-nm repulsive obstacle

Many of our vortex nucleation techniques rely on moving the BEC past an obstacle, namely the repulsive potential due to a blue-detuned 660-nm laser beam propagating vertically through the BEC as shown in Figs. 2.4 and 2.5. The exact implementation of the 660-nm beam depends on the desired $1/e^2$ beam radius and range of travel of the beam with respect to the BEC center. We will present a basic overview here and leave a discussion of specific implementations to the relevant sections as necessary.

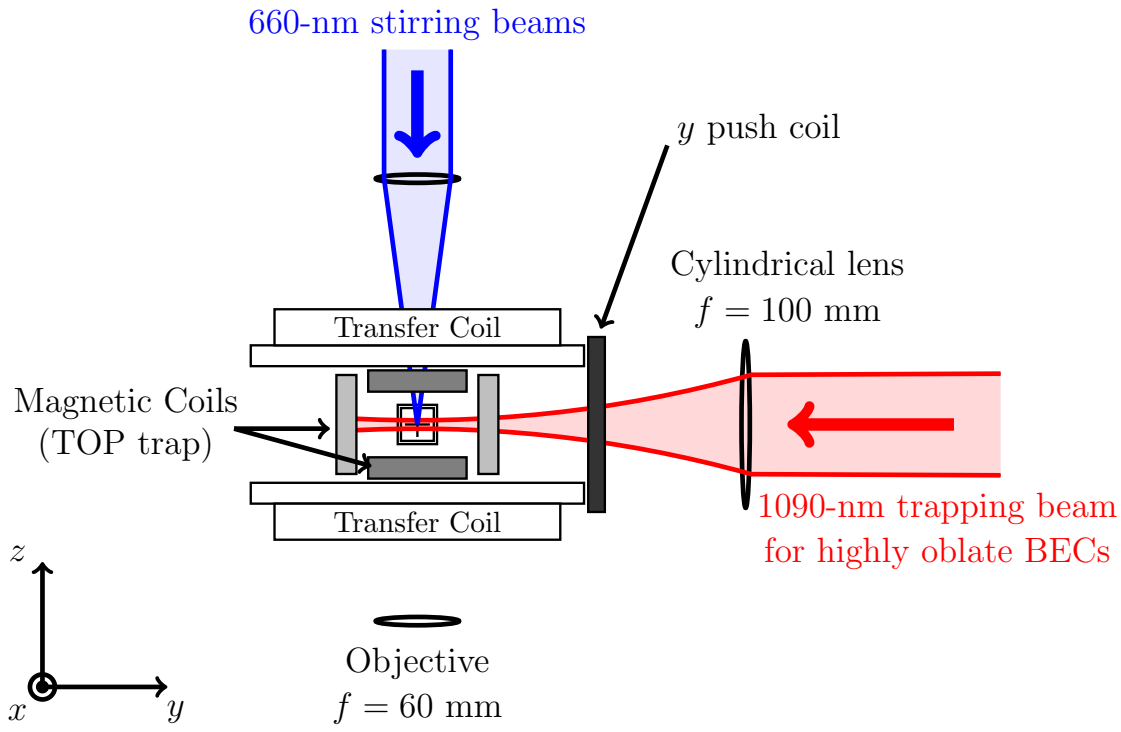


Figure 2.4: Layout of the hybrid trap with 660-nm stirring beams - $M \sim 5$ imaging system.

### 2.3.1 PZT-controlled stirring beam

As shown in Fig. 2.6, the 660-nm stirring beam is controlled by a set of two PZT-controlled stirring mirrors labeled A in the image. We have a second set of stirring mirrors, labeled B, although for the experiments in this dissertation we never required two stirring beams. Each mirror has one tilt axis that is controlled by applying a voltage to a PZT stack (Noliac SCMAP02), while the other is controlled with a standard fine-thread screw. The two mirrors combined give complete control of the beam position in the horizontal plane at the BEC location. To increase the beam travel in the $x$-$y$ plane at the BEC, the 660-nm beam passes through a minifying telescope with magnification $M$. Since angular magnification is inversely proportional to spatial magnification, the deflection of the beam due to the PZT mirrors is magnified, while the $1/e^2$ beam radius of the collimated 660-nm beam exiting

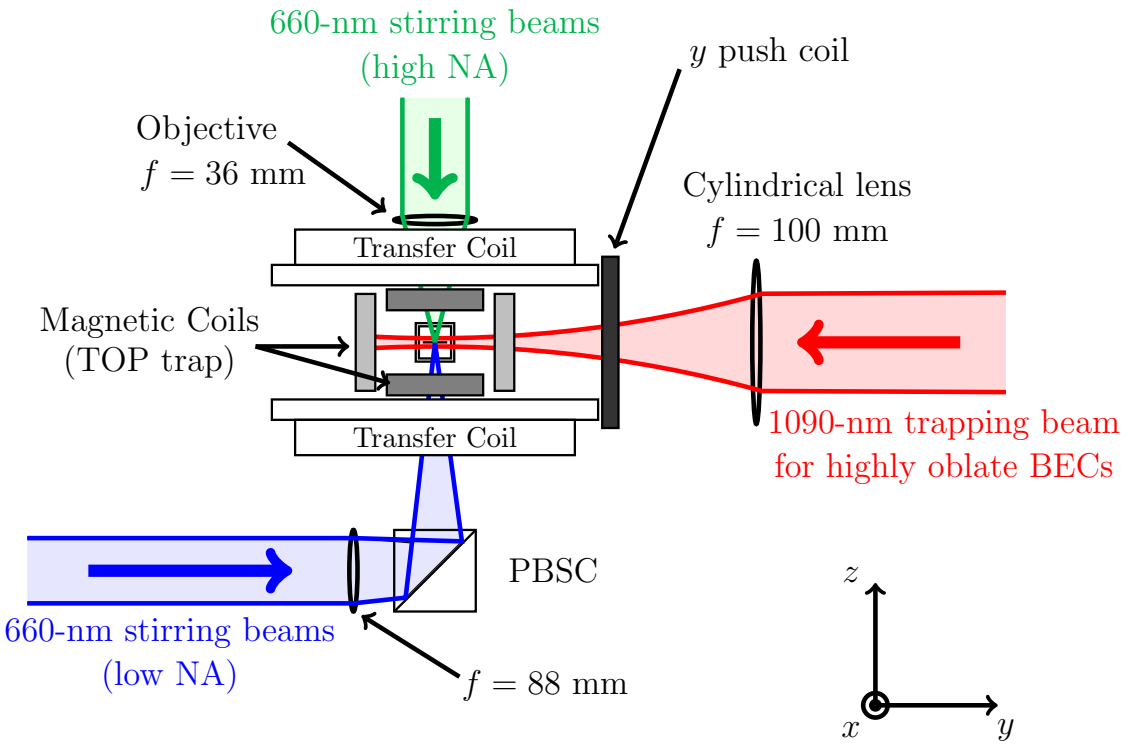


Figure 2.5: Layout of the hybrid trap with 660-nm stirring beams - $M \sim 11$ imaging system.

the telescope is reduced. This reduction in the collimated 660-nm beam radius results in a larger focused beam radius at the location of the BEC. For the configuration shown in Fig. 2.6, with $M \sim 1/2$ ($f_1 = 300$ mm, $f_2 = 150$ mm), the collimated beam was focused with a lens with a focal length $f = 88.3$ mm (Newport KPX091), and directed upwards through the BEC cell, along the low NA path shown in Fig. 2.5. This configuration resulted in a $1/e^2$ beam radius of 8 $\mu$m and an overall beam travel of approximately 70 $\mu$m along either $\hat{x}$ or $\hat{y}$ in the $x$-$y$ plane at the location of the BEC.

For the vortex generation experiments discussed in Chapter 4, we used a PZT mirror setup similar to the one shown in Fig. 2.6 but directed the beam down through the center of the BEC cell through an $f = 75$ mm lens as shown in Fig. 2.4.

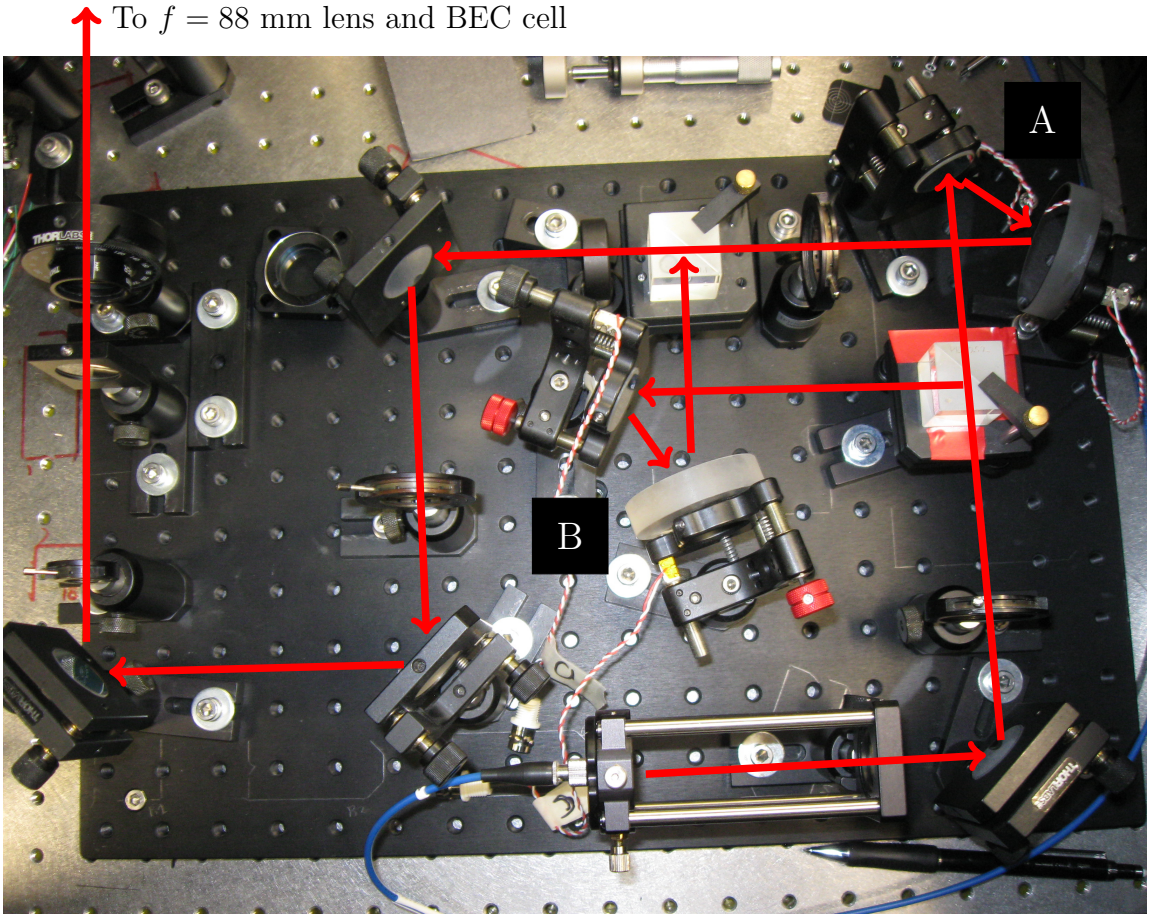


Figure 2.6: PZT-controlled stirring beam setup - below cell. The red arrows show the 660-nm beam path, with (A) and (B) denoting the PZT-controlled mirrors. While similar to the original implementation used with the $M \sim 5$ imaging system, this particular implementation was put in place after the implementation of the $M \sim 11$ imaging system.

### 2.3.2 Push coils

While the PZT-controlled stirring mirrors provide fine control over the 660-nm beam position in the horizontal plane at the BEC, their range is limited, and increasing the range of 660-nm beam travel comes at the expense of the focused $1/e^2$ beam radius of the 660-nm beam, in that we end up with a wider repulsive obstacle at the BEC. With that in mind, we have an alternate method for moving the beam relative to the BEC, employing a pair of

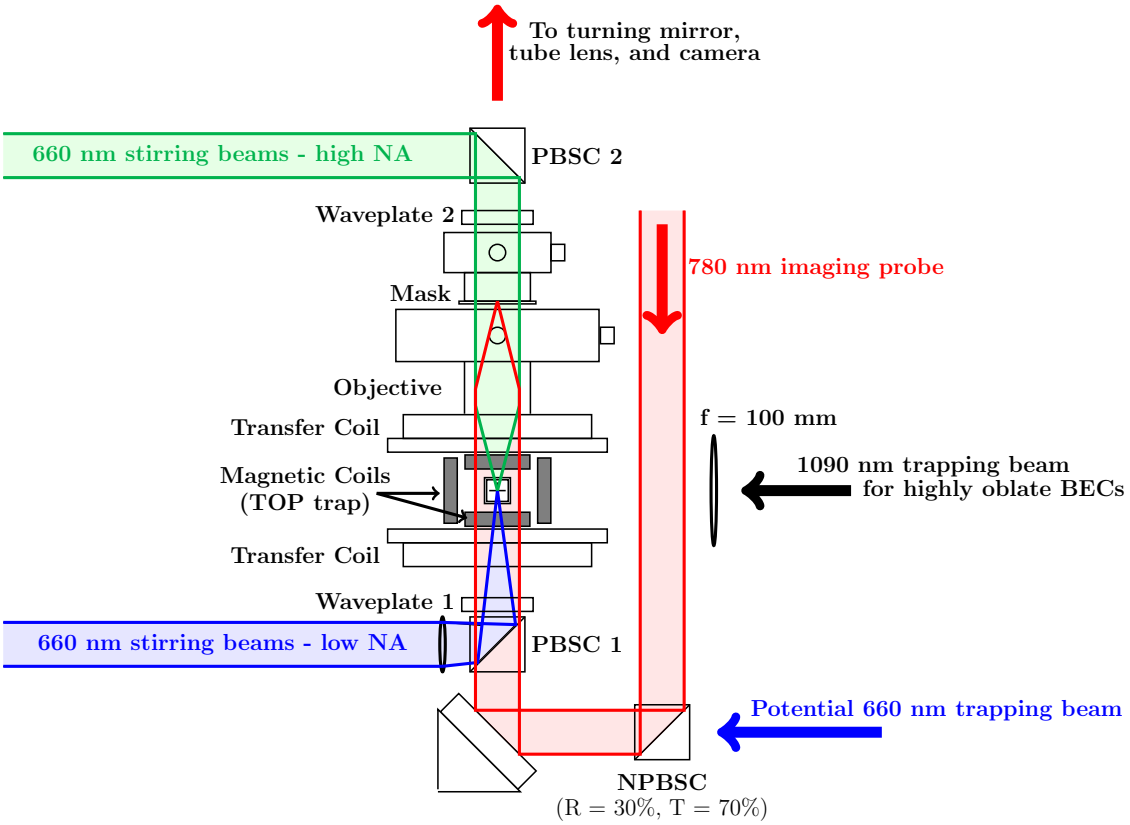


Figure 2.7: Layout of the QVM2 - Beam paths.

orthogonal electromagnetic 'push' coils to translate the zero-point of the magnetic trapping potential in the horizontal plane. By moving the trap center we move the BEC position relative to a stationary beam. The push coil response is approximately linear over a range of 240 $\mu$m. While the push coil method allows us to move the entire BEC past the 660-nm obstacle, moving the BEC across structure in the 1090-nm beam may result in unwanted heating. Generally we find it works better to move the BEC along the axis of propagation of the 1090-nm beam ($y$-axis) rather than across the beam along the $x$-axis.

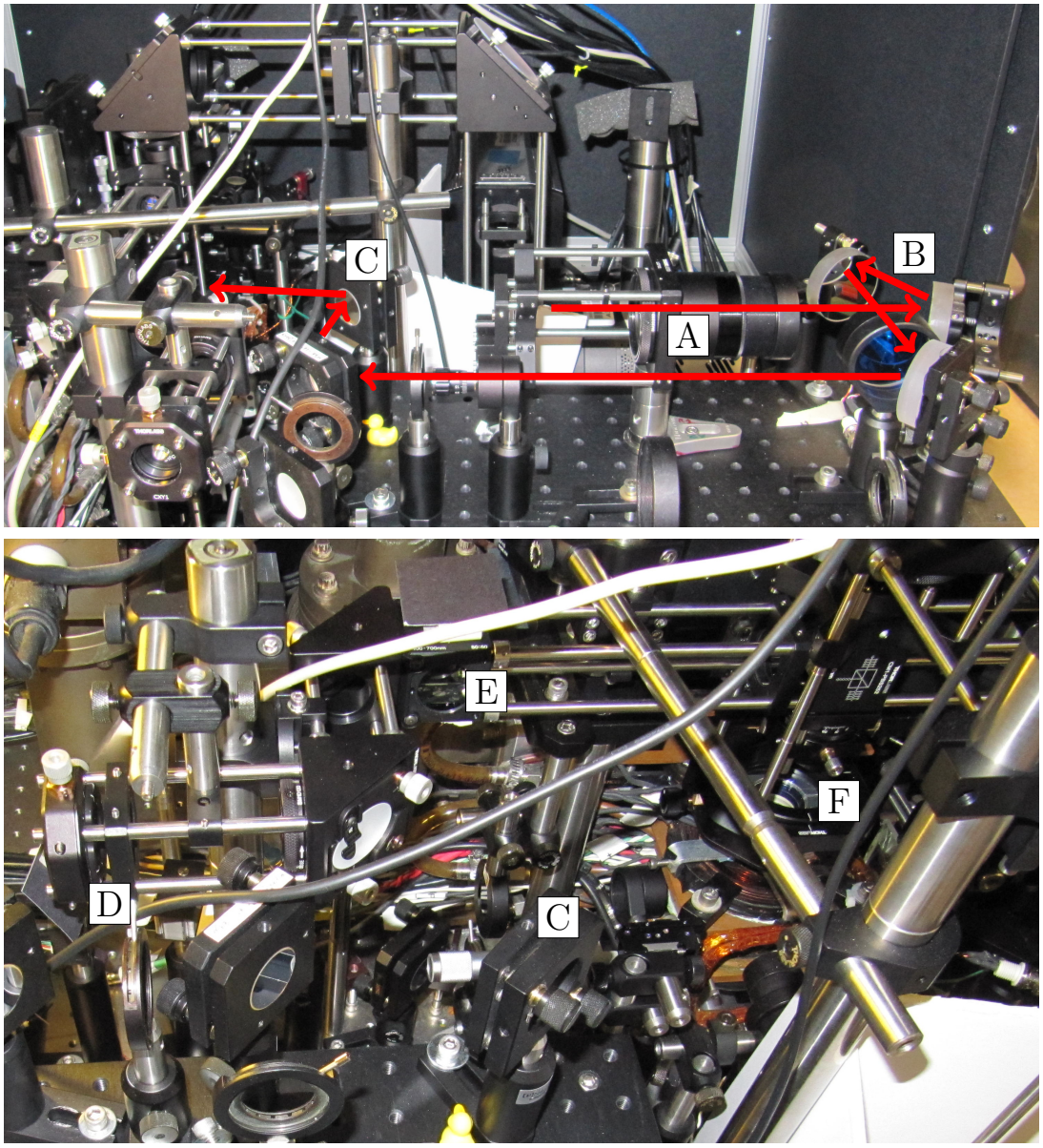


Figure 2.8: High NA 660-nm stirring beams - above cell. Red arrows show the 660-nm beam path for the PZT-controlled beam. (A) Collimation optics for PZT-controlled beam. (B) Pair of PZT-controlled mirrors. (C) Final steering mirror for PZT-controlled beam. (D) Collimation optics for stationary 660-nm beam. (F) Beamsplitter cube to combine the stationary and PZT-controlled beam paths. (F) QVM2 microscope objective.

### 2.3.3 High NA 660-nm beam paths

The implementation of both the high NA PZT-controlled 660-nm stirring beam and a stationary 660-nm beam is shown in Fig. 2.8. The red arrows in the upper image show the 660-nm beam path for the PZT-controlled beam. For this implementation, the output of a fiber is collimated with an $f = 175$ mm lens (A), reflected off the pair of PZT-controlled mirrors (B), minified with an $M \sim 1/8$ ($f_1 = 300$ mm, $f_2 = 40$ mm) telescope to increase the angular deflection, reflected off two steering mirrors (C), directed to the QVM2 with a beamsplitter cube (E) and focused at the BEC with the QVM2 microscope objective (F). This choice of focal lengths results in a focused $1/e^2$ beam radius $w_0 \sim 7$ $\mu$m and a PZT-controlled beam travel of approximately 80 $\mu$m. Refer to the lab notebook pages corresponding to 11/7/14 and 2/1/15 for further discussion of the implementation of the high NA PZT-controlled stirring beam. In addition to the high NA PZT-controlled stirring beam, we also implemented a stationary 660-nm beam to be used as a narrow repulsive obstacle in conjunction with the push coils. The stationary beam is collimated (D), reflected off a pair of steering mirrors, transmitted through the beamsplitter cube (E), and focused at the BEC with the QVM2 microscope objective (F). The focused $1/e^2$ beam radius of the stationary beam can be varied by changing the focal length of the collimating lens (D). We note that when using the PZT-controlled mirrors with the high NA microscope objective, we found that the system was less forgiving to the deflected beams hitting the objective off-axis, resulting in asymmetry in the focused beam profile. Ideally we would benefit from a more compact PZT-controlled beam path.

## 2.4 Expansion coil

When imaging in expansion we use an additional magnetic field coil referred to as the 'expansion coil.' The expansion coil is located above the BEC cell, concentric with the final pair of transfer coils. When the field due to the expansion coil is combined with the TOP trap's DC quadrupole magnetic field, the fields balance gravity, allowing the BEC

to remain at an approximately constant vertical position during the period of ballistic expansion prior to imaging [31].

## 2.5 Syncing TTL timing events

When imaging after a period of expansion, we observed a significant shot-to-shot variation in the final position of the BEC. We found that syncing the switchover between the trapping field configuration (TOP coils on, expansion coil off) and the expansion field configuration (AC coils off, expansion coil on and DC gradient on) improved the consistency in the BEC location during the image. In addition to switching magnetic field coils, we make use of the sync circuit and a variable duty / delay circuit to sync the image pulse with the rotating bias field. Syncing is fairly straight-forward using a D-type flip-flop clocked on the 4-kHz rotating bias field as described in the lab notebook pages reproduced in Appendix B.

## 2.6 Imaging systems

We employ three imaging systems to acquire information from our BECs. Figure 2.9 shows the horizontal ($x$-axis) and vertical ($z$-axis) for the original $M \sim 5$ imaging systems. An additional $M \sim 3.3$ horizontal imaging system travels out of the page along the $y$-axis and is primarily used for characterization of the 1090-nm beam. Over the course of this dissertation, the $M \sim 5$ vertical imaging system was upgraded twice, first with the $M \sim 20$, NA = 0.25 imaging system described in Chapter 6 and used to acquire the *in situ* images of a vortex lattice reported in Ref. [9], and second with the $M \sim 11$, NA = 0.26 imaging system, introduced as phase two of our quantum vortex microscope (QVM2) and described in detail in Chapter 8. For the $M \sim 5$ and $M \sim 20$ vertical imaging systems, the probe light traveled downwards through the cell as shown in Fig. 2.9, whereas for the $M \sim 11$ imaging system the probe light traveled upwards through the cell. The horizontal imaging system shown in Fig. 2.9 is the same as the one described in Ref. [31], and phase-contrast images taken with this system remain our primary metric for characterizing the quality

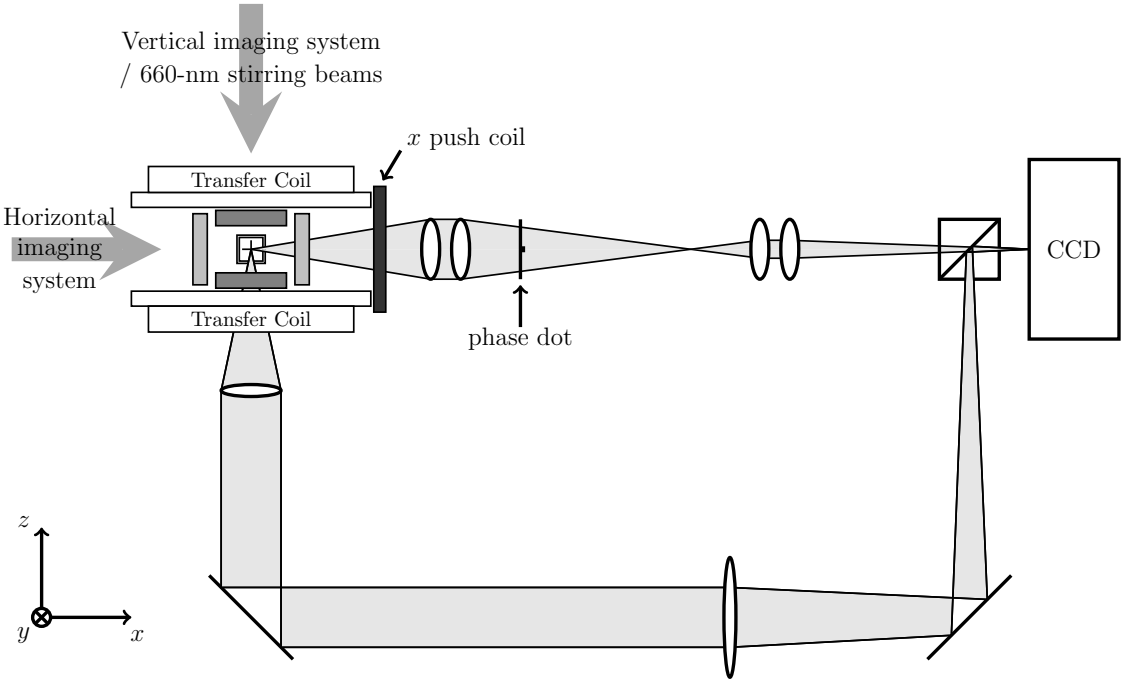


Figure 2.9: Layout of the original horizontal and vertical imaging systems. Both systems had $M \sim 5$. An additional $M \sim 3.3$ horizontal imaging system traveled out of the page along the $y$-axis and was primarily used for characterization of the 1090-nm beam.

of the bulk BEC. Regardless of the choice of vertical imaging system, the horizontal and vertical imaging paths are recombined with a PBSC just prior to the Pixis 1024 BR back-illuminated CCD camera with 13 x 13-$\mu$m pixels.

In the course of implementing the QVM2, the $M \sim 3.3$ $y$-axis imaging system was replaced with an $M \sim 2$ imaging system which employs a Point Grey Firefly MV CMOS camera with $6 \times 6$-$\mu$m pixels rather than the Pixis CCD camera. As we will discuss further in Chapter 9, the $M \sim 11$ QVM2 allows for imaging with either our standard Pixis CCD camera, or with the addition of a turning mirror, a Photometrics Cascade 512B electron multiplying CCD (EMCCD) camera with 16 x 16-$\mu$m pixels.

We have a number of available imaging probes whose utility depends on the transition and detuning we choose for a particular imaging technique. For phase-contrast imaging

we use a dichroic-atomic-vapor laser lock (DAVLL) [38] to lock a diode laser 900 MHz red-detuned from the $|F = 1\rangle \rightarrow |F' = 2\rangle$ hyperfine transition, but we do not temperature stabilize the cell or magnetic field coils used for the locking signal. The DAVLL technique works well for red-detuned frequency shifts on the order of 300-900 MHz but the locking signal tends to drift and it is difficult to achieve locking precision beyond about 20 MHz. For absorption imaging on the $|F = 1\rangle \rightarrow |F' = 2\rangle$ transition we use resonant light picked off from the MOT repump beam. For absorption imaging on the $|F = 2\rangle \rightarrow |F' = 3\rangle$ hyperfine transition we use a probe beam picked off from the MOT cooling light, along with optical pumping from $|F = 1\rangle \rightarrow |F' = 2\rangle$. The frequency of the MOT cooling light is adjusted via a double-pass AOM and can be tuned about 6-10$\Gamma$ on either side of the transition, where $\Gamma = 2\pi \times 5.9$ MHz is used for the natural linewidth for $^{87}$Rb. Note that Ref [39] reports $\Gamma = 6.07$ MHz for the natural linewidth of the $D_2$ transition of $^{87}$Rb, however thanks to an error in institutional memory, we have used $\Gamma = 5.9$ MHz for all calculations in this dissertation, except where noted explicitly. Lastly we found it useful for dark-field imaging to have a probe locked near the $|F = 1\rangle \rightarrow |F' = 2\rangle$ transition with finer precision than the DAVLL provides. To achieve this we used the 0th-order beam from the single-pass repump AOM (locked 80 MHz above the transition), and sent it through a double-pass 210-MHz AOM, and then a single-pass 110-MHz AOM. By adjusting the frequency on the double-pass AOM we can select the probe frequency within a range of about 20-120 MHz blue-detuned from the transition, although the power in the probe beam drops appreciably at the edges of this range. For detunings within a range of $\Delta \sim \pm 25$ MHz from the $|F = 1\rangle \rightarrow |F' = 2\rangle$ transition, we can skip the double-pass configuration, and simply shift the drive frequency of the 80-MHz single-pass repump AOM via computer control after the atoms are transferred to the science cell. Again, the power in the probe beam drops appreciably at the edges of this range. Sketches and further details regarding AOM configurations for the repump beam are provided in Appendix C.

## 2.7 Debugging slosh

Sloshing of the BEC in the TOP and hybrid traps has been a significant impediment to the operation of our apparatus. In the TOP trap we observe this slosh as an oscillation in the BEC position in both the horizontal and vertical directions with a phase that varies from shot to shot. We have had some success damping out slosh using a 660-nm beam to add an asymmetry to the harmonic trap prior to the sag RF cut.

# Chapter 3
# Imaging Techniques

This chapter provides an overview of the four imaging techniques commonly used in our lab to acquire information about both bulk properties of BECs and vortex distributions. We refer to these techniques as phase-contrast, absorption, Faraday, and dark-field imaging. We provide a basic introduction to the atom-photon interaction and the parameters that have the biggest effect on successful imaging, with sample images and corresponding parameters. We discuss the advantages of each technique in the context of minimally-destructive imaging and resolving vortex distributions.

## 3.1 Introduction to light-matter interaction

When light travels through a cloud of atoms, it acquires a phase shift due to the real component of the index of refraction and is attenuated due to the imaginary component of the index of refraction. BEC imaging techniques generally fall into two categories, those that rely on information that can be acquired from the attenuation or absorption of the probe light, and those that rely on the phase information imprinted on the probe beam as it passes through the BEC. All of our imaging is done within the hyperfine manifold of the $^{87}$Rb $D_2$ line shown in Fig. 3.1.

Following the method of Ref. [40], we treat the BEC as a thin lens. A monochromatic laser with electric field amplitude $E_0$ propagating along the $z$-axis and incident on the BEC acquires a phase shift

$$\phi(x,y) = -\tilde{n}(x,y)\sigma_0 \left( \frac{\Delta/\Gamma}{1 + 4(\Delta/\Gamma)^2 + I_0/I_{\text{sat}}} \right), \tag{3.1}$$

and is attenuated by

$$\alpha(x,y) = \frac{-\tilde{n}(x,y)\sigma_0}{2}\left(\frac{1}{1+4(\Delta/\Gamma)^2 + I_0/I_{\text{sat}}}\right), \tag{3.2}$$

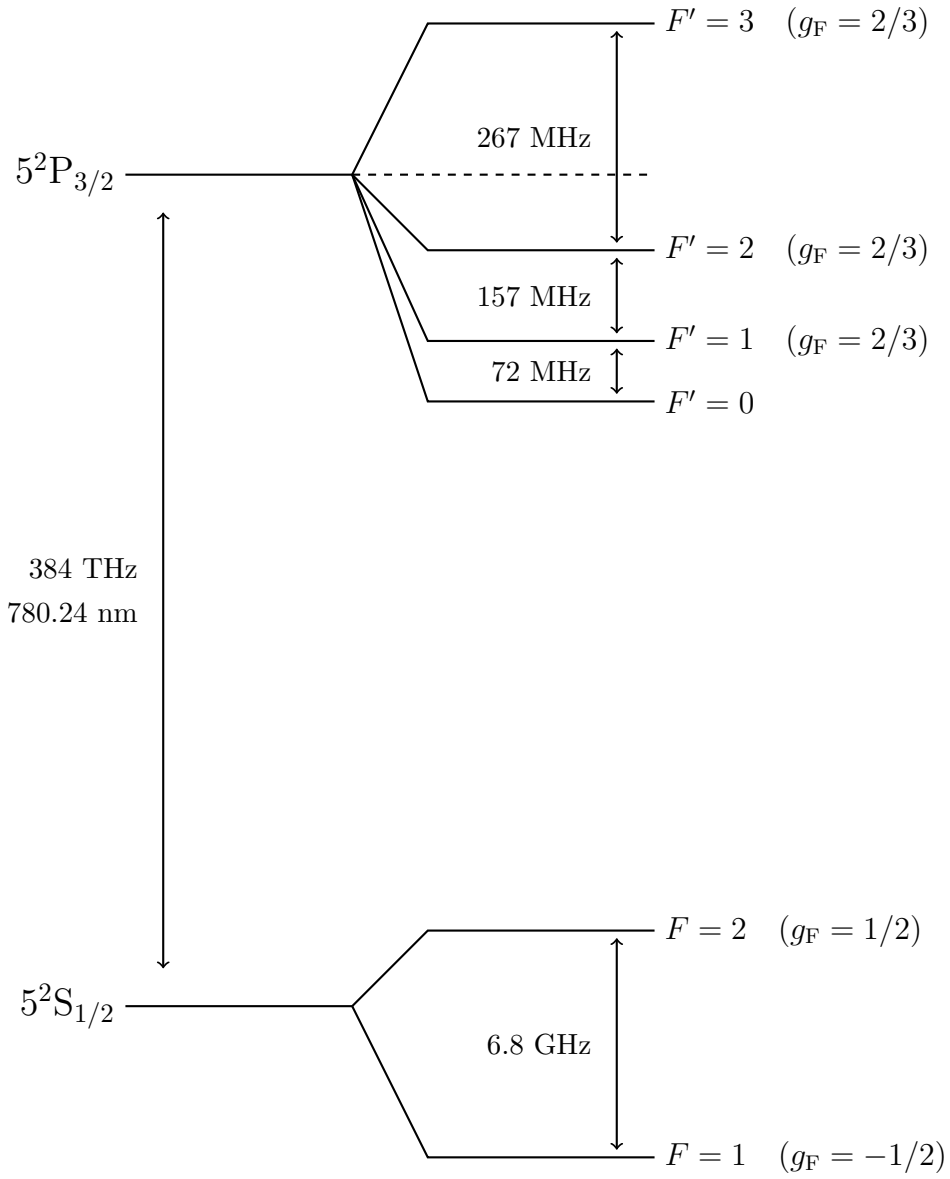


Figure 3.1: Hyperfine manifolds for $^{87}$Rb $D_2$ line; splittings shown are not to scale. The values for frequency splittings come from Ref. [39].

such that the field after passing through the BEC is

$$E = tE_0 e^{i\phi} \tag{3.3}$$

where $t = e^{\alpha}$. The destructiveness of the imaging process can be estimated by the rate at which an atom scatters photons,

$$R_{\text{scat}} = \frac{\Gamma}{2}\left(\frac{I_0/I_{\text{sat}}}{1 + 4(\Delta/\Gamma)^2 + I_0/I_{\text{sat}}}\right). \tag{3.4}$$

In these expressions, $\tilde{n}(x, y) = \int n(x, y, z)dz$ is the integrated column density along the probe beam propagation direction $\hat{z}$, $\sigma_0 = \hbar\omega_0\Gamma/2I_{\text{sat}}$ is the resonant atom-photon cross section, $\Delta = \omega - \omega_0$ is the probe detuning from resonance, $\Gamma$ is the natural linewidth of the $^{87}$Rb $D_2$ transition, $I_0 = \frac{1}{2}c\epsilon_0|E_0|^2$ is the incident probe intensity (assumed to be uniform in the transverse plane), and

$$I_{\text{sat}} = \frac{c\epsilon_0\Gamma^2\hbar^2}{4|\hat{\epsilon}\cdot\vec{d}|^2} \tag{3.5}$$

is the saturation intensity of the atomic transition, where $c$ is the speed of light, $\epsilon_0$ is the permittivity of free space, $\hat{\epsilon}$ is the polarization vector for the probe beam ($\hat{\sigma}_+, \hat{\sigma}_-, \hat{\pi}$), and $\vec{d}$ is the atomic dipole moment. The dipole matrix element $\hat{\epsilon}\cdot\vec{d}$ varies with both the relative strength of the atomic transition in question and the polarization of the light. See Refs. [39, 41] for more detail regarding the calculation of $I_{\text{sat}}$.

The calculation of saturation intensity is fairly complicated especially in cases that lack a well-defined quantization axis; this is often the case in our experiments given that the majority of our science is done with a BEC confined in a trap with a rotating magnetic field in the $x$-$y$ plane as described in Chapter 2. The situation is further complicated as soon as we consider imaging scenarios where an atom undergoes multiple transitions, given that there is no closed cycling transition available for atoms in the $5^2S_{1/2}$ $|F = 1, m_F = -1\rangle$ hyperfine state. The simplest case given $^{87}$Rb atoms magnetically trapped in the $5^2S_{1/2}$ $|F = 1, m_F = -1\rangle$ ground state occurs when we image on the $5^2S_{1/2}$ $|F = 1, m_F = -1\rangle \rightarrow$ $5^2P_{3/2}$ $|F' = 2, m_{F'} = -2\rangle$ transition with $\sigma_-$ polarized probe light and consider imaging

parameters where $R_{\rm scat} < 1$. For this scenario, we only need to consider the dipole matrix element for a single transition; here $I_{\rm sat} = 32$ W/m$^2$, and $\sigma_0 = 1.5 \times 10^{-13}$ m$^{-2}$. If multiple transitions are possible then we need to calculate $I_{\rm sat}$ and $\sigma_0$ for each transition. The situation is further complicated if we consider optical pumping from $5^2{\rm S}_{1/2}\ |F = 1\rangle$ to $5^2{\rm S}_{1/2}\ |F = 2\rangle$ prior to imaging on the $5^2{\rm S}_{1/2}\ |F = 2\rangle \rightarrow 5^2{\rm P}_{3/2}\ |F' = 3\rangle$ transition, at which point proper treatment requires a master equation that accounts for the relative transition probabilities and decay rates for all accessible transitions [39].

### 3.1.1 Imaging in a TOP trap

In general, when imaging we would like a well-defined quantization axis for the $m_{\rm F}$ states. Experimentally, this means we need the dominant magnetic field to be aligned with the imaging axis, providing a quantization axis and lifting the degeneracy of the Zeeman $m_{\rm F}$ sublevels. Such a magnetic field is easy to come by for expansion images where the net field due to the DC quadrupole coil and the expansion coil is $B_{\rm z} \sim 40$ G aligned with the vertical imaging axis. However, when imaging *in situ* in either a sagged TOP trap or the highly oblate hybrid trap, the AC bias field remains on, rotating with a frequency of 4kHz, resulting in a 5-G magnetic field rotating in the $x$-$y$ plane. This $B_0 = 5$ G rotating bias field is of the same order of magnitude as the DC magnetic field at the sag position $B_{\rm z} \sim 3$ G, due to the TOP trap quadrupole field, so that the net magnetic field traces out a cone with an angle of about 60° from the vertical imaging axis.

To address the need for a net magnetic field aligned with the imaging axis, we transitioned to a 1D TOP trap by ramping off one axis of the AC bias field mid evaporation as described in Sec. 2.1.2. We note that BECs in both the 1D and the standard TOP traps are well within the 3D BEC regime with similar aspect ratios. In our implementation of a 1D TOP trap, the bias field oscillates in the $y$-direction only, with the net bias field $B_{\rm y}(t) = 0$ twice per $\tau_{\rm TOP} = 250$-$\mu$s cycle. Atoms trapped in the $|F = 1, m_{\rm F} = -1\rangle$ hyperfine state adiabatically follow the net magnetic field vector $\vec{B}_{\rm net} = B_{\rm z}\hat{z} + B_{\rm y}(t)\hat{y}$. By syncing imaging

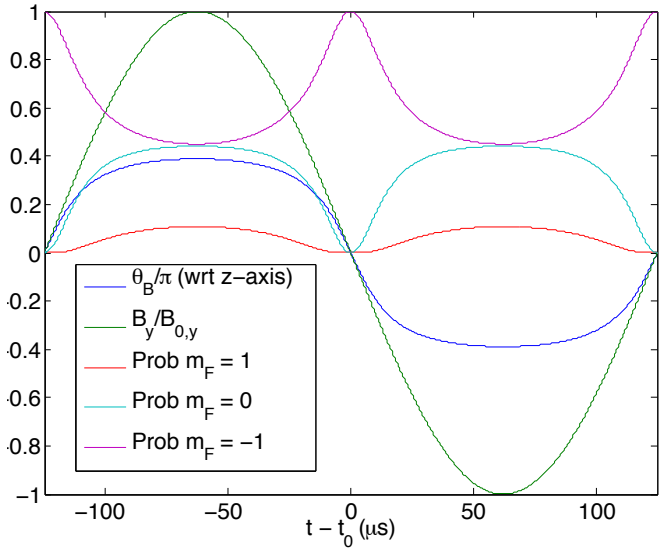


Figure 3.2: Plot of $m_{\mathrm{F}}$ populations projected onto the vertical imaging axis ($z$-axis) as a function of time, assuming the trapped atoms adiabatically follow the net magnetic field vector $\vec{B}_{\mathrm{net}} = B_{\mathrm{z}}\hat{z} + B_{\mathrm{y}}(t)\hat{y}$ with $m_{\mathrm{F}} = -1$. We chose $t_0$ such that $B_{\mathrm{y}}(t_0) = 0$ at which point the imaging axis coincides with the quantization axis defined by $\vec{B}_{\mathrm{net}}$.

probe pulses with the period of time when $B_{\mathrm{y}}(t) \sim 0$, we can ensure that we image along the quantization axis defined by $\vec{B}_{\mathrm{net}}$. Figure 3.2 plots the relative $m_{\mathrm{F}}$ populations projected onto the vertical imaging axis ($z$-axis) as a function of time, assuming that all atoms have $m_{\mathrm{F}} = -1$ when projected onto the axis defined by $\vec{B}_{\mathrm{net}}$. While the probability of the imaging probe accessing an atom with $m_{\mathrm{F}} = -1$ falls off quickly, a 4-$\mu$s pulse centered at $t_0$ where $B_{\mathrm{y}}(t_0) = 0$ restricts the angle between $\vec{B}_{\mathrm{net}}$ and the vertical imaging axis to $\theta_{\mathrm{B}} \sim 2.5°$, such that nearly all of the atoms that the probe beam interacts with will have $m_{\mathrm{F}} = -1$.

The downside to this approach is that a 20-$\mu$s image pulse now takes five 250-$\mu$s cycles of the rotating bias field, assuming that we sync to the 4-kHz bias field. We can improve this to 2.5 cycles by syncing to an 8-kHz clock and accessing both $B_{\mathrm{y}} = 0$ points in the 250-$\mu$s cycle. Note that the turnover time for a pair of vortex cores with the same circulation is on the order of 15 to 20 ms. To avoid blurring we want our imaging times to be a small

fraction of this turnover time, on the order of 1 ms or less.

### 3.1.2 Optical pumping

For the imaging techniques used in our lab, we consider transitions on the $^{87}$Rb $D_2$ line between two possible hyperfine transitions, $5^2S_{1/2}\ |F = 1\rangle \rightarrow 5^2P_{3/2}\ |F' = 2\rangle$ and $5^2S_{1/2}\ |F = 2\rangle \rightarrow 5^2P_{3/2}\ |F' = 3\rangle$ shown in Fig. 3.1. Given that atoms confined in our magnetic trap are in the $5^2S_{1/2}\ |F = 1, m_F = -1\rangle$ ground state, imaging on the $5^2S_{1/2}\ |F = 2\rangle \rightarrow 5^2P_{3/2}\ |F' = 3\rangle$ hyperfine transition requires first optically pumping atoms from $5^2S_{1/2}\ |F = 1\rangle$ to $5^2S_{1/2}\ |F = 2\rangle$. This is generally done with a pulse of light resonant with the $5^2S_{1/2}\ |F = 1\rangle \rightarrow 5^2P_{3/2}\ |F' = 2\rangle$ transition, after which roughly half of the atoms decay to the $5^2S_{1/2}\ |F = 2\rangle$ hyperfine state as shown in the schematic in Fig. 3.3. The optical pumping light is picked off from the repump laser beam used for the MOT, and travels in parallel with the imaging probe beam through the vertical imaging system shown in Fig. 2.9, with both beams coupled into the same fiber. This has the advantage of illuminating optically dense clouds evenly across the plane perpendicular to the vertical imaging axis, but the disadvantage that probe light and atom signal from both the optical pumping beam and the actual imaging probe beam reach the camera. Generally the signal from the probe beam is much greater than that of the optical pumping beam so that we can ignore the contribution from the optical pumping beam, but for certain sets of imaging parameters the overlay of the signal can cause confusion.

Previously the optical pumping beam was aligned such that its axis of propagation was in the plane perpendicular to the vertical axis, at about a 45° angle from the horizontal phase-contrast imaging axis. This caused problems when imaging optically dense clouds in that the optical pumping beam would be absorbed part way through the BEC. Our method of optical pumping is somewhat inefficient in that we rely on a fraction of the atoms decaying into a particular state rather than driving a direct transition between the $5^2S_{1/2}\ |F = 1, m_F = -1\rangle$ and $5^2S_{1/2}\ |F = 2, m_F = -2\rangle$ ground states. Other groups use a two-

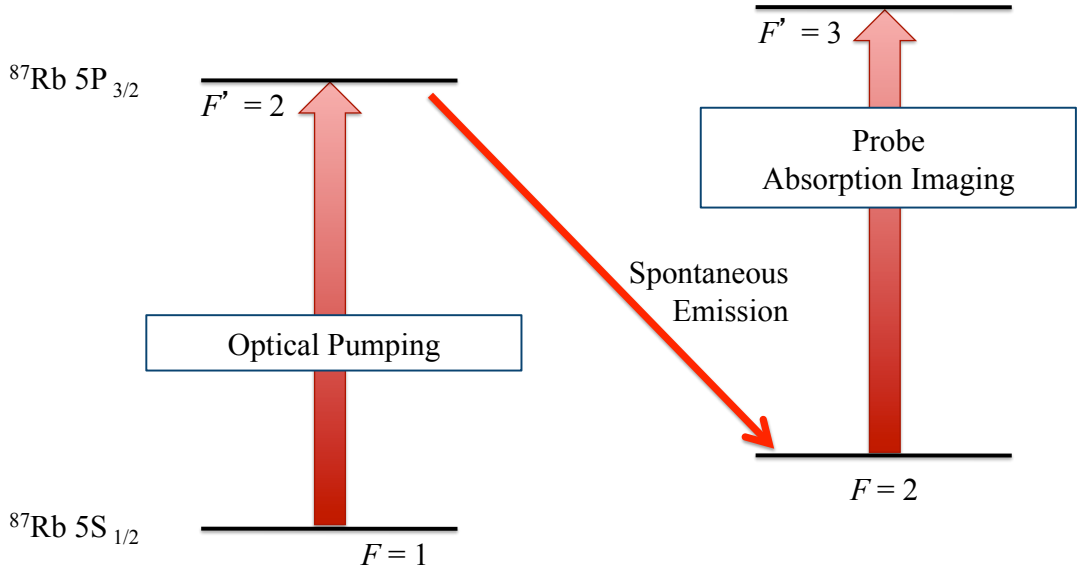


Figure 3.3: Optical pumping scheme used for transferring atoms from $5^2\mathrm{S}_{1/2}\ |F = 1\rangle$ to $5^2\mathrm{S}_{1/2}\ |F = 2\rangle$, prior to imaging on the $5^2\mathrm{S}_{1/2}\ |F = 2\rangle \rightarrow 5^2\mathrm{P}_{3/2}\ |F' = 3\rangle$ hyperfine transition.

photon microwave pulse to drive this transition directly [42, 43]. The primary reason for optically pumping to $5^2\mathrm{S}_{1/2}\ |F = 2\rangle$ is that the transitions between the $5^2\mathrm{S}_{1/2}\ |F = 2, m_\mathrm{F} = \pm 2\rangle$ and $5^2\mathrm{P}_{3/2}\ |F' = 3, m_{\mathrm{F}'} = \pm 3\rangle$ hyperfine states are closed or cycling transitions when driven with $\sigma_\pm$ polarized light. These transitions have the largest transition strength, with $I_\mathrm{sat} = 16\ \mathrm{W/m^2}$ and $\sigma_0 = 3 \times 10^{-13}\ \mathrm{m}^{-2}$, and can be driven through many cycles. From this point forward we will use $|F, m_\mathrm{F}\rangle$ to denote hyperfine states in the $5^2\mathrm{S}_{1/2}$ manifold, and $|F', m_{F'}\rangle$ to denote hyperfine states in the $5^2\mathrm{P}_{3/2}$ manifold.

## 3.2 Phase-contrast imaging

Our application of phase-contrast imaging is fairly standard. Refer to Ref. [40] for further explanation of the theory, and Ref. [31, 32] for details relevant to the implementation of phase-contrast imaging along the horizontal imaging axis in our apparatus. Briefly, phase-contrast imaging is a homodyne detection technique where the unrefracted probe

beam is used as the local oscillator to interfere with the portion of the probe beam that is coherently scattered by the BEC. In our implementation, the unrefracted probe beam undergoes a $3\pi/2$ phase shift, when it passes through a phase dot in the Fourier plane as shown in Fig. 2.9. The signal measured at the camera is the interference between this local oscillator and the fraction of the probe that acquired a phase shift while passing through the BEC. For small phase shifts $\phi << 1$, the phase-contrast signal $I_{\mathrm{PC}}$ is proportional to $\phi$. The advantage of phase-contrast imaging is that it is minimally destructive; we commonly use a probe with a detuning of $\Delta/2\pi = -900$ MHz, and can take up to 10 images. Like any imaging technique that measures the phase of the light, phase-contrast imaging is susceptible to phase winding, but for $|\Delta/2\pi| \sim 1$ GHz, this effect is not generally a problem, although we do sometimes observe phase winding when imaging BECs in the hybrid trap along the horizontal imaging axis.

## 3.3 Near-resonant absorption imaging

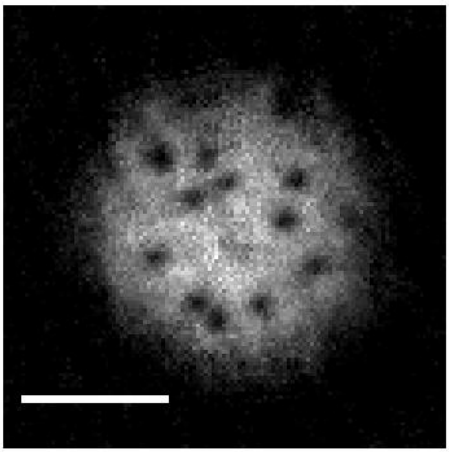

Figure 3.4: Representative BEC image - bright-field absorption imaging. An absorption image of a vortex distribution within a BEC taken after a 22-ms period of expansion with the 1090-nm beam on for the first 10 ms of expansion. The white scale bar in the image represents 50 $\mu$m. Imaging parameters: $\Delta/2\pi = 0$ MHz from $|F = 1\rangle \rightarrow |F' = 2\rangle$.

Again, our application of absorption imaging is fairly standard. Refer to Ref. [40] for

further theory, and Ref. [44] for additional details regarding lensing affects for near-resonant imaging. Briefly, we use absorption imaging either on resonance with the $|F = 1\rangle \rightarrow |F' = 2\rangle$ transition, or within a detuning range of several linewidths from the $|F = 2\rangle \rightarrow |F' = 3\rangle$ transition, after optically pumping from $|F = 1\rangle$ to $|F = 2\rangle$. Resonance absorption imaging on $|F = 1\rangle \rightarrow |F' = 2\rangle$ works better for *in situ* imaging with an optically dense cloud. Images appear saturated if the intensity of the probe light is too low, such that the probe is essentially completely absorbed by the atoms, with the result that regions of lower atom density appear to have the same optical depth as regions of higher atom density. When imaging in expansion, we primarily image on $|F = 2\rangle \rightarrow |F' = 3\rangle$. Saturation effects show up in these images when we are detuned too close to resonance or if the power in the probe beam is too high. When imaging in expansion we generally turn the magnetic fields off 1-2 ms prior to imaging to avoid having to account for Zeeman shifting of $\omega_0$ due to the magnetic field gradient needed to oppose gravity. See Fig. 3.4 for a representative absorption image, and imaging parameters.

## 3.4 Faraday imaging

Conceptually, the idea behind Faraday imaging is that in the presence of a magnetic field aligned along the imaging axis, $\sigma_+$ and $\sigma_-$ polarized probe light experience a different phase shift when passing through the BEC. Given that a linearly polarized probe beam $\vec{E} = E_0\hat{x} = E_0(\hat{\sigma}_- - \hat{\sigma}_+)/\sqrt{2}$ can be decomposed into an equal superposition of $\sigma_+$ and $\sigma_-$ polarized light, the net effect of the birefringence is to rotate the polarization of an initially linearly polarized probe beam by the Faraday angle $\theta_{\mathrm{F}} = (\phi_+ - \phi_-)/2$, where $\phi_\pm$ is the phase acquired by the component of the probe beam with $\sigma_\pm$ polarization. In our implementation of Faraday imaging we orient a half-wave plate to dump as much of the non-rotated probe beam as possible out the port of a PBSC as shown in Fig. 3.5. The resulting intensity of the signal after the PBSC is $I_{\mathrm{F}} = I_0 \sin^2 \theta_{\mathrm{F}}$. This implementation is sometimes referred to as dark-field Faraday imaging [45] but we will call it Faraday

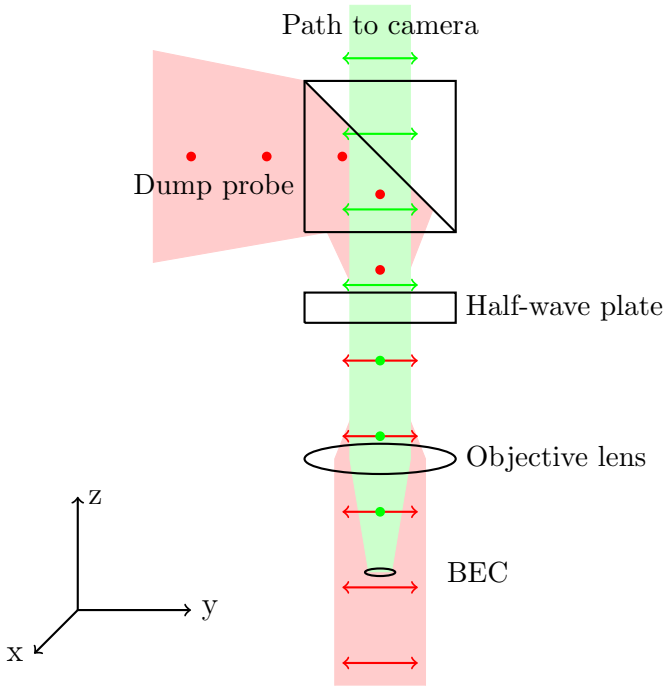


Figure 3.5: Diagram of a generic imaging system arranged for Faraday imaging. The birefringence of the BEC acts to rotate the polarization of the imaging light. The rotated component of the probe light is shown in green. The half-wave plate is used to switch the system between Faraday imaging, where the probe light shown in red is removed by the PBSC, and bright-field absorption imaging where the probe light is allowed to propagate to the camera.

imaging to distinguish from the dark-field imaging described in Sec. 3.5. Note that by rotating the half-wave plate we are able to switch between Faraday imaging where only the light rotated by the BEC birefringence reaches the camera, and bright-field absorption imaging where the non-rotated portion of the probe beam reaches the camera. In between these two extremes it is possible to implement something similar to phase-contrast imaging where the non-rotated probe beam acts as a local oscillator and interferes with the rotated component [46].

The phase shifts $\phi_{\pm}$ depend on the strength of the magnetic field $B_z$ as well as the relative values for $\sigma_0$ and $I_{sat}$ for a given transition and polarization. If we consider the

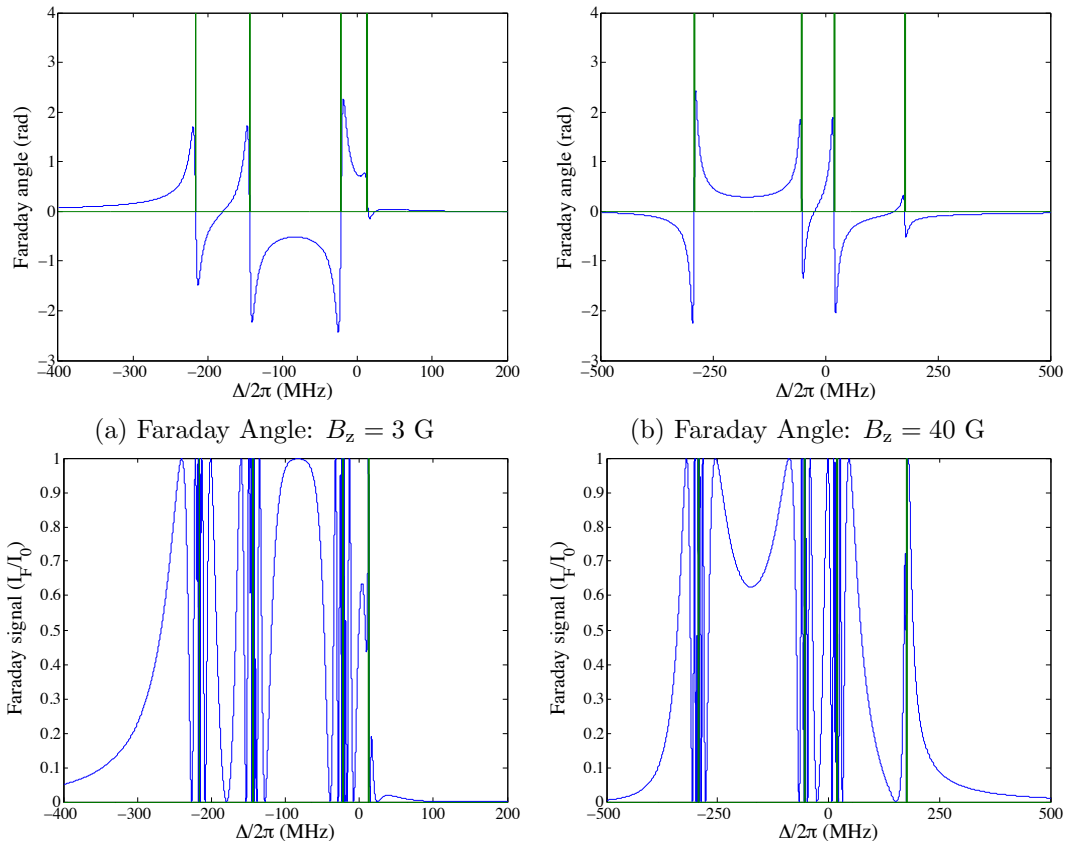


(a) Faraday Angle: $B_z = 3$ G

(b) Faraday Angle: $B_z = 40$ G

(c) Faraday Signal: $B_z = 3$ G

(d) Faraday Signal: $B_z = 40$ G

Figure 3.6: Plots of Faraday angle $\phi_F$ (radians) and Faraday signal $I_F/I_0$ versus detuning $\Delta/2\pi$ (MHz) from the $|F = 1\rangle \rightarrow |F' = 2\rangle$ transition for a given magnetic field $B_z$ aligned with the imaging axis. (a) and (b) are plots of Faraday angle versus detuning for $B_z = 3$ G and $B_z = 40$ G respectively. (c) and (d) are plots of Faraday signal versus detuning for $B_z = 3$ G and $B_z = 40$ G respectively. Green vertical lines denote the Zeeman-shifted hyperfine transitions. The Faraday signal was calculated using a constant integrated atom column density $\tilde{n}(r) = 4.4 \times 10^{14}$ m$^{-2}$, $I_0 = 6.7$ W/m$^2$, and $\Gamma = 2\pi \times 6.07$ MHz.

simplest case where we image on $|F = 1, m_F = -1\rangle \rightarrow |F' = 2\rangle$ and assume that at most an atom undergoes one transition, we have

$$\phi_+ = \sum_{i=0}^{2} -\tilde{n}(r)\sigma_{0,i}\left(\frac{\Delta_i/\Gamma}{1 + 4(\Delta_i/\Gamma)^2 + I_0/I_{\mathrm{sat},i}}\right) \tag{3.6}$$

$$\phi_- = -\tilde{n}(r)\sigma_{0,i=2}\left(\frac{\Delta_{i=2}/\Gamma}{1+4(\Delta_{i=2}/\Gamma)^2+I_0/I_{\mathrm{sat},i=2}}\right) \tag{3.7}$$

where the subscript $i$ denotes the hyperfine level of the excited state. Here the detuning $\Delta_i$ includes the $m_{\mathrm{F}}$ dependent Zeeman shift due to the presence of the magnetic field $\Delta_{\mathrm{Z}} = g_{\mathrm{F}} m_{\mathrm{F}} \mu_{\mathrm{B}} B_{\mathrm{z}}/\hbar$. Given the transition rules, an atom in $|F=1, m_{\mathrm{F}}=-1\rangle$ can be driven to $|F'=2, m_{\mathrm{F}'}=-2\rangle$ by $\sigma_-$ polarized light, and driven to $|F'=i, m_{\mathrm{F}'}=0\rangle$, $i=0,1,2$, by $\sigma_+$ polarized light. Figs. 3.6 show plots for $\theta_F(\Delta/2\pi)$ and $I_F(\Delta/2\pi)$ for $B_{\mathrm{z}} = 3$ G and $B_{\mathrm{z}} = 40$ G corresponding to the approximate magnetic field along the imaging axis at the BEC location for the TOP trap and the expansion configuration respectively. Note that the Faraday angle is maximized near the hyperfine transitions and that phase winding is prevalent near the transitions. Experimentally we found $\Delta/2\pi \sim -80$ MHz from the $|F=1\rangle \rightarrow |F'=2\rangle$ transition to be in the optimal range of high signal and minimal phase winding for *in situ* imaging, while $\Delta/2\pi \sim -160$ MHz or $\Delta/2\pi \sim -240$ MHz worked better for expansion images. The *in situ* Faraday images shown in Fig. 3.7,show the predicted phase winding for probe light tuned near one of the hyperfine transitions, such as $\Delta/2\pi = -160$ MHz from the $|F=1\rangle \rightarrow |F'=2\rangle$ transition.

As shown in Fig. 3.8, the Faraday signal is significantly improved when the imaging axis aligns with the quantization axis for the Zeeman $m_{\mathrm{F}}$ sublevels, defined by the net magnetic field vector $\vec{B}_{\mathrm{net}} = B_{\mathrm{z}}\hat{z} + B_{\mathrm{y}}(t)\hat{y}$. Figure 3.8 shows *in situ* Faraday images of a BEC taken at two extremes of the bias field cycle, $B_{\mathrm{y}} = 0$ and $B_{\mathrm{y}} = B_{0,\mathrm{y}}$. All images are scaled to the range of -50 to 500 counts per $13 \times 13$-$\mu$m pixel, with an exposure time $t_{\mathrm{exp}} = 10$ $\mu$s. A detuning of $\Delta/2\pi = -80$ MHz from $|F=1\rangle \rightarrow |F'=2\rangle$ was used for the images shown in Figs. 3.8(a) and (b), and $\Delta/2\pi = -120$ MHz was used for the images shown in Figs. 3.8(c) and (d). The images shown in Figs. 3.8(a) and (c) were taken when $B_{\mathrm{y}} \sim B_{0,\mathrm{y}}$ so that the populations of the $m_{\mathrm{F}}$ sublevels were as mixed as possible when projected onto the imaging axis, while the images shown in Figs. 3.8(b) and (d) were synced with $B_{\mathrm{y}} \sim 0$ where the net magnetic field was aligned within 6° of the vertical imaging axis. Note the improved

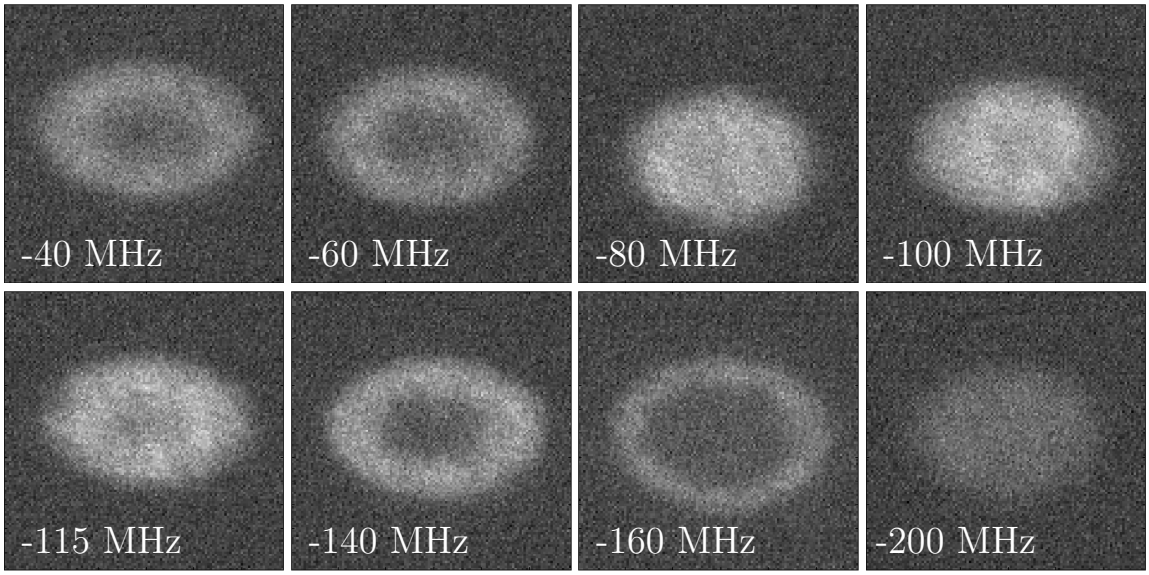


Figure 3.7: $130 \times 130$-$\mu$m *in situ* Faraday images of a BEC confined in the hybrid 1D TOP trap with additional axial confinement. All images are scaled to the range of -50 to 250 counts per $13 \times 13$-$\mu$m pixel. The image pulse was synced to $B_{\mathrm{y}} \sim 0$ G. The degree of phase winding varies with the detuning shown on each image. $P_{\mathrm{BEC}} \sim 75$ $\mu$W ($P_{\mathrm{fiber}} = 300$ $\mu$W) and $t_{\mathrm{exp}} = 8$ $\mu$s for all images.

signal in Figs. 3.8(b) and (d), and the phase winding evident in Fig. 3.8(d).

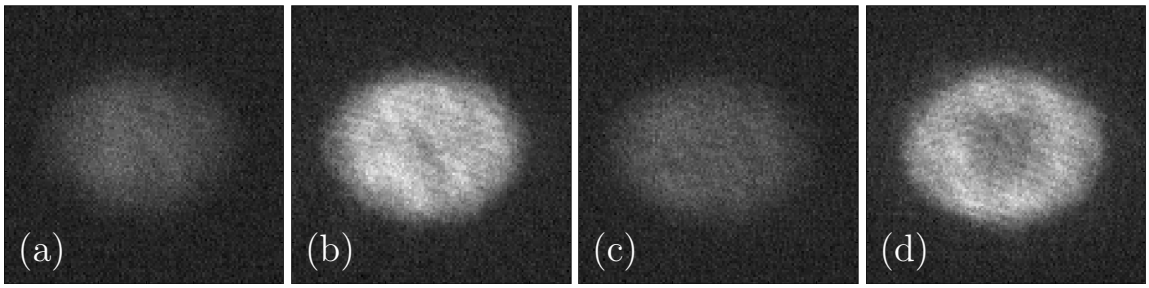


Figure 3.8: $130 \times 130$-$\mu$m *in situ* Faraday images of a BEC confined in the hybrid 1D TOP trap with additional axial confinement, taken at varying points in the bias field cycle. All images are scaled to the range of -50 to 500 counts per $13 \times 13$-$\mu$m pixel. A detuning of $\Delta/2\pi = -80$ MHz from $|F = 1\rangle \rightarrow |F' = 2\rangle$ was used for images (a) and (b), and $\Delta/2\pi = -120$ MHz was used for images (c) and (d). The exposure time was $t_{\mathrm{exp}} = 10$ $\mu$s. Images (a) and (c) were taken when $B_{\mathrm{y}} \sim B_{0,\mathrm{y}}$, while images (b) and (d) were synced with $B_{\mathrm{y}} \sim 0$. Note the improved signal in (b) and (d), and the phase winding evident in (d).

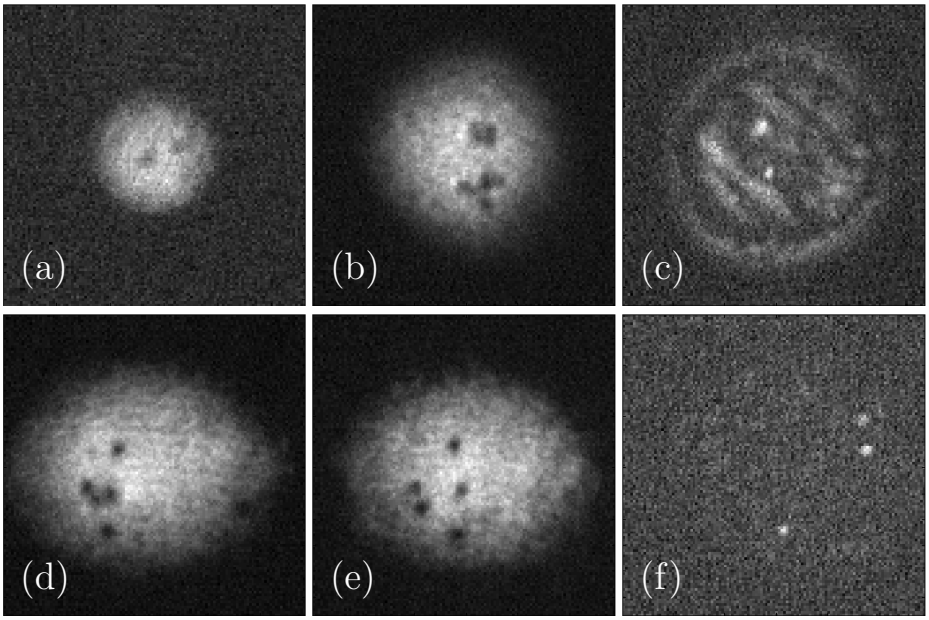


Figure 3.9: Representative BEC images for Faraday imaging. (a) *In situ* image of a BEC confined in the hybrid trap employing the standard TOP trap, taken with the Cascade EMCCD camera. Images shown in (b)-(f) were taken with the Pixis CCD camera after a period of expansion allowed the vortex cores to be resolved. (b)-(c) show images of BECs originally confined in the hybrid trap employing the standard TOP trap, while (d)-(f) correspond to images of BECs originally confined in a hybrid trap with a 1D oscillating bias field. (c) and (f) are dark-field Faraday images where a mask was placed in the Fourier plane to block the Faraday signal from the bulk BEC. Imaging parameters: (a) $\Delta/2\pi = -80$ MHz from $|F = 1\rangle \rightarrow |F' = 2\rangle$, $t_{\rm exp} = 10$ $\mu$s, imaged *in situ*. (b) $\Delta/2\pi = -240$ MHz from $|F = 1\rangle \rightarrow |F' = 2\rangle$, imaged after $t_{\rm 2D} = 10$ ms of 2D expansion in the 1090-nm beam and $t_{\rm 3D} = 5$ ms of 3D expansion. (c) $D_{\rm mask} \sim$ 0.8-1 mm, $\Delta = 1\Gamma$ from $|F = 2\rangle \rightarrow |F' = 3\rangle$, $t_{\rm exp} = 40$ $\mu$s, imaged after $t_{\rm 2D} = 10$ ms. (d)-(e) $\Delta = 2\Gamma$ from $|F = 2\rangle \rightarrow |F' = 3\rangle$, $t_{\rm exp} = 40$ $\mu$s, imaged after $t_{\rm 2D} = 10$ ms and $t_{\rm 3D} = 15$ ms. (f) $D_{\rm mask} \sim$ 1mm, $\Delta = -2\Gamma$ from $|F = 2\rangle \rightarrow |F' = 3\rangle$, $t_{\rm exp} = 4 \times 8$ $\mu$s, imaged after $t_{\rm 2D} = 10$ ms and $t_{\rm 3D} = 15$ ms.

A primary advantage of our implementation of Faraday imaging is the low background signal, in that nearly all of the non-rotated probe beam is prevented from reaching the camera. Representative Faraday images with vortices are shown in Fig. 3.9. Due to the minimal background signal, our implementation of Faraday imaging is particularly well-suited for use with an electron multiplying CCD (EMCCD) camera. With the proper choice

of detuning and intensity, Faraday imaging can be used nondestructively and Gajdacz *et al.* report the acquisition of hundreds of images of a single bulk BEC [45]. While we have found minimally-destructive Faraday imaging useful for tracking down BEC slosh, we have yet to find a set of imaging parameters that optimizes minimally-destructive *in situ* imaging of vortex cores with simultaneous Faraday imaging and dark-field imaging, analogous to the destructive dark-field Faraday expansion images shown in Figs. 3.9(c) and (f). We suspect that the problem is over-constrained since both Faraday imaging and the frequency filtering inherent in dark-field imaging of vortex cores work for a narrow range of imaging parameters.

## 3.5 Dark-field imaging

While our implementation of Faraday imaging described in Sec. 3.4 is technically a variation of dark-field imaging in that the non-rotated portion of the probe beam is dumped out of the imaging path by the PBSC, we reserve the term 'dark-field' for cases where the non-refracted portion of the imaging probe is physically blocked by a mask in the Fourier plane of the imaging system as described in Chapter 7. Dark-field imaging plays a large role in our attempts at *in situ* imaging of vortex cores and is described in detail in Chapters 6 and 7.

Briefly, in dark-field imaging, we consider the BEC as a phase object that coherently refracts light from an imaging probe beam, such that the probe beam acquires the phase shift $\phi(x, y)$ defined in Eqn. 3.1. An opaque mask placed on-axis in the Fourier plane of the imaging system acts as a high-pass spatial filter, blocking the unrefracted component of the probe beam but allowing light refracted by the BEC to reach the camera [40, 47]. For small phase shifts, the dark-field signal $I_{\mathrm{DF}}$ is proportional to $\phi^2$. As we will discuss in Chapters 6 and 7, the size of the mask can be chosen to block the light refracted by the bulk BEC as well, allowing only the light refracted by sharp features such as vortex cores to reach the camera. Figure 3.10 shows representative dark-field BEC images.

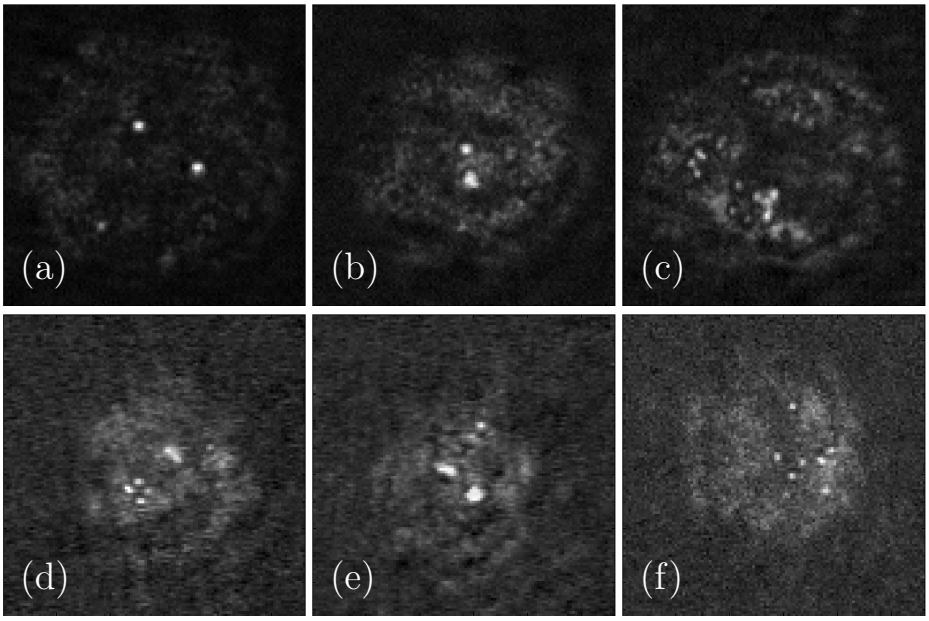


Figure 3.10: Representative BEC images for dark-field imaging. All images shown were taken after a period of expansion. Note that vortices show up as bright points of light on a dark background. The images in the bottom row show cores visible after a short period of 3D expansion with $t_{3D} = 7$ ms (d), $t_{3D} = 9$ ms (e), and $t_{3D} = 11$ ms (f).

## 3.6 Minimally-destructive imaging

Minimally-destructive imaging requires $R_{\text{scat}} << 1$ which can be achieved with either low probe intensity or large probe detunings. In the low intensity limit $I_0 << I_{\text{sat}}$, signal is linear with respect to both $I_0$ and $t_{\text{exp}}$, however as we increase $I_0$ the overall phase shift decreases with $\phi \propto I_{\text{sat}}/I_0$ in the limit $I_0 >> I_{\text{sat}}$. The signal remains linear with respect to $t_{\text{exp}}$, but the exposure time is limited by the need to sync to the $B_y \sim 0$ portion of the bias field oscillation. The maximum phase shift occurs at $\Delta = \pm 0.5\Gamma$, then decreases as we increase $\Delta$ for $|\Delta| > 0.5\Gamma$. In the limit of large detunings, $R_{\text{scat}} \propto \Delta^{-2}$ falls off faster than $\phi \propto \Delta^{-1}$. Generally, for low signals we want to use an imaging technique where $I_{\text{sig}} \propto \phi$ such as phase-contrast imaging described in Sec. 3.2, rather than $I_{\text{sig}} \propto \phi^2$ such as the implementations of Faraday and dark-field imaging described in Secs. 3.4

and 3.5 respectively. However, advances in camera technology such as the use of EMCCD cameras allow for similar signal-to-noise ratios (SNR) for all three imaging techniqus. See Refs. [45, 48] for a discussion of the SNR of various BEC imaging techniques. Minimally-destructive *in situ* imaging of vortex cores changes the game, since now parameters such as detuning and intensity need to be chosen to maximize core signal rather than bulk signal. Sadly, Faraday imaging which produces beautiful images for the bulk BEC signal, and for vortex imaging in an expanded BEC, no longer seems to be ideal.

## 3.7 Choosing between imaging techniques

Generally, we use phase-contrast imaging along the horizontal axis to image the bulk BEC. This allows us to measure the Thomas-Fermi radii and other BEC parameters such as temperature and atom number. We reserve the absorption, Faraday and dark-field imaging techniques for the vertical imaging axis. If all we want is to characterize the bulk BEC then absorption imaging or Faraday imaging on $|F = 1\rangle \rightarrow |F = 2'\rangle$ give the best signal. For imaging vortex distributions in expansion, absorption imaging on $|F = 2\rangle \rightarrow |F = 3'\rangle$ or Faraday imaging on either transition is preferred. Faraday imaging has the advantage of removing almost all noise associated with structure on the probe beam. Finally, when imaging vortices *in situ*, spatial filtering in the Fourier plane allows us to isolate the vortex core signal and to observe sharp density features that would not normally be visible. We note however, that for certain cases such as the vortex lattices and multiply-charged vortex dipoles imaged with the QVM2, vortex cores are visible with bright-field absorption, Faraday, and dark-field imaging techniques. We will discuss this further in Chapter 9.

# Chapter 4

# Generation of vortex distributions with signatures of turbulence

As discussed in Chapter 1, experimental studies of 2DQT in BECs currently lag theory and numerics, with significant but surmountable technical challenges that must be overcome prior to implementing parallel experimental studies. One such technical hurdle is that of generating an initial vortex distribution that exhibits robust signatures of turbulence, while minimizing the acoustic energy introduced to the system. In particular, we would like to experimentally initiate a 2D vortex distribution with a sufficiently high point-vortex energy such that we might observe the vortex aggregation dynamics predicted to accompany Onsager-Kraichnan condensation [25, 27].

The article *Experimental Methods for Generating Two-Dimensional Quantum Turbulence in Bose-Einstein Condensates* [4] reproduced in Appendix A outlines a number of techniques for initiating disordered 2D vortex distributions that may show signatures of turbulence. The techniques described were developed over the course of this dissertation and the dissertations of Tyler Neely [33] and Carlo Samson [34]. In particular, the article reviews the initial observation of vortex dipole dynamics and meta-stable vortex aggregates [3], vortex distributions resulting from modulation of the harmonic trapping potential [33, 34], vortex nucleation and bulk BEC behavior resulting from modulation of a 660-nm blue-detuned potential [34], and vortex nucleation via a small circular stir with a 660-nm stirring beam, and the subsequent formation of a large-scale persistent current [22]. The primary motivation behind the development of these vortex nucleation techniques was to explore methods for generating 2D vortex distributions that could be used for studies of forced and decaying 2DQT. For the purpose of the article we adopted a phenomenological definition of turbulence, associating 2DQT with a large disordered distribution of

vortices with a large range of inter-vortex separations, a 2D analog to the vortex tangle predicted by Feynman for 3DQT [15]. Other phenomenological characteristics of turbulence include rapid mixing, and nondeterministic dynamics where a small deviation in the initial conditions results in a wildly different final state.

We include adapted excerpts from the article [4] in Secs. 4.3 and 4.4. Combined with our more recent work aimed at generating vortex clusters and described in Secs. 4.5 and 4.6, the techniques presented in this chapter provide a representative sample of recent efforts towards forcing vortex cores into a BEC in a manner that produces 2D vortex distributions that support both phenomenological and statistical definitions of turbulence.

## 4.1 Vortices: building blocks of quantum turbulence

A dilute gas BEC is a quantum mechanical entity that is often well described by an order parameter, or macroscopic wave function,

$$\psi(\vec{r},t) = \sqrt{n(\vec{r},t)}e^{-i\phi(\vec{r},t)} \tag{4.1}$$

where $n(\vec{r},t)$ is the density profile, and $\phi(\vec{r},t)$ is the phase profile associated with the BEC wavefunction. In the mean-field approximation the evolution of the BEC wavefunction is governed by the Gross-Pitaevski equation (GPE)

$$i\hbar\frac{\partial\psi}{\partial t} = -\frac{\hbar^2}{2m}\nabla^2\psi + V(\vec{r},t)\psi + g|\psi|^2\psi \tag{4.2}$$

where $g = 4\pi\hbar^2 a_\mathrm{s}/m$ is the interaction strength between atoms, $a_\mathrm{s}$ is the s-wave scattering length and $V(\vec{r},t)$ is the potential due to the trap and other perturbing potentials [5]. For a highly oblate BEC with strong axial harmonic confinement along the $z$-axis, we can define an effective 2D interaction parameter $g_2 = g/\sqrt{2\pi}\ell_\mathrm{z}$, where $\ell_\mathrm{z} = \sqrt{\hbar/m\omega_\mathrm{z}}$ is the harmonic oscillator length in the $z$-direction [26]. In this limit, Eqn. 4.2 reduces to

$$i\hbar\frac{\partial\psi}{\partial t} = -\frac{\hbar^2}{2m}\nabla_\perp^2\psi + V(x,y,t)\psi + g_2|\psi|^2\psi \tag{4.3}$$

where $\nabla_{\perp}^2 = \frac{\partial^2}{\partial x^2} + \frac{\partial^2}{\partial y^2}$, and $\psi$ is now a function of $x$ and $y$ (the full wavefunction incorporates the lowest single-particle mode for the $z$-direction). A number of phenomena that we observe experimentally in the highly oblate BECs formed in the hybrid trap are accurately modeled by spit-step evolution of Eqn. 4.3.

From a hydrodynamic perspective, a dilute gas BEC is a tiny droplet of superfluid that supports vortices of quantized circulation. These quantized vortices are coherent, metastable structures associated with an integer $2\pi$-phase winding and, due to the single-valued nature of the condensate wave-function, an associated region of zero density. The size of a vortex core is characterized by the healing length $\xi$ which gives a measure of the smallest length scale over which the order parameter can drop from its bulk value to zero.

In a distribution of vortices in a homogeneous system, an individual vortex core moves in the velocity field created by the other cores in the distribution [1]. In a bound system such as a trapped BEC, the method of images can be used to account for the effect of the system boundary on vortex motion. Image vortices, analogous to image charge in electricity and magnetism, are placed outside the system boundary to cancel out any fluid flow perpendicular to the boundary. In an inhomogenous system such as a BEC in a harmonic trap, the inhomogeneity of the BEC density profile also affects the motion of the vortex. For a BEC in a harmonic trap containing a single vortex, the effect of the quadratic density profile is to cause the vortex to move towards the edge of the BEC [49].

In addition to single vortex cores of either circulation, structures consisting of multiple vortices may also be observed. A singly-charged vortex dipole consists of a vortex-antivortex pair in which one vortex has clockwise fluid circulation and the other vortex has counter-clockwise fluid circulation. While a single vortex is associated with circular fluid flow, and consequently angular momentum, a vortex dipole, considered as a single entity, is associated with linear momentum and can be identified in simulations as a pair of cores traveling together. In the absence of other vortex cores in a BEC confined in a harmonic trap, Neely *et al.* observed that a vortex dipole will orbit the BEC with each

core tracing out an orbit in half of the BEC [3]. Of greater interest for studies of turbulence was their observation of multiply-charged vortex dipoles which provided evidence for long-lived vortex aggregates or clusters of cores with the same circulation. In general, we associate a vortex cluster with two or more vortices of the same sign of circulation that group together for timescales that are much longer than the cluster turnover time. This turnover time can be estimated to be on the order of 15-20 ms for a cluster consisting of two singly-charged vortices of the same circulation. While multiply-charged vortices are energetically unstable, both vortex dipoles and vortex clusters are meta-stable structures that have been observed to exist on timescales on the order of seconds.

## 4.2 Experimental observations of vortices

One of the current challenges in experimental studies of 2DQT is the determination of the circulation of individual vortex cores. In an ideal scenario we would have access to both the BEC density and phase profiles at any point in time, which would give us access to the complete BEC wavefunction $\psi(\vec{r}, t)$ as it evolved in time. A direct measurement of $\psi(\vec{r}, t)$ would allow us to both map out the vortex dynamics and to calculate the incompressible kinetic energy spectrum, enabling us to link the vortex core dynamics with statistical measures of turbulence commonly used to characterize 2D classical turbulence.

A single image of a vortex distribution in a BEC is fairly easy to obtain with a traditional bright-field absorption image of an expanded BEC. These images allow us to measure $n(\vec{r})$ for an instant in time as shown in Fig. 4.1. Here vortices are identified as a region of near-zero density. For certain deterministic vortex distributions such as the vortex lattice in Fig. 2.3 or the vortex dipole orbit mapped out by Neely *et al.* [3], the circulation of the vortex may be inferred from the nucleation process. In the case of a vortex lattice, if we know the direction, clockwise or counter-clockwise, in which the BEC is rotated to spin up the lattice, then we can infer that the vortices that comprise the lattice must have the corresponding circulation. However, experimental measurements of the condensate's

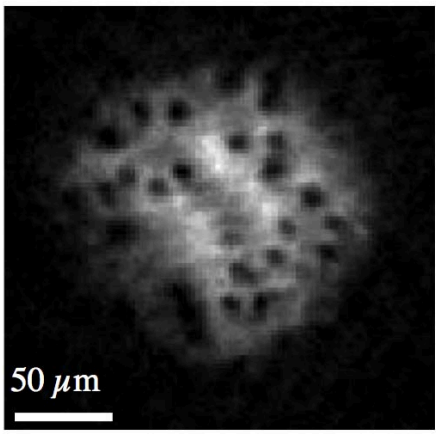


Figure 4.1: A representative bright-field absorption image of a disordered 2D vortex distribution obtained after expanding from the highly oblate hybrid trap.

phase profile are generally much more difficult. One possible approach is a matterwave interference measurement [44, 50, 51, 52] where the $2\pi$-phase winding associated with the vortex core is observed as a forking in the interference pattern. However, to our knowledge, this has not yet been applied to turbulent or highly disordered vortex distributions in a single-component BEC where the presence of numerous, closely spaced forkings would complicate the interpretation of the interference pattern, and where acoustic excitations may reduce the contrast.

Another approach would be to directly measure the BEC's momentum-space distribution $|\tilde{\psi}(\vec{k})|^2$. This can be done through either free-space expansion of the BEC, or by waiting a quarter of the trap period in a harmonic trap. Given the inherent BEC interaction energy, a true Fourier transform is achievable only if we turn off the inter-atom scattering with a Feshbach resonance [53, 54], or subject the BEC to such rapid expansion that the interaction term quickly goes to zero [55]. Measuring the momentum-space distribution does not actually allow us to infer the phase profile of the BEC wavefunction, but there have been recent analytical efforts to link the momentum-space distribution with a quantum kinetic energy spectrum [26].

Alternatively, if we had the capability to acquire a large number of minimally-destructive images from a single BEC we could map out the vortex density distribution as a function of time. Since we know the fluid flow corresponding to a quantized vortex and we know that the velocity field is calculated from the gradient of the phase profile as in Eqn. 1.7, in the limit of low acoustic energy, we should be able to infer (with some undetermined error) the circulation of individual vortex cores by tracking their motion over a period of time, and build up an approximate phase profile based on the locations and circulations of each vortex [6]. However, current BEC imaging techniques that allow for multiple images from a single BEC, such as the stroboscope technique developed by Freilich *et al.* [43], do not have the temporal resolution to track a large number of vortex cores. While the *in situ* imaging technique presented in Chapter 6 has the potential to trace out vortex dynamics in real time, at present the low signal-to-noise ratio restricts us to a single image. That said, the need for real-time velocity measurements is a primary motivation for the dark-field vortex imaging technique presented in Chapter 6.

Lastly, Powis *et al.* have proposed a gyroscopic technique to detect the sign of the vortex circulation [56].

## 4.3 Rotating a highly oblate BEC

As described in Sec. 4.2, the straightforward method of expansion imaging used in our experiments does not easily permit measurement of the circulation of vortices. While the interferometric or dynamic methods mentioned in Sec. 4.2 can be used for this purpose, these have not yet been applied to turbulent states of BECs. In order to look for the clustering of vortex cores of like-circulation, an alternative is to examine statistics of vortex distributions containing only large numbers of cores of identical circulation. One possible approach to generate such distributions is by rotating the trapping potential, as has been utilized in numerous experiments of BECs with different aspect ratios, such as Refs. [36, 37, 57]; see also Ref. [2] for an overview of numerous other experiments that utilized this

technique. Our approach follows such previous work, and is implemented by squeezing and rotating the magnetic trapping field as first implemented by Hodby *et al.* [36] and described in Sec. 2.2.

Our investigations of highly oblate BECs subjected to trap deformation and rotation started with a BEC in the combined magnetic and optical harmonic trap. We then applied the magnetic field ellipticity and spun in the highly oblate harmonic trap for time $t_{\rm s}$ at frequency $\omega_{\rm s}$ with ellipticity $B_\epsilon$. After spinning we returned to the symmetric harmonic trap and held for time $t_{\rm h}$ while the BEC shape deformations damped out. Finally, we let the condensate expand and we imaged the cloud.

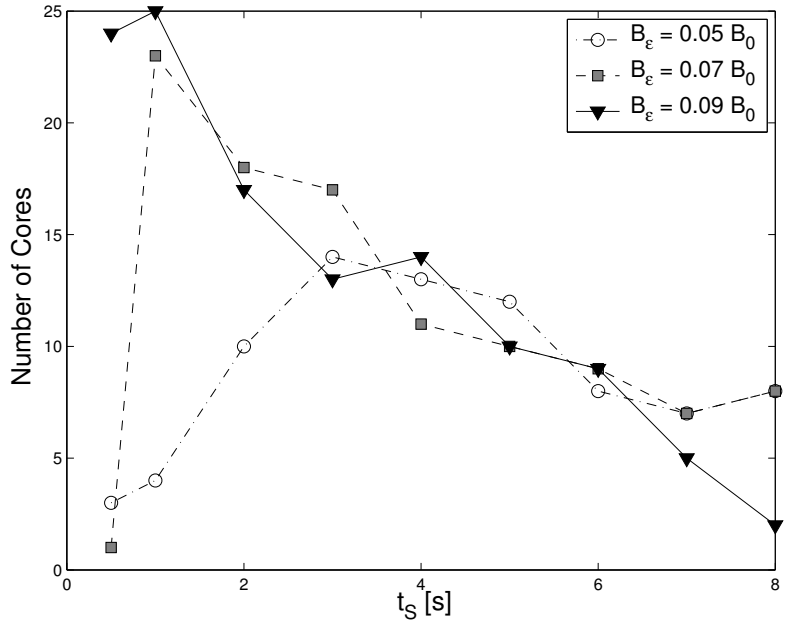


Figure 4.2: Comparison of number of vortex cores versus spin time for different ellipticities. All data points were generated by spinning at $\omega_{\rm s} = 2\pi \times 6$ Hz for a variable spin time $t_{\rm s}$ and then holding for 2.5 s after the spin prior to expansion. Open circles represent a single set of data taken with $B_\epsilon = 0.05\,B_0$, gray squares represent $B_\epsilon = 0.07\,B_0$, and black triangles represent $B_\epsilon = 0.09\,B_0$. Both the peak number of vortex cores and $t_{\rm s}$ corresponding to the peak number of vortex cores seem to be dependent on ellipticity but all three ellipticities show decreasing vortex number for longer spin times.

By varying spin frequencies, we found a resonance condition for generating large numbers of vortices at $\omega_s = 2\pi \times 6$ Hz. Here $\omega_s \sim 0.75\omega_r$ is consistent with previous observations of exciting the quadrupole mode in 3D harmonic traps at $\omega_s \sim 0.7\omega_r$ [58]. We measured the number of vortex cores versus spin time for different ellipticities at this resonance frequency. Figure 4.2 shows three sets of data corresponding to ellipticities of $B_\epsilon = 0.05\,B_0$, $0.07\,B_0$ and $0.09\,B_0$. All data points were generated by spinning for a variable spin time $t_s$ and then holding for $t_h = 2.5$ s after the spin and before expansion. Both the peak number of vortex cores and $t_s$ corresponding to the peak number of vortex cores appear to be dependent on ellipticity with peak vortex number occurring at a much shorter spin time for $B_\epsilon = 0.09\,B_0$ and $0.07\,B_0$ than for $B_\epsilon = 0.05\,B_0$. All three ellipticities show decreased vortex numbers for longer spin times on the order of $t_s$= 8 s indicating that vortex cores may be annihilating or leaving the system before crystalizing into a lattice.

Figure 4.3 visually tracks the evolution of the condensate during spinning. Figures 4.3(a) and 4.3(c) show successive images at 100 ms intervals for $t_s = 0.1$ to 1.0 s. The BECs were imaged directly after spinning with no hold in the axially symmetric harmonic trap ($B_\epsilon = 0$) prior to expansion. Figures 4.3(b) and 4.3(d) show successive images at 100 ms intervals for $t_s = 0.1$ to 1.0 s with an additional 400 ms hold time in the axially symmetric harmonic trap prior to expansion and imaging. The hold time in the symmetric harmonic trap seems important for the nucleation of vortices as vortex cores appear after $t_s = 400$ ms and $t_h = 400$ ms, but do not appear until $t_s = 1.0$ s for the case of $t_h = 0$.

Figures 4.4 and 4.5 show additional distributions of vortex cores nucleated by spinning and relaxing over subsequent hold times. Here $t_s = 1.0$ s is held constant and the BECs are imaged after increasing values of $t_h$. Vortices appear to be nucleated on the outer edge of the BEC. Presumably there is net angular momentum added to the condensate, so we expect the vortex cores to be predominately of the same circulation, at least once the system has relaxed to a meta-stable configuration. However, it may be the case that the net circulation is large, but that numerous vortices of the opposite circulation are also

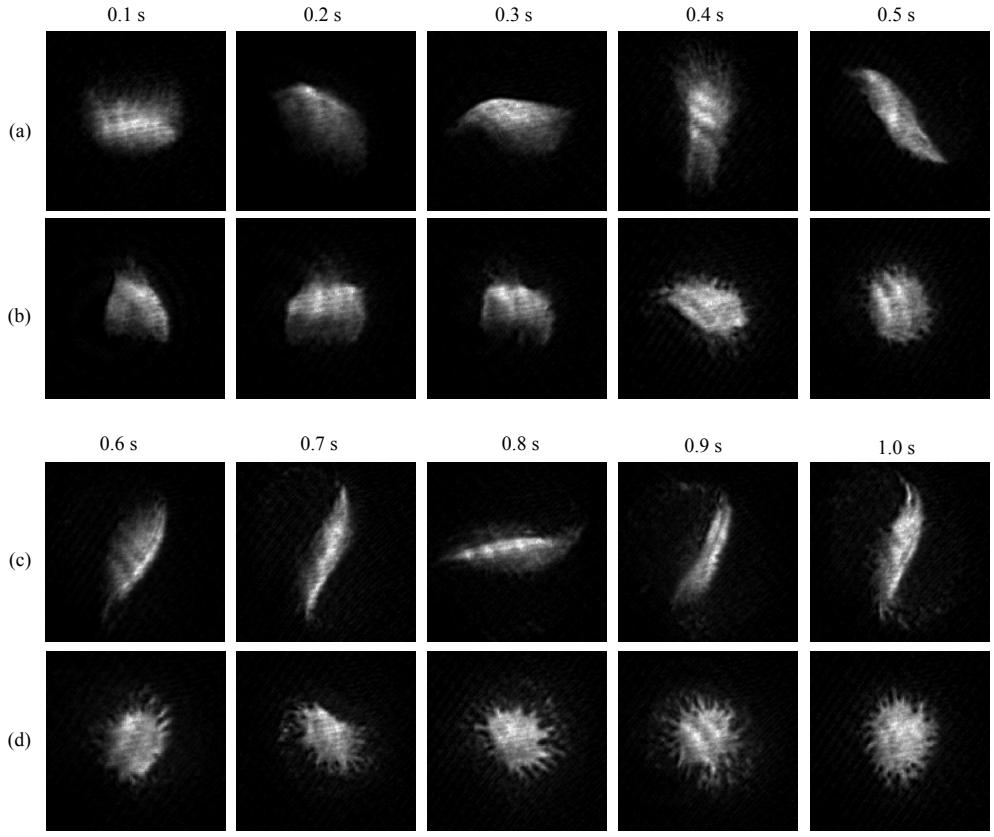


Figure 4.3: 350-$\mu$m-square expansion images of an oblate BEC for varying $t_{\rm s}$ (indicated above images) at increments of 100 ms. Spin frequency and ellipticity were held constant at $\omega_{\rm s} = 2\pi \times 6$ Hz and $B_\epsilon = 0.07 B_0$. (a) and (c) BECs were expanded and imaged directly after spinning, $t_{\rm h} = 0$. (b) and (d) BECs were held for 400 ms after spinning, $t_{\rm h} = 400$ ms, then expanded and imaged.

generated and present in these images, at least prior to the point at which a disordered distribution is uniformly distributed throughout the BEC. If vortices are indeed of the same circulation in images such as the ones in the bottom row of Fig. 4.4, then such states may be candidates for experimental measurement of vortex power-law distributions in a BEC, as has been analytically described for homogeneous BECs [25].

As observed, large, disordered vortex distributions can be generated by exciting col-

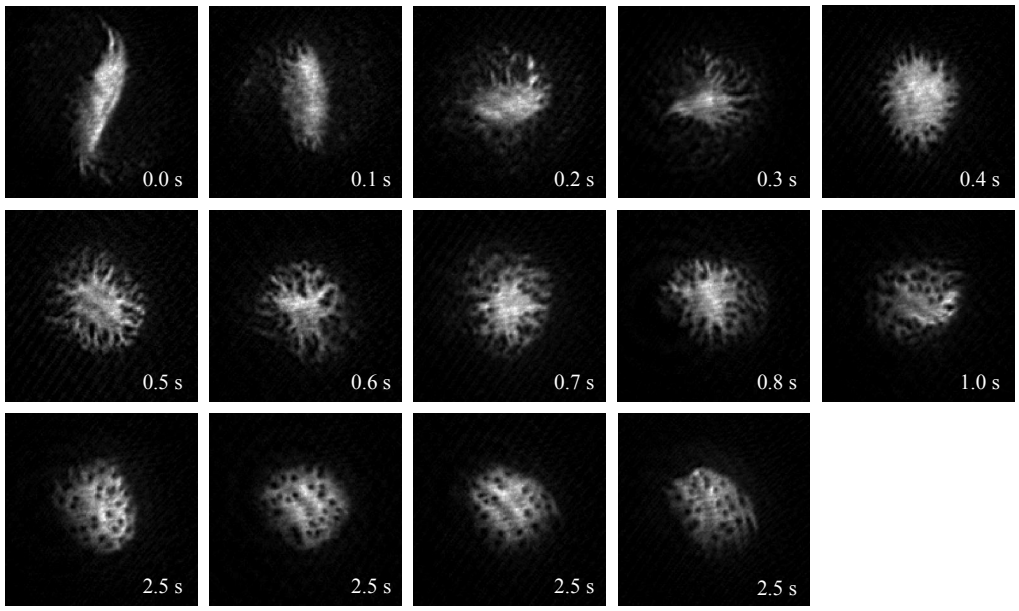


Figure 4.4: 350-$\mu$m-square expansion images of vortex distributions in the highly oblate BEC for varying $t_{\rm h}$. Spin time, frequency, and ellipticity were held constant at $t_{\rm s} = 1.0$ s, $\omega_{\rm s} = 2\pi \times 6$ Hz and $B_\epsilon = 0.07 B_0$. Images were taken for variable $t_{\rm h}$ from 0 to 2.5 s. Multiple images for $t_{\rm h} = 2.5$ s are shown to give a representative sample of the variation in vortex distribution.

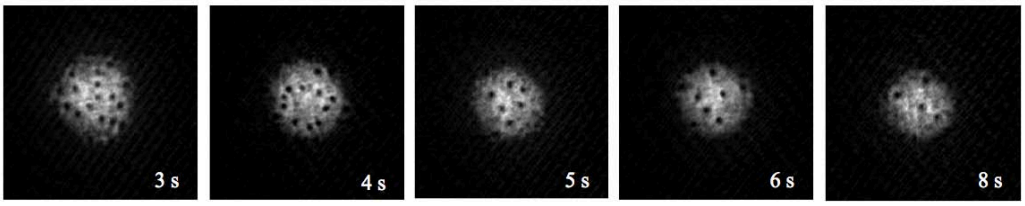


Figure 4.5: 350-$\mu$m-square expansion images of vortex distributions in the highly oblate BEC for the varying hold times $t_{\rm h}$ shown from 3 to 8 s. By this time, BEC shape deformations have largely damped out. Spin time, frequency, and ellipticity were held constant at $t_{\rm s} = 1.0$ s, $\omega_{\rm s} = 2\pi \times 6$ Hz and $B_\epsilon = 0.07 B_0$.

lective modes of the BEC. The shape deformations damp more quickly than the number of vortex cores, leaving open the possibility of finding parameters where studies of decaying 2DQT could be performed before the system spins down to a state with no vortices.

Spinning introduces a net angular momentum into the condensate and should result predominately in vortex cores of the same circulation, making this a possible system in which to observe vortex aggregates without time-resolved dynamics measurements. Nevertheless, this vortex excitation technique does not appear to satisfy the particular goal of continuous forcing, although it appears to be a candidate for studies of decaying 2DQT. It is interesting to note that even for long hold times we find no evidence of a vortex lattice in the highly oblate BEC. Thermalization times for a lattice in a highly oblate BEC may be beyond the lifetime of our BECs; see Ref. [59] for further discussion of this issue.

## 4.4 Modulating 660-nm beam power

In the experiments described in this section, we investigated the response of a BEC to time-dependent perturbations of the intensity of a focused blue-detuned laser beam that pierced the BEC. In all cases in this section, the relative position between the beam and the BEC was stationary. Our aim in these experiments was to locally excite the BEC as an empirical probe of the existence of thermal counterflow [60, 61] in a region where the BEC was locally depleted of atoms. While vortices were observed in all methods examined, the mechanisms for vortex nucleation remain unclear and merit further experimental and numerical investigation.

In this experiment we formed a highly oblate BEC in the purely harmonic trap, then turned on and sinusoidally modulated the intensity of a focused blue-detuned Gaussian beam for a varying time $t_{\rm mod}$. After the modulation we held the BEC in the purely harmonic trap for varying time $t_{\rm h}$, then expanded and imaged. The blue-detuned beam had a $1/e^2$ radius of 10 $\mu$m and was directed axially through the center of the condensate, as shown in Fig. 2.4. During the modulation time the optical potential $U(t)$ generated by the beam followed

$$U(t) = U_0 \sin^2(\omega_{\rm mod} t/2) \tag{4.4}$$

for $0 < t < t_{\rm mod}$, with maximum repulsive potential energy $U_0$, and frequency $\omega_{\rm mod}$. For all

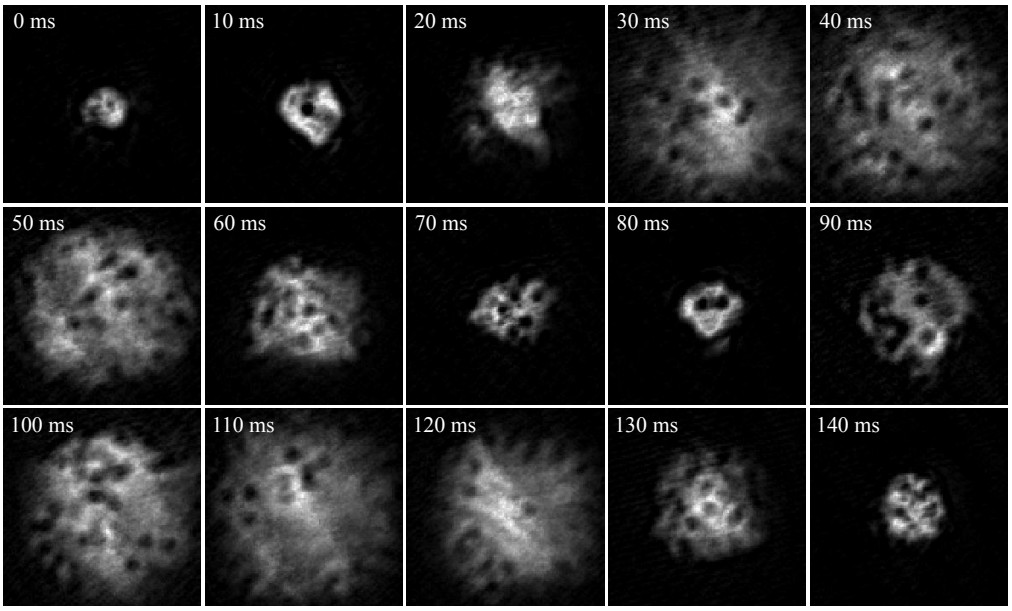


Figure 4.6: 250-$\mu$m-square absorption images acquired after the hold times $t_{\rm h}$ indicated. The condensate undergoes large breathing oscillations in the trap, and this oscillation leads to a periodic variation in expanded BEC radius between $\sim 40\,\mu$m and $\sim 180\,\mu$m.

other times, the beam was turned completely off. We fixed the modulation time at integer multiples of the modulation period, $\tau_{\rm mod} = 2\pi/\omega_{\rm mod}$, such that the intensity of the blue-detuned beam always started and ended at zero, and we did not have to be concerned with ramping off the blue-detuned beam for imaging. Here the blue-detuned beam acted as a perturbation to the confining potential. Figure 4.6 shows a sequence of images for varying values of $t_{\rm h}$ after modulating for $t_{\rm mod} = 187.5$ ms, with $U_0 \sim 0.3\mu_0$ (where $\mu_0 \sim 8\hbar\omega_{\rm z}$), and frequency $\omega_{\rm mod} = 2\pi \times 16$ Hz. This was approximately twice the radial trap frequency. An *in situ* image of the BEC in the harmonic trap with the blue-detuned beam aligned in the center is shown in the leftmost image of Fig. 4.7.

While this method generated a large number of vortex cores, we also observed large-scale breathing oscillations in the radial dimension of the condensate. The radius of the expanded cloud oscillated between $\sim 40$ $\mu$m and $\sim 180$ $\mu$m with a period of $\sim 70$ ms and

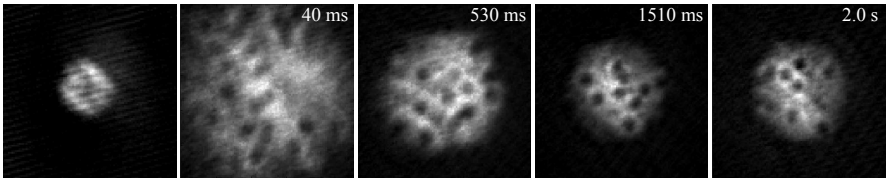


Figure 4.7: 250-$\mu$m-square absorption images acquired after the hold times $t_{\rm h}$ indicated. The first image is an *in situ* image of the BEC in the harmonic trap with the blue-detuned beam partially penetrating the condensate; note that the optical potential strength is well below the BEC chemical potential.

eventually damped out with an exponential decay time constant $\tau_{\rm damp} \sim 500$ ms. As shown in Fig. 4.7, a disordered distribution of vortex cores remained in the condensate even after the bulk oscillations subsided, with $\sim 8$ cores remaining for $t_{\rm h} = 2$ s. It is not entirely surprising that we induced bulk fluid oscillations, given that we were forcing the BEC at a frequency that was twice the radial trapping frequency. However, further study is needed for positively identifying the vortex generation mechanism in this experiment.

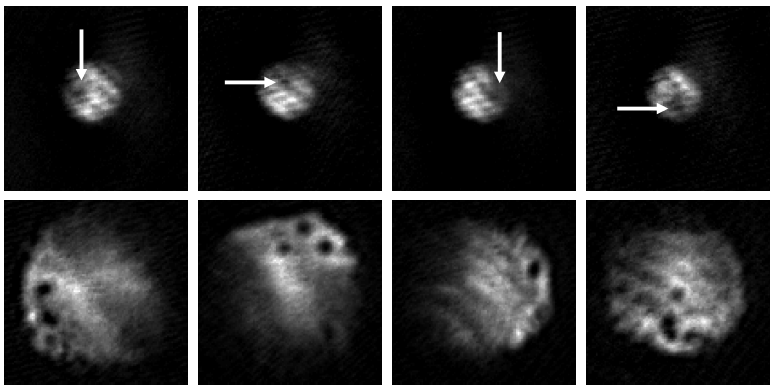

Figure 4.8: Localization of vortex cores at the location of the blue-detuned beam. All images are 250-$\mu$m-square absorption images. The top row of images were taken with the BEC in the harmonic trap and the maximum height of the blue-detuned potential at $U_0 \sim 0.3\mu_0$. The locations of the laser beam correspond to the positions designated by the arrow. The bottom row of images were acquired after $t_{\rm h} = 40$ ms followed by the expansion procedure. Note the correlation between beam position and the position of the vortex cores in each vertical pair of images.

In the sequence of images shown in Fig. 4.6, it is unclear where vortex nucleation occurs. To further explore the nucleation mechanism, we aligned the blue-detuned beam near the edge of the BEC, and modulated for $t_{\rm mod} = 62.5$ ms, equivalent to one sinusoidal pulse of the laser light, with $U_0 \sim 0.3\mu_0$, and frequency $\omega_{\rm mod} = 2\pi \times 16$ Hz. After modulation, we held the BEC in the purely harmonic trap for $t_{\rm h} = 40$ ms, then expanded and imaged the BEC. As shown in Fig. 4.8, the vortex cores that resulted from the modulation appear to form near the location of the focused laser beam.

Lastly, we replaced the axially symmetric ($w_{0\rm x} = w_{0\rm y}$) focused blue-detuned Gaussian beam with a blue-detuned light sheet, focused along the $x$-axis with a $1/e^2$ radius $w_{0\rm x} = 10$ $\mu$m, spatially extended along the $y$ direction, and directed axially (along $z$) through the center of the BEC. The width of the beam along the $y$-axis was much larger than the diameter of the condensate so that the beam extended beyond the edge of the condensate in the $y$-direction. Figure 4.9(a) is a vertical absorption image of the unexpanded highly oblate BEC with the elongated blue-detuned beam partially penetrating the condensate. We modulated at $\omega_{\rm mod} = 2\pi \times 16$ Hz for $t_{\rm mod} = 62.5$ ms and $U_0 \sim 0.3\mu_0$, held for $t_{\rm h}$, then expanded and imaged the BEC. Figures 4.9(b) and 4.9(c) were taken after $t_{\rm h} = 40$ ms. Here the vortices appear to be nucleated along the long axis of the elongated beam. The vortex cores shown in these images are not completely resolved but we suspect that the vortices are being nucleated as dipoles in a similar manner to the breakdown of a soliton due to the snake instability in a BEC [62, 63, 64]. Alternatively, these features may be acoustic precursors to vortex dipole formation [65].

As with the axially symmetric blue-detuned potential, we observed bulk excitations in the condensate. Figure 4.10 shows a sequence of images taken with $\omega_{\rm mod} = 2\pi \times 16$ Hz, $t_{\rm mod} = 62.5$ ms, and $U_0 \sim 0.5\mu_0$, for varying hold times $t_{\rm h}$. The oscillations in $x$ and $y$ are now out of phase by $\sim 90^\circ$. Vortex cores appear to be generated at the location of the beam and move to the outer boundary. In particular the images corresponding to $t_{\rm h} < 40$ ms show vortices aligned with the long axis of the beam, but by $t_{\rm h} = 50$ ms the vortices

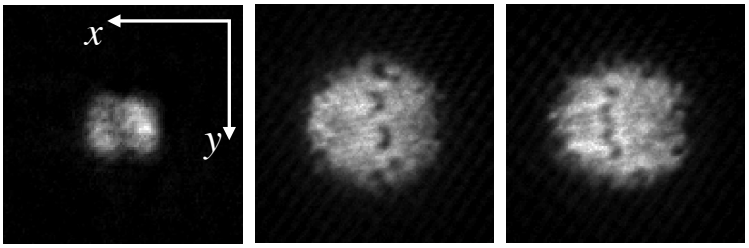


Figure 4.9: Localization of vortex cores at the location of the blue-detuned beam. All images are 250-$\mu$m-square absorption images. (a) taken with the BEC in the harmonic trap and the blue-detuned potential on at a strength of $U_0 \sim 0.5\mu_0$. In (b) and (c), expansion images were taken after $t_{\rm h} = 40$ ms. For these images $U_0 \sim 0.3\mu_0$. Note that the vortex cores are localized along the long axis of the blue-detuned beam and that they appear to be nucleating in pairs.

are located along the outer boundary of the condensate with no cores in the center. Later images show more disordered distributions of cores. Again, the mechanism for nucleation is not clear.

In both of these methods, intensity modulations of a blue-detuned laser beam were observed to be effective for nucleating vortices in a BEC. Although the mechanisms for vortex nucleation remain unclear, we observe correlations between the position of the laser beam and the site of vortex generation within the BEC. With careful parameter selection, it may be possible to use this method for controlled vortex generation rates. However, one must also be careful not to significantly excite shape oscillations, as these would make studies of 2DQT difficult. Perhaps with further adjustment of the modulation rates and times, shape oscillations could be minimized, and methods of this sort could be utilized for 2DQT studies.

As an extension, *in situ* imaging of vortex distributions, such as that described in Chpts. 6 and 9, would allow us to image the vortex distribution while the 660-nm beam power remains at a non-zero value. With the removal of this constraint on the final value

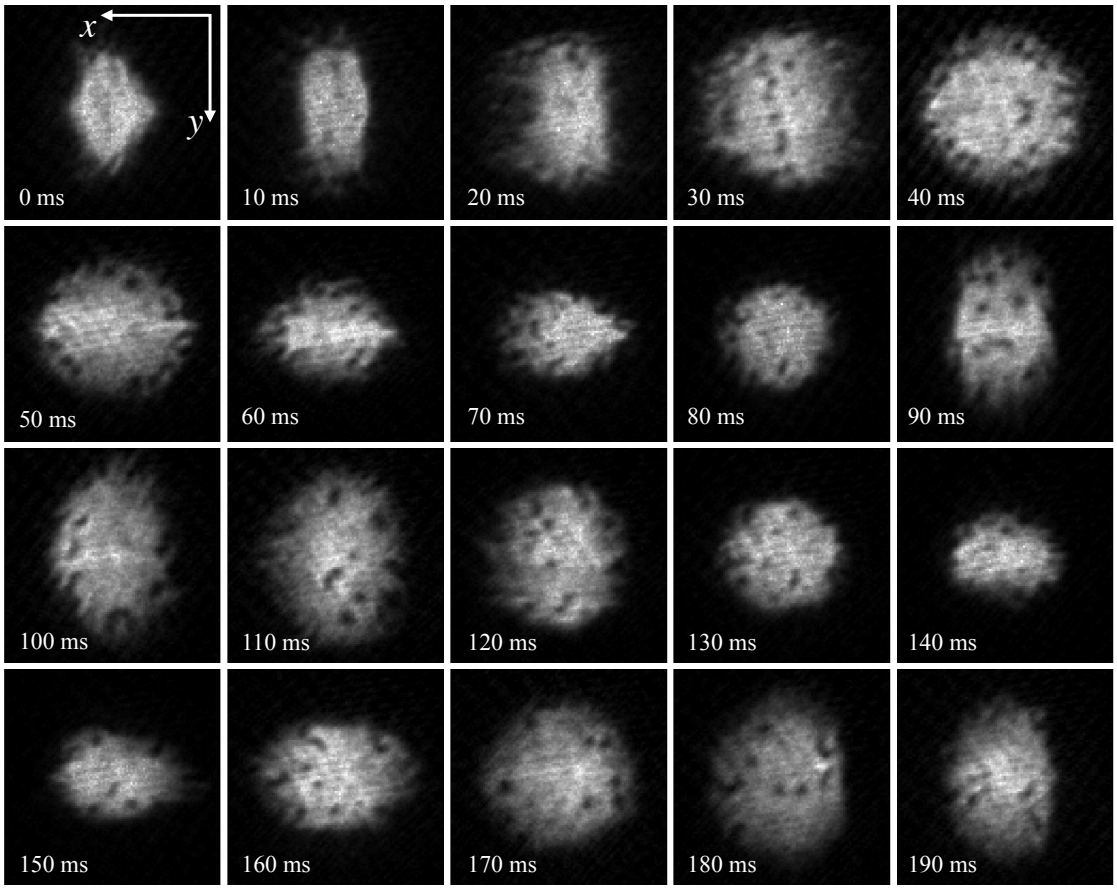


Figure 4.10: 250-$\mu$m-square absorption images acquired after the hold times $t_{\mathrm{h}}$ indicated. The condensate undergoes bulk oscillations that are out of phase in $x$ and $y$. Vortex cores appear to nucleate at the location of the beam and then move throughout the BEC.

of the 660-nm beam power, we might consider a very small amplitude oscillation of beam power about an offset on the order of the chemical potential, as a way of nucleating vortex cores while mitigating the bulk oscillation of the BEC. It is possible that the constraint requiring the beam power to start and stop at zero meant that the blue-detuned potential underwent a larger oscillation than was truly necessary to nucleate vortex cores. We suspect that the large oscillations in the strength of the repulsive potential at frequencies near the axial trap frequency were responsible for the observed oscillations in the bulk BEC. It

may be possible to find a threshold value for the blue-detuned potential such that small oscillations about this threshold power nucleate vortices, but are too small to generate oscillations of the bulk BEC. However, any modulation at the trap frequency does have the potential to excite resonant bulk excitations.

## 4.5 Vortex clusters: stirring with constant beam power

The following method for injecting vortex cores and clusters resulted from an initial effort to reproduce the numerical results of Reeves *et al.* [27] as part of a broader search for experimentally realizable vortex nucleation techniques that may show statistical signatures of turbulence. In their numerical study, they stirred a highly oblate BEC by moving a repulsive stirring beam with a $1/e^2$ beam radius of $\sigma = 4\xi$ in a circle with a radius of $0.4R_{\mathrm{TF}}$, where $R_{\mathrm{TF}}$ is the radial Thomas-Fermi radius of the highly oblate BEC. They identified three different stirring regimes resulting in the emission of vortex dipoles, vortex clusters, and oblique solitons respectively. They mapped out the parameter space for these regimes by varying both the stirring speed $v_{\mathrm{stir}}$ relative to the condensate speed of sound $c_{\mathrm{s}}$, and the height of the stirring potential $U_0$ relative to the condensate chemical potential $\mu_0$. Roughly, they found that the transitions between regimes occurred when $v_{\mathrm{stir}} > c_{\mathrm{s}}$ (transition between dipole and cluster emission), and when $U_0 > \mu_0$ (transition between dipole/cluster emission and oblique soliton regime).

Our experimental procedure followed the timing sequence shown in Fig. 4.11. The 660-nm beam ramps on to a maximum value of $U_0$ over $t_{\mathrm{ramp}} = 6$ s. The beam power is held constant through the final 8-s evaporation stage, and the first circular stir, occurring over a time $t_1 = \tau$, where $\tau$ is the stirring period. The 660-nm beam power ramps off over a second circular stir for time $t_2 \leq \tau$, allowing for immediate BEC expansion after the completion of the stirring process. Generally both circular stirs complete a full spatial circle with period $\tau$ and radius $r_{\mathrm{stir}}$, but occasionally we employed a partial second stir with the stirring beam ramping off over some fraction of $\tau$. We measured the radius of the

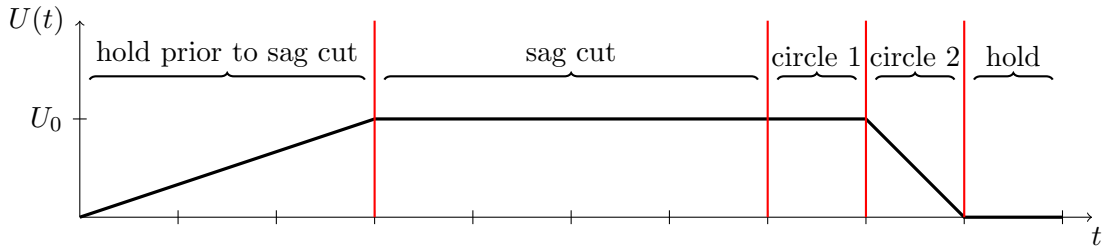


Figure 4.11: 660-nm beam power timing sequence for circular stirring with constant beam power (not to scale). The 660-nm beam ramps on to $U_0$ over $t_{\mathrm{ramp}} = 6$ s. The beam power is held constant through the final 8-s evaporation stage, and the first circular stir $t_1 = \tau$. The 660-nm beam ramps off over a second circular stir, with a variable ramp-off time $t_2$. Generally $t_2 = \tau$ but occasionally it is beneficial to ramp off the beam over a fraction of a circular stir $t_2 < \tau$.

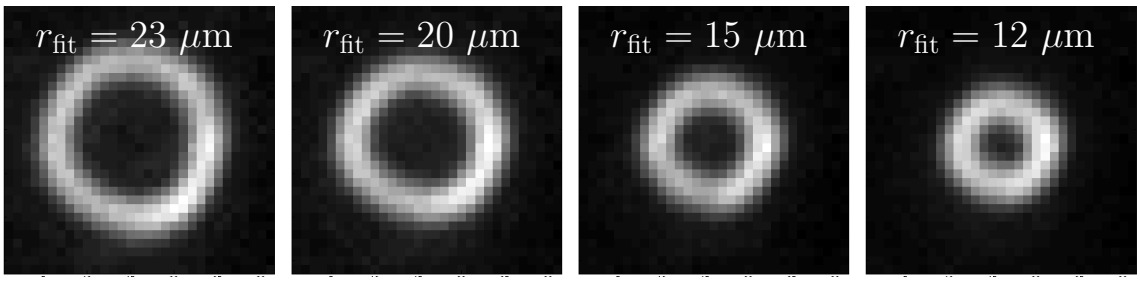


Figure 4.12: This set of images shows the 660-nm beam path for a circle of radius $r_{\mathrm{fit}}$ shown on the image. The 660-nm beam has a $1/e^2$ beam radius of 8 $\mu$m.

circular stir using two different methods, directly imaging the path of the 660-nm beam as shown in Fig. 4.12, and imaging the density-dip due to the repulsive blue-detuned beam within the BEC as shown in Fig. 4.24. We are not sure why these radii do not agree. The radii calculated from fits to the 660-nm beam traces shown in Fig. 4.12 are consistently smaller, however we choose to use the these radii with the understanding that we may be underestimating the radius of a circular stir by a couple of microns.

The set of images shown in Fig. 4.13 follows the timing sequence described above with a circular stirring period of $\tau = 100$ ms. The circle inscribed by the blue-detuned stirring beam had a radius $r_{\mathrm{stir}} \sim 12$ $\mu$m resulting in the repulsive obstacle traveling with a velocity $v_{\mathrm{stir}} \sim 0.44 c_{\mathrm{s}}$, where $c_{\mathrm{s}} \sim 1700$ $\mu$m/s is the theoretical speed of sound for our experimental

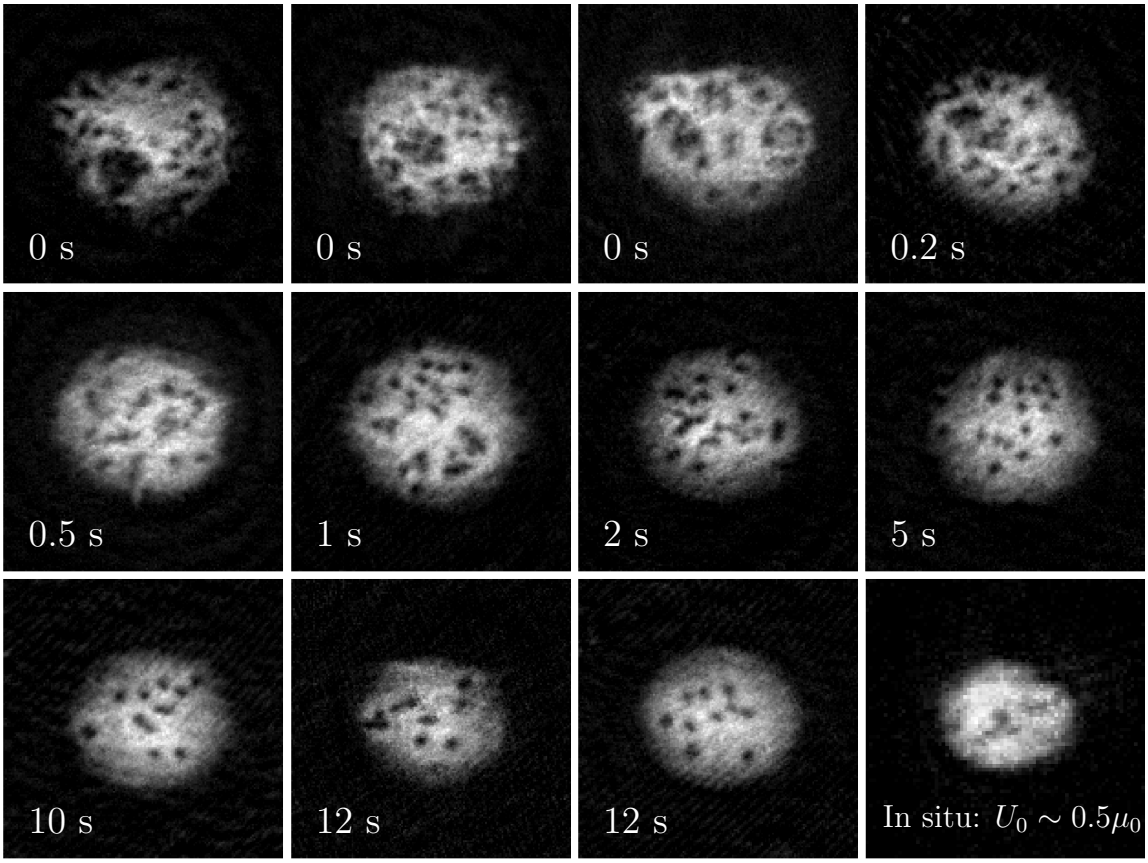


Figure 4.13: This set of 400 × 400-$\mu$m square images follows the timing sequence shown in Fig. 4.11 with $\tau = 100$ ms. The circle inscribed by the blue-detuned stirring beam had a radius $r_{\mathrm{stir}} \sim 12$ $\mu$m resulting in $v_{\mathrm{stir}} \sim 0.44 c_{\mathrm{s}}$, where $c_{\mathrm{s}} \sim 1700$ $\mu$m/s is the speed of sound for our parameters. Multiple images taken with $t_{\mathrm{h}} = 0$ s are included to give a representation of the variability of the process. The right-most image in the third row shows an *in situ* image of the BEC with the stirring beam partially penetrating the center of the BEC at a strength $U_0 \sim 0.5\mu_0$.

parameters [3]. After the second full circular stir and simultaneous ramp off of the 660-nm beam power over $t_2 = \tau$, the BEC was held in the hybrid trap for the variable hold time $t_{\mathrm{h}}$ shown on each image. Multiple images taken with $t_{\mathrm{h}} = 0$ s are included to give a representation of the variability in the resulting vortex distributions. The right-most image in the third row is an *in situ* image of the BEC with the stirring beam partially penetrating

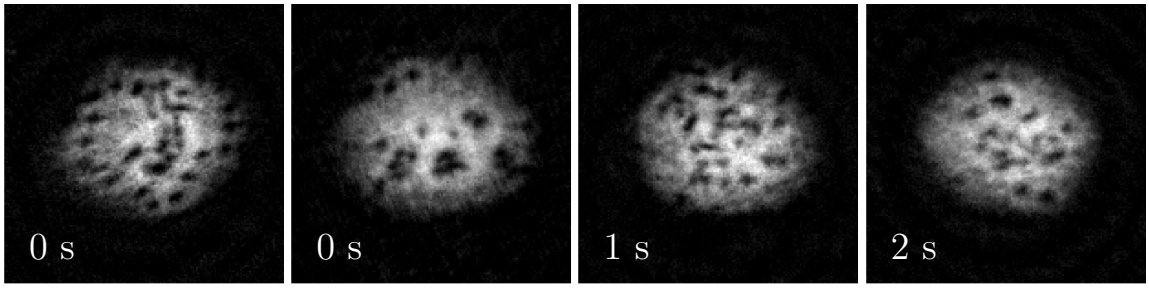


Figure 4.14: This set of images follows the timing sequence shown in Fig. 4.11, with $\tau = 200$ ms. The circle inscribed by the blue-detuned stirring beam had a radius $r \sim 12$ $\mu$m resulting in $v_{\mathrm{stir}} \sim 0.22 c_{\mathrm{s}}$, where $c_{\mathrm{s}} \sim 1700$ $\mu$m/s is the speed of sound for our parameters. Beam height is the same as that shown in Fig. 4.13.

the center of the BEC at a strength $U_0 \sim 0.5\mu_0$; the beam potential is determined with the beam centered in the BEC. Given the penetrable stirring potential $U_0 \sim 0.5\mu_0$ and subsonic beam velocity $v_{\mathrm{stir}} \sim 0.44 c_{\mathrm{s}}$, we expect to be in the dipole emission regime identified by Reeves *et al.* Fig. 4.14 shows a similar set of images but using a slower stirring speed $v_{\mathrm{stir}} \sim 0.22 c_{\mathrm{s}}$, which according to the parameter space mapped out by Reeves *et al.* should be on the boundary between dipole emission and no vortex emission at all. However, we observe large numbers of vortices, as well as possible vortex clusters for both stirring speeds. One possible reason could be that the local mean-field energy at the stirring radius is less than the BEC chemical potential due to the quadratic density profile enforced by the harmonic trapping potential. It is also possible that the differences between system parameters may account for differences between the experimental and numerical maps of parameter space, although we expect that transitions between regimes at $v_{\mathrm{stir}}/c \sim 1$ and $U_0/\mu_0 \sim 1$ should be observable in both experimental and numerical systems. Based on the previous dipole nucleation experiment performed by Neely *et al.* [3], we expect to observe vortex dipoles nucleated by the stirring beam for speeds above a critical velocity $v_c$. Neely measured $v_c \sim 0.1 c_{\mathrm{s}}$ for a linear stir through the center of the BEC with $U_0 \sim 1.2\mu_0$.

The requirement that we ramp off the 660-nm beam and expand the BEC prior to imaging complicates analysis of the resulting vortex distributions. We suspect the time

required for ramping off the 660-nm stirring beam and subsequent BEC expansion exceeded the lifetime of the oblique soliton, so that if we had succeeded in creating an oblique soliton the only signature that we would observe would be a train of vortex dipoles; see Ref. [27] for simulations showing oblique soliton formation and dissolution. In addition to making it difficult to observe oblique solitons, we generally ramped off the stirring beam power over the course of a second full circular stir, meaning that we complicated the vortex distribution generated by the first stir by stirring through the existing distribution as we ramped off the beam. We suspect this may make it difficult to distinguish between vortex dipoles and clusters, and that the stirring beam could break up clusters. However, we do observe vortex distributions such as those in top row of Fig. 4.13 where we appear to have nucleated aggregates of closely spaced cores. However, in large-disordered distributions such as these, we need some way to track the cores over time in order to distinguish between clusters of cores with the same circulation and vortex dipoles.

Figure 4.15 shows vortex distributions resulting from varying the stirring radius $r_{\rm stir}$ while keeping $U_0 \sim 1.8\mu_0$ constant. Again the 660-nm beam power timing sequence follows that shown in Fig. 4.11. Reported circle radii are determined through fits to the long-exposure images of the 660-nm beam, with the exception of $r_{\rm stir} \sim 2$ $\mu$m which is extrapolated from the other radii. The stirring period was $\tau = 100$ ms for Fig. 4.15(a) and (c) and $\tau = 200$ ms for Fig. 4.15(b) and (d), so that for a given $r_{\rm stir}$, columns (a) and (c) correspond to twice the stirring speed as that used for columns (b) and (d). Increasing the stirring radius results in an increase in the stirring speed, a decrease in the local speed of sound, and an increase in the height of the potential relative to the local mean-field energy. Hence, we expect to observe just a handful of cores in the images corresponding to $r_{\rm stir} \sim 2$ $\mu$m, and to be approaching the oblique dark soliton regime for the images corresponding to $r_{\rm stir} \sim 23$ $\mu$m. The images in Fig. 4.15(c) correspond to the fastest stirs with $v_{\rm stir} \sim 0.85 c_{\rm s}$ for the bottom image where $r_{\rm stir} \sim 23$ $\mu$m and seem to indicate heating of the BEC. We are not sure if we ever make it into a regime where we should expect to

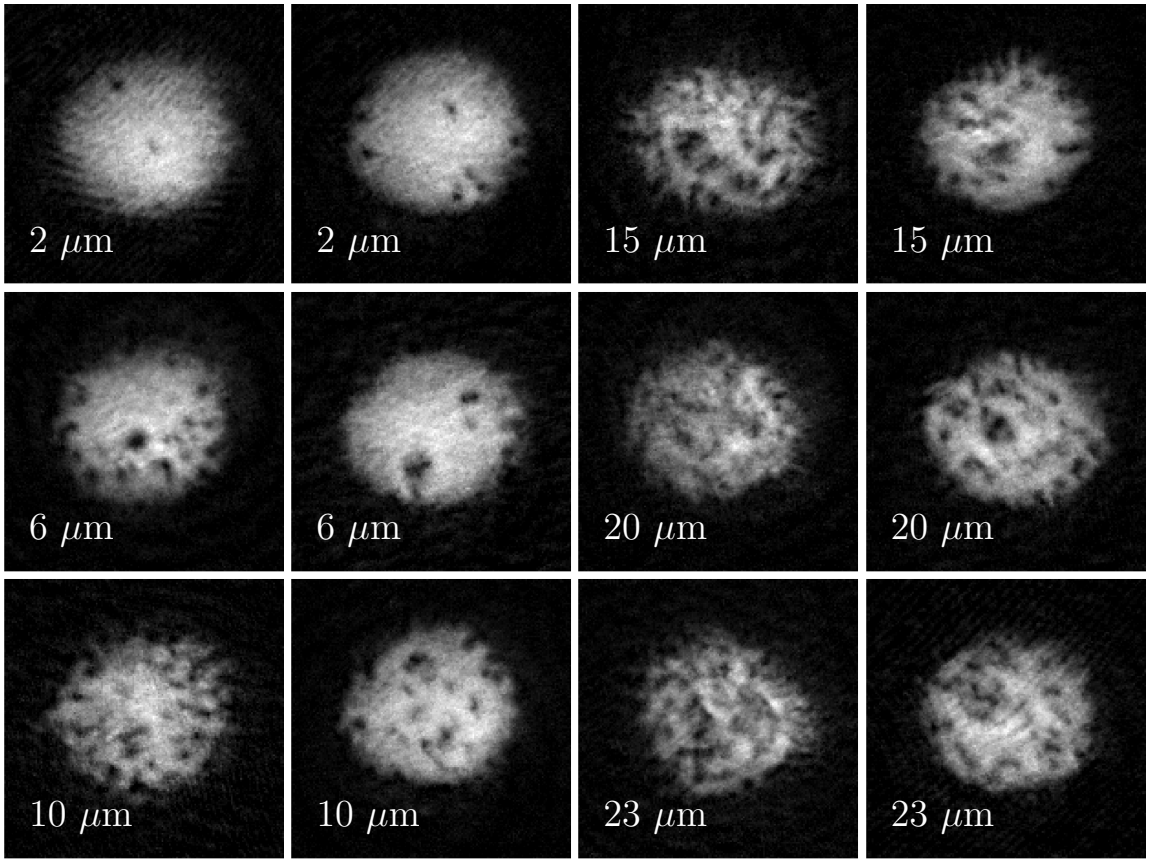


Figure 4.15: $400 \times 400$-$\mu$m square images of expanded BECs after circular stirring. The 660-nm beam power timing sequence follows that shown in Fig. 4.11. Reported circle radii are determined through fits to the long-exposure images of the 660-nm beam, with the exception of $r_{\mathrm{stir}} \sim 2$ $\mu$m which is extrapolated from the other radii. Columns (a) and (c) correspond to circular stirs with a period of $\tau = 100$ ms, while columns (b) and (d) correspond to $\tau = 200$ ms. The maximum potential height for all stirs is $U_0 \sim 1.8\mu_0$. Note that increasing the stir radius, while keeping $U_0$ and $\tau$ constant, results in an increase in stir velocity, a decrease in the local speed of sound, and an increase in the height of the stirring potential relative to the local mean-field energy.

see an oblique dark soliton since even the fastest stirs are subsonic.

In order to isolate the effect of the stirring beam potential, we kept the stirring radius $r_{\mathrm{stir}} \sim 15$ $\mu$m, period $\tau = 200$ ms, and therefore $v_{\mathrm{stir}} \sim 0.3c_{\mathrm{s}}$ constant, while varying the

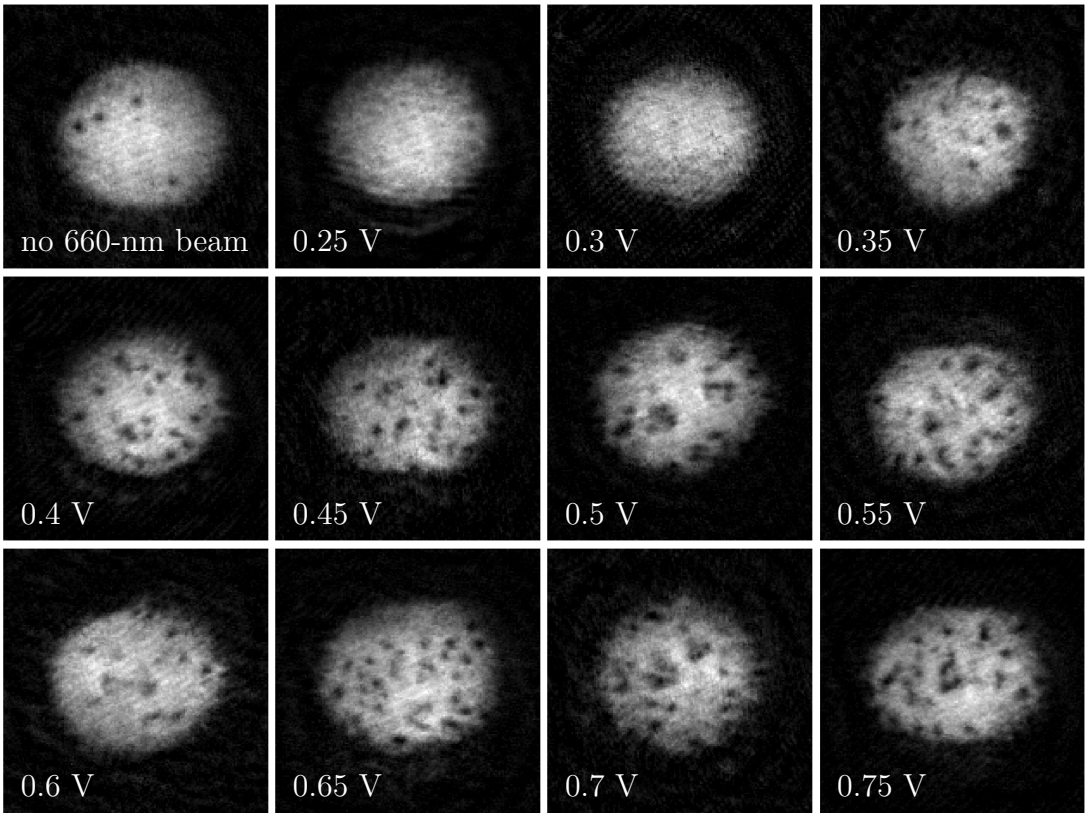


Figure 4.16: $400 \times 400$-$\mu$m square images of expanded BECs. The timing sequence for the 660-nm beam potential corresponds to that shown in Fig. 4.11 with $\tau = 200$ ms, although the lab book is unclear and it is possible $\tau = 150$ ms. The radius of the circular stir is $r_{\rm stir} \sim 15$ $\mu$m, resulting in $v_{\rm stir} \sim 0.3c_{\rm s} - 0.4c_{\rm s}$. $U_0$ varies as denoted on each image with values of $V_{660} > 1.0$V corresponding to potentials above the chemical potential. We denote $U_0$ by the voltage sent from the DAC to the 660-nm laser current controller. The 660-nm beam power is linearly related to this voltage, with V = 1.0 V corresponding to $U_0 \sim \mu_0$, while $V_{660} = 0.5$ barely makes a dimple in the BEC.

power in the 660-nm beam as shown in the images in Fig. 4.16 and 4.17. It is possible that the stirring period used for Fig. 4.16 is actually $\tau = 150$ ms, the labnote book is unfortunately ambiguous. However, we can still get a feel for the transition between the regime with zero vortices and the vortex dipole regime which we observe at $V_{660} = 0.35$ V. For the images shown in Figs. 4.16 and 4.17, we denote $U_0$ by the voltage sent from timing computer to the 660-nm laser current controller, via a digital to analog converter.

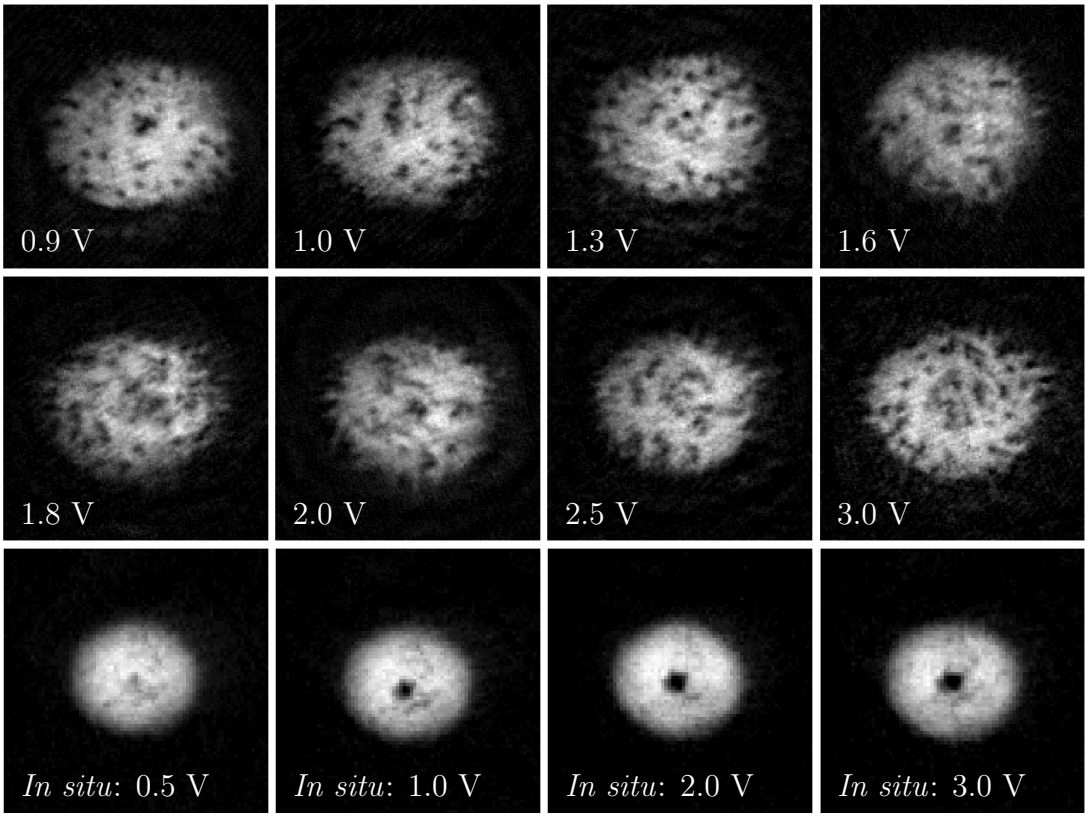


Figure 4.17: $400 \times 400$-$\mu$m square images of expanded BECs. The timing sequence for the 660-nm beam potential corresponds to that shown in Fig. 4.11 with $\tau = 200$ ms. The radius of the circular stir is $r_{\rm stir} \sim 15$ $\mu$m, resulting in $v_{\rm stir} \sim 0.3 c_{\rm s}$. $U_0$ varies as denoted on each image with values of $V_{660} > 1.0$V corresponding to potentials above the chemical potential. We denote $U_0$ by the voltage sent from the DAC to the 660-nm laser current controller. The 660-nm beam power is linearly related to this voltage, with V = 1.0 V corresponding to $U_0 \sim \mu_0$, while $V_{660} = 0.5$ barely makes a dimple in the BEC.

The 660-nm beam power is approximately linearly related to this voltage, with $V_{660} = 1.0$ V corresponding to $U_0 \sim \mu_0$. As shown in Fig. 4.17, $V_{660} = 0.5$ V barely makes a dimple in the BEC. With that in mind it is somewhat surprising that we begin to see vortices at such a low beam potential. The images shown in Fig. 4.17 correspond to beam heights with $U_0 \geq \mu$. The bottom row of images are *in situ* images of a BEC with the 660-nm penetrating the center for values of $V_{660}$ shown on each image.

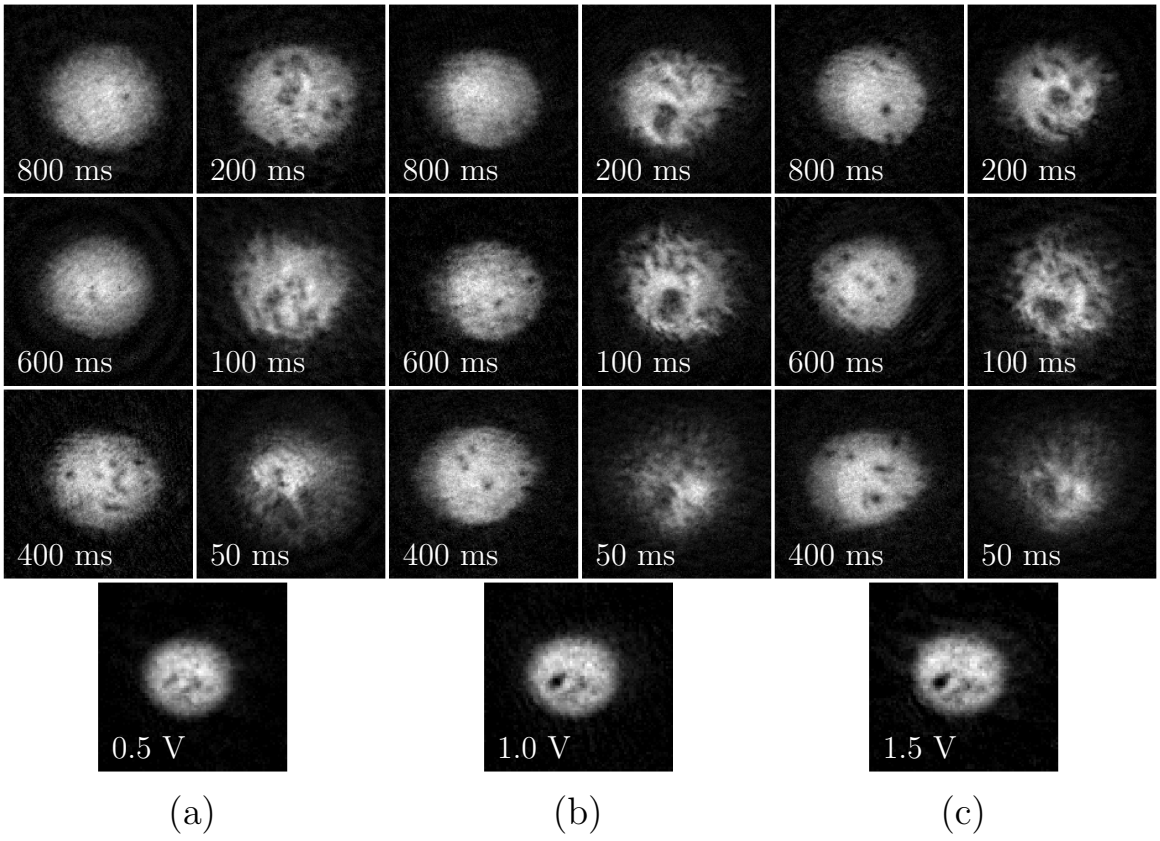


Figure 4.18: $400 \times 400$-$\mu$m square images of expanded BECs for circular stirs with varying $\tau$ over the range $\tau = 800$ ms down to $\tau = 50$ ms. The timing sequence for the 660-nm beam potential corresponds to that shown in Fig. 4.11 with the exception that the beam ramps off over a fraction of the second circular stir such that $t_1 = \tau$ and $t_2 = 35$ ms. The radius of the circular stir is $r_{\rm stir} \sim 15$ $\mu$m, resulting in a range of velocities from $v_{\rm stir} \sim 0.07 c_{\rm s}$ for $\tau = 800$ ms to $v_{\rm stir} \sim 1.1 c_{\rm s}$ for $\tau = 50$ ms. The bottom row of images are *in situ* images with the 660-nm beam on and at the beam position corresponding to $t = \tau/2$. $U_0$ varies as denoted on each image with values of $V_{660} > 1.0$V corresponding to potentials above the chemical potential. We denote $U_0$ by the voltage sent from the DAC to the 660-nm laser current controller. The 660-nm beam power is linearly related to this voltage, with V = 1.0 V corresponding to $U_0 \sim \mu_0$, while $V_{660} = 0.5$ barely makes a dimple in the BEC.

Finally we varied the stirring speed by varying the stir period while holding the beam power and the stir radius constant. In an attempt to avoid stirring a second time through the vortex distribution nucleated by the first complete circular stir, we ramped the 660-nm

beam off over a fraction of the second stir with $t_2 = 35$ ms. Figs. 4.18(a), (b), and (c) correspond to the 660-nm beam at 0.5 V, 1.0 V, and 1.5 V respectively. As with the images shown in Fig. 4.17, $V_{660} = 1.0$ V corresponds to $U_0 \sim \mu_0$, while $V_{660} = 0.5V$ results in a 660-nm beam that is barely noticeable within the BEC. The bottom image in Figs. 4.18(a)-(c) is an *in situ* image of the BEC with the 660-nm beam on, and located at the position corresponding to halfway through the circular stir. These images show the beam height compared to the local mean-field energy at the stir radius rather than the maximum mean-field energy at the center of the BEC. Each of the three sets of images shows the vortex distributions generated by stirring over a range of speeds from $v_{\rm stir} \sim 0.07c_{\rm s}$ corresponding to $\tau = 800$ ms to $v_{\rm stir} \sim 1.1c_{\rm s}$ corresponding to $\tau = 50$ ms. For beam potentials $U_0 \leq \mu_0$ shown in Figs. 4.18(a) and (b), vortices appear for $\tau \leq 400$ ms, where as in Fig. 4.18(c) a few vortices are observed in the image corresponding to $\tau = 800$ ms, although it is possible that these are spontaneous cores nucleated during the BEC transition rather than a result of the stirring. We observe large density features that may correspond to poorly resolved clusters in the images corresponding to $\tau = 100$ ms and $\tau = 200$ ms in Figs. 4.18(b) and (c). However, it is possible that $t_2 = 35$ ms is too short of a time over which to ramp off the 660-nm beam power, and that this rapid ramp down of the beam power could result in density features or vortex nucleation. When we stir at supersonic speeds where we might expect to form an oblique soliton in the wake of the stirring beam, the BEC is nearly destroyed regardless of the beam height. One possible reason for the destroyed BEC may be the 5-ms update interval for the timing sequence dictated by the buffer size of the DIO card used for timing control of the DACs. A 5-ms update interval results in the 50-ms stir being comprised of 10 discrete steps which might be too choppy.

Based on the preliminary study described in this section, stirring seems to be an effective way to inject a large disordered vortex distribution into the BEC without the large bulk oscillations associated with modulating the 660-nm beam power in the technique described in Sec. 4.4. However, our results do not seem to match up very well with the numerical study

of Reeves *et al.*, and the need to ramp off the 660-nm beam prior to imaging complicated our analysis.

## 4.6 Vortex clusters: stirring with sinusoidal variation of beam power

As we search for experimental methods to drive the BEC into a turbulent state with statistical signatures of turbulence that will support Onsager-Kraichnan condensation [25], we would like to initialize vortex distributions with high point-vortex energy. With this in mind, we present a technique for intentionally nucleating vortex clusters with minimal accompanying acoustic energy.

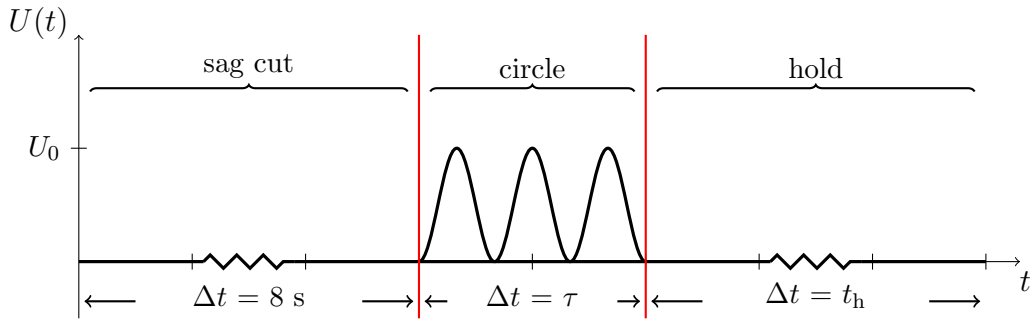


Figure 4.19: 660-nm beam power timing sequence corresponding to the images in Fig. 4.20, with beam power modulation during the circular stir defined by Eqn. 4.5. The beam power is zero during the sag cut, undergoes a sinusoidal oscillation for a time $\Delta t = \tau$ during the single spatial stir, and returns to zero for a hold period $\Delta t = t_{\mathrm{h}}$.

The cluster injection technique described here is similar to that described in Sec. 4.5, where piezo-controlled steering mirrors are used to move a 660-nm stirring beam in a circle of radius $r_{\mathrm{stir}}$ and period $\tau$. In addition to the spatial circle inscribed by the stirring beam, the beam power is modulated sinusoidally such that

$$U(t) = U_0 \sin^2\left(\frac{\pi N t}{\tau}\right) \tag{4.5}$$

where $U_0$ is the maximum potential, $\tau$ is the period of a circular stir, and $N$ is the number of 660-nm power cycles in one spatial revolution of the stirring beam. Figure 4.19 shows

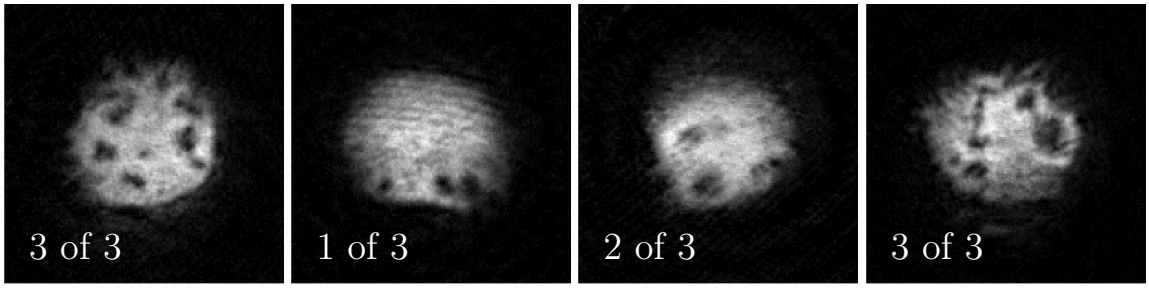


Figure 4.20: $400 \times 400$-$\mu$m square images of expanded BECs with cores that appear to be arranged in clusters. Images correspond to $x$ of $N$ power oscillations shown on each image. We allowed the BEC to expand and then imaged directly after the 660-nm beam had completed $x$ of 3 power oscillations and $x/3$ of a single circular stir. The height of the repulsive potential associated with the stirring beam follows the timing sequence shown in Fig. 4.19, with stirring parameters $r_{\rm stir} \sim 15$ $\mu$m, $U_0 \sim 0.5\mu_0$, $t_{\rm h} = 0$ ms, and $N = 3$. The leftmost image corresponds to $\tau = 210$ ms, and the rest of the images have $\tau = 180$ ms.

the height of the stirring beam throughout the timing sequence used for the images shown in Fig. 4.20. Requiring $N$ to be an integer ensures that the initial and final beam heights are zero and avoids unwanted density perturbations due to ramping off the 660-nm beam power at the end of the timing sequence. After the stirring process, the BEC is held for a variable time $t_{\rm h}$, and then imaged after the usual period of expansion.

Figure 4.20 shows images of expanded BECs after the BEC has completed $x$ of $N = 3$ power oscillations as shown on each image. Here $r_{\rm stir} \sim 15$ $\mu$m, $U_0 \sim 0.5\mu_0$, and $t_{\rm h} = 0$ ms. As shown in the leftmost image, we observe what appears to be a cluster of cores associated with the location where the beam ramps on above some threshold value and again when the beam ramps off. Cluster formation has been previously observed by Neely *et al.* [3] in their study of vortex dipole dynamics. In this study, multiply-charged vortex dipoles were observed for linear stirring speeds above $v_{\rm s} \sim 200$ $\mu$m/s, for a repulsive obstacle with $U_0 \sim 1.2\mu_0$. These multiply-charged vortex dipoles can be thought of as a dipole formed with a cluster of vortices and a cluster of anti-vortices. In the case of a linear stir through the center of the BEC, both clusters should be shed by the stirring beam simultaneously. For the BEC images shown in Figs. 4.20, 4.22, and 4.23, we suspect that the observed

asymmetry in cluster shedding has to do with the beam being off center with respect to the BEC, such that the cluster shed on either side of the beam sees a different chemical potential. The boundary of the BEC also plays a role in vortex dynamics.

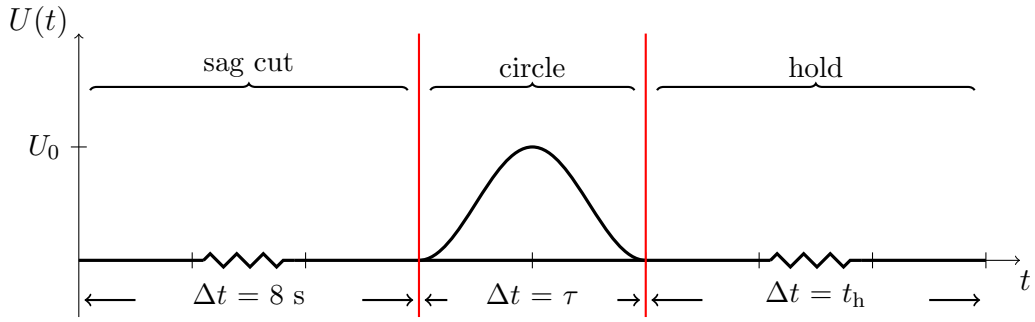


Figure 4.21: 660-nm beam power timing sequence corresponding to the images in Figs. 4.22 and 4.23, with a beam power modulation defined by Eqn. 4.5. The beam power is zero during the sag cut, undergoes a sinusoidal oscillation for a time $\Delta t = \tau$ during the single spatial stir, and returns to zero for a hold period $\Delta t = t_{\mathrm{h}}$.

Figures 4.22 and 4.23 follow the 660-nm beam power timing sequence shown in Fig. 4.21, with stir parameters $U_0 \sim 0.55\mu_0$, $\tau = 200$ ms, $N = 1$, and $r_{\mathrm{stir}} \sim 13$ $\mu$m held constant, while we varied the hold time $t_{\mathrm{h}}$ after the stir. The radius of the stir was interpolated from the radii determined via fits to the long-exposure images of the 660-nm stirring beam, shown in Fig. 4.12. *In situ* images of the BEC with the 660-nm beam at locations corresponding to intervals of $\tau/4$ along the stirring beam path are shown in Fig. 4.24, with $U_0 \sim 0.55\mu_0$.

The images in Fig. 4.22(a) show BECs with no hold after the stir so $t_{\mathrm{h}} = 0$ ms. The stirring procedure produces two aggregates of vortex cores with decent reproducibility. The clusters occur in 7 out of a set of 9 experimental runs, with the cores appearing in approximately the same location as in each of the three BEC images shown. After a hold time of 200 ms as shown in Fig. 4.23(a), the vortex cores are still primarily grouped into two locations, leading us to believe that the grouping of cores are indeed clusters of like-signed vortices, however the locations of these clusters within the BEC varies from shot to shot. By $t_{\mathrm{h}} = 300$ ms, as shown in the images in Fig. 4.23(b), the clusters have

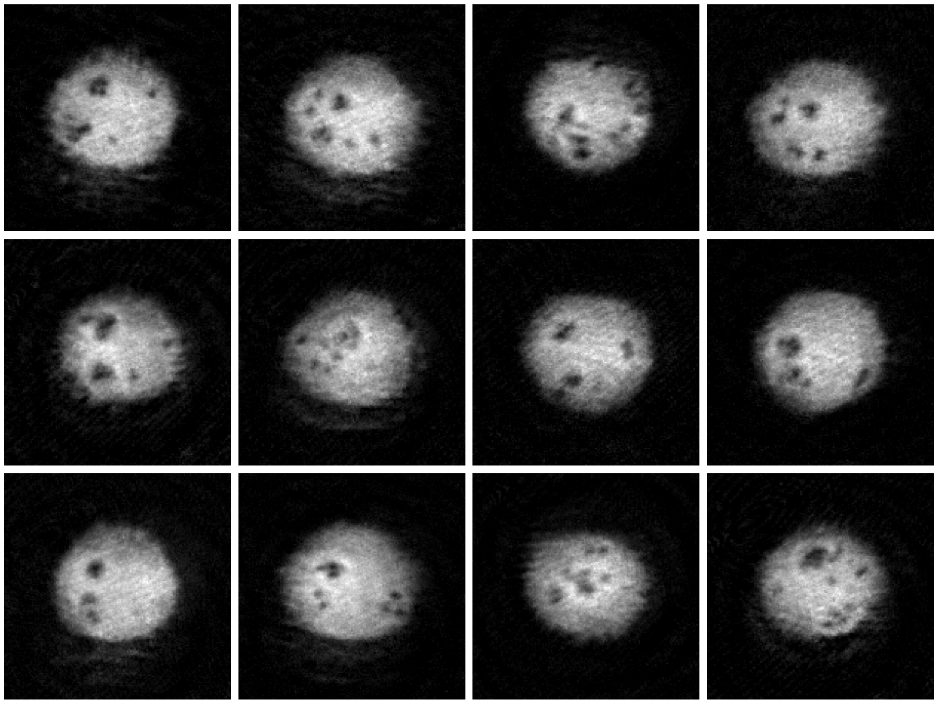

(a) 0 ms (b) 25 ms (c) 50 ms (d) 100 ms

Figure 4.22: $400 \times 400$-$\mu$m square images of expanded BECs for varying hold times after a single circular stir. This set of images follows the 660-nm beam power sequence shown in Fig. 4.21. Stir parameters are $r_{\mathrm{stir}} \sim 13$ $\mu$m, interpolated from the radii determined through fits to long-exposure images of the 660-nm beam, $\tau = 200$ ms, $N = 1$ 660-nm beam power oscillation per circle, and $U_0 \sim 0.55\mu_0$. After the single circular stir the BEC is held for a variable time $t_{\mathrm{h}}$. Each column is labeled with the appropriate hold time. Multiple images are shown for each hold time to demonstrate the shot-to-shot variability in the process.

mostly dissociated, although the bottom image in Fig. 4.23(e) appears to still have loose aggregates of vortex cores after a hold time of 800 ms.

In an attempt to force more clusters into the BEC, we performed a similar stirring procedure with the timing sequence shown in Fig. 4.25. The primary difference was to perform multiple stirs with $N = 2$ 660-nm beam power oscillations per stir. As shown in Fig. 4.26 we drive a large number of vortex cores into the BEC. However, there appears

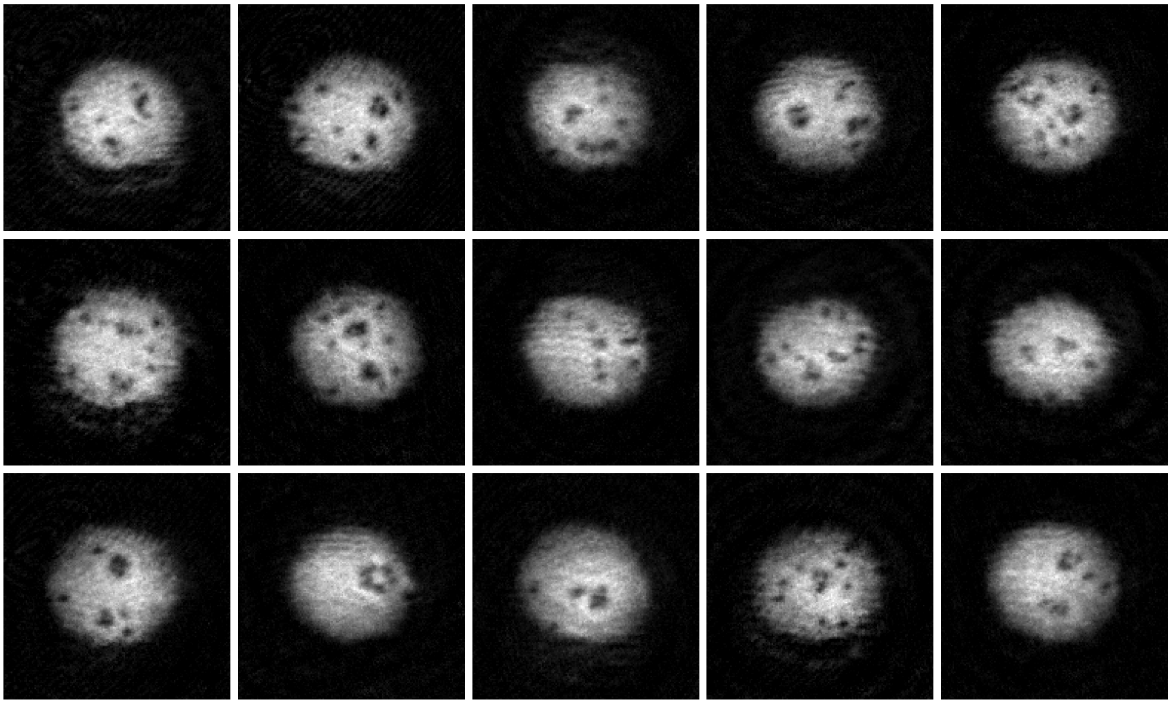

(a) 200 ms (b) 300 ms (c) 400 ms (d) 600 ms (e) 800 ms

Figure 4.23: $400 \times 400$-$\mu$m square images of expanded BECs for varying hold times after a single circular stir. This set of images follows the 660-nm beam power sequence shown in Fig. 4.21. Stir parameters are $r_{\mathrm{stir}} \sim 13$ $\mu$m, interpolated from the radii determined through fits to long-exposure images of the 660-nm beam, $\tau = 200$ ms, $N = 1$ 660-nm beam power oscillation per circle, and $U_0 \sim 0.55\mu_0$. After the single circular stir the BEC is held for a variable time $t_{\mathrm{h}}$. Each column is labeled with the appropriate hold time. Multiple images are shown for each hold time to demonstrate the shot-to-shot variability in the process. The images in this figure are a continuation of the sequence begun in Fig. 4.22.

to be a limit to the number of cores that can be forced into the BEC, and there appear to be fewer cores after 20 complete circular stirs than after 15. It is possible that the size of the BEC limits the number of cores that can be forced. Heating is also a potentially limiting factor, as well as vortex-antivortex annihilation. It would be interesting to try multiple stirs with a non-integer $N$ so that the maximum power portion of the stir occurs at different spatial positions for each subsequent stir.

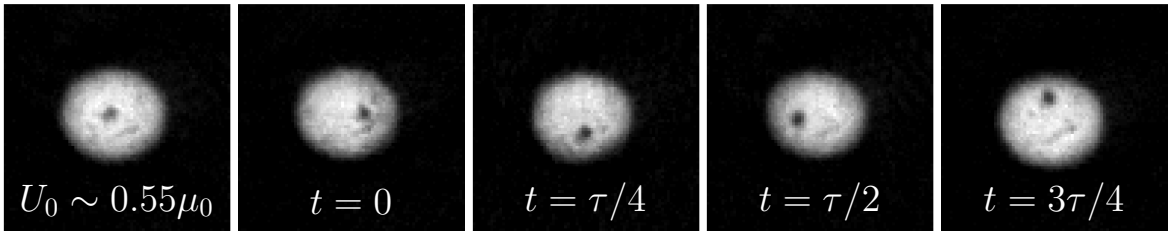


Figure 4.24: $200 \times 200$-$\mu$m *in situ* images showing the 660-nm stirring beam in the BEC for $r_{\mathrm{stir}} \sim 13$ $\mu$m, interpolated from the radii determined through fits to long-exposure images of the 660-nm beam.

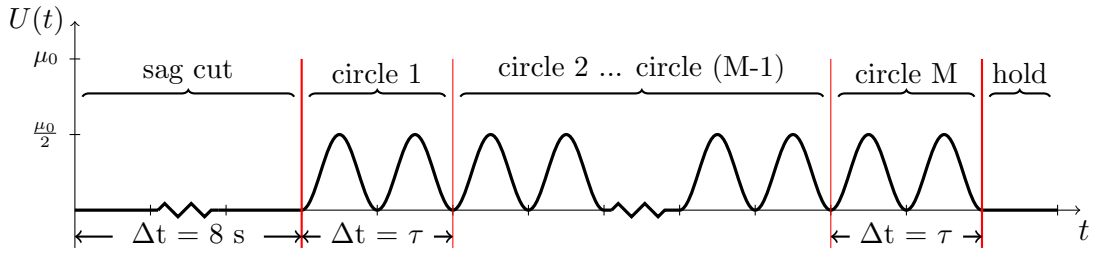


Figure 4.25: 660-nm beam power timing sequence used for the images shown in Fig. 4.26. $N = 2$ 600-nm beam power oscillations for each circular stir.

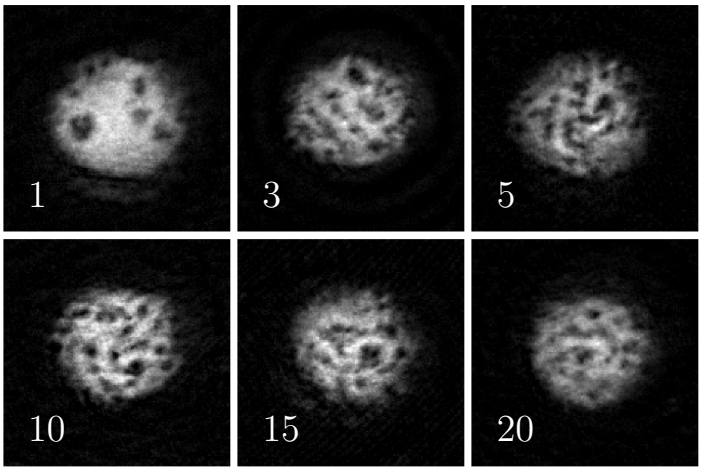


Figure 4.26: $400 \times 400$-$\mu$m square images of expanded BECs imaged after the number of circular stirs shown on each image. This set of images follows the 660-nm beam power timing sequence shown in Fig. 4.25. Stir parameters are $U_0 \sim 0.5\mu_0$, $r_{\mathrm{stir}} \sim 15$ $\mu$m, $\tau = 200$ ms, $t_{\mathrm{h}} = 0$ ms, $N = 2$ 660-nm beam power oscillations per circular stir.

In general, this technique appears to have the potential to inject clusters of vortex cores that persist for long timescales, i.e. aggregates of vortices are still visible after hold times on the order of 300 to 400 ms, long compared to cluster turnover times on the order of 15-20 ms. Based on comparison to numerical GPE propagation, we will associate these long-lived vortex aggregates with clusters of like-signed cores. While we clearly observe the nucleation of clusters comprised of several vortex cores, we have yet to observe Onsager condensation of vortices with this technique. While two clusters, or even the five or six clusters observed in the leftmost image of Fig. 4.20, might not involve sufficiently high point-vortex energies to expect to see the negative-temperature states predicted by Onsager [7] and discussed in Chapter 1, it is possible that this technique may be extended to inject more clusters into the BEC. When it comes to injecting a large number of clusters we are limited by the size of our system, since stirring for multiple revolutions tends to disrupt the existing clusters. However, it may be possible to increase the number of clusters by using a narrower stirring beam, or to stir in concentric circles within the BEC to avoid retracing the same path. In addition we may need to find the appropriate balance between system size and cluster fraction of the initial vortex distribution in order to observe the merging of clusters indicative of Onsager's negative-temperature vortex states. That said, this technique is a promising method for cluster injection and bears further investigation.

# Chapter 5

# Tomography of vortices in 3D BECs

Superfluid flow in a BEC depends greatly on the trap geometry. BECs in highly oblate traps [3] exhibit predominately 2D fluid flow with vortices aligned along a single axis [17]. In more spherical BECs, with aspect ratios approaching $R_z : R_r \sim 1 : 1$, we expect complex vortex dynamics that involve vortex tilting, bending, and crossings that can produce vortex rings [63, 66]. These phenomena are at the heart of 3D quantum turbulence. In pursuing tomographic imaging of 3D BECs, our goal was to develop a way to measure 3D vortex distributions in order to better understand their dynamics. Conventional absorption imaging integrates over the imaging axis, reducing the contrast of vortex cores that are tilted with respect to the imaging axis, and making it difficult to observe structures such as vortex rings. To image such structures, we employed a tomographic technique where we imaged a set of thin horizontal slices spaced along the vertical axis of an expanding BEC. Spatially selective imaging of a single cross-section through a BEC has been used previously to image interference fringes, vortex rings, and solitons [66, 67, 68]. What makes our system unique is the rapid sequential imaging of a set of horizontal planes of the BEC as demonstrated in Fig. 5.8. Each image provides a cross section through the overall vortex distribution, and when taken as a whole, the set of images allows us to piece together a complicated 3D vortex distribution that would otherwise be blurred out when integrating over the entire BEC. The work presented in this chapter was presented as the poster *Imaging the 3D structure of vortex cores in Bose-Einstein condensates* at the APS Division of Atomic, Molecular and Optical Physics yearly meeting in 2011.

## 5.1 Tomographic imaging

The images presented in this chapter were taken after a period of approximately 62 ms of expansion with an $M = 5$, NA $\sim 0.2$ imaging system with the objective located below the BEC cell as shown in Fig. 5.1. Expansion was necessary for vortex core resolution given the low magnification and numerical aperture of the imaging system.

Conceptually, our realization of 3D vortex imaging relies on optically pumping a thin slice of atoms from the $^{87}$Rb $5^2S_{1/2}$ $|F = 1, m_F = -1\rangle$ ground state to the $^{87}$Rb $5^2S_{1/2}$ $|F = 2\rangle$ level as described in Sec. 3.1.2. The portion of the atoms outside of the horizontal slice that we image remain in the $^{87}$Rb $5^2S_{1/2}$ $|F = 1, m_F = -1\rangle$ ground state and are unaffected by the $|F = 2\rangle \rightarrow |F' = 3\rangle$ imaging pulse.

The optical pumping beam is controlled with two acousto-optic modulators (AOMs), one driven near 210-MHz and the other driven near 110-MHz. The beam exits the fiber and passes first through the 110-MHz AOM in a double-pass configuration. The beam then passes through the 210-MHz AOM in a single-pass configuration. As shown in Fig. 5.1, following the single-pass AOM, the beam is expanded by a factor of 4 and then focused into a sheet at the BEC with an $f = 100$ mm cylindrical lens, the same cylindrical lens used to create the 1090-nm sheet for the highly oblate hybrid trap. When light passes through an AOM, the frequency of the light is shifted by the driving frequency, and the beam is deflected, such that the new wave-vector $\vec{k'}$ is the vector sum of the wave-vector of the incident beam $\vec{k}$, and the wave-vector associated with the acoustic wave in the AOM crystal $q\vec{\kappa}$ where $q$ is the diffraction order. By controlling the drive frequency of the single-pass AOM, we are able to shift the position of the optical pumping sheet at the location of the BEC as shown in Fig. 5.2. However, varying the drive frequency has the undesired effects of shifting the frequency of the light off resonance and varying the power in the optical pumping beam. To correct for these undesired effects, we adjust the driving frequency and power of the AOM in the double-pass configuration. A correctly aligned double-pass AOM shifts the frequency of the light by twice the drive frequency, while the

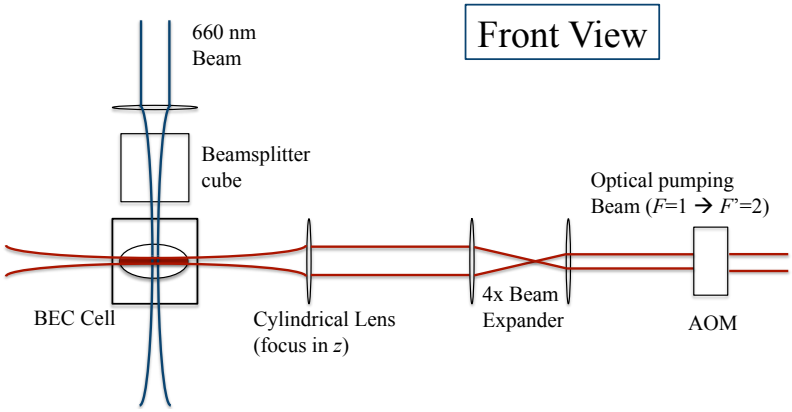


(a) Front view

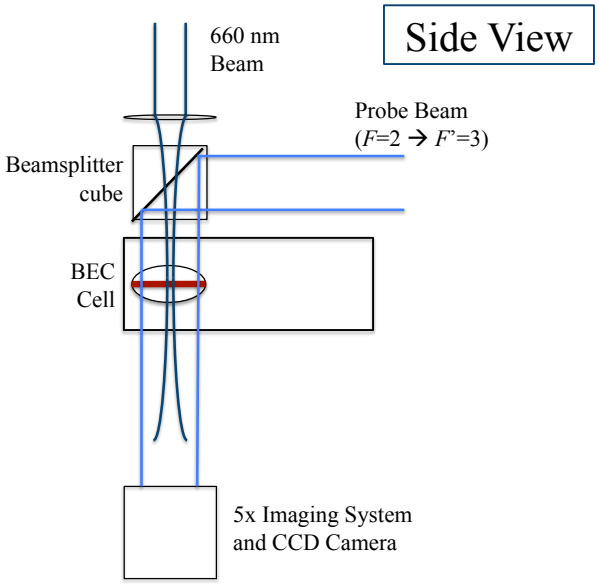


(b) Side view

Figure 5.1: Front and side views of the experimental set up (not to scale). Note the path of the optical pumping beam through the AOM and then the 4x beam expander. The objective lens for the $M = 5$ imaging system is located below the BEC cell.

momentum kicks cancel out with $\vec{k'} = \vec{k} + \vec{\kappa} - \vec{\kappa}$. The drive frequency of both AOMs and the drive amplitude of the double-pass AOM are controlled by the experimental timing program through digital-to-analog converters (DACs).

Due to the small active area of the AOM crystal, a beam passing through the AOM is

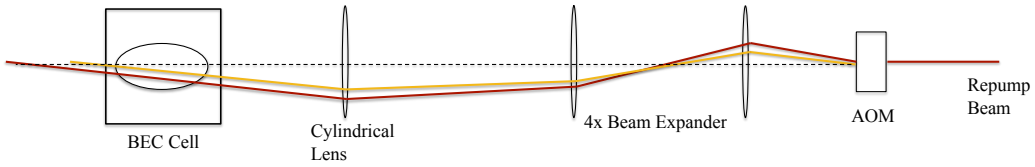


Figure 5.2: Diagram showing the vertical shift of the optical pumping beam for different AOM deflections. Image is not to scale.

generally brought to a weak focus at the AOM. However for our purposes, we needed the AOM to provide angular deflection of a collimated beam. This required starting with a small collimated beam and then magnifying the beam after the AOM so that it could be focused into a narrow sheet, with $1/e^2$ beam radius $w_z = 14$ $\mu$m, by the cylindrical lens. We note that angular magnification and spatial magnification are inversely proportional so while a beam expander with a high magnification would allow us to illuminate a thinner sheet of atoms, it would also reduce the beam deflection from the single-pass AOM. This deflection is what accounts for the shift in vertical beam position at the BEC, and smaller deflection angles correspond to smaller shifts in vertical position, as shown in Fig. 5.2.

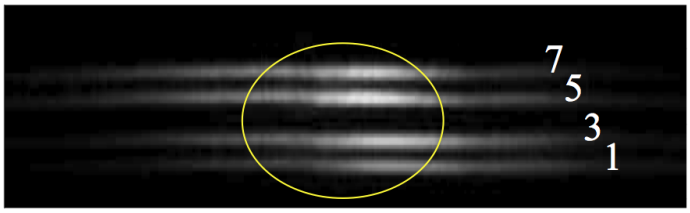


Figure 5.3: Overlaid images of the optical pumping beam for a range of AOM frequencies. The images were taken along the $y$-axis and even numbered slices are not shown. Each slice has a beam waist of 14 $\mu$m at the BEC. Slices 1 and 3 have a vertical separation of 27 $\mu$m

.

In the end, the $M = 4$ beam expander was chosen as a balance between needing a large beam prior to the cylindrical lens to allow for a tightly focused optically pumping sheet, and being able to achieve a sufficient vertical shift at the BEC location. Figure 5.3 shows a set of overlaid images of the optical pumping beam for varying 210-MHz AOM frequencies.

The images of the optical pumping beam were taken along $y$-axis, the propagation axis of the optical pumping beam, so that each image shows a transverse ($x$-$z$ plane) cross section of the optical pumping beam at the BEC location.

## 5.2 Timing

In order to take a sequence of images in quick temporal succession, we used the Winview kinetics mode feature with the Pixis 1024 BR CCD camera. In order to operate in kinetics mode, a razor blade is placed in front of the camera shutter. The blade blocks most of the CCD array, allowing only the upper (lab frame) $1024/N_{\mathrm{I}}$ rows of pixels to be illuminated by the probe beam, where $N_{\mathrm{I}}$ is the number of images. After each image, all pixels values are shifted down by $1024/N_{\mathrm{I}}$ rows, so that a new image can be recorded in the upper portion of the CCD array. After $N_{\mathrm{I}}$ images the entire CCD array is read out to the imaging computer. The shift process occurs on the order of 5 ms, much faster than the approximately 600 ms required to read out the entire CCD array. Figure 5.4 shows the timing sequence. We note that occasionally the pixel shift for the first image of the set of $N_{\mathrm{I}}$ BEC images would be off by a couple of rows meaning that the background subtraction would be off for that image only. We were able to account for this error in the image processing.

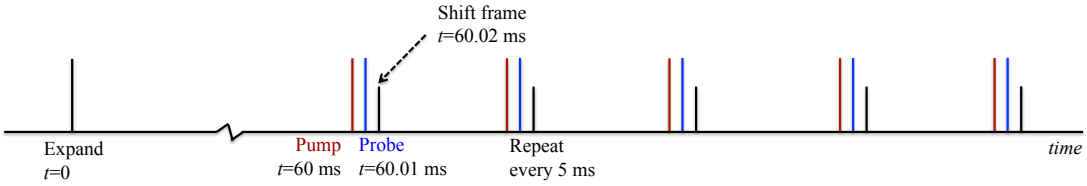


Figure 5.4: Timing sequence. Each image consists of a 10-$\mu$s optical pumping pulse, a 10-$\mu$s imaging pulse, and a pixel shift waiting period of approximately 5 ms.

## 5.3 Proof-of-principle images

Our ultimate goal was to image a tangle of vortex cores, but to start we used our trusty test target, the vortex lattice, as shown in Fig. 5.5. As expected for a lattice where the

cores align with the axis of rotation and imaging, the core pattern looks approximately the same in all three images.

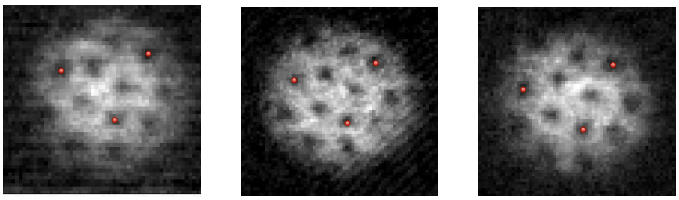

Figure 5.5: Set of three sequential slices of a vortex lattice. From left to right, the images correspond to the top, middle and bottom layers of an expanded BEC containing a vortex lattice. The red dots were added to guide the eye to connect the layers.

As a second test, we used a blue-detuned beam to swipe across the BEC and nucleate a vortex dipole in the manner similar to that described by Neely *et al.* [3], but with a BEC confined in a TOP trap. Figure 5.6 shows *in situ* images of the BEC with the 660-nm beam at the initial and final swipe positions. These experiments were conducted prior to the development of the PZT-controlled mirrors so the swipe was implemented by pushing the BEC past a stationary 660-nm beam rather than moving the beam.

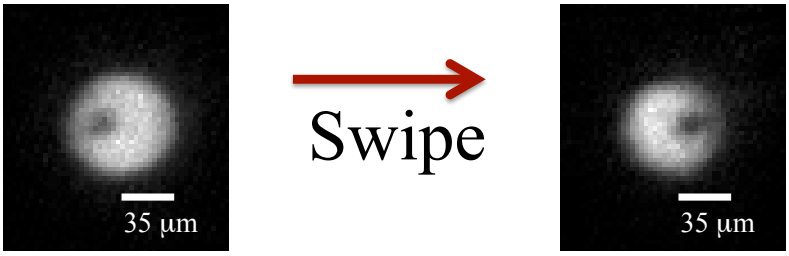


Figure 5.6: *In situ* bright-field absorption images showing the 660-nm swiping beam within the BEC. The left image shows the initial position of the 660-nm beam with respect to the BEC, and the image on the right shows the final position. Blue-detuned beam swipe parameters: Power $\sim$ 300 mW, $1/e^2$ beam radius $\sim$ 8 $\mu$m, swipe velocity $\sim$ 100 to 300 $\mu$m/sec

.

Figure. 5.7 shows full column density images of an expanded BEC after swiping. We expect a dipole in a spherical BEC to decay into a vortex ring [17]. However, for our

$R_r : R_z = 2 : 1$ TOP trap we predominately observe good contrast for vortex dipoles as shown in Fig. 5.7, and suspect that the dipoles are mostly aligned along the imaging axis. The first three images in Fig. 5.7 have good core contrast. The fourth image has structure that would be well suited to imaging with the slice technique.

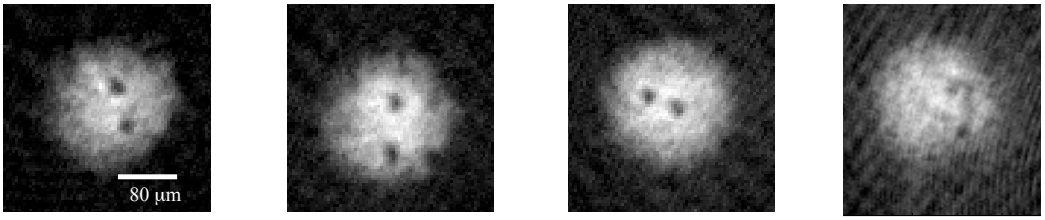


Figure 5.7: Full column density expansion images where the entire BEC has been simultaneously optically pumped into the $5^2S_{1/2}$ $|F = 2\rangle$ state and then imaged. In the first three images the cores are aligned with the imaging axis and show up clearly. The fourth image has structure that would be well suited to imaging with the slice technique.

The right column of images in Fig. 5.8 shows a set of six slices of an expanded TOP trap BEC with a vortex dipole imaged along the vertical imaging axis. As we suspected based on the contrast in the full column density images shown in Fig. 5.7, the core positions appear in approximately the same location in each slice. The left column of images shows a corresponding side view of each slice imaged along the horizontal imaging axis. For both sets of images, the optical pumping beam illuminated a thin horizontal slice of the expanded BEC.

## 5.4 Limitations and suggested improvements

The primary obstacle to tomographic imaging with our apparatus was the observed shot-to-shot fluctuation in the final BEC position after expansion. Generally this fluctuation can be mitigated by syncing the turn off of the TOP rotating bias field and the turn on of the expansion coil to the 4kHz rotating bias field. We have since discovered that the

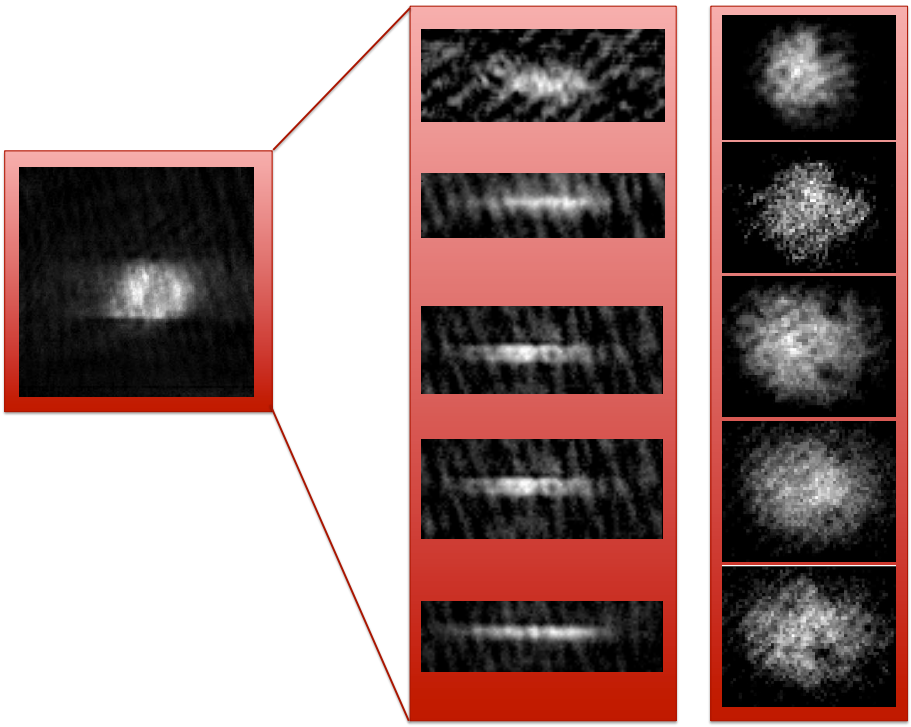

Figure 5.8: Leftmost image: Image of the full BEC from the side, imaged along the horizontal axis. Left column: Side-view of a set of sequential horizontal slices of a BEC (different $z$-position), imaged along the horizontal axis. Right column: Top-view of a set of five sequential horizontal slices (different $z$-position) of a BEC containing a vortex dipole, imaged along the vertical axis such that each image shows the transverse profile ($x$-$y$ plane) of a thin slice of the BEC.

sync circuit employed during our attempt at tomographic imaging was faulty; it synced if the expansion coil TTL went high in one half of the bias field cycle but not the other. After replacing the faulty sync circuit with a simple flip-flop, we observed less shot-to-shot variation in the BEC position post expansion.

The signal-to-noise ratio (SNR) is also a consideration, as thinner slices allow for better resolution of the vortex distribution, but at the same time result in lower optical depth for imaging. We know that good SNR is possible since Hall's group at Amherst achieves sufficient SNR to resolve vortex cores while out-coupling and imaging just 5% of the atoms

in their BEC [43]. We suspect that we could improve the SNR with Faraday imaging and an EMCCD camera. As discussed in Sec. 3.4, the primary advantage of Faraday imaging is the removal of the majority of the background probe signal. This greatly reduces noise due to structure in the probe beam profile. Additionally, we might gain signal by careful fine-tuning of the frequency of the optical pumping beam and the probe beam to account for Zeeman shifts of the resonant frequency due to the large $B_z \sim 40$ G magnetic field during expansion. Lastly, our optical pumping scheme is inefficient, with roughly half of the atoms decaying to the desired $|F = 2\rangle$ ground state. This inefficiency can be overcome to some extent by increasing the length of the optical pumping pulse. An alternative pumping scheme that other groups employ involves a microwave transition directly between the two $5^2S_{1/2}$ hyperfine states.

In the future we may consider using a stationary (no translation along the z-axis) optical pumping sheet in conjunction with dark-field imaging to observe density features such as shockwaves or dark solitons *in situ* in the $R_r : R_z = 2 : 1$ TOP trap BECs. As discussed further in Chapter 9, integrating over the full column density confuses the interpretation of the density features generated by moving the BEC rapidly past a blue-detuned obstacle. Additionally we could consider using this type of tomography to image Kelvin waves and map out the Kelvin wave excitation spectrum.

# Chapter 6
# Proof-of-Principle In Situ Vortex Imaging

In this chapter we present a signature result of this dissertation, namely the first *in situ* observation of a 2D distribution of bare vortex cores in a single-component BEC. The paper, *In situ observation of two-dimensional vortex distributions in Bose-Einstein condensation*, describing this work was published in Physical Review A [9], and the current chapter is largely excerpts from this paper. This result has far reaching implications ranging from enabling vortex studies in trapping geometries that are not conducive to self-similar expansion, to ultimately enabling direct observations of the dynamics of vortex cores and other superfluid density features. As discussed in Chapter 4, direct observation of vortex dynamics is a primary experimental goal that must be achieved in order to enable experimental studies of 2DQT in BECs to move beyond measurements of vortex number statistics. For studies of 2DQT where a primary goal is to link kinetic energy spectra and other statistical measures of turbulence to the vortex distribution and subsequent vortex dynamics, we need to identify ways to experimentally determine the circulation of a vortex core, as well as ways to observe real-time vortex dynamics.

While our ultimate goal is the acquisition of tens of images of a vortex distribution taken from a single BEC, even two such vortex images would allow us to begin to correlate initial and final vortex distributions, reducing our dependency on vortex number statistics, and enabling direct measurement of vortex lifetimes. Lastly, as we move towards experiments with BECs confined in flat-bottomed potentials to better align our experiments with the homogenous fluids used for numerics, the trapping potentials will no longer be conducive to self-similar expansion, and even single-shot images of vortex distributions will require *in situ* imaging techniques.

## 6.1 Introduction

Quantized vortices in superfluids are localized indicators of the superfluid's dynamics. 2D vortex distributions are especially relevant in recent experimental efforts to better understand the fluid dynamics of BECs, including vortex dipole and cluster formation [3], 2D quantum turbulence [22, 24], formation and decay of persistent currents [22, 69, 70, 71], and the Berezinskii-Kosterlitz-Thouless transition [72, 73, 74]. However, laboratory visualization of vortex cores in a minimally-destructive manner that allows for real-time tracking of vortex motion has remained a considerable challenge. Given the sub-micron size of a vortex core, most experiments involving vortex imaging have relied on a period of ballistic expansion of the BEC prior to image acquisition, limiting observations to a single image of the BEC from trap geometries that support self-similar expansion; see Ref. [2] for an overview of such experiments. Stroboscopic expansion and probing of small fractions of condensed atoms has enabled the determination of few-vortex dynamics in a single BEC [43], although the utility of this technique in measurements of many-vortex dynamics has not yet been established. In order to detect the motions of numerous vortices, as well as to obtain single-shot imaging of vortex distributions in cases where BEC expansion is impractical, new imaging procedures must be explored. Here we demonstrate single-shot *in situ* imaging of a 2D vortex distribution in a rotating BEC, obtained by applying a high-angle dark-field imaging technique that is similar to methods commonly employed in other applications of microscopy [75]. With additional modifications, this imaging method should be amenable to the acquisition of single images of 2D vortex distributions in non-harmonically trapped BECs, and multiple images of a single BEC, offering the potential for experimental determination of the dynamics of 2D vortex distributions.

To date, the most versatile demonstrated method for imaging the dynamics of an arbitrary few-vortex distribution in a BEC is that of Freilich *et al.* [43], in which a few percent of the atoms from a single BEC are pumped into an untrapped state, whereupon they ballistically expand and are probed via absorption imaging. By repeating this extraction

procedure, this stroboscopic technique allows for the acquisition of sequential absorption images of a single BEC. However, since it relies on a period of expansion before vortex cores are resolvable, this method may present difficulties in determining the positions of vortices within a tightly packed vortex cluster or in cases where the BEC density distribution does not self-similarly magnify during expansion, such as expansion from a square well potential. Additionally, the required expansion time limits the acquisition rate of these images, making the motion of many vortex cores difficult to track as inter-vortex distances decrease and cores move more rapidly within the BEC. Minimally-destructive, *in situ* observations of vortex dynamics in a single BEC have also been obtained by filling the vortex core with atoms of a different atomic state [49]. Filling the core increases the size of the vortex and enables the position of the core to be determined *in situ* with phase-contrast imaging techniques, but interactions between the two atomic states strongly affect the dynamics of the quantum fluid.

## 6.2 Dark-field approach to *in situ* imaging

Our imaging approach involves an adaptation of dispersive dark-field imaging [75]. Conceptually, in dark-field imaging, the BEC is treated as a phase object that coherently refracts light from an imaging probe beam. Briefly, with a monochromatic probe laser beam of approximately uniform intensity $I_0$ propagating along the $z$ direction, the spatially dependent phase shift $\phi(x, y)$ acquired as the probe passes through the BEC is given by

$$\phi(x, y) = -\tilde{n}(x, y)\ \sigma_0 \left( \frac{\Delta/\Gamma}{1 + 4(\Delta/\Gamma)^2 + I_0/I_{\text{sat}}} \right). \tag{6.1}$$

In this expression, $\tilde{n}(x, y) = \int n(x, y, z)\ dz$ is the $z$-integrated column density of the BEC obtained from the full atomic density distribution $n(x, y, z)$, $\sigma_0$ is the resonant atom-photon scattering cross section, $\Delta = \omega - \omega_0$ is the detuning of the probe frequency $\omega$ from atomic resonance $\omega_0$, $\Gamma$ is the natural linewidth of the atomic transition, and $I_{\text{sat}}$ is the transition saturation intensity. As illustrated in Fig. 6.1(a), an opaque mask placed on-axis

in the Fourier plane of an imaging system acts as a high-pass spatial filter, blocking the unrefracted component of the probe beam, but allowing the light refracted by the BEC to reach the camera. Andrews *et al.* [47] first applied dispersive dark-field BEC imaging as a minimally-destructive alternative to absorption imaging, and demonstrated multi-shot imaging of a single BEC. More recently, Pappa *et al.* [76] employed near-resonant dark-field imaging to make highly sensitive measurements of the components of a spinor BEC, reporting a detection limit of about seven atoms. In both of these applications of the dark-field technique, the intent was to image the bulk profile of the BEC, rather than locate microscopic density features within the BEC. See Chapter 7 and Ref. [40] for a more detailed discussion of this imaging method.

We use dark-field imaging to isolate the imaging light scattered by sub-micron features within the BEC, and in particular, to identify the positions of vortex cores. A vortex core is free of condensed atoms, and therefore the core position corresponds to a steep density gradient over a distance on the order of the healing length [5], approximately 400 nm for our parameters. Such a sharply localized density feature acts as a strong lens that refracts light into high spatial frequencies. By carefully selecting the size of the dark-field mask, we remove the low spatial frequencies associated with the more gradual changes in the BEC density profile, allowing primarily the light refracted by the vortex cores to reach the camera. Without the large background signal of the bulk BEC, it is then feasible to pick out the refracted signal due to each vortex core without expanding the BEC. We describe this process as *in situ* vortex imaging due to the ability to detect vortex cores without using a period of ballistic expansion. *In situ* vortex imaging opens the possibility of minimally-destructive imaging of vortex distributions, although all BEC imaging procedures are at least somewhat destructive.

For the images of vortices reported here, we formed BECs of $5^2\mathrm{S}_{1/2}\ |F = 1, m_F = -1\rangle$ $^{87}$Rb atoms in a magnetic time-averaged orbiting potential (TOP) trap [30], with radial and axial trap frequencies of $(\omega_\mathrm{r},\, \omega_\mathrm{z}) \sim 2\pi \times (8, 16)$ Hz, BEC atom numbers of approximately

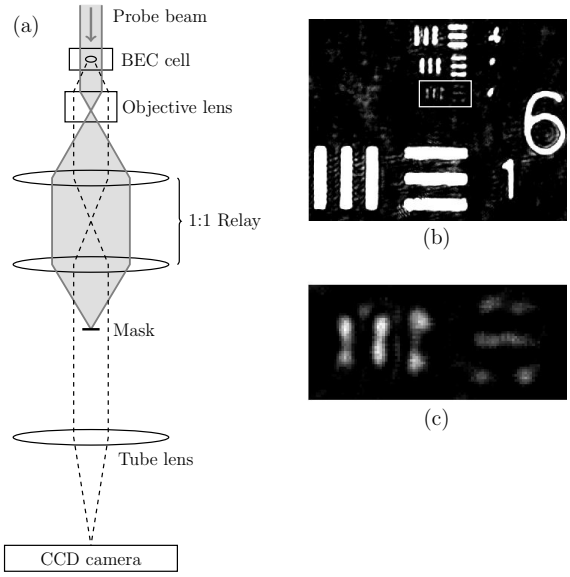


Figure 6.1: (a) BEC imaging optics (not to scale). 780-nm probe light (shaded in gray) is directed towards the BEC along the vertical (axial) imaging axis. Light refracted by the BEC (represented by dashed lines) is collected with a microscope objective, and imaged onto the CCD camera. A mask placed in the intermediate Fourier plane of the imaging system provides a high-pass spatial filter. (b) Image of a US Air Force resolution test target, obtained with an offline replica of the imaging system using 780-nm laser light and showing group 6, element 1 (bottom row), and group 7, elements 4-6 (top three rows). (c) Zoomed image of group 7, element 6, the features enclosed in the superimposed white box in (b). These features are the smallest features on our test target, with a width of 2.19 $\mu$m and a center-to-center separation of 4.38 $\mu$m. The image of the target is used to determine a measured magnification of $M = 19.7 \pm 0.4$, where the error is due to our uncertainty in measuring the periodicity in the test target image. All images obtained with the offline imaging system were taken with a Point Grey Firefly MV CMOS camera with 6 $\mu$m x 6 $\mu$m pixels.

1.8 x $10^6$, and BEC Thomas-Fermi radii of $(R_\mathrm{r}, R_\mathrm{z}) \sim (35, 19)$ $\mu$m. Following Hodby *et al.* [36], we modified the TOP trap's rotating bias field to form a slowly rotating elliptical potential well, which in turn spun up the BECs such that a triangular lattice of vortices was formed. The vortex lattice provided a reproducible and easily recognizable pattern of vortex cores for our imaging tests.

As illustrated in Fig. 6.1(a), our imaging system consists of an infinite-conjugate Olym-

pus SLMPLN 20X microscope objective with a numerical aperture NA=0.25, a theoretical diffraction-limited resolution of 1.9 $\mu$m at a wavelength of $\lambda = 780$ nm [77], a working distance of 25 mm, and a focal length of 9 mm. The objective is followed by a 1:1 relay lens pair, comprised of two 75-mm focal length achromatic doublets separated by 150 mm. The mask for dark-field imaging is placed at the intermediate Fourier plane, located at the rear focal plane of the relay, between the final relay lens and the tube lens. The relay lens pair is necessary because the initial Fourier plane where the mask would ideally be placed is located within the objective lens housing. Finally, a singlet lens with a focal length of 175 mm is used as the tube lens. All BEC images were obtained with a Princeton Instruments PIXIS 1024 BR back-illuminated CCD camera with 13 $\mu$m x 13 $\mu$m pixels. The imaging system has a magnification of $M = 19.7 \pm 0.4$. We used a variety of dark-field mask shapes and sizes in our imaging tests, described below. For the proof-of-principle tests reported here, the choice of mask shape (circular vs. wire) was based on the masks available rather than an optimal shape.

## 6.3 Nanofiber

As a first test of the capabilities of our imaging system, we constructed the system offline with a microscope slide in place of the 1-mm-thick glass wall of the vacuum chamber, and imaged a silica nanofiber [78, 79] with 660-nm laser light. The nanofiber, with a diameter of approximately 500 nm, provides an example of a sub-micron phase object with approximately the same diameter as a vortex core, and thus serves as a suitable imaging test object. Figures 6.2(a)-(c) show images of the nanofiber obtained by varying dark-field mask size, each image acquired using a 2.5-ms exposure time. The bright-field image shown in Fig. 6.2(d) is provided for comparison, and was acquired with a 0.25-ms exposure.

Despite its sub-micron thickness, the nanofiber's position can be clearly determined in both the bright-field and dark-field images. However, in the bright-field image shown in Fig. 6.2(d), the detected signal depth from the nanofiber is the same order of magnitude as

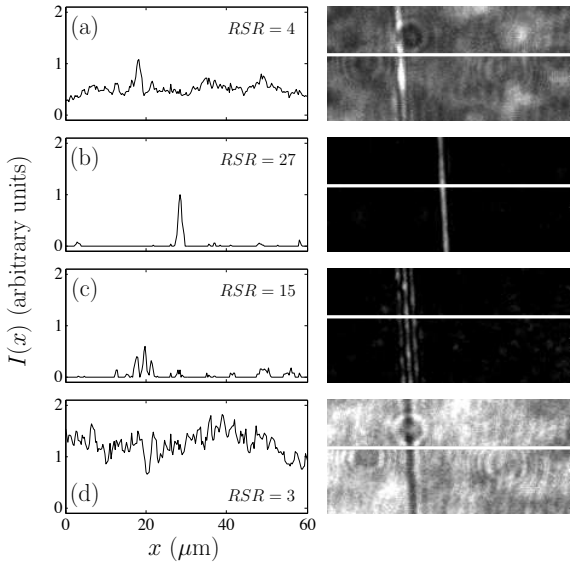


Figure 6.2: Raw 60-$\mu$m-wide images (right panels) of a section of silica nanofiber with a diameter of $\sim$500 nm (vertically oriented in each image in the panels on the right), shown without the use of background subtraction or other signal-enhancing techniques. 660-nm imaging light was used for all images. Panels on the left show horizontal ($x$-direction) cross sections through each corresponding image on the right along the white line superimposed on the images; image intensity $I(x)$ is plotted vs. $x$ (arbitrary units are the same for each cross section). (a) - (c) Dark-field images taken with a 2.5-ms exposure and using masks with diameters of 100 $\mu$m, 370 $\mu$m, and $\sim$1.5 mm respectively. Circular masks were used for (a) and (c), whereas a wire mask, aligned approximately parallel to the fiber, was used for (b). (d) Bright-field image of the nanofiber with no mask in place, taken with a 0.25-ms exposure. See text for a discussion of the calculated relative signal ratio (RSR) for the cross sections [80].

background features due to structure on the probe beam and etaloning at the camera, with a relative signal ratio (RSR) of 3, a measure of the signal relative to the variations and noise in the background signal [80]. As shown in Figs. 6.2(a)-(c), RSR increases with mask size until the mask begins to alter the profile of the nanofiber signal due to clipping of the lowest spatial frequency components in the refracted signal. Given that the fiber primarily refracts light in the direction perpendicular to its length, we characterize the mask size by the projection of the mask in the direction perpendicular to the fiber. Thus, for a circular

mask, or a wire mask oriented parallel to the fiber, the relevant parameter is the mask diameter rather than the actual shape of the mask. The dark-field image of Fig. 6.2(b) has an RSR of 27, almost an order-of-magnitude improvement over the bright-field image of Fig. 6.2(d). The 370-$\mu$m-diameter wire mask used for the image of Fig. 6.2(b) is the same wire used for *in situ* vortex imaging described below, and the resulting image of the nanofiber has a full width at half maximum (FWHM) of 1.18 $\pm$ 0.03 $\mu$m, an approximate measure of the resolution limit of the imaging system rather than the true size of the nanofiber. The FWHM was found by fitting a Gaussian to the intensity profile, and the uncertainty is due to the uncertainty from the fit combined with the uncertainty reported above for the system magnification. For the 660-nm probe wavelength, the calculated diffraction limit of the objective is 1.61 $\mu$m [77], which corresponds to a FWHM of 1.36 $\mu$m for a diffraction-limited point object. Note that the high-pass spatial frequency filtering inherent in the dark-field imaging process acts to narrow the FWHM of the central intensity peak while increasing the power in the side lobes of the Airy diffraction pattern. Because of this filtering process, it is possible to obtain an image of a point object that has a FWHM that is slightly smaller than the diffraction limit, as we observe. This narrowing of the FWHM is a secondary benefit of dark-field imaging; the primary benefit is the removal of noise inherent in the low spatial frequency signal.

Although our ultimate goal is to image arbitrary 2D vortex distributions in highly oblate BECs, we chose a vortex lattice for our initial *in situ* imaging tests because a lattice is an easily recognizable pattern of vortices that can be reliably reproduced. Additionally, the increase in angular momentum due to rotating the BEC causes the BEC's radial width to increase, its axial width to decrease, and the vortices comprising the lattice to align with the rotation and imaging axis. A rotating BEC thus serves as a suitable proof-of-principle test target for investigating the feasibility of imaging arbitrary 2D vortex distributions in highly oblate BECs, which we ultimately intend to study.

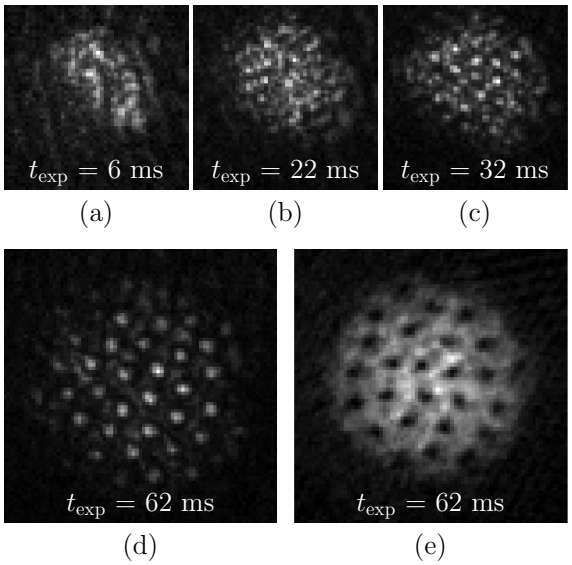


Figure 6.3: Images of expanded BECs with a vortex lattice, using an $M = 5$, NA = 0.2 imaging system. (a)-(c) show a 135-$\mu$m-wide field of view, and (d)-(e) show a 200-$\mu$m-wide field of view. For each image, the BEC was released from the trap and allowed to expand for a variable time $t_{\rm exp}$ shown on the image. (a)-(d) Raw dark-field images of an expanded BEC with a vortex lattice taken at varying expansion times, with no background subtraction. A circular mask with diameter of $\sim 1.6$ mm was used for all dark-field images. The lattice becomes resolvable between $t_{\rm exp} = 22$ ms and $t_{\rm exp} = 32$ ms. For this figure only, $t_{\rm exp}$ refers to expansion time instead of exposure time. (e) Reference absorption image of an expanded BEC with a vortex lattice, obtained using standard methods of bright-field imaging with background subtraction and grayscale contrast inversion.

## 6.4 Vortex lattice

As a basis for comparison of the $M \sim 20$ optical system's ability to image vortex distributions, we used our standard, non-diffraction-limited, $M = 5$, NA = 0.2 imaging system to obtain dark-field images of vortices with a BEC after a period of expansion. After spinning up a lattice, turning off the trapping fields, and allowing the BEC to expand for a variable expansion time, we optically pumped the atoms from the $5^2\mathrm{S}_{1/2}$ $|F = 1\rangle$ level to the $|F = 2\rangle$ level and then imaged on the transition to the $5^2\mathrm{P}_{3/2}$ $|F' = 3\rangle$ level. We obtained images of vortex cores using both dark-field imaging, as shown in Figs. 6.3(a)-(d),

and standard bright-field absorption imaging, as shown in Fig. 6.3(e). A circular mask with a diameter of ∼1.6 mm was used for all of the dark-field images shown in Fig. 6.3, and the probe detuning ranged from -1Γ to -2Γ from the $|F = 2\rangle \rightarrow |F' = 3\rangle$ hyperfine transition. As shown in Figs. 6.3(a)-(d), vortex core resolvability increased for longer expansion times. The low magnification and NA of the imaging system limited our ability to resolve two neighboring cores for expansion times less than about 30 ms. While cores may be resolvable at expansion times less than 30 ms, the corresponding smaller atom cloud should result in a higher percentage of the light refracted from the bulk BEC bypassing the mask, thereby reducing contrast between vortex cores and the bulk BEC in the absence of further optimization of mask size.

To image vortex cores within a *trapped* BEC, we used the $M \sim 20$, NA = 0.25 imaging system previously described. Representative *in situ* dark-field images of a BEC confined within the TOP trap are shown in Fig. 6.4. The dark-field images show a clear distinction between a BEC without a vortex lattice, Fig. 6.4(a), and one with a lattice, Figs. 6.4(b)-(d). For comparison, an *in situ* bright-field image of a BEC without a vortex lattice and an image of a BEC with a vortex lattice are shown in Fig. 6.4(e) and Fig. 6.4(f), respectively. Unlike the dark-field vortex lattice images, Fig. 6.4(f) shows no clear vortex cores, as it is difficult to distinguish between the weak transmission feature corresponding to a vortex core and structure on the probe beam or other imaging artifacts. For the images in Fig. 6.4(a)-(c), we used an imaging probe with a $1/e^2$ beam radius of $\sim 2$ mm, a power of $\sim 0.5$ mW, a detuning of $\Delta = 4.5\Gamma$ from the $|F = 2\rangle \rightarrow |F' = 3\rangle$ transition, and an exposure time of 20 $\mu$s. For the vortex lattice shown in Fig. 6.4(b), we measured the separation between vortex cores to be $a \sim 9$ $\mu$m, as shown in Fig. 6.4(g). The FWHM of the central vortex core of Fig. 6.4(g), as determined from the cross section given in Fig. 6.4(h), was measured to be $\delta$=2.4±0.5 $\mu$m, indicating that the imaging system should be capable of resolving two vortex cores separated by approximately this distance. The FWHM is a measure of the point-spread function for our imaging system rather than the actual size

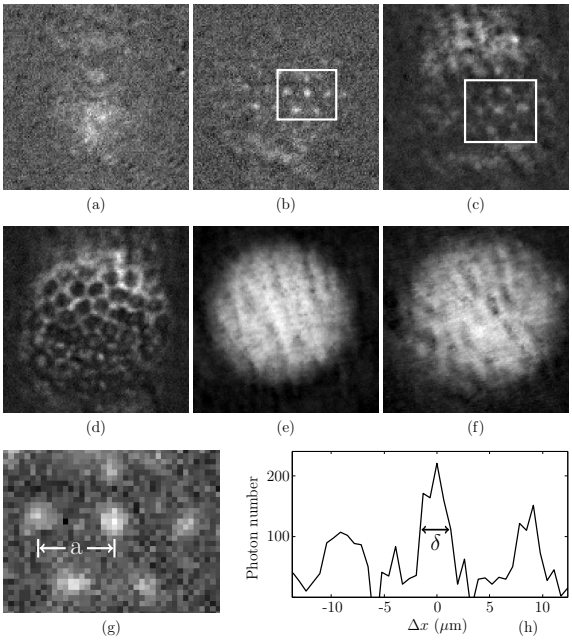


Figure 6.4: (a)-(f) 80-$\mu$m-wide *in situ* images of BECs obtained with our $M \sim 20$, NA = 0.25 imaging system. Dark-field images of the BEC are shown (a) without a vortex lattice, and (b) with a vortex lattice. The wire mask used for both images had a diameter of 370 $\mu$m, and was aligned horizontally with respect to the image. (c) Dark-field image of a BEC with a vortex lattice, but with a 250-$\mu$m-diameter wire mask; vortices are visible within the superimposed white rectangle, but not as apparent as in (b), as additional refracted light from the BEC reaches the camera. (d) Dark-field image obtained with a rotating BEC with a vortex lattice when the imaging system is not properly focused. All dark-field images have been processed by subtraction of a background image taken in the absence of a BEC. Reference *in situ* absorption images are shown for (e) a non-rotating BEC, and (f) a rotating BEC that is expected to contain vortices. Bright-field images were obtained using standard methods of bright-field imaging with background subtraction and grayscale contrast inversion. (g) Magnified view of the region bounded by the white rectangle in (b), with pixelation due to the 13 $\mu$m x 13 $\mu$m camera pixels. Neighboring vortex cores are separated by $a \sim 9$ $\mu$m. (h) Cross section along the middle row of vortex cores shown in (e); the vertical scale is proportional to image intensity per pixel, calibrated to number of photons; the horizontal plot axis shows the distance $\Delta x$ away from the central vortex core, with the scale corresponding to real distances at the object plane. The FWHM of the central vortex core is $\delta$=2.4$\pm$0.5 $\mu$m. The FWHM was found by fitting a Gaussian to the intensity profile, and the reported error is due to the uncertainty from the fit.

of the vortex core. The detuning was chosen to maximize the signal from the vortex cores for the 370-$\mu$m-diameter mask. Such close detuning was destructive to the BEC, and with these parameters we are limited to acquiring a single image per BEC. Additionally, due to the low signal level of these images, we utilized background subtraction to remove features due to the unrefracted probe light that were not obstructed by the mask.

As discussed, the size of the dark-field mask determines the spatial frequency cutoff of the spatial filter. Figure 6.4(c) shows a dark-field image taken using a mask diameter of 250 $\mu$m. The smaller mask size allows more of the light refracted from the bulk BEC to reach the camera, reducing the contrast of the vortex cores. In comparison, the 370-$\mu$m-diameter wire mask used for Fig. 6.4(b) blocks almost all of the light refracted by the bulk BEC. Fig. 6.4(d) shows a representative out-of-focus image of a vortex lattice, obtained with a detuning of $\Delta = 4\Gamma$ and a 30-$\mu$s exposure. The lattice takes on a honeycomb appearance similar to that observed in an out-of-focus bright-field absorption image of a vortex lattice. Note that with the exception of the out-of-focus lattice, we primarily see vortex cores in the center of the BEC. We speculate that this could be due to the decrease in density at the edge of the BEC, and correspondingly smaller angles of refraction associated with the vortex cores, due to the increase in healing length and decrease of integrated optical density along the probe propagation direction. Additionally, the use of a wire mask introduces an asymmetry in the background signal since all spatial frequencies are blocked in the direction parallel to the wire. For the results presented here, the choice to use a wire mask instead of a circular mask was based on the masks available; given the radial symmetry of the BEC, a circular mask is preferable. We anticipate that using a precision circular mask with an optimized size, and imaging vortices in BECs held in a flat-bottomed potential [29], will improve our ability to detect vortices across the BEC.

## 6.5 Conclusions and suggested improvements

The single-shot, *in situ* images of bare vortex cores presented here serve as a promising proof-of-principle indication that complex vortex dynamics may be measurable in trapped BECs with additional optimization of the imaging system and imaging parameters. In numerical studies of 2D quantum turbulence, our particular area of interest, vortex-antivortex annihilation and bound pairs of vortices of the same sign of circulation appear to show minimum inter-vortex separation distances of approximately 2 $\mu$m for our parameters [22]. Resolutions approaching this scale are already achievable with our imaging system.

The primary hurdle in extending this technique to capturing multiple images of a single BEC is the achievement of a sufficient RSR, given the large probe detuning and low probe intensity desired for minimally-destructive imaging. While the Olympus objective used for the imaging system reported here appears to be a suitable commercial objective given the physical constraints of our apparatus, this microscope objective is optimized for visible light, and its transmission is approximately 60% for our operating wavelength of 780 nm. Additionally, the relay lenses required to place the mask in an accessible intermediate Fourier plane introduce aberrations to the imaging system, making it more difficult to block all of the weakly scattered imaging light and obtain the best possible RSR.

We are currently implementing modifications to the imaging system that should improve both the image quality and the RSR. We are installing a custom objective, optimized for 780-nm imaging probe light, with an accessible rear focal plane, based on the design of Ref. [81]; we have measured the transmission of this objective to be 88% at 780 nm. We also anticipate that using a CCD camera with electron multiplying (EMCCD) gain capabilities, in conjunction with dark-field imaging, will result in a significant increase in the overall signal-to-noise ratio, and will enable the use of imaging light further detuned from resonance. Recently Gajdacz *et al.* have used an EMCCD camera and dark-field Faraday imaging to obtain thousands of images of a single BEC [45]. In situations with low signal, but also low background light levels, the pre-readout amplification of an EMCCD

camera should be beneficial in imaging vortex distributions.

One significant advantage of dark-field imaging is the minimization of background light, allowing for weak signals to be obtained and amplified without the need for background image subtraction. This potential advantage will be especially useful for measurements of vortex dynamics where the time between images is expected to be on the order of 10 ms. In the dark-field *in situ* images presented here, background image subtraction was necessary due to low vortex signal levels and relatively high levels of weakly scattered probe light reaching the camera, and further optimization of the probe beam profile and dark-field mask will be necessary to utilize raw images without the need for background subtraction, and to take advantage of the pre-readout amplification of an EMCCD camera.

Numerical calculations for the propagation of the dark-field signal due to a BEC containing a central vortex are discussed in detail in Chapter 7. Our calculations assume propagation through an imaging system with a magnification of $M = 11$, with a probe beam that is tuned near the $|F = 1\rangle \rightarrow |F' = 2\rangle$ transition. Our calculations indicate that for a probe detuning of $\Delta = +200$ MHz, a probe intensity of $I = 6.4$ W/m$^2$, an exposure time of 50 $\mu$s, a dark-field mask of radius 520 $\mu$m, and an assumed transmission of 75%, vortex signals should be on the order of 160 photons on a central 16-$\mu$m $\times$ 16-$\mu$m square camera pixel. For these same parameters, the maximum signal from the bulk BEC should be on the order of 10 photons per pixel. We have tested the destructiveness of these imaging probe parameters and found that after 8 images, approximately 50% of the atoms remain. Given our demonstrated capability to observe vortex signals with photon numbers on the order of 200 photons per pixel with a non-electron-multiplying CCD camera as shown in Fig. 6.4(h), we anticipate that the imaging parameters used for our numerical calculations should yield experimentally observable vortex cores in at least 2 or 3 images, with further optimization likely with EMCCD cameras that are sensitive to much lower signal levels than the target signal levels of this numerical study.

We have demonstrated single-shot *in situ* imaging of vortex cores in a BEC. Based on

this result and our numerical calculations, we anticipate that the improvements detailed here will enable the ability to obtain multi-shot, *in situ* imaging of vortices and their dynamics within a single BEC, and to obtain images of vortex distributions in BECs that cannot be readily determined from images after ballistic expansion. Access to such images will open up new possibilities for experiments to study numerical and theoretical predictions of 2D quantum turbulence [6, 25, 26, 82], our primary goal, and an even wider range of superfluid dynamics, such as shock wave and soliton dynamics.

# Chapter 7
# Numerical Modeling of Dark-field Imaging

In order to better understand the dark-field imaging process we modeled the propagation of a plane wave, imprinted with the BEC phase profile, through the imaging system described in Chapter 8. Ideally the numerical model will allow us to narrow down the parameter space, and find parameters that yield good dark-field vortex core signal. In any case, the numerical calculations were necessary to provide a convincing argument for the feasibility of minimally destructive *in situ* imaging. This chapter is an extension of the appendix for the paper reproduced in Chapter 6 [9].

## 7.1 BEC density profile

We first consider a cylindrically symmetric BEC without a vortex. The BEC is assumed to have a three-dimensional density distribution in the Thomas-Fermi limit,

$$n(r,z) = \begin{cases} n_0\left(1 - r^2/R_{\mathrm{r}}^2 - z^2/R_{\mathrm{z}}^2\right) & r^2/R_r + z^2/R_z^2 < 1 \\ 0 & \text{otherwise} \end{cases} \tag{7.1}$$

where $z$ is the axial coordinate corresponding to the imaging axis, $r$ is the radial coordinate at the BEC, $R_{\mathrm{r}}$ and $R_{\mathrm{z}}$ are radial and axial Thomas-Fermi radii, and $n_0$ is the peak BEC density. When integrated along $z$, this density distribution leads to a two-dimensional integrated column density distribution

$$\tilde{n}_c(r) = \begin{cases} n_{2\mathrm{D}}\left(1 - r^2/R_{\mathrm{r}}^2\right)^{3/2} & r \le R_r \\ 0 & r > R_r \end{cases} \tag{7.2}$$

where $n_{2\mathrm{D}} = 5N/2\pi R_{\mathrm{r}}^2$, with $N$ the number of condensed atoms.

With a vortex in the center of the BEC, we assume an integrated column density distribution of $\tilde{n}_{\mathrm{v}}(r) = \chi(r)\,\tilde{n}_{\mathrm{c}}(r)$, where the contribution from the vortex, $\chi(r)$, has the

form of an inverted Lorentzian,

$$\chi(r) = \frac{r^2}{r^2 + (\xi/\Lambda)^2}, \tag{7.3}$$

where $\xi$ is the BEC healing length calculated for peak density $n_0$, and $\Lambda \approx 0.825$ is a constant that ensures the vortex density distribution has the analytically obtained exact slope near the center of the vortex core [25]. We neglect both the variation of the healing length along the axial direction as well as modifications to the overall BEC shape due to the presence of the vortex, except near the center of the BEC where the vortex is located.

From an experimental standpoint we would normally control the trap frequencies and the atom number but for ease of the numerics we let $N$, $R_\mathrm{r}$, and $R_\mathrm{z}$ be the free parameters which then fix the rest of the BEC parameters, including the trap frequencies, chemical potential, and atom density. In the Thomas-Fermi limit the BEC volume is

$$V = \frac{4\pi}{3} R_\mathrm{r}^2 R_\mathrm{z}, \tag{7.4}$$

which then determines the density (in 3D)

$$n_0 = \frac{5N}{2V}, \tag{7.5}$$

which in turn fixes the healing length

$$\xi = \frac{1}{\sqrt{8\pi n_0 a_\mathrm{s}}}, \tag{7.6}$$

where $a_\mathrm{s}$ is the scattering length. The chemical potential is

$$\mu_0 = \frac{\hbar^2}{2m\xi^2} \tag{7.7}$$

where $m$ is the mass of $^{87}$Rb, and the trap frequencies are

$$\omega_i = \sqrt{\frac{2\mu_0}{mR_i^2}} \tag{7.8}$$

where $i = r, z$ for the radial and axial trap frequencies respectively. The BEC parameters used for the numerics are listed in Table 7.1

Table 7.1: Trap specific parameters - numerics

| | |
|---|---|
| BEC atom number | $N = 2 \times 10^6$ atoms |
| Axial Thomas-Fermi radius | $R_z = 7\mu$m |
| Radial Thomas-Fermi radius | $R_r = 49\mu$m |
| Healing length | $\xi = 325$ nm |
| Axial trap frequency | $\omega_z = 2\pi\times$ 49 Hz |
| Radial trap frequency | $\omega_r = 2\pi\times$ 7 Hz |

## 7.2 Phase shift acquired by passing through BEC

Following the method of Ref. [40], as introduced in Chapter 3, we treat the BEC as a thin lens that coherently scatters the probe beam. For dark-field imaging, a mask in the Fourier plane blocks the unscattered probe light such that the dark-field electric field $E_{\mathrm{DF}}$, i.e., the component of the probe beam that has been coherently scattered, is

$$E_{\mathrm{DF}} = E_0(te^{i\phi} - 1). \tag{7.9}$$

Here $E_0$ is the amplitude of the incident field, $\phi$ is the phase shift defined in Eqn. 3.1, and $t = e^{\alpha}$ where $\alpha$ is the attenuation defined in Eqn. 3.2. The imaging parameters used for the numerical model of dark-field imaging are listed in Table 7.2.

Table 7.2: Parameters for imaging system - numerics.

| | |
|---|---|
| Polarization | $\sigma_-$ |
| Transition | $\lvert F = 1, m_F = -1\rangle \rightarrow \lvert F' = 2, m_{F'} = -2\rangle$ |
| Saturation intensity | $I_{\mathrm{sat}} = 32$ W/m$^2$ |
| Resonant cross-section | $\sigma_0 = 1.5 \times 10^{-13}$ m$^2$ |
| Objective lens | $f_{\mathrm{Obj}} = 36$ mm, $R_{\mathrm{Pupil}} = 9.4$ mm |
| Tube lens | $f_{\mathrm{Tube}} = 400$ mm, $R_{\mathrm{Pupil}} = 12.5$ mm |
| Mask radius | $R_{\mathrm{Mask}} = 520$ $\mu$m, $R_{\mathrm{Pupil}} = 11$ mm |
| Transmission through imaging system | 75% |
| Camera pixel size | 16 $\mu$m $\times$ 16 $\mu$m |
| Image pulse detuning | 200 MHz |
| Image pulse length | 50 $\mu$s |
| Image probe intensity | $I_0 = I_{\mathrm{sat}}/5$ |
| Photons scattered | 0.04 / atom |

## 7.3 Propagation of dark-field signal

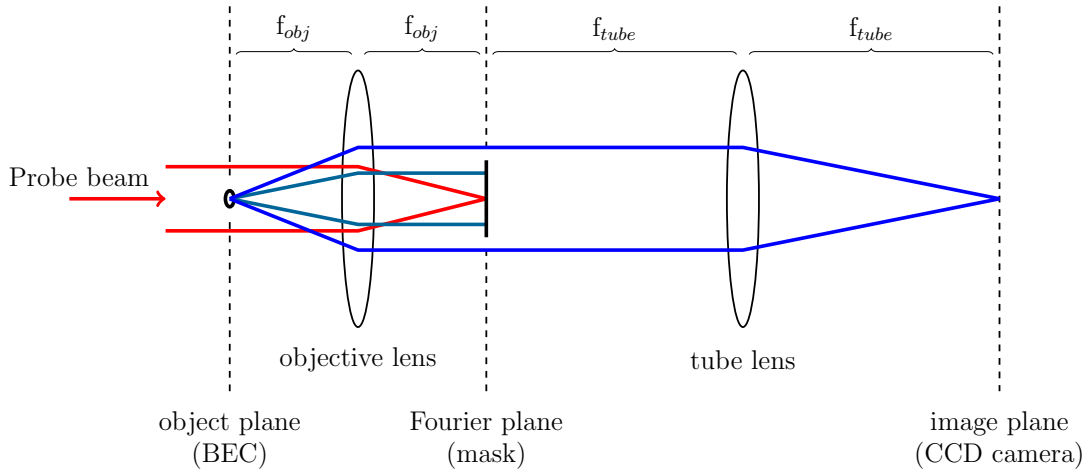


Figure 7.1: Simplified dark-field imaging system.

As shown in Fig. 7.1, the imaging system is arranged such that in the Fresnel diffraction regime, each lens does a 2D Fourier transform in Cartesian coordinates, i.e., the object is located at the front focal plane of the lens, with the Fourier plane coincident with the rear focal plane. For a radially symmetric field such as a BEC with a central vortex, the 2D Fourier transform can be reduced to a 1D Hankel transform. The Hankel transforms can then be performed as numerical integration over $rJ_0(ar)\mathrm{d}r$, where $J_0$ is the zeroth order Bessel function of the first kind, $r$ is the radial coordinate, and $a$ scales the radial coordinate. In this model we treat both the tube lens and the objective as thin lenses that apply a quadratic phase curvature to the incident field [83].

As described in Sec. 7.2, the coherently scattered field directly after the BEC is $E_{\mathrm{BEC}}(r) = E_{\mathrm{DF}}$. To determine the field at the Fourier plane we first propagate over free space from the BEC to the front face of the objective lens, over a propagation distance $z = f$, where $f$ is the focal length of the objective lens,

$$E_{\mathrm{lens}}(w) = \frac{2\pi}{i\lambda f} e^{i\pi w^2/\lambda f} \int_0^\infty r E_{\mathrm{BEC}}(r) e^{i\pi r^2/\lambda f} J_0\left(\frac{2\pi w r}{\lambda f}\right) \mathrm{d}r. \tag{7.10}$$

Here we employed the Fresnel diffraction integral for free space propagation [83], where $E_{\text{lens}}(w)$ is the field incident on the objective, $\lambda = 780$ nm is the wavelength of the probe light, and $w$ is the real-space, radial coordinate in the plane of the objective lens. Note that in cylindrical coordinates with radial symmetry $E(r)$, the free space propagation simplifies to a 1D Hankel transform with an extra cylindrically-symmetric quadratic phase curvature.

Next, we apply the pupil function $P(w)$ to account for the finite numerical aperture of the lens, and the phase curvature due to the lens,

$$\tilde{E}_{\text{lens}}(w) = E_{\text{lens}}(w)P(w)e^{-i\pi w^2/\lambda f}, \tag{7.11}$$

where $\tilde{E}_{\text{lens}}(w)$ is the field directly after the lens. Lastly we propagate from the lens to the mask location in the Fourier plane of the imaging system, a distance $z = f$ behind the lens.

$$E_{\text{FP}}(\rho) = \frac{2\pi}{i\lambda f}e^{i\pi\rho^2/\lambda f}\int_0^\infty w\tilde{E}_{\text{lens}}(w)e^{i\pi w^2/\lambda f}J_0\left(\frac{2\pi\rho w}{\lambda f}\right)\mathrm{d}w. \tag{7.12}$$

$E_{\text{FP}}(\rho)$ is the field at the Fourier plane, where $\rho$ is the real-space radial coordinate in the Fourier plane. Inserting Eqn. 7.11 into Eqn. 7.12 results in

$$E_{\text{FP}}(\rho) = \frac{2\pi}{i\lambda f}e^{i\pi\rho^2/\lambda f}\int_0^\infty wE_{\text{lens}}(w)P(w)J_0\left(\frac{2\pi\rho w}{\lambda f}\right)\mathrm{d}w \tag{7.13}$$

for the field at the Fourier plane of the imaging system. Note that the quadratic phase curvature from the objective lens exactly cancels the quadratic phase curvature due to the free space propagation over a distance $z = f$. We apply the mask

$$M(\rho) = \begin{cases} 0 & \rho \leq \rho_{\text{M}} \\ 1 & \rho > \rho_{\text{M}} \end{cases} \tag{7.14}$$

to the field in the Fourier plane,

$$\tilde{E}_{\text{FP}}(\rho) = E_{\text{FP}}(\rho)M(\rho), \tag{7.15}$$

such that $M(\rho)$ is effectively a high-pass spatial filter with a spatial frequency cutoff set by $\rho_{\text{M}}$.

To determine the field in the image plane, we propagate the filtered field $\tilde{E}_{\mathrm{FP}}(\rho)$ from the mask in the Fourier plane to the front face of the tube lens, where the propagation distance is equal to $F$, the focal length of the tube lens,

$$E_{\mathrm{LENS}}(W) = \frac{2\pi}{i\lambda F} e^{i\pi W^2/\lambda F} \int_0^\infty \rho \tilde{E}_{\mathrm{FP}}(\rho) e^{i\pi\rho^2/\lambda F} J_0\left(\frac{2\pi W\rho}{\lambda F}\right) \mathrm{d}\rho, \tag{7.16}$$

Here $E_{\mathrm{LENS}}(W)$ is the field incident on the tube lens, and $W$ is the real-space, radial coordinate in the plane of the tube lens. Inserting Eqn. 7.15 into Eqn. 7.16 results in

$$E_{\mathrm{LENS}}(W) = \frac{2\pi}{i\lambda F} e^{i\pi W^2/\lambda F} \int_0^\infty \rho E_{\mathrm{FP}}(\rho) M(\rho) e^{i\pi\rho^2/\lambda F} J_0\left(\frac{2\pi W\rho}{\lambda F}\right) \mathrm{d}\rho \tag{7.17}$$

for the field incident on the tube lens. Next, we apply the pupil function $Q(W)$ to account for the finite numerical aperture of the tube lens, and the phase curvature due to the tube lens.

$$\tilde{E}_{\mathrm{LENS}}(W) = E_{\mathrm{LENS}}(W) Q(W) e^{-i\pi W^2/\lambda F}, \tag{7.18}$$

where $\tilde{E}_{\mathrm{LENS}}(W)$ is the field directly after the lens prior to any free space propagation.

Lastly, we propagate from the tube lens to the image plane at the camera,

$$E_{\mathrm{CAM}}(R) = \frac{2\pi}{i\lambda F} e^{i\pi R^2/\lambda F} \int_0^\infty W \tilde{E}_{\mathrm{LENS}}(W) e^{i\pi W^2/\lambda F} J_0\left(\frac{2\pi RW}{\lambda F}\right) \mathrm{d}W, \tag{7.19}$$

where $E_{\mathrm{CAM}}(R)$ is the field at the camera, with R the real-space, radial coordinate in the camera (image) plane. Inserting Eqn. 7.18 into Eqn. 7.19 results in

$$E_{\mathrm{CAM}}(R) = \frac{2\pi}{i\lambda F} e^{i\pi R^2/\lambda F} \int_0^\infty W E_{\mathrm{LENS}}(W) Q(W) J_0\left(\frac{2\pi RW}{\lambda F}\right) \mathrm{d}W \tag{7.20}$$

where the quadratic phase curvature due to the tube lens exactly cancels the quadratic phase curvature due to the free space propagation over a distance $z = F$.

## 7.4 Numerical implementation

The propagation of the dark-field signal $E_{\mathrm{DF}}$ from BEC to camera described above can be calculated numerically with four integration steps: BEC to objective lens (Eqn. 7.10),

objective lens to Fourier plane (Eqn. 7.13), Fourier plane to tube lens (Eqn. 7.17), and tube lens to camera (Eqn. 7.20). Our primary reason for limiting the numerics to a BEC with a central vortex core was to take advantage of the radial symmetry and cut down on the integration time by transforming the problem from 2D to 1D. The high spatial frequencies needed to represent microscopic features such as a vortex, combined with the large range in real-space needed to represent the optical system, meant that we needed the grids for the numerical integration to be both large and finely spaced, requiring a substantial amount of computing power. Figure 7.2 shows the radial intensity profile of the dark-field signal at the BEC (object) plane, Fig. 7.3 shows the intensity profile after propagation to the Fourier plane and application of the dark-field mask, and Fig. 7.4 shows the intensity profile at the camera (object) plane.

Table 7.3: Spatial grids for numerical integration

| | |
|---|---|
| Real space at the BEC (object plane) | $r_{\max} = 100\ \mu$m<br>$n_{\mathrm{r}} = 2^{13}$ |
| Real space at the objective lens | $w_{\max} = 9.4$ mm (radius of pupil)<br>$n_{\mathrm{w}} = 2^{13}$ |
| Real space at the Fourier plane (mask location) | $\rho_{\max} = 11$ mm<br>$n_{\rho} = 2^{13}$ |
| Real space at the tube lens | $W_{\max} = 12.5$ mm (radius of pupil)<br>$n_{\mathrm{W}} = 2^{13}$ |
| Real space at the image plane (camera) | $R_{\max} = 800\ \mu$m<br>$n_{\mathrm{R}} = 50$ |

The intensity profiles shown in Figs. 7.2-7.4 were calculated using the Fresnel diffraction integrals in Sec. 7.3, the BEC parameters listed in Table 7.1, the imaging parameters in Table 7.2, and the grid parameters defined in Table 7.3. In each plot, the solid green line corresponds to the profile due to the bulk BEC with no vortex present, and the blue circles correspond to the dark-field signal for a BEC with a central vortex.

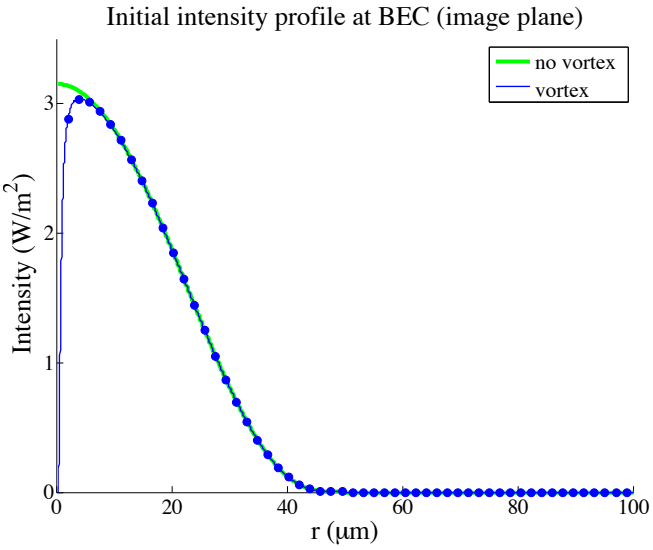


Figure 7.2: Intensity profile of the dark-field signal corresponding to the coherently scattered component of the probe beam, in the BEC (object) plane, directly after the probe passes through the BEC. The green line corresponds to the profile for a BEC without a vortex, and blue circles correspond to a BEC with a central vortex.

## 7.5 Optimization of dark-field vortex signal

The dark-field signal corresponding to a vortex depends heavily on the cutoff frequency of the high-pass spatial filter, i.e., the mask radius. This cutoff frequency needs to be matched to the phase shift $\phi$ acquired as the imaging probe passes through the BEC, with the phase shift depending on the integrated BEC density, as well as the detuning $\Delta$ and intensity $I_0$ of the probe light, as discussed in Chapter 3. As shown in Fig. 7.5(a), for a given intensity, the maximum phase shift $\phi$ occurs for $\Delta = \pm 0.5\Gamma$. Here we consider the low intensity limit with $I_0 = 0.1 I_{\rm sat}$. In general, increasing $I_0$ decreases $\phi$, and in the limit $I_0 >> I_{\rm sat}$, Eqn. 3.1 approaches $\phi \propto I_{\rm sat}/I_0$. Figure 7.5(b) shows the phase shift as a function of the intensity in terms of $I_{\rm sat}$, for a given detuning $\Delta = 0.5\Gamma$. Figures 7.5(c) and (d) plot the number of scattered photons per atom as a function of detuning and intensity respectively, for the same parameters used for Figs. 7.5(a) and (b). All plots in Fig. 7.5

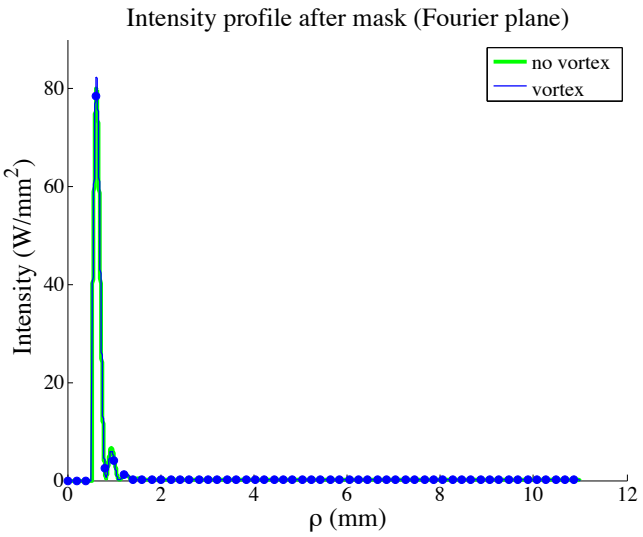


Figure 7.3: Intensity profile of the dark-field signal in the Fourier plane, directly after the probe is filtered by the mask. The green line corresponds to the profile for a BEC without a vortex, and blue circles correspond to a BEC with a central vortex.

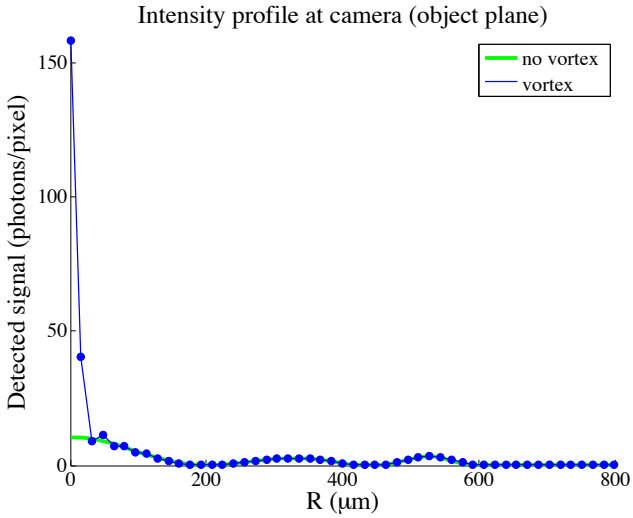


Figure 7.4: Intensity profile of the dark-field signal in the camera (image) plane. The green line corresponds to the profile for a BEC without a vortex, and blue circles correspond to a BEC with a central vortex.

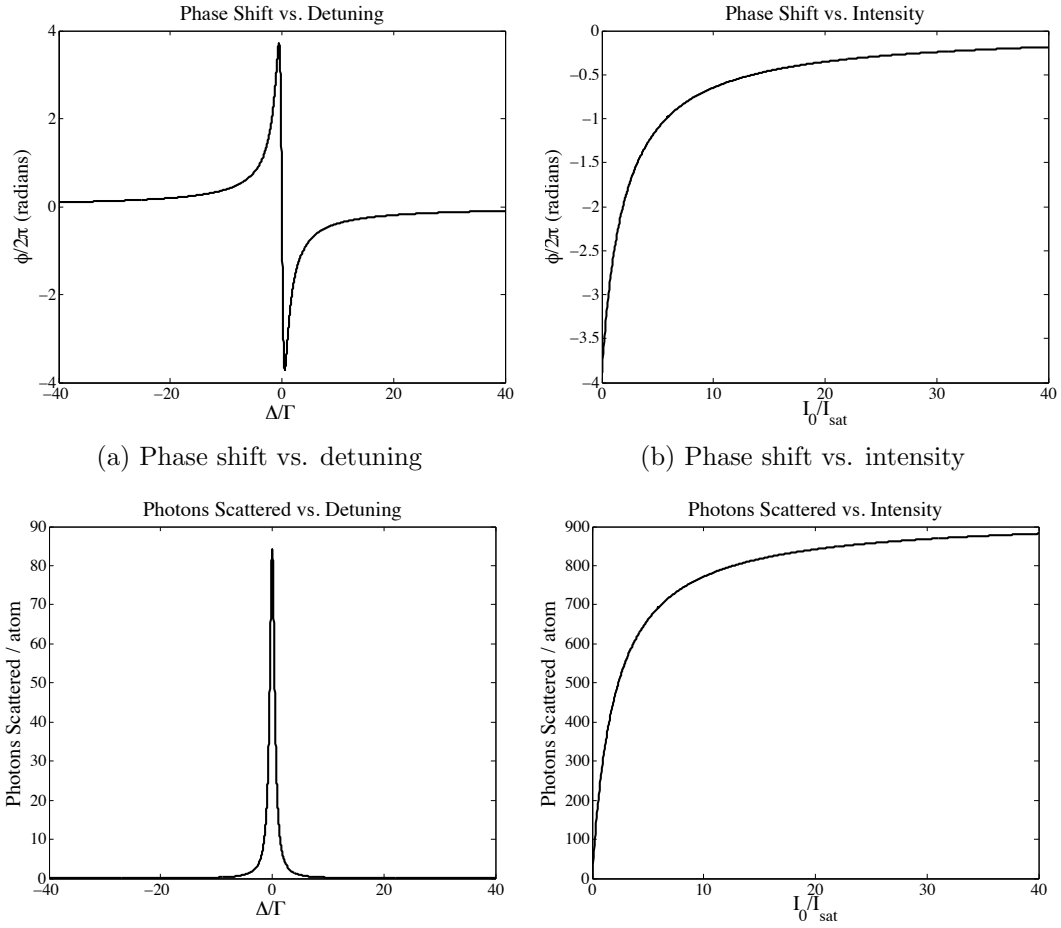


(a) Phase shift vs. detuning

(b) Phase shift vs. intensity

(c) Photons scattered per atom vs. detuning

(d) Photons scattered per atom vs. intensity

Figure 7.5: Phase shift (a) and (b) and photons scattered per atom (c) and (d) as functions of intensity and detuning. (a) Phase shift $\phi$ versus detuning $\Delta/\Gamma$ measured in linewidths, at constant intensity $I_0/I_{\rm sat} = 0.1$. (b) Phase shift $\phi$ versus intensity $I_0/I_{\rm sat}$ in terms of the saturation intensity, at detuning $\Delta/\Gamma = 0.5$. (c) Number of photons scattered per atom versus detuning $\Delta/\Gamma$ measured in linewidths, at constant intensity $I_0/I_{\rm sat} = 0.1$, and exposure time $t_{\rm exp} = 50$ $\mu$s. (d) Number of photons scattered per atom versus intensity $I_0/I_{\rm sat}$ in terms of the saturation intensity, at detuning $\Delta/\Gamma = 0.5$ and $t_{\rm exp} = 50$ $\mu$s.

were calculated using the BEC parameters in Table 7.1, with exposure time $t_{\rm exp} = 50$ $\mu$s where relevant. Our goal of non-destructive imaging requires us to find values for $R_{\rm mask}$, $I_0$ and $\Delta$ that give good vortex signal while minimizing the number of photons scattered per

atom. Based on the plots shown maximum phase shift should occur for low probe intensity ($I_0/I_{\rm sat} = 0.1$) at $\Delta \sim 4\Gamma$ corresponding to $\phi \sim 2\pi$. For closer detunings we expect to experience phase winding. However, even at low probe intensity, a detuning of $\Delta \sim 4\Gamma$ is still destructive with more than one photon scattered per atom. In this section we vary the imaging parameters to optimize the number of photons incident on the central $16 \times 16$-$\mu$m square pixel in the dark-field image, the pixel located at $R = 0$ $\mu$m in the camera plane, for a BEC with a central vortex. In addition to optimization of the absolute vortex signal, we also consider the ratio of the number of photons incident on that central $R = 0$ $\mu$m pixel due to a BEC with a central vortex to the number of photons from a BEC with no vortex.

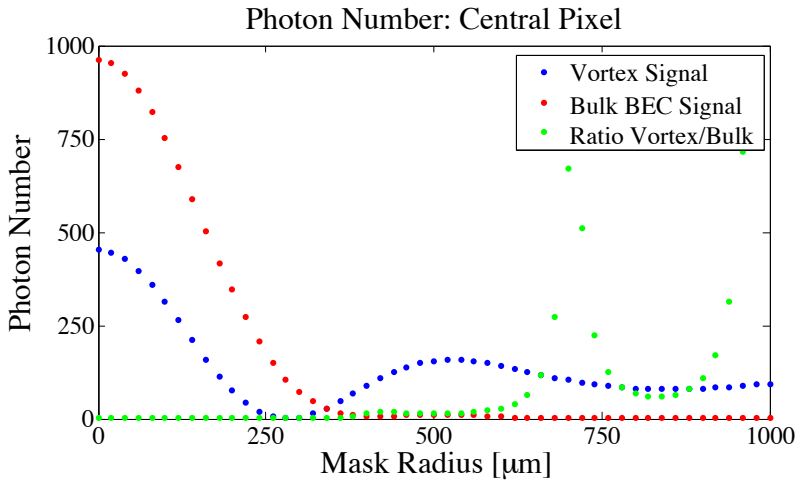


Figure 7.6: Photon number detected at the central $16 \times 16$-$\mu$m square pixel as a function of mask radius. Imaging parameters are listed in Table 7.2 and the BEC parameters are listed in Table 7.1.

Figure 7.6 plots the results from our numerical model for the number of photons incident on the central $16 \times 16$-$\mu$m square pixel in the dark-field image as we vary the mask size $R_{\rm mask}$. The region of interest is the region centered about $R_{\rm mask} = 520$ $\mu$m where we have both a detectable vortex signal of 160 photons per pixel, and a relatively high ratio of vortex signal to bulk BEC signal incident on the central pixel. For $R_{\rm mask} = 520$ $\mu$m

the signal from the bulk BEC on the central pixel is 10 photons, an order of magnitude less than the signal due to the vortex core. For the results shown in Fig. 7.7 we kept the mask radius constant at $R_{\text{mask}} = 520$ $\mu$m and varied the detuning of the imaging probe from resonance. $\Delta/2\pi = 0$ MHz corresponds to imaging light that is resonant with the $|F = 1\rangle \rightarrow |F' = 2\rangle$ hyperfine transition. For $R_{\text{mask}} = 520$ $\mu$m, the maximum photon number occurs at $\Delta/2\pi \sim 43$ MHz compared to the $\Delta/2\pi = 200$ MHz used for our analysis of mask size. However, the number of photons scattered at $\Delta/2\pi = 43$ MHz is a factor of 22 times the number scattered at $\Delta/2\pi = 200$ MHz.

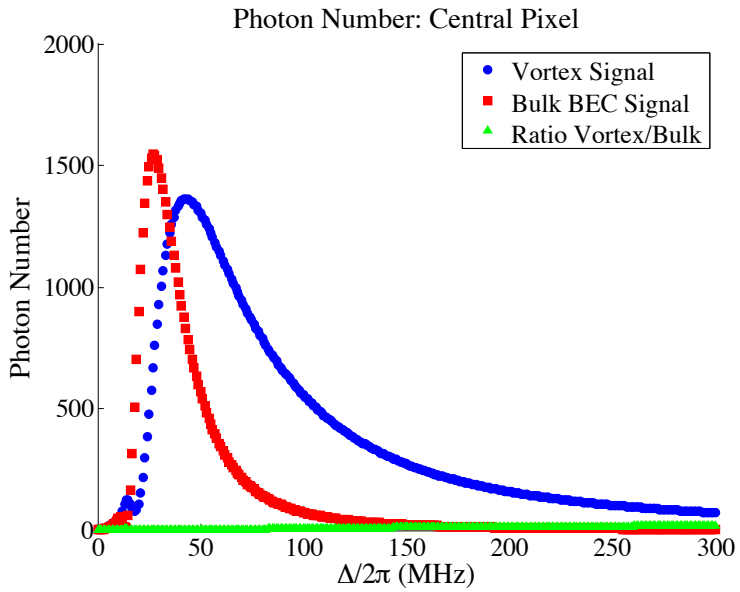


Figure 7.7: Photon number detected at the central 16-$\mu$m square pixel as a function of the detuning of the probe light. The mask radius is held constant at $R_{\text{mask}} = 520$ $\mu$m. Maximum vortex signal corresponds to $\Delta/2\pi = 43$ MHz. The maximum ratio of vortex to bulk BEC signal occurs at $\Delta/2\pi = 300$ MHz (the upper limit of the range of detuning considered here)

Lastly we consider the effect of defocus on the vortex signal. As described in Sec. 7.3, when propagating from the BEC to the objective lens, the propagation distance is $z = f$ where $f$ is the focal length of the objective lens. To investigate the consequence of the imaging system being out of focus, we let $z = f + \Delta f$, so that $\Delta f = 0$ $\mu$m corresponds

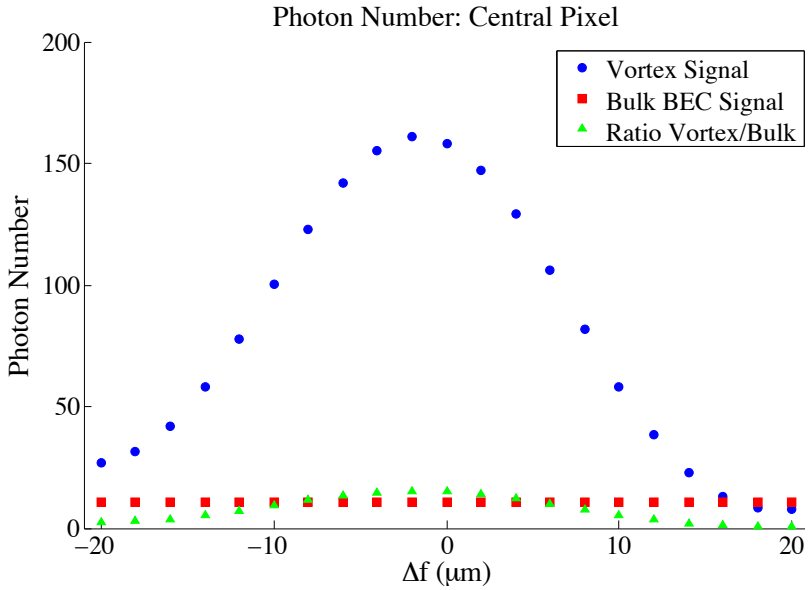


Figure 7.8: Photon number detected at the central $16 \times 16$-$\mu$m square pixel as a function of the shift in BEC position from the front focal plane of the objective lens. When propagating from the BEC to the objective lens, the propagation distance is $z = f + \Delta f$. $\Delta f = 0$ $\mu$m corresponds to a BEC located at the front focal plane of the objective, $z = f$. $R_{\text{mask}} = 520$ $\mu$m and $\Delta/2\pi = 200$ MHz were held constant while we varied $\Delta f$.

to the BEC located at the front focal plane of the objective. Figure 7.8 plots the photon number incident on the central ($R = 0$ $\mu$m) pixel on the camera as a function of $\Delta f$. As we might expect, the signal due to the bulk BEC, i.e., the BEC without a central vortex, is almost constant over the range $\Delta f = \pm 20$ $\mu$m. However, focus appears to be critical for a small feature such as a vortex with the vortex signal decreased by a factor of two for $\Delta f = \pm 10$ $\mu$m. Optimal focus, and maximum vortex signal, can be achieved by adjusting either the position of the objective relative to the BEC or the position of the camera relative to the tube lens. The position of the mask relative to the Fourier plane is not very sensitive, which makes sense given that the dark-field signal should be approximately collimated in the region between the objective and the tube lens.

Chapter 8

# Quantum Vortex Microscope Mark II

This chapter covers the design, offline characterization, and online implementation of the second quantum vortex microscope, dubbed the QVM2. While the first quantum vortex microscope (QVM1) described in Chapter 6 allowed us to obtain proof-of-principle *in situ* images of a 2D vortex distribution, obtaining sufficient vortex signal above the background noise remained a significant technical challenge. In particular, the Olympus microscope objective used for the images obtained with the QVM1 was designed for use with visible light, with transmission falling to approximately 60% at our operating wavelength of $\lambda = 780$ nm. Given the constraints of our BEC apparatus, namely the positions of the magnetic field coils used to transfer atoms from the MOT to the BEC location, as well as the coils used for the TOP trap, most commercial objectives just would not fit in the space available, shown in Fig. 8.1. For reference, comparable long-working-distance, near-infrared Mitituyo objectives have an outer diameter (OD) of at least 34 mm. This left us with a choice to either reconfigure the magnetic field coils to accommodate a commercial catalog microscope objective, or to design a custom microscope objective using catalog lenses. Ultimately we decided that modifying an existing objective design [81] would be more straightforward than redesigning the magnetic field coils.

## 8.1 Optics primer

We will begin with a brief primer of some of the metrics that are commonly used to characterize a microscope objective and imaging system. In general we reference Greivenkamp's SPIE field guide [84] for all things geometrical optics, and Goodman's *Fourier Optics* [83] for all things physical optics. After all, Goodman's textbook is reputed to be like a good

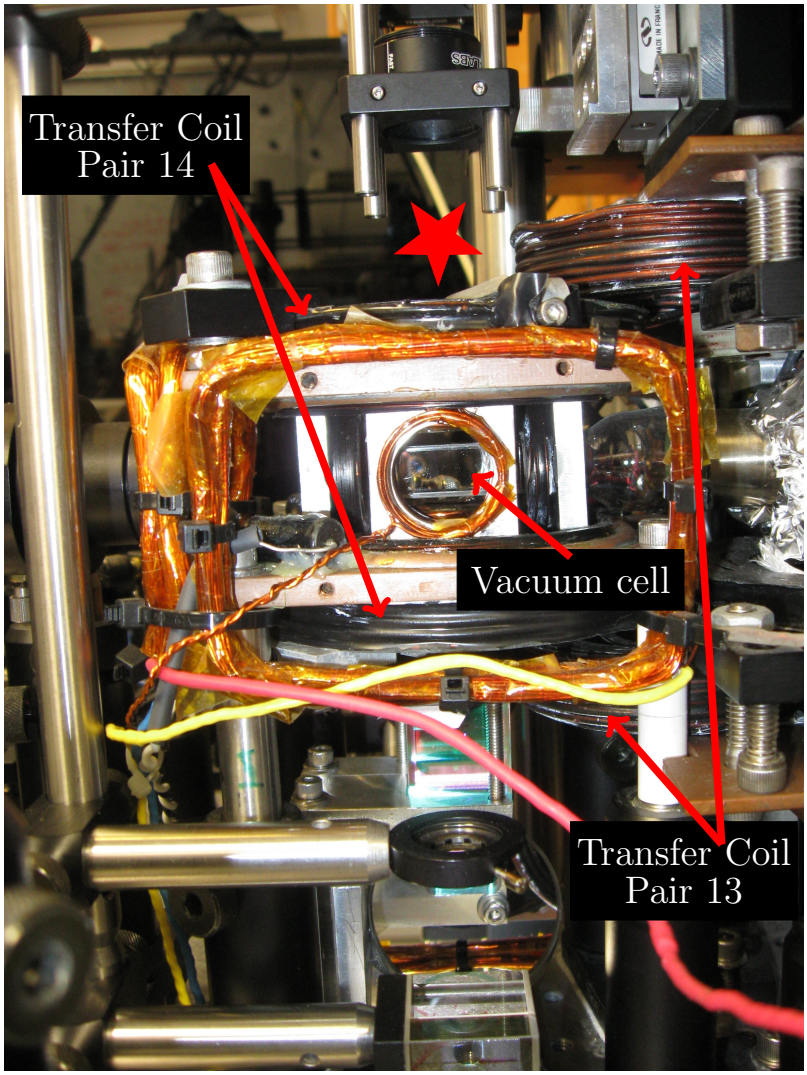


Figure 8.1: BEC cell and surrounding magnetic field coils. The space limitations are due to transfer coil pair 13 which constrains the outer diameter of the objective lens housing and the copper plates used to mount transfer coil pair 14 which put a lower limit on the working distance of the objective lens. The red star marks the approximate location for the objective lens.

wine, that gets better and better with age.

### 8.1.1 Optics terminology

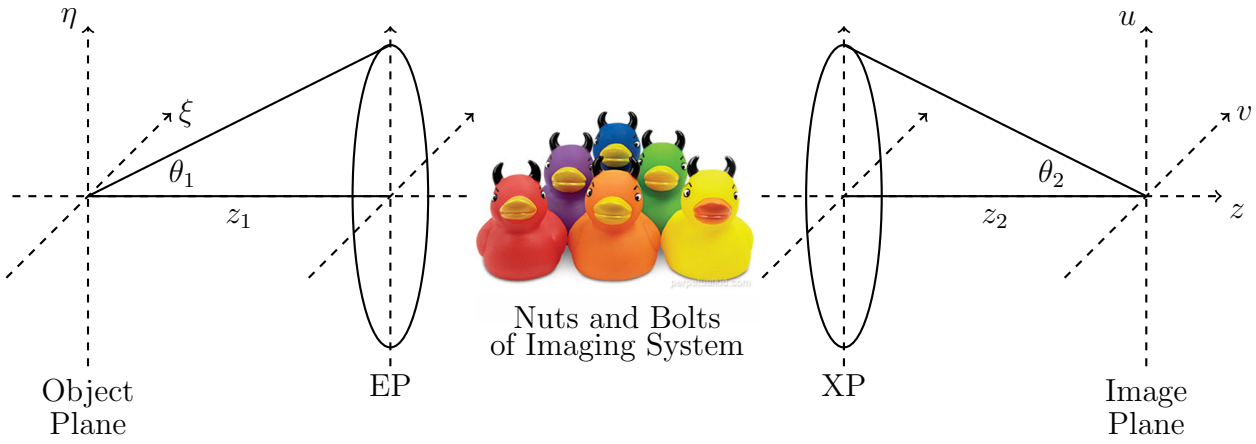


Figure 8.2: Diagram of a generic imaging system.

The primary metric for characterizing a microscope objective is its numerical aperture (NA) which 'is defined in object space as the half-angle of the accepted input ray bundle' [84]. Mathematically,

$$\mathrm{NA} = n \sin \theta_1 \tag{8.1}$$

where $n$ is the index of refraction, and $\theta_1$ is the half-angle that defines the cone of light that enters the optical system as shown in Fig. 8.2. The larger the NA, the higher the resolution of the imaging system. In physical optics, diffraction due to the finite radius of the objective lens results in an impulse-response or point-spread-function (PSF) that has the form of an Airy intensity pattern.

$$I_{\mathrm{Airy}} = I_0 \left( \frac{2J_1(\sigma r)}{(\sigma r)} \right)^2 \tag{8.2}$$

where $\sigma = 2\pi \mathrm{NA}/\lambda$. The Airy pattern has its first zero when $r_{\mathrm{Airy}} = 1.22\lambda/2\mathrm{NA}$

The diffraction-limited resolution of the objective can be estimated from the NA

$$R = \frac{0.61\lambda}{\mathrm{NA}} \tag{8.3}$$

where $\lambda$ is the wavelength of the imaging light. This definition of resolution comes from the criterion that two incoherent point sources are resolvable when the center of the Airy pattern due to the first point source is coincident with the first zero of the Airy pattern due to the second point source. While this definition assumes incoherent point sources, it still provides a useful estimate for the resolution of a microscope objective that utilizes coherent light.

The working distance (WD) is defined as the distance from the front edge of the objective lens to the object plane. In general it is difficult to design an objective with both a high NA and a long WD, although one way around this difficulty is to increase the diameter of the lenses that comprise the objective [85].

The depth of field (DOF) is a measure of the axial deviation from the in-focus object plane over which the system is still diffraction limited. One of the downsides of increasing the NA is the resulting narrower DOF. For a given NA, the DOF can be estimated as

$$\mathrm{DOF} = \frac{n\lambda}{\mathrm{NA}^2}. \tag{8.4}$$

### 8.1.2 Incorporating diffraction in an imaging system

For a given field in the object plane $U_0(\xi, \eta)$, a perfect imaging system produces the ideal image predicted by geometrical-optics

$$U_{\mathrm{g}}(u, v) = \frac{1}{|M|} U_0\left(\frac{u}{M}, \frac{v}{M}\right) \tag{8.5}$$

where $u, v$ are the image plane coordinates, and $\xi, \eta$ are object plane coordinates shown in Fig. 8.2. The ideal image is scaled by the magnification $M = -z_2/z_1$ of the imaging system, where $z_1$ is the distance from the object to the entrance pupil and $z_2$ is the distance from the exit pupil to the image. The distances are absolute values and the explicit negative sign accounts for the inversion inherent in the imaging process. Apologies are due to Greivenkamp in that we have decided to adopt Goodman's sign convention.

Diffraction is introduced due to the finite NA of the imaging system. The effect of diffraction on the resulting image can be determined by convolving the ideal geometrical-optics image $U_{\mathrm{g}}(u,v)$ with the impulse response of the system.

$$U_{\mathrm{i}}(u,v) = \tilde{h}(u,v) \otimes U_{\mathrm{g}}(u,v) \tag{8.6}$$

where the impulse response function is defined as

$$\tilde{h}(u,v) = \int_{-\infty}^{\infty}\int_{-\infty}^{\infty} P(\lambda z_2 \tilde{x}, \lambda z_2 \tilde{y}) e^{-j2\pi(u\tilde{x}+v\tilde{y})} d\tilde{x} d\tilde{y} \tag{8.7}$$

Here $\tilde{x} = x/\lambda z_2$ and $\tilde{y} = y/\lambda z_2$ are scaled coordinates in the plane of the exit pupil. For a diffraction-limited imaging system the impulse response is simply the Fraunhofer diffraction pattern associated with the exit pupil [83]. If we assume a circular aperture, then

$$\tilde{h}(w) = \frac{2J_1(\sigma w)}{\sigma w} \tag{8.8}$$

where $J_1$ is the first-order Bessel function of the first kind, $w = \sqrt{u^2+v^2}$ is the radial coordinate in the image plane, and $\sigma = 2\pi \mathrm{NA}_{\mathrm{img}}/\lambda$. $\mathrm{NA}_{\mathrm{img}} \sim R_{\mathrm{XP}}/z_2$ is the numerical aperture of the system in the image plane, where $R_{\mathrm{XP}}$ is the radius of the exit pupil of the imaging system, and $z_2$ is the distance from the exit pupil to the image plane.

We make one last comment regarding imaging with coherent versus incoherent light. When imaging with coherent light, the impulse response is linear for the propagation of the field, so we convolve the Airy field pattern $\tilde{h}(u,v)$ defined in Eqn. 8.8 with the ideal field in the image plane $U_{\mathrm{g}}(u,v)$. When imaging with incoherent light the impulse response is linear for intensity, so we would convolve the Airy intensity pattern $|\tilde{h}(u,v)|^2$ with the ideal intensity in the image plane $I_{\mathrm{g}}(u,v)$.

## 8.2 Objective design constraints

Critical to the implementation of the QVM2 was the design and implementation of a low cost, custom microscope objective. The custom microscope objective had to meet the

following design constraints in order to enable *in situ* imaging of vortex distributions and fit within the physical constraints of the BEC apparatus.

1. The numerical aperture needed to be greater than NA = 0.25 in order to resolve cores separated by approximately 2 $\mu$m. In simulations of turbulence using our experimental parameters, vortex cores are found to have a minimum separation distance of approximately 2 $\mu$m [22].

2. The working distance needed to be greater than WD = 23 mm due to the existing framework of copper plates and magnetic field coils surrounding the BEC cell, shown in Fig. 8.1.

3. The OD had to be less than 30 mm due to the placement of transfer coil pair 13 shown in Fig. 8.1, and the expansion coil which has an inner diameter (ID) of 39 mm.

4. The BEC is imaged through the 1.0-mm thick pyrex wall of the vacuum cell. The design needed to account for spherical aberrations introduced by the pyrex.

5. The rear focal plane of the objective needed to be located outside of the lens housing to avoid any extra aberrations due to relay lenses such as those used in the QVM1 described in Chapter 6.

6. The objective needed to be optimized for 780-nm imaging light, both in terms of minimizing spherical aberrations, and maximizing transmission. Ideally it should have an anti-reflection (AR) coating that covers both 780-nm and 660-nm light.

7. The budget for the project was on the order of $2,000, considerably less than the $30,000 or more required to purchase a commercial custom-designed objective.

From an optics perspective, an NA of 0.25 is fairly low. The difficultly for our imaging system lies in integrating the optics into the existing framework of magnetic field coils, and

achieving NA $\sim$ 0.25 within the limits of a long working distance and a maximum lens diameter of approximately 25 mm. A common method to compensate for the long-working distance while maintaining a large NA is to increase the diameter of the lenses, which was not a solution available to us [85].

## 8.3 Zemax assisted design

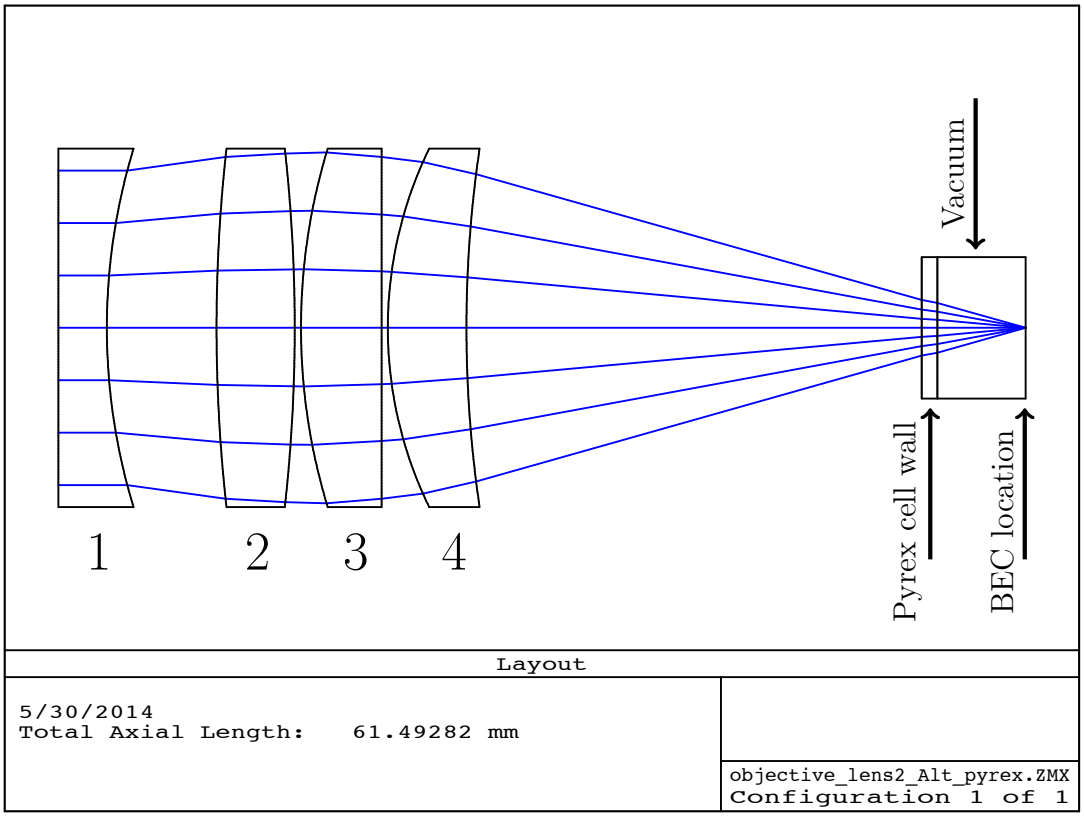


Figure 8.3: Objective lens layout from Zemax model. Numbered lenses correspond to the four lenses listed below.

We used Zemax to modify an existing design for a diffraction-limited, long working distance objective with NA $\sim$ 0.25 [81] This design uses the four LENS-Optics catalog lenses listed below [86], and arranged according to the layout shown in Fig. 8.3. All lenses

are have an AR coating over the range $\lambda$ = 650 - 1100 nm.

1. plano-concave lens with R = 39.08 mm
2. double-convex lens with R1 = R2 = 103.29 mm
3. plano-convex lens with R = 39.08 mm
4. positive meniscus lens with R1 = 26 mm and R2 = 78.16 mm

The objective was originally designed for imaging through a 5-mm thick silica window with a wavelength $\lambda$ = 852 nm [81]. Our modification of the original objective takes into account the 1-mm thick pyrex wall of the vacuum chamber, the approximate sag position of the BEC, and the wavelength of the imaging light, using the RMS spot size as our primary optimization metric. We set up a model in Zemax using the lenses listed above, sent a collimated beam backwards through the objective as shown in Fig. 8.3 and varied the distance between the optical elements to minimize the focused RMS spot size at the BEC location. In particular, the distance between lenses 2 and 3 in Fig. 8.3 was decreased from 8.20 mm in the original design to 6.975 mm in our design, and the distance between lens 4 and the vacuum cell wall was increased from 21.55 mm to 28.948 mm. Most discrepancies between our design parameters and actual distances, such as the BEC location with respect to the pyrex cell wall, can be accounted for by adjusting the distance between the entire lens group and the vacuum cell wall. The upper left spot diagram in Fig. 8.4 shows the spot diagram given optimized lens spacings and an on-axis beam with no tilt or decentering, in other words, the best possible spot diagram. The other three spot diagrams show the aberrations that occur as the angle of incidence of the collimated beam is increased from 0.0° to 0.4°, although for the small angles shown the aberrations lie within the Airy radius so we do not expect to be able to resolve them.

Our Zemax model, with the lens separations listed in Table 8.1, results in a microscope objective with a focal length of 36.7 mm, a theoretical diffraction-limited spot size of 1.75

Table 8.1: Surface data summary (Zemax)

| Surface | Radius (mm) | Thickness (mm) | Material | Lens Diameter (mm) | Comment |
|---|---|---|---|---|---|
| Object | $\infty$ | $\infty$ | - | - | input beam |
| Stop | $\infty$ | 3.080 | BK7 | 20.0 | lens 1 - front |
| 2 | 39.08 | 6.975 | - | 22.8 | back / air |
| 3 | 103.29 | 4.970 | BK7 | 22.8 | lens 2 - front |
| 4 | -103.29 | 0.400 | - | 22.8 | back / air |
| 5 | 39.08 | 5.120 | BK7 | 22.8 | lens 3 - front |
| 6 | $\infty$ | 0.400 | - | 22.8 | back / air |
| 7 | 26.00 | 5.000 | BK7 | 22.8 | lens 4 - front |
| 8 | 78.16 | 28.948 | - | 22.8 | back / air |
| 9 | $\infty$ | 1.000 | Pyrex | 9.0 | cell wall front |
| 10 | $\infty$ | 5.600 | Vacuum | 9.0 | back / vacuum |
| Image | $\infty$ | - | - | - | BEC location |

$\mu$m at $\lambda = 780$ nm, a theoretical numerical aperture of 0.26, working distance of 35.6 mm, and back focal distance of 20.2 mm.

We combined the objective with an $f = 400$ mm achromat (Thorlabs AC508-400-B) to form a simple diffraction-limited imaging system as shown in Fig. 8.5, with the system stop assumed to be the final surface of the objective lens with an aperture of $r = 10$ mm. Figure 8.6 shows the spot diagrams in the image plane of the QVM2 for various off-axis point objects. Looking at the lower-left spot diagram, an object can be off-axis by 200 $\mu$m and the image will still be contained within the Airy radius. With an on-axis object, the tube lens can be translated off-axis by 10 mm with minimal effect on image quality. The placement of the objective is much more sensitive; it can be moved off-axis up to approximately 200 $\mu$m before the coma is visible beyond the radius of the Airy disk.

## 8.4 Manufacture of the objective

Using the catalog lenses from LENS-Optics, the same company that supplied the lenses for the original objective [81], made modification of the design fairly trivial. For our modified design, LENS-Optics did the final calculation of the lens separations, as well as

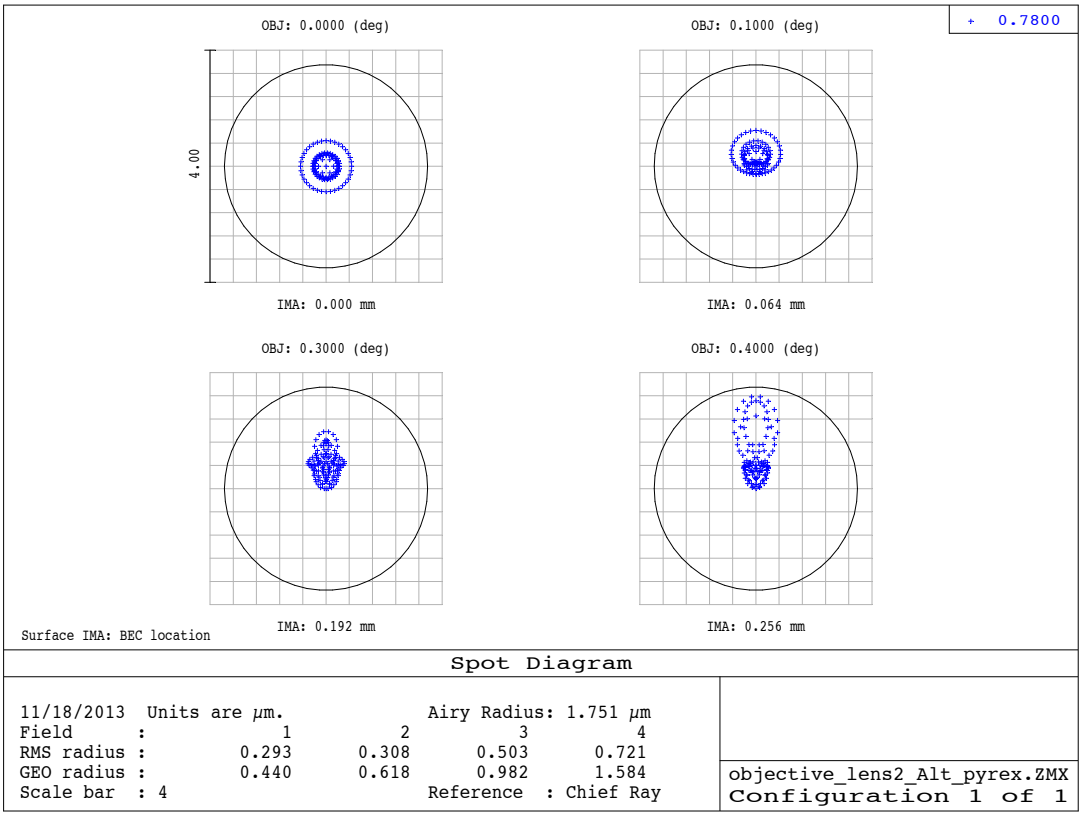


Figure 8.4: Spot diagrams for the objective lens calculated in Zemax using $\lambda = 780$ nm. Note that the rays fall well within the Airy radius of 1.75 $\mu$m.

the actual mounting of the lenses for the relatively low cost of approximately $1,300 USD. The optics were mounted in a lens tube with an OD of 30 mm. Spacer rings were used to separate the lenses by the desired distances. Refer to Fig. 8.7 for a diagram of the mounted lenses provided by LENS-Optics. The one downside to using a German company involved incompatibility between metric and imperial systems; all of Thorlabs components that claim to be compatible with lens tubes with OD = 30 mm are actually designed for OD = 30.5 mm lens tubes. This slight difference in OD meant that we needed to machine a custom collar for our objective lens that allowed it to interface with the Thorlabs cage system used for the framework of the QVM2.

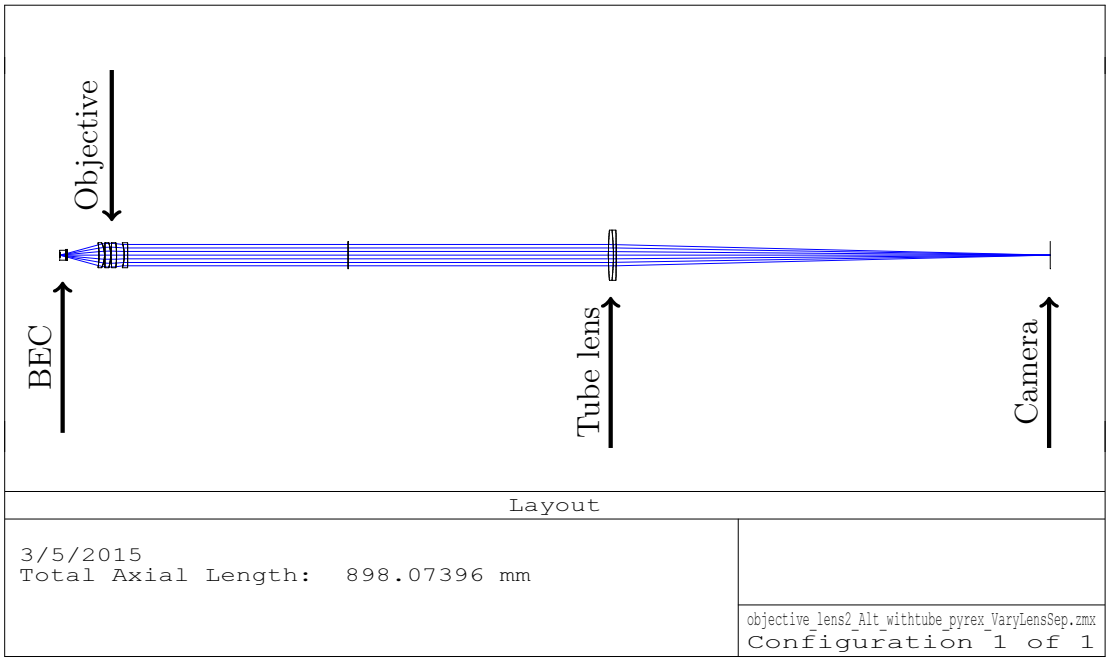


Figure 8.5: Optical layout for the QVM2 - Zemax

## 8.5 Offline tests of the QVM2

Prior to integrating the QVM2 into the BEC apparatus, we did a series of offline tests similar to those performed with QVM1 and described in Chapter 6. We measured the transmission at $\lambda = 780$ nm to be 88%, and determined that the objective is able to resolve the smallest features on our United States Air Force (USAF) resolution test target corresponding to a width of 2.19 $\mu$m, and center-to-center separation of 4.38 $\mu$m, as shown in Figs. 8.8 and 8.9. For the offline tests of the QVM2, we used an $f = 400$ mm achromat (Thorlabs AC508-400-B) for the tube lens, a 1-mm thick microscope slide in place of the pyrex vacuum cell wall, and a USAF resolution test target as a test object, as shown in Fig. 8.8. Images were acquired with a Point Grey Firefly MV CMOS camera with $6 \times 6$-$\mu$m square pixels.

The features associated with group 6, elements 1-6 of the USAF test target, were

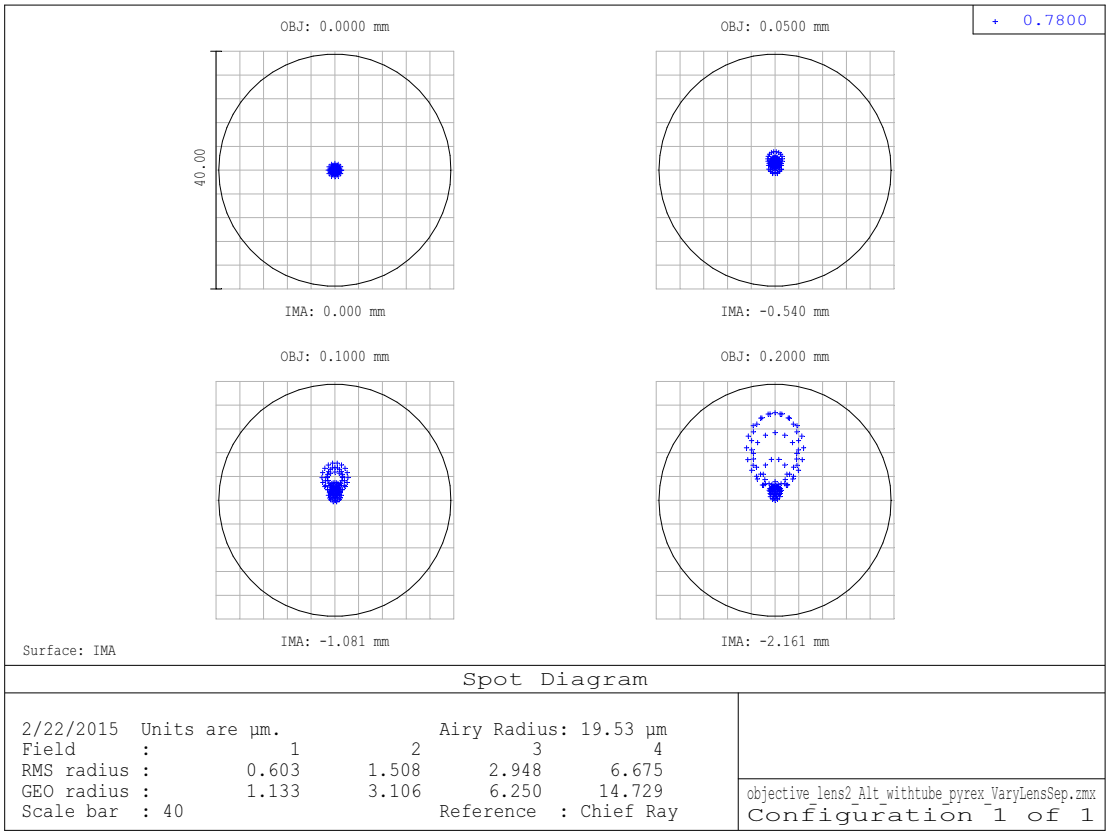


Figure 8.6: Spot Diagrams for the QVM2 - Zemax. The circle shows the Airy radius of 19.53 $\mu$m in the image plane. The upper left spot diagram corresponds to an on-axis object. As shown in the lower right spot diagram, an object located off-axis by up to 200 $\mu$m still resides within the Airy radius.

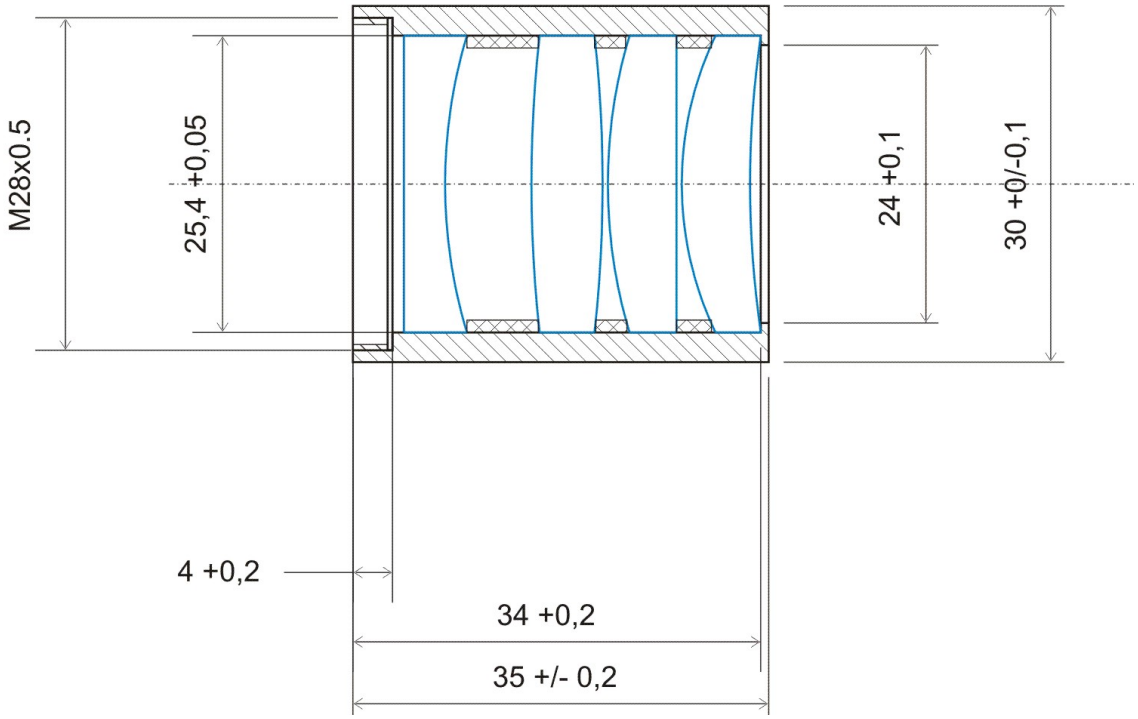


Figure 8.7: Diagram of lenses mounted in a lens tube with an OD of 30 mm. Diagram was provided by LENS-Optics. Lenses are outlined in blue.

used to calculate the magnification of the offline QVM2 to be $M = 11.4 \pm 0.5$. $M$ was calculated by fitting a set of three sinc functions to each bar triplet, taking the ratio of the separation between the fitted sincs to the known center-to-center bar separation for each triplet, and then averaging the six calculated magnifications. The uncertainty was determined by assuming an error of one 6-$\mu$m pixel-width in the fit to center-to-center bar separation.

### 8.5.1 Depth of field measurement

We measured the DOF of the QVM2 by moving the test target with respect to the objective along the imaging axis to locate the range over which the smallest test target features were

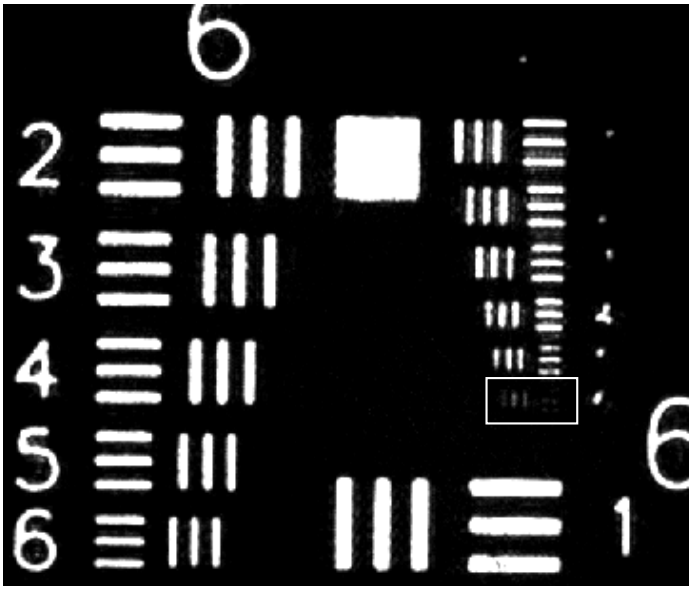


Figure 8.8: USAF resolution test target imaged with the offline mockup of the QVM2. The image shows groups 6 and 7 with the smallest visible features, marked by the white box, corresponding to group 7 element 6. The image was taken with a Point Grey Firefly CMOS camera with 6 x 6-$\mu$m pixels. The features associated with group 6, elements 1-6, were used to calculate the magnification of the offline QVM2 to be $M = 11.4 \pm 0.5$. $M$ was calculated by fitting a set of three sinc functions to each bar triplet, taking the ratio of the separation between the fitted sincs to the known center-to-center bar separation for each triplet, and then averaging the six calculated magnifications. The uncertainty was determined by assuming an error of one 6-$\mu$m pixel-width in the fit to center-to-center bar separation.

resolvable. Group 7, element 6, the smallest feature on our USAF test target, is clearly resolved for $\Delta z = \pm 5$ $\mu$m from the optimal focus position as shown in Fig. 8.9. This feature consists of bars of width 2.19 $\mu$m with a center-to-center separation of 4.38 $\mu$m. Note that while the vertical bars in Fig. 8.9 look much cleaner and better resolved than the horizontal bars, we believe this is a feature of the test target rather than an asymmetry in resolution of the imaging system since rotating the target by 90° in the object plane results in a higher quality image of the horizontal bars and a reduction in the image quality for the vertical bars. Images of the USAF test target taken with the QVM2 objective show similar

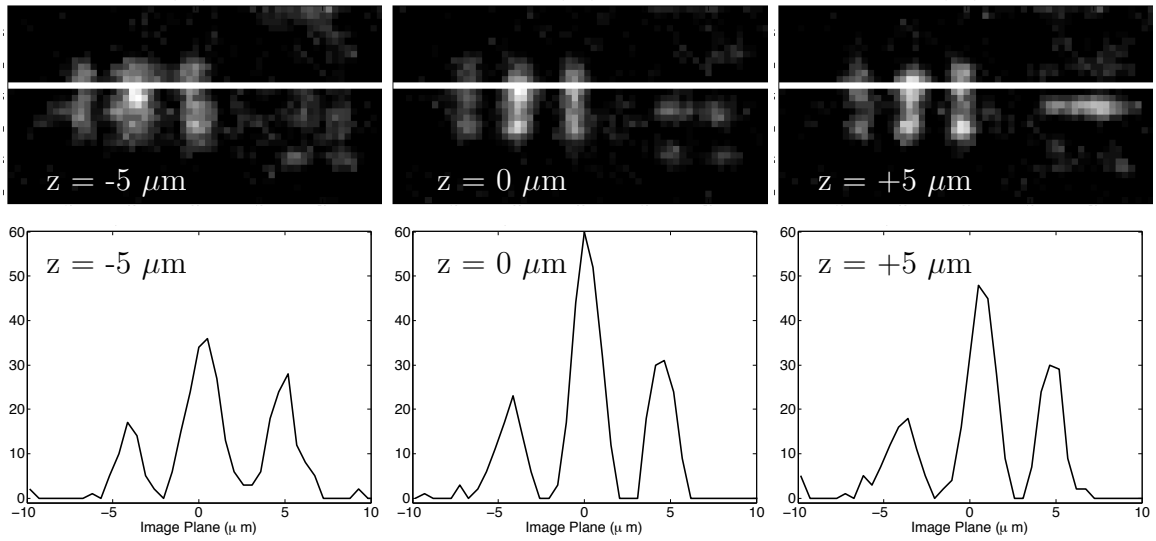


Figure 8.9: DOF measurement for the QVM2 microscope objective. z = 0 $\mu$m corresponds to the best focus position. Each panel in the top row represents a 360 x 180-$\mu$m region in the camera (image) plane. Each image shows group 7, element 6 of the USAF resolution test target, the feature enclosed in the white box in Fig. 8.8. This pattern consists of bars of width 2.19 $\mu$m with a center-to-center separation of 4.38 $\mu$m. The bottom row shows cross sections along the white line shown in the corresponding panel in the top row.

resolution to those taken with the Olympus microscope objective described in Chapter 6, at least to the limits of our test target. As expected, stopping down the objective aperture, effectively reducing the NA of the objective, increases the DOF at the expense of resolution.

### 8.5.2 Pinhole

To estimate the impulse response, or point spread function (PSF), of the QVM2 we imaged a pinhole with a 1-$\mu$m radius using the imaging system shown in Fig. 8.5. As described in Sec. 8.1.2, the field $U_{\mathrm{i}}(w)$ associated with the pinhole image at the camera plane is determined by the convolution of the pinhole aperture $U_0(\rho)$ with the impulse response of the imaging system. For an ideal diffraction-limited imaging system imaged with coherent light, the impulse response should be the Airy field pattern associated with the exit pupil

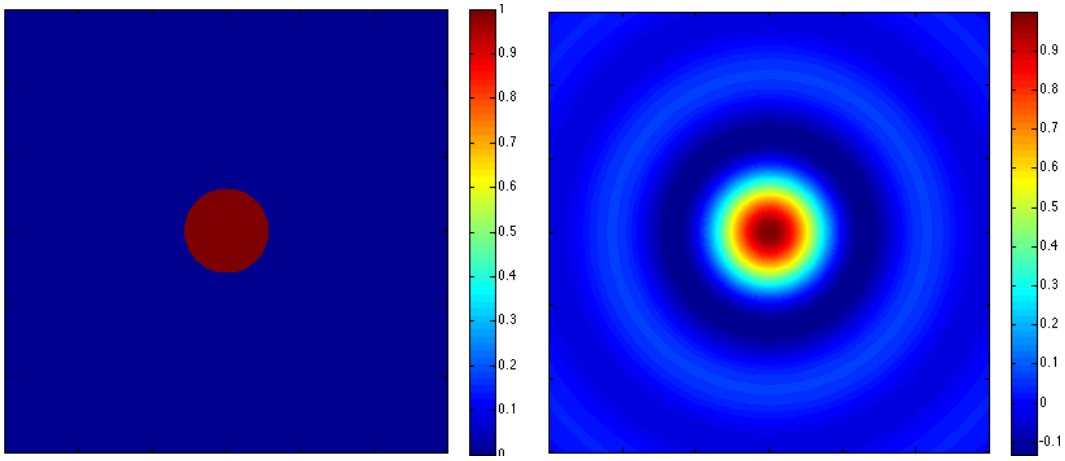

(a) Pinhole ideal image - image plane

(b) Airy field pattern - $R_{\text{Airy}} = 19.53$ $\mu$m

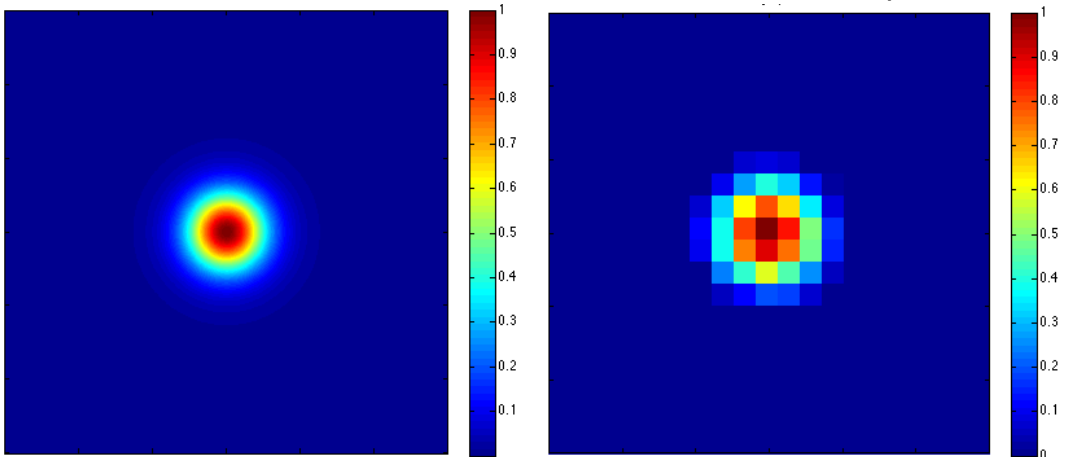

(c) Convolution - image plane

(d) Actual image of pinhole

Figure 8.10: Pinhole PSF test. We imaged a 1-$\mu$m radius pinhole to experimentally characterize our PSF. Each image is 120 x 120-$\mu$m in the image plane. (a) Ideal geometrical-optics image field profile $U_{\text{g}}(u,v)/U_{\text{g,max}}$ of the pinhole using $M = 11.4$. (b) Field impulse response function $U_{\text{Airy}}(u,v)/U_{\text{Airy,max}}$ assuming a diffraction-limited imaging system constrained by the circular aperture of the exit pupil. The Airy field pattern was calculated using $R_{\text{Airy}} = 19.53$ $\mu$m from our Zemax model of the QVM2. (c) Predicted intensity profile $I_{\text{i}}(u,v)/I_{\text{i,max}}$ for the pinhole in the image plane calculated by convolving the ideal pinhole image field profile with the field impulse response function and then taking the modulus squared of the convolved field profile. (d) Actual intensity profile for the pinhole image taken with a Point Grey Firefly MV CMOS camera with 6 x 6-$\mu$m square pixels.

aperture of the imaging system given in Eqn. 8.8. From our Zemax model we estimate $\mathrm{NA}_{\mathrm{img}} = 0.0252$, and $R_{\mathrm{Airy}} = 19.53$ $\mu$m.

Table 8.2: HWHM for various approximations of the pinhole image.

| **Method** | **HWHM** |
|---|---|
| 2D Gaussian fit to image ($\sigma_{\mathrm{x}} = \sigma_{\mathrm{y}}$) | 10.59 $\mu$m |
| 2D Airy intensity pattern fit to image | 11.24 $\mu$m |
| Use Fresnel diffraction integral to propagate through imaging system | 9.06 $\mu$m |
| 2D convolution of pinhole and Airy intensity pattern | 10.92 $\mu$m |
| 2D convolution of pinhole and Airy field pattern | 8.76 $\mu$m |

Table 8.2 lists methods of characterizing the pinhole image and the resulting half width at half maximum (HWHM) in the image plane. If we had a sub-micron point source then we might expect that the 2D Airy intensity pattern (PSF) would be a good fit to the actual image. However, the spatial extent of our 1-$\mu$m-radius pinhole is sufficiently large that we need to consider the convolution of the field PSF with the ideal geometrical-optics pinhole image as described in Sec. 8.1.2. The convolution acts to wash out the lobes of the Airy pattern as shown in Fig. 8.10. For the convolutions we calculated $U_{\mathrm{g}}(u, v)$ using $M = 11.4$ as measured with the USAF air force target and the offline imaging system, and $\tilde{h}(u, v)$ using $\sigma = 1.22\pi/R_{\mathrm{Airy}}$. All reported HWHM are calculated from the radial intensity profile $I(r)$ in the image plane. For the case of numerically propagating the field through the imaging system, we used a method similar to that described in Chapter 7, using an $f = 36$ mm objective and an $f = 400$ mm tube lens. The 2D convolution of the pinhole and Airy field pattern most closely matched the numerics, while the convolutions of the intensities provided the best fit to the actual image, as shown in Figs. 8.12 and 8.13.

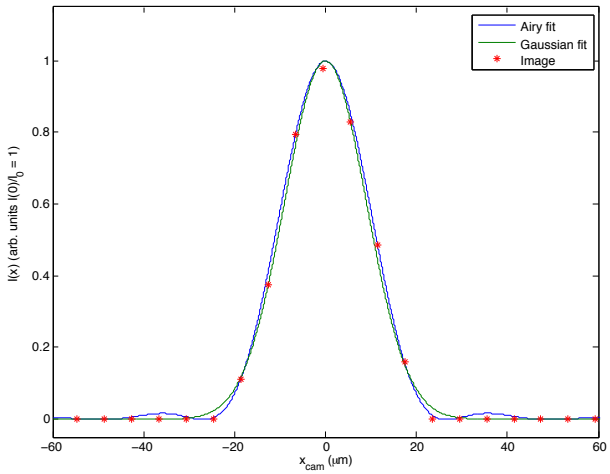


Figure 8.11: Cross sections of intensity profiles for the image of the $r = 1$ $\mu$m pinhole. Red asterisks denote pixel values from the actual image. The blue plot is a cross section of the 2-D Airy intensity pattern that best fits the measured intensity profile. The green plot is a cross section of the 2-D Gaussian that best fits the measured intensity profile. Each intensity is scaled by $I_{\max}$ and plotted versus distance in the image plane.

### 8.5.3 Nanofiber

We used the QVM2 to image the nanofiber described in Chapter 6 in order to compare the performance of the QVM2 to that of the QVM1. Unlike the $D = 2$ $\mu$m pinhole with its hard aperture and radius larger than the diffraction limit of the imaging system, the $D \sim 500$ $\mu$m nanofiber provides a submicron phase object of approximately the same size as a vortex. Figure 8.14 shows images of the nanofiber taken with the QVM2. The right column of Fig. 8.14 shows 60 x 40-$\mu$m panels with the nanofiber, and the left column contains cross sections along the white line shown in the corresponding panel. The relative signal ratio (RSR) is a measure of the magnitude of the signal to the noise in the image. In particular, $RSR$ is the average of all the $RSR_{\text{cross}}$ values calculated for individual cross sections perpendicular to the nanofiber orientation. $RSR_{\text{cross}} = |I_{\text{sig}} - \bar{I}_{\text{BG}}|/\sigma_{\text{BG}}$, where $I_{\text{sig}}$ is the pixel value at the peak of the nanofiber signal, $\bar{I}_{\text{BG}}$ is the average pixel value, and $\sigma_{\text{BG}}$ is the standard deviation. When calculating $\bar{I}_{\text{BG}}$ and $\sigma_{\text{BG}}$, the 14 pixels on either side

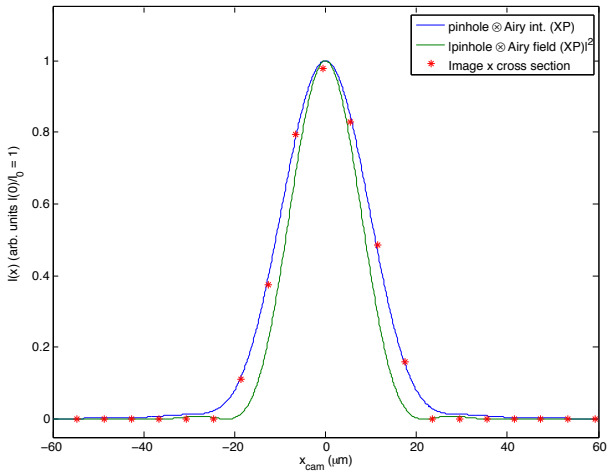


Figure 8.12: Cross sections of intensity profiles for the image of the $r = 1$ $\mu$m pinhole. Each intensity is scaled by $I_{\max}$ and plotted versus distance in the image plane. Red asterisks denote pixel values from the actual image. The blue plot is the convolution of the ideal pinhole intensity profile with the Airy intensity pattern. The green plot is the intensity profile calculated by first convolving the ideal pinhole field profile with the Airy field pattern and then calculating the intensity from the convolved field profiles. The intensity profile determined from convolving the fields underestimates the actual pinhole size leading us to suspect that the actual resolution of the imaging system is larger than that predicted by our Zemax model.

of the signal peak are not used. We suspect that the $RSR = \infty$ reported for Fig. 8.14(b) and (e) are due to the limited dynamic range of the Firefly camera, but report the values because they still indicate a low noise floor and a much better $RSR$ than the bright-field images shown in Fig. 8.14(a) and (c).

To enable a more direct comparison to the QVM1, we calculated the FWHM of the nanofiber from the images in Fig. 8.14(d) and (e) to be 1.59 $\pm$0.16 $\mu$m and 1.36 $\pm$0.11 $\mu$m respectively. These images were taken with a $\lambda = 660$ nm probe beam and mask diameters of 370 $\mu$m and $\sim 1$ mm respectively. The FWHMs were calculated by fitting to each cross section of the nanofiber and then averaging all fits with a root-mean-square-error (RMSE) less than two. Here the reported error incorporates the error in the calculation of $M$ and the standard deviation of all FWHM fits included in the average. For comparison, the FWHM

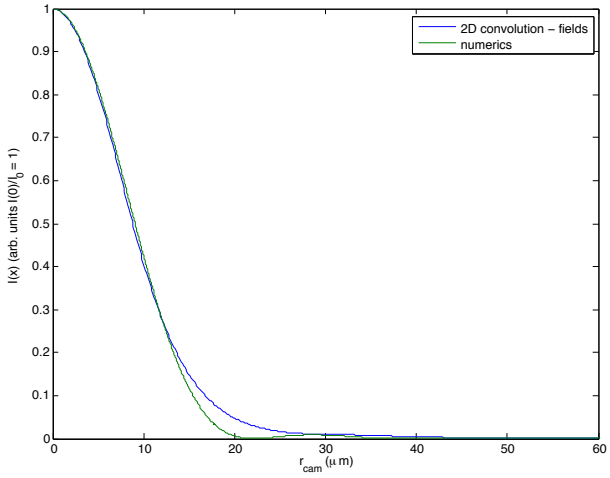


Figure 8.13: Cross sections of intensity profiles generated by numerical propagation of the field due to a $r = 1$ $\mu$m pinhole. Each intensity is scaled by $I_{\max}$ and plotted versus distance in the image plane. The green plot is the intensity profile from the Fresnel diffraction numerics. The blue plot is intensity profile calculated by first convolving the ideal pinhole field profile with the Airy field pattern and then calculating the intensity from the convolved field profiles.

of the nanofiber imaged with the QVM1 and a wire mask with a diameter of 370 $\mu$m, had a FWHM of $1.18 \pm 0.03$ $\mu$m (based on the single cross section shown in Fig. 6.2, with reported error including error in magnification). Note that the FWHM values reported here are a measure of the PSF of the imaging system, either the QVM1 or the QVM2, and not the actual size of the nanofiber. For an imaging system with NA $\sim 0.25$ we expect a theoretical FWHM of 1.36 $\mu$m. As expected the FWHM of the nanofiber signal decreases as we increase the mask size and filter out more of the low frequency signal.

The mask sizes and corresponding spatial cutoff frequencies do not translate directly between the $M \sim 20$ and $M \sim 11$ imaging systems. This is mostly due to the differences in the objective lenses. The $M \sim 20$ imaging system employs an infinite conjugate Olympus SLMPLN 20X microscope objective with an effective focal length of 9 mm. While the commercial objective is a black box to us for obvious intellectual property reasons, the rear aperture of the lens housing with a radius of approximately 2.5 mm places an upper

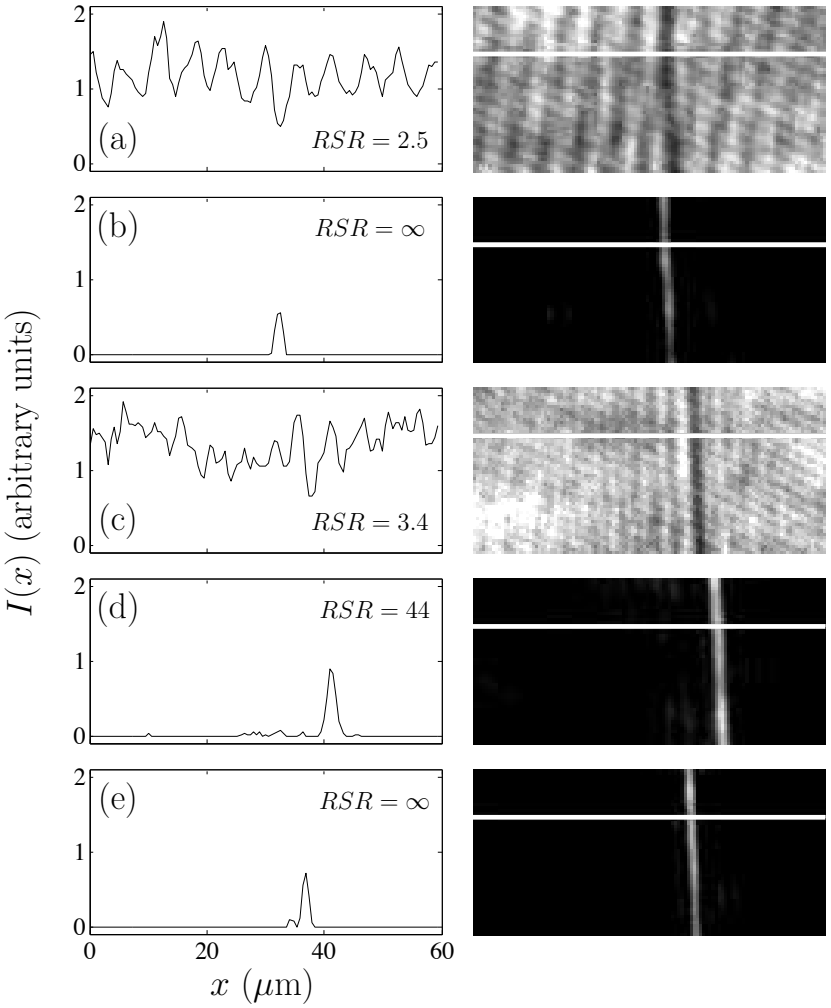


Figure 8.14: Nanofiber images taken with the offline mockup of the QVM2. Panels on the right are images of the nanofiber representing 60 x 40-$\mu$m in the object plane ($M = 11.4$). Cross sections on the left are 60 $\mu$m in the object plane along the white line shown in the each corresponding panel on the right. (a) Bright-field image with probe wavelength $\lambda = 780$ nm. (b) Corresponding dark-field image taken with $\lambda = 780$ nm, using a wire mask with a diameter of 370 $\mu$m. (c) Bright-field image with probe wavelength $\lambda = 660$ nm. (d) and (e) Corresponding dark-field image taken with $\lambda = 660$ nm, using a wire mask with $D = 370$ $\mu$m and a circular mask with $D \sim 1$ mm respectively. Bright field images were taken with an exposure time of 0.125 ms. Dark-field images were taken with an exposure time of 1.25 ms. See text for a discussion of the $RSR$.

bound on the physical extent of a collimated beam exiting the objective. Since we are working with an infinite-conjugate objective we can use this upper bound to estimate the radial position in the Fourier plane of the highest spatial frequencies that can be collected by the microscope objective. With the same reasoning, our custom objective used for the $M \sim 11$ imaging system has a rear aperture, in this case the actual system stop, with a radius $r_{\text{stop}} = 10$ mm, about a factor of four times larger than the rear aperture of the Olympus objective. Therefore we estimate that the mask sizes corresponding to a given spatial cutoff frequency should also scale by a factor of about four and we expect the 370-$\mu$m diameter mask used with the $M \sim 20$ imaging system to provide more spatial filtering than the 1-mm diameter mask used with the $M \sim 11$ imaging system, meaning that the larger FWHM reported for the QVM2 may be partly explained by the difference in spatial filtering between the two imaging systems.

### 8.5.4 Summary of offline tests

In summary, in our offline characterization of the QVM2 we found $M = 11.4 \pm 0.5$, and estimate the depth of field to be DOF $= \pm 5$ $\mu$m. The QVM2 is capable of resolving the smallest features on our USAF resolution test target corresponding to bars with a width of 2.19 $\mu$m and center-to-center separation of 4.38 $\mu$m. Further tests of the PSF of the QVM2 involved imaging a 2-$\mu$m-diameter pinhole and an approximately 500-nm-diameter nanofiber. We fit a Gaussian to the pinhole intensity profile and measured the HWHM to be 11.6 $\mu$m, approximately 20% larger than the HWHM predicted by convolution of the Airy field pattern associated with the QVM2 exit pupil and the perfect pinhole image. This suggests that the actual diffraction limited resolution of the imaging system is approximately 20% larger than the 1.8 $\mu$m predicted with our Zemax model.

Lastly, we compared the QVM1 and the QVM2 by imaging a 500-nm diameter nanofiber in dark-field with varying mask sizes. We measured the FWHM of the nanofiber to be $1.18 \pm 0.03$ $\mu$m using the QVM1 and a $D_{\text{mask}} = 370$ $\mu$m dark-field mask. With the QVM2,

we measured the FWHM of the nanofiber to be $1.59 \pm 0.16$ $\mu$m using $D_{\text{mask}} = 370$ $\mu$m, and $1.36 \pm 0.11$ $\mu$m with $D_{\text{mask}} \sim 1$ mm. The nanofiber images were taken using a 660-nm laser. For reference the theoretical limit on the resolution of the imaging system estimated by the FWHM of the Airy intensity pattern for an imaging system with NA $\sim 0.25$ and $\lambda = 660$ nm is 1.36 $\mu$m. As discussed in Chapter 6, the dark-field technique can do better than the theoretical resolution limit of the imaging system due to filtering of the low frequency signal. It is unclear if the larger nanofiber FWHM reported for the QVM2 are due to using effectively smaller masks, or if they represent a fundamental difference between the PSFs associated with the QVM1 and the QVM2. In any case, the QVM2 with our custom microscope objective seems to provide comparable image quality to the QVM1 employing the commercial Olympus objective.

## 8.6 Mechanical components of the QVM2

The framework of the QVM2 is a Thorlabs cage system shown in Figs. 8.15 and 8.16. Integrating the microscope objective required the construction of a custom mount shown in Fig. 8.17. Sub-micron control of the vertical position of the microscope objective is provided by a $z$-axis translation stage (Newport UMR3.5) with a differential micrometer (Newport DM11-5) with a fine adjust sensitivity of 0.1 $\mu$m. The $z$-axis translation stage is mounted onto a 4 x 6 x 0.5-in breadboard (Thorlabs MB4) with a baseplate (Newport M-PBN3). Horizontal translation of the microscope objective is provided by an $x$-$y$ translator that couples with a 60-mm cage system (Thorlabs CXY2). We machined the plate used to couple the $x$-$y$ translation cage mount with the $z$-axis translation stage, and a custom adapter that allows the 30-mm OD objective to interface with the $x$-$y$ translation stage. In addition, we machined the mirror mount shown in Fig. 8.18 which incorporates a turning mirror, PBSC and quarter-wave plate into a single element that fits below the BEC cell and directs the imaging probe beam upwards through the BEC cell. Figure 8.19 shows the various beam paths through the QVM2, including the imaging probe beam and the

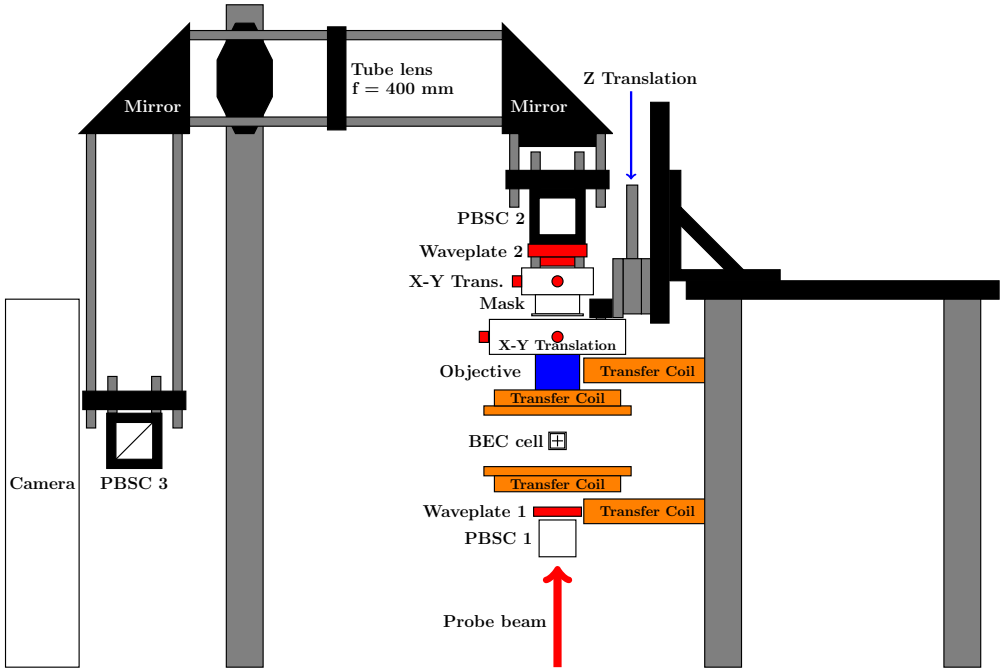


Figure 8.15: Layout of the QVM2 - side view.

660-nm beams used for stirring.

## 8.7 Implementation and alignment

The initial alignment was done with the original $M \sim 5$ imaging system still in place below the BEC cell. Prior to placing the QVM2 objective or tube lens, a 660-nm laser beam was directed backwards through the cage system and an $f = 75$ mm lens was used to focus the 660-nm beam in the plane of the BEC. The entire cage system was then translated in the horizontal plane (lab frame) until the 660-nm guide beam was positioned at the BEC location. Unfortunately in the development of the new Pixis control software, the images

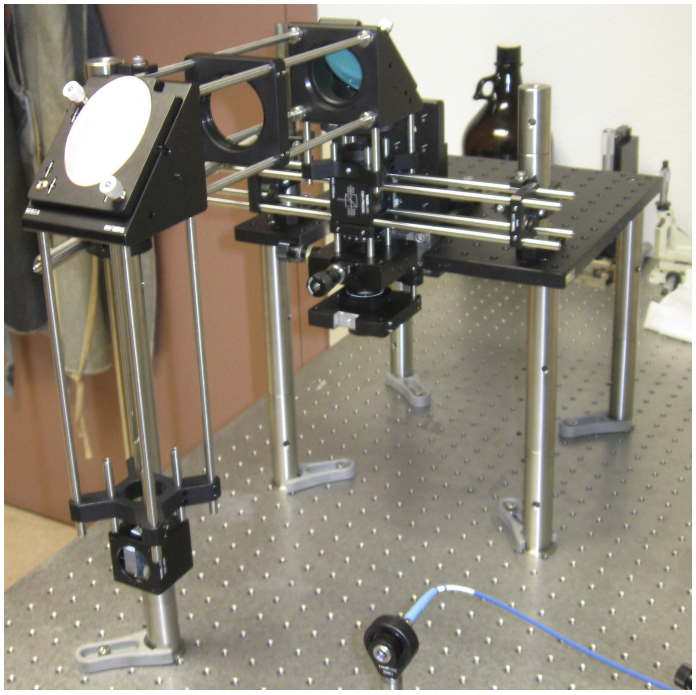

Figure 8.16: Photograph of the QVM2 - side view.

acquired via FocusProfile and those acquired with CaptureFrames were transposed with respect to each other meaning that while we thought we positioned the system to bore-sight the BEC we were off by about 500 $\mu$m. This can be corrected either by translating the microscope objective in the $x$-$y$ plane (lab frame) or by translating the BEC. We should note that in our Zemax model bore-sighting the objective is critical to minimize aberrations, but moving the tube lens off-axis by as much as 10 mm does not have a significant effect. It is possible that this initial misalignment may account for some of our difficulty in observing vortex cores.

## 8.8 Initial focusing efforts

Initial coarse attempts at focusing involved stepping the objective lens vertically and looking for the traditional BEC lensing defocus effects [44]. The edges of the range $\Delta z = 600$ $\mu$m

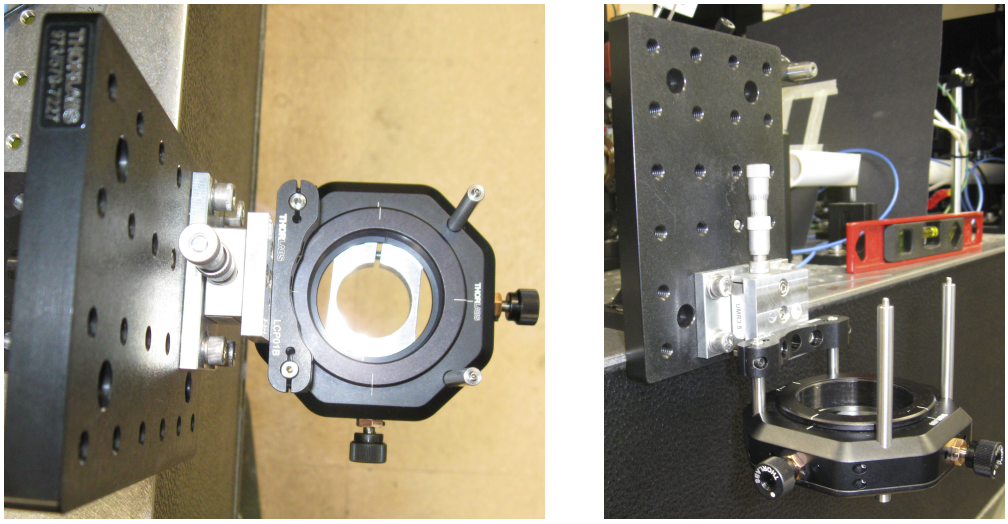

(a) Top View (b) Side View

Figure 8.17: Custom objective mount.

with no clear out of focus features were identified, and the objective was placed in the center of this range at $z = 3.30$ mm, with $z$ measured on the coarse micrometer for the z-axis translation stage. During the coarse focusing, the vertical position of the BEC as measured with the horizontal phase-contrast imaging system and the Pixis CCD camera was 280 pixels, with the camera $z$-axis micrometer set at 8.00 mm.

Attempts at fine-tuning the focus of the objective involved imaging vortex dipoles after a short ($t < 10$ ms) period of expansion, and *in situ* imaging of a vortex lattice as described in Chapters 6 and 9. However, both of these test targets resulted in a relatively large range $\Delta z \sim 50 - 100$ $\mu$m over which cores could be resolved, much larger that the measured $\pm 5$-$\mu$m DOF for features of a size on the order of 2 $\mu$m as described in Sec. 8.5.1. We did notice that when using Faraday imaging and imaging a vortex lattice, there was a step in objective lens position where the amplitude of the core signal switched from positive to negative as shown in Fig. 8.20, which may coincide with crossing the focal plane. Aside from this step in the Faraday signal, we were unable to locate a position where we felt confident that we were within the $\pm 5$-$\mu$m DOF, with the vortex lattice as our test target.

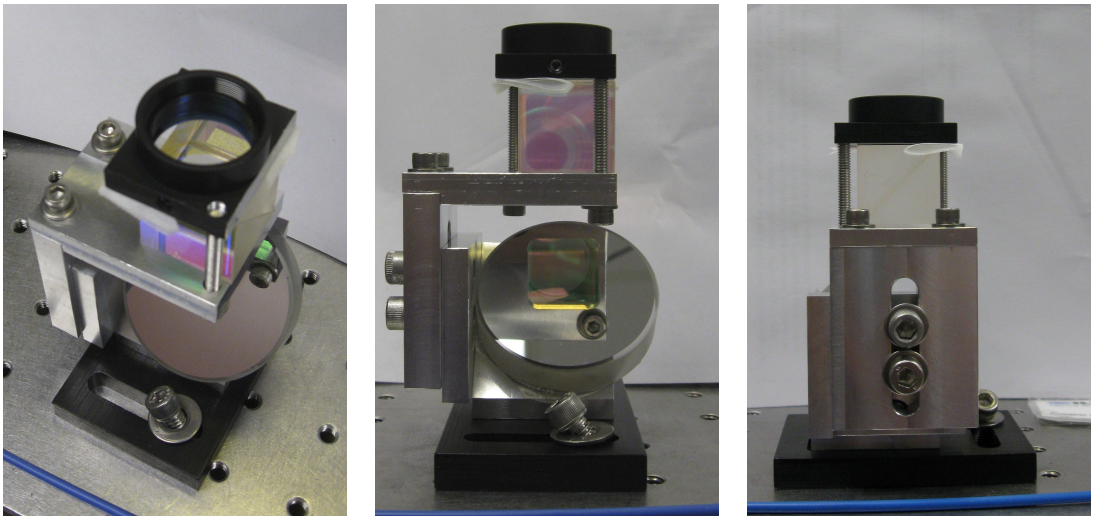

(a) Top View (b) Front View (c) Side View

Figure 8.18: Custom mirror and wave plate mount.

We suspect there may be something odd with the vortex lattice because we observe the vortex lattice *in situ* with bright-field absorption, Faraday, and dark-field imaging. Given that we are able to resolve the lattice over a large depth of field, so we suspect that the radius of the cores comprising the vortex lattice are most likely larger than that of vortex cores in the highly oblate trap. See Chapter 9 for further discussion of both the vortex lattice images taken with the QVM2, and continued fine-tuning of focus.

## 8.9 Imaging probe profile

One of the key frustrations regarding the QVM2 is that despite no longer needing the pair of achromats employed in the relay, we still observe a substantial amount of weakly scattered probe light bypassing the mask in the Fourier plane, approximately 1% of the total probe power incident on the mask. We suspect that the quality of the probe beam and light scattered by dust on the cell may contribute to this problem. We performed a preliminary investigation of probe beam quality in a mock setup using various probe collimation optics and objectives. The probe beam was imaged at the mask location in

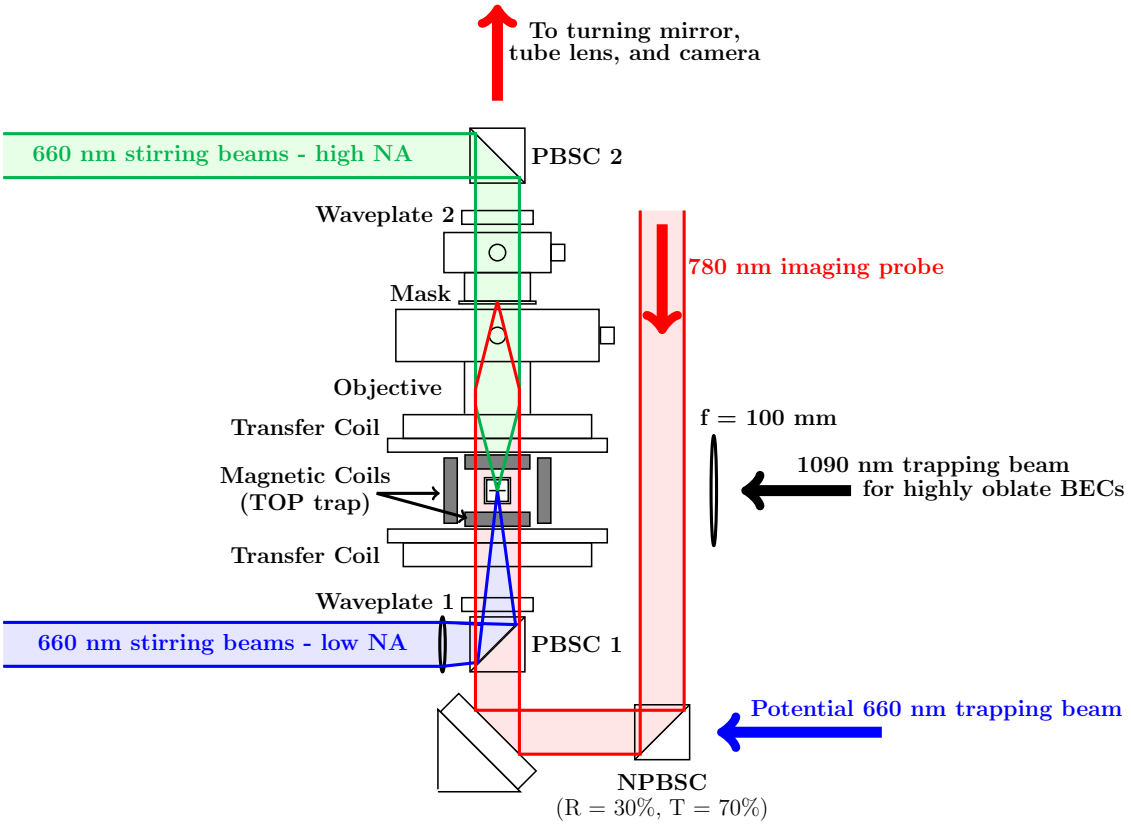


Figure 8.19: Layout of the QVM2 showing the beam paths.

the Fourier plane to identify the amount of probe power bypassing the mask. In these offline tests we found 0.1% to 3% of the probe power bypasses the mask, depending on the mask size, probe quality, and probe alignment. In retrospect, knowing that weakly scattered light from the probe beam contributed to the poor signal-to-noise in the QVM1 dark-field images, we would have benefited from a careful analysis of probe beam quality and masking effectiveness in our initial offline testing of the QVM2. However, the amount of light scattered by dust fused to the BEC cell is still unknown and it is unclear whether light scattered by dust or poor probe beam quality is the dominant reason for the high background signal observed at the camera.

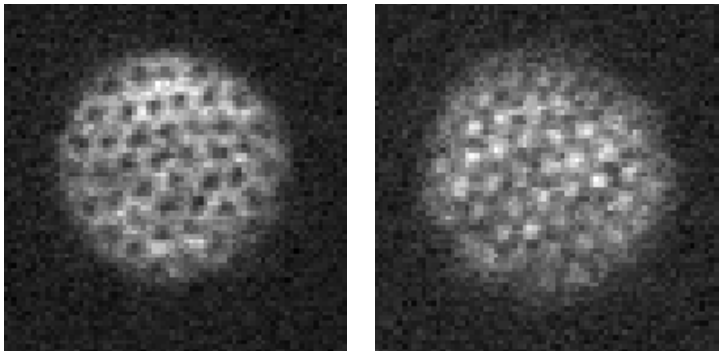

(a) $z_{\mathrm{obj}} = 3.38$ mm (b) $z_{\mathrm{obj}} = 3.36$ mm

Figure 8.20: [*In situ* Faraday images of a vortex lattice imaged on $|F = 2\rangle \rightarrow |F' = 3\rangle$. (a) Objective lens $z$-axis translation stage position is (a) $z = 3.38$ mm and (b) $z = 3.36$ mm. Note that the vortex core signal switches from a dip (a) to a peak (b).

## 8.10 Mask manufacture

Mask manufacture has been another challenge. We have several approaches for making prototypes.

1. For the proof-of-principle images we used a section of magnet wire. The advantage of wire is that we do not need to image through a plate of glass, and the wire is completely opaque. The disadvantage is that the wire blocks all spatial frequencies along the length of the wire and thereby reduces the signal from the vortex cores.

2. We used caulk applied to a microscope cover slip to make an approximately circular opaque mask. The disadvantage of the caulk masks is that it is difficult to make them circularly symmetric, and to make masks smaller than $D_{\mathrm{mask}} \sim 800$ $\mu$m.

3. We have a few masks that were made by machining a plastic rod down to the desired diameter, then gluing a thin sliver trimmed from the end of the rod onto a coverslip. These masks are round and opaque, but the process is limited to masks larger than $D_{\mathrm{mask}} \sim 1$ mm, and also much more involved than caulk masks.

4. Tom Milster's group made us a set of chrome masks with their Maskless Lithography

Tool. Unfortunately the open aperture of these masks is on the order of $r \sim 6 - 7$ mm which reduces the vortex signal by blocking the highest spatial frequencies, effectively reducing the NA of imaging system. In addition, the masks were printed on microscope slides which introduced etaloning.

Most of our techniques for mask manufacture are quick and cheap which was the priority given that we are still in the prototype stage. Eventually we would like to have a nice set of circular masks with diameters ranging from about 500 $\mu$m to 2 mm, with open apertures of $r = 12$ mm, and printed on thin, AR-coated coverslips.

# Chapter 9
# Initial Applications of the QVM2

In this chapter we discuss the current state of imaging with the QVM2. The images presented in this chapter represent the state-of-the-art for *in situ* imaging of vortex distributions, and superfluid density features, such as shockwaves and solitons, in single-component dilute-gas BECs. They demonstrate the potential of the dark-field imaging technique, as well as the limitations of the current iteration of our quantum vortex microscope. The goal of this chapter is to provide some analysis of the preliminary QVM2 images, identify limitations of both the dark-field imaging technique and the QVM2, and suggest improvements to be implemented in the next iteration of the quantum vortex microscope, the QVM3. In addition, we present new and unexpected results regarding *in situ* observation of vortex cores with both Faraday and bright-field absorption imaging techniques, and discuss the implications of these observations on the design of the QVM3.

As discussed in Chapter 8, preliminary focusing of the QVM2 was done by observing lensing effects in bright-field absorption images as we stepped the microscope objective through focus [44]. This allowed us to identify a range of a few hundred microns over which the bulk BEC appears in focus, and we placed the microscope objective at the center of this range. We predict, based on our Zemax model, and our offline testing of the QVM2, that in order to observe tiny density features such as vortex cores *in situ*, we need to find the true focal plane of our imaging system to within the narrow DOF $\sim \pm 5$ $\mu$m. The DOF based on our field-propagation numerics is slightly more forgiving, with the predicted central vortex signal falling to approximately half maximum for $\Delta f \sim \pm 10$ $\mu$m.

Optimization of a vortex imaging system differs substantially from optimizing a biological microscope. Our focal plane, or object plane, is inside a vacuum system, so we cannot use a static test target such as a USAF resolution test target. Instead our test targets are

vortices and other microscopic density features within a BEC. Each BEC exists for about 30 s and we make anywhere from 50 to 200 BECs on a given day. The reproducibility of our test target, i.e., the vortex distribution within the BEC, varies with both the technique and the BEC quality. The end result is that when optimizing focus and signal-to-noise, we operate within a large parameter space, with an optimization metric, increased vortex core signal, that relies on a test target which exists for only a fraction of the time and may not necessarily exist even if a BEC is present. In addition, the vortex core signal is strongly dependent on the BEC aspect ratio, something that we did not fully realize until the final stages of the optimization process, and the best-focus position seems to vary with feature size and imaging conditions.

A primary challenge for focusing the QVM2 and optimizing vortex signal-to-noise is to generate a reliable distribution of vortices with a pattern that allows us to pick the vortex signal out of the noise. The most obvious test target is the vortex lattice used in proof-of-principle demonstrations of the *in situ* dark-field imaging technique, as discussed in Chapter 6 and Sec. 9.1 of this chapter. However, the vortex lattice appears in focus over a range larger than the expected DOF. In addition, since the lattice is formed in the TOP trap, the axial extent of the BEC, $\Delta z \sim 30$ $\mu$m given an axial Thomas-Fermi radius of $R_{\mathrm{z}} \sim 15$ $\mu$m, is larger than the predicted DOF of the imaging system. With that in mind, we created a test target consisting of a set of 'bars' of approximately the same width as a vortex by merging two BECs together in the hybrid trap to form a soliton array as described in Sec. 9.2. While this technique produced some intriguing images with hints of vortices, it proved too unreliable for focusing tests, and we ultimately returned to spinning to form a vortex test target, this time in a weak hybrid trap with aspect ratio $R_{\mathrm{r}} : R_{\mathrm{z}} \sim 3 : 1$. Lastly, we used the QVM2 to return to our search for the oblique dark solitons introduced in Sec. 4.5.

## 9.1 *In situ* imaging of a vortex lattice

As discussed in Chapter 6, a vortex lattice makes, in many ways, an ideal test target in that it provides an easily recognizable, regular pattern of vortex cores which can be reliably reproduced. In addition, the rotation causes the vortex cores to align with the axis of both rotation and imaging, and the added angular momentum increases the aspect ratio of the BEC. Our method for spinning up a lattice is described in Sec. 2.2. Briefly, we modify the TOP trap's rotating bias field to form a slowly rotating elliptical potential well, which in turn spins up the BEC such that a triangular lattice of vortices is formed, as shown in the set of dark-field images in Fig. 9.1. For the images shown in this section, we used $B_\epsilon \sim 0.06 B_0$. Vortex cores are clearly visible in all four frames shown in Fig. 9.1, demonstrating the first multi-shot *in situ* imaging of a lattice of vortex cores from a *single* BEC. The Fourier transform of each real-space image is shown in the bottom row of Fig. 9.1 where the six point $k$-space signature corresponding to the triangular lattice structure is clearly visible even as the real-space core contrast deteriorates.

While we anticipated *in situ* observation of vortex cores in dark-field based on the dark-field vortex lattice images taken with the QVM1, we were surprised to discover that the vortex lattice was resolvable with both Faraday and bright-field absorption imaging. Figure 9.2 shows a representative vortex lattice taken with (a) Faraday, (b) bright-field absorption post-processing, and (c) dark-field imaging. The Faraday image is particularly stunning. Except where noted explicitly, a background image is subtracted from all BEC images, and all bright-field absorption images have been converted to optical depth and inverted such that regions of low integrated column density (vortex cores) appear dark. We note that background subtraction is mostly redundant for the Faraday images given that nearly all of the background light is polarized such that it never reaches the camera. From left to right, each row in Fig. 9.2 contains a series of 1D Gaussians fit to the line of vortex cores denoted by the horizontal line in the central BEC image, an image of a BEC with a vortex lattice, and the Fourier transform of the vortex lattice image. Note that the

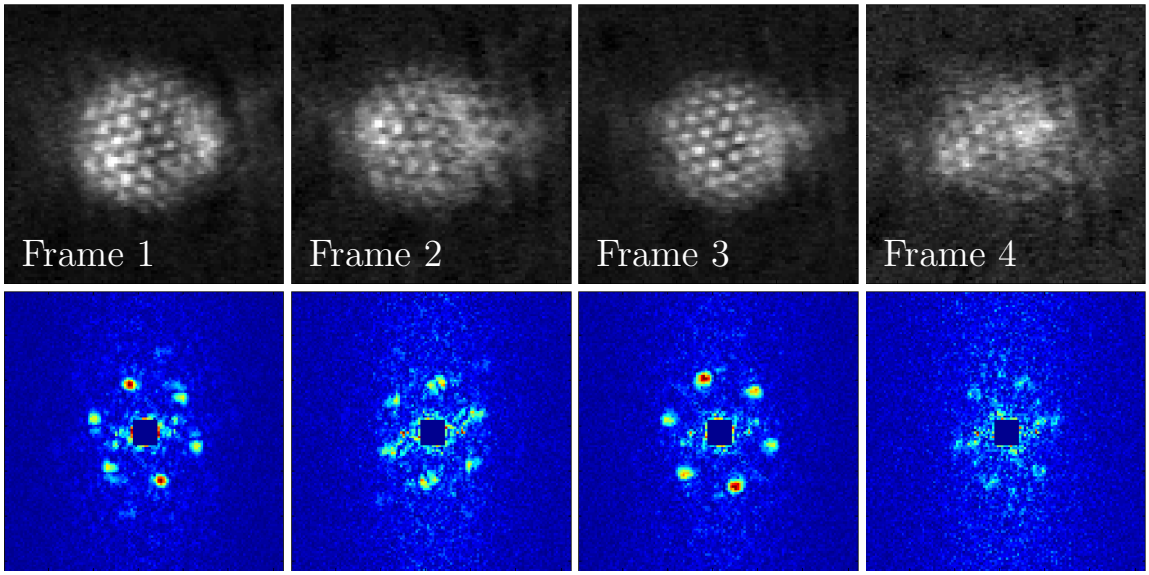


Figure 9.1: Top row: 120 × 120-$\mu$m *in situ* dark-field images of a vortex lattice in a rotating BEC in the TOP trap, with $t_{\mathrm{s}} = 15$ s and $t_{\mathrm{h}} = 10$ s. Bottom row: corresponding Fourier transform for each real space image. Frames are separated by 101.5 ms. Dark-field imaging parameters are $D_{\mathrm{mask}} = 800$ $\mu$m, $\Delta/2\pi = 20$ MHz from $|F = 1\rangle \rightarrow |F' = 2\rangle$, $P_{\mathrm{BEC}} \sim 12$ $\mu$W ($P_{\mathrm{fiber}} \sim 50$ $\mu$W), and $t_{\mathrm{exp}} = 100$ $\mu$s.

Fourier transform clearly shows the triangular lattice structure, and that the structure is particularly prevalent in the Fourier transform of the Faraday image.

When fitting to the line of vortex cores in the Faraday or dark-field images, we fit to a series of 1D Gaussians, one Gaussian for each core, and accounted for the background signal with a flat offset. Vortex core apparent FWHM ranged from 3.4 $\mu$m to 4.8 $\mu$m for the Faraday image and from 3.5 $\mu$m to 7.3 $\mu$m for the dark-field image. The reported FWHM are given for the object plane, using $M = 11.2$ for images taken with the Cascade EMCCD camera. When fitting to the line of vortex cores in the processed bright-field absorption image where vortices appear as dark regions within the bright bulk BEC, we fit to a series of 1D Gaussians subtracted from a quadratic Thomas-Fermi profile with $R_{\mathrm{r}} \sim 49$ $\mu$m determined from the fit. Vortex core FWHM ranged from 5.7 $\mu$m to 8.4 $\mu$m with the larger cores generally on the edges of the vortex line.

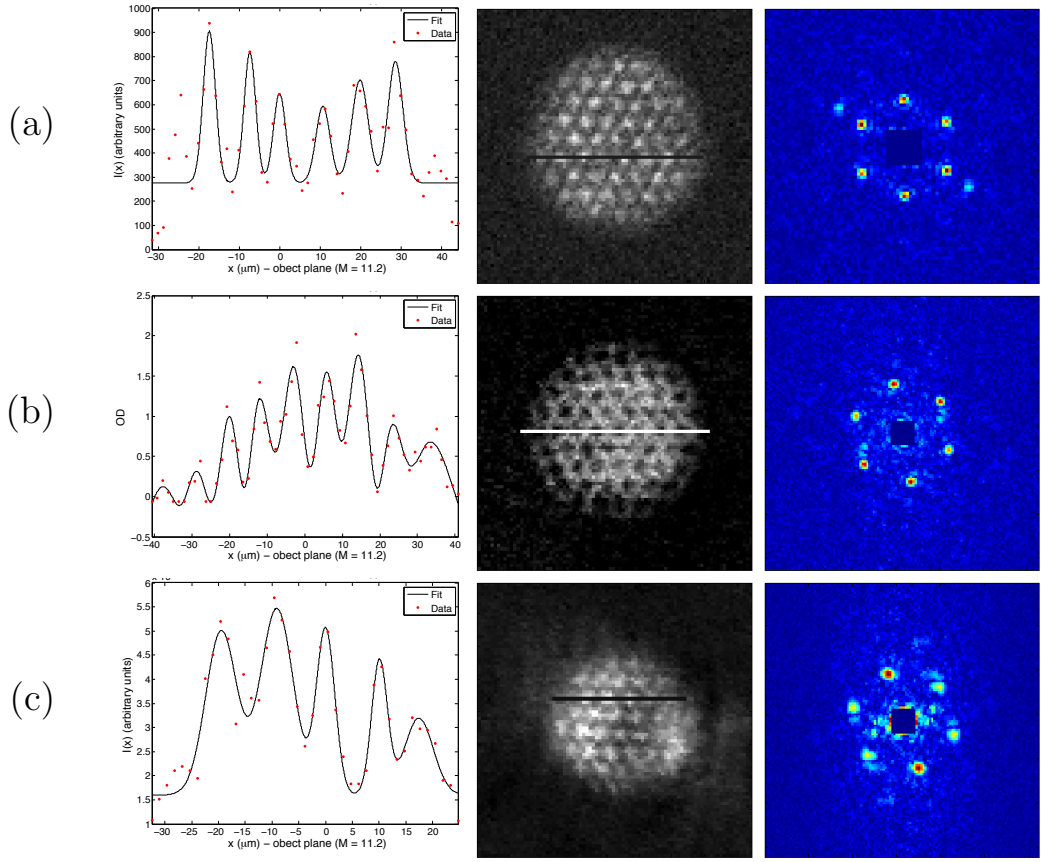


Figure 9.2: *In situ* vortex lattice images taken with (a) Faraday, (b) bright-field absorption, and (c) dark-field imaging. From left to right, each row contains a fit of a series of 1D Gaussians to the line of vortex cores denoted by the white or black horizontal line in the central BEC image, an image of a BEC with a vortex lattice, and the Fourier transform of the vortex lattice image. (a) Faraday image taken with $\Delta = 2\Gamma$ from $|F = 2\rangle \rightarrow |F' = 3\rangle$. FWHM of the Gaussian fit to the peaks corresponding to each vortex in the cross section are 3.6 $\mu$m, 3.4 $\mu$m, 3.6 $\mu$m, 4.1 $\mu$m, 4.8 $\mu$m, and 4.4 $\mu$m, from left to right. (b) Bright-field absorption image post processing. The image was taken using $\Delta/2\pi = 0$ MHz from $|F = 1\rangle \rightarrow |F' = 2\rangle$. FWHM of the Gaussian fit to the dip corresponding to each vortex in the cross section are 7.2 $\mu$m, 7.1 $\mu$m, 5.7 $\mu$m, 7.7 $\mu$m, 6.2 $\mu$m, 6.3 $\mu$m, 5.9 $\mu$m, and 8.4 $\mu$m, from left to right. (c) Dark-field image taken using $\Delta/2\pi = 20$ MHz from $|F = 1\rangle \rightarrow |F' = 2\rangle$, and $D_{\text{mask}} = 800$ $\mu$m. FWHM of the Gaussian fit to the peak corresponding to each vortex in the cross section are 6.9 $\mu$m, 7.3 $\mu$m, 4.1 $\mu$m, 3.5 $\mu$m, and 6.3 $\mu$m, from left to right. All FWHM are reported in the scale of the object plane using $M = 11.2$.

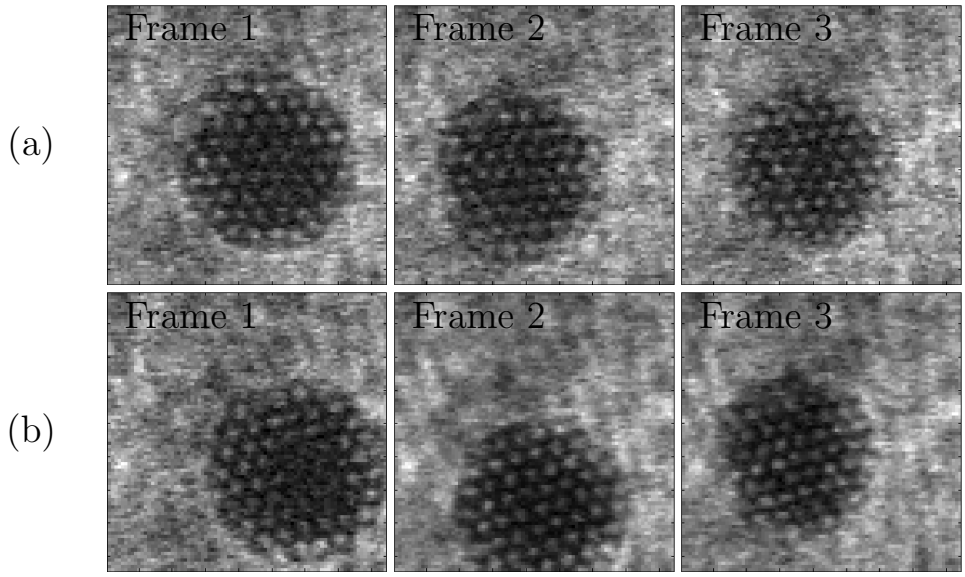


Figure 9.3: $120 \times 120$-$\mu$m raw (no background subtraction or processing) *in situ* bright-field absorption images of a vortex lattice in a rotating BEC in the TOP trap, with $t_{\rm s} = 15$ s and $t_{\rm h} = 20$ s. Each row is a set of three images from a single BEC. Frames are separated by 27.26 ms. Bright-field imaging parameters are $\Delta/2\pi = 0$ MHz from $|F = 1\rangle \rightarrow |F' = 2\rangle$, and $P_{\rm BEC} \sim 25$ $\mu$W ($P_{\rm fiber} \sim 100$ $\mu$W). Frames 2 and 3 in the bottom row of images had $t_{\rm exp} = 40$ $\mu$s, while $t_{\rm exp} = 20$ $\mu$s for all other frames.

One of the reasons for pursuing dark-field imaging is that the vortex core is a tiny transmission feature and we generally do not expect to be able to observe the vortex core signal against the noisy background of the bulk BEC. However, in the case of the vortex lattice images taken with the QVM2, the cores are clearly observable and we were even able to acquire multiple bright-field absorption images from a single BEC, as shown in Fig. 9.3(a), by imaging on the $|F = 1\rangle \rightarrow |F' = 2\rangle$ hyperfine transition and using very low probe light power, $P_{\rm BEC} \sim 25$ $\mu$W ($P_{\rm fiber} \sim 100$ $\mu$W). Here $P_{\rm fiber}$ is the probe power measured after the beam collimation and magnification optics, and $P_{\rm BEC} \sim 0.25 P_{\rm fiber}$ is the estimated probe power at the BEC. We often observe cores more clearly in the second, or third frame of a multi-shot image as shown in Fig. 9.3(b). This runs contrary to what we observed with the QVM1 as shown in Fig. 6.4 where vortex cores were observable in

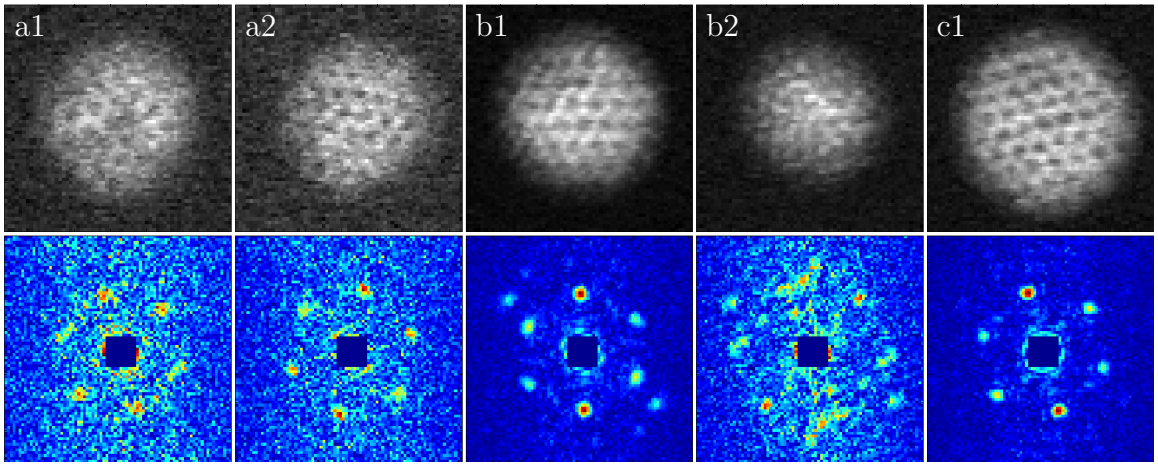


Figure 9.4: Top row: $90 \times 90$-$\mu$m *in situ* Faraday images of a vortex lattice in a rotating BEC in the TOP trap, with $t_{\rm s} = 15$ s and $t_{\rm h} \sim 10 - 20$ s. Bottom row: corresponding Fourier transforms; note the hexagonal lattice signature in each Fourier transform. Faraday imaging parameters are $\Delta/2\pi = -40$ MHz from $|F = 1\rangle \rightarrow |F' = 2\rangle$ and $t_{\rm exp} = 30$ $\mu$s for all images. Imaging power $P_{\rm BEC} \sim 25$ $\mu$W (a) and $P_{\rm BEC} \sim 125$ $\mu$W (b) and (c). Images labeled a1-a2, and b1-b2 correspond to a pair of images with each pair of images taken from a single BEC.

the dark-field images only.

We were also able to obtain multiple Faraday images by imaging with light detuned $\Delta/2\pi = -40$ MHz from the $|F = 1\rangle \rightarrow |F' = 2\rangle$ hyperfine transition, as shown in Fig. 9.4, where the images (a1) and (a2) are two images from a single BEC, as are the images (b1) and (b2). The vortex core contrast in the multi-shot Faraday images is not as good as that observed in the bright-field absorption or dark-field images, however core contrast might be improved with a different choice for detuning and probe power. Again the lattice $k$-space signature is readily apparent. Figures 9.5 and 9.6 show Faraday images of a lattice that has been loaded from the TOP trap into a hybrid trap over $t_{\rm load} \sim 100$ ms and then held in the hybrid trap for $t_{\rm hold} = 200 - 500$ ms. Figures 9.5(c) and (d) show the BEC aspect ratio before ($R_{\rm r} : R_{\rm z} \sim 3 : 1$) and after ($R_{\rm r} : R_{\rm z} \sim 4 : 1$) loading, respectively. Vortex lattice contrast decreases after loading but vortex cores remain visible.

One key difference between our experimental method for spinning up a lattice used for

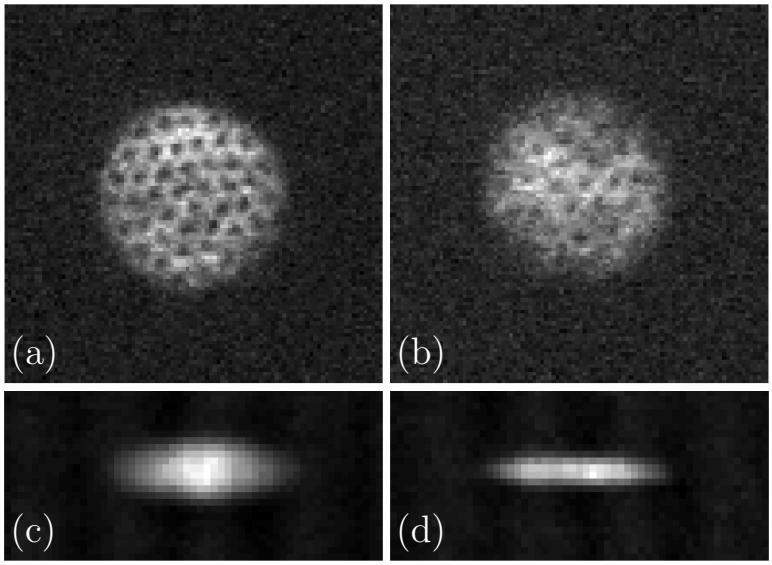


Figure 9.5: *In situ* images of a vortex lattice before and after loading into a hybrid trap. (a) $140 \times 140$-$\mu$m Faraday image and (c) $140 \times 70$-$\mu$m corresponding phase-contrast image of a vortex lattice in a rotating BEC in the standard TOP trap ($R_\mathrm{r} : R_\mathrm{z} \sim 3 : 1$) with $t_\mathrm{s} = 15$ s and $t_\mathrm{h} = 10$ s. (b) Faraday image and (d) corresponding phase-contrast image of a vortex lattice $t_\mathrm{hold} = 200$ ms after loading the rotating BEC into a hybrid trap ($R_\mathrm{r} : R_\mathrm{z} \sim 4 : 1$). Faraday imaging parameters: $\Delta = 2\Gamma$ from $|F = 2\rangle \rightarrow |F' = 3\rangle$, $P_\mathrm{BEC} \sim 300$ $\mu$W (probe), and $P_\mathrm{BEC} \sim 112$ $\mu$W (repump)

the images shown in this section, and the method for spinning up a lattice used in the rest of the dissertation, is that we greatly increased both the spin time $t_\mathrm{s}$, and the hold time $t_\mathrm{h}$ when waiting for the lattice to crystalize, while holding the RF frequency at close to the sag cut value during both the spin and the hold periods. Typical times for the images in this section are $t_\mathrm{s} \sim$ 10-20 s and $t_\mathrm{h} \sim$ 10-20 s, resulting in relatively large lattices, containing on the order of 50 cores, with low thermal component. We note that, while a lattice of 50 cores is large for our apparatus, other groups report lattices of several hundred cores [87]. The long spin and hold times were critical for creating a lattice with vortex cores observable with bright-field absorption imaging, which leads us to consider whether the process of spinning significantly depleted the BEC atom number and as a result increased the healing length $\xi$. We observed that images taken prior to rotating the BEC show a bimodal BEC,

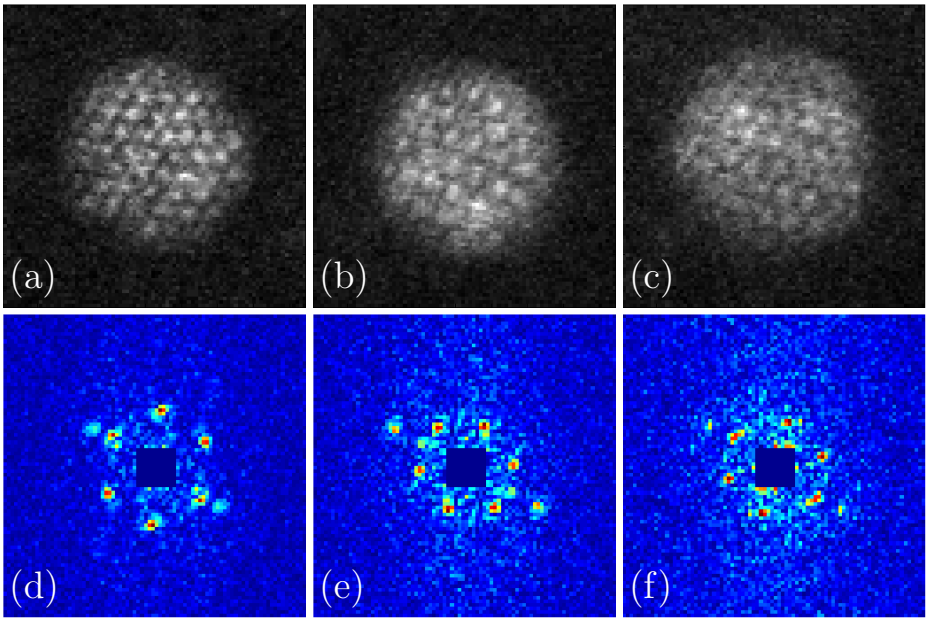


Figure 9.6: *In situ* images of a vortex lattice before and after loading into a hybrid trap. (a) 120×120-$\mu$m Faraday image and (d) corresponding Fourier transform of a vortex lattice in a rotating BEC in the standard TOP trap ($R_\mathrm{r} : R_\mathrm{z} \sim 3 : 1$) with $t_\mathrm{s} = 15$ s and $t_\mathrm{h} = 10$ s. (b) Faraday image and (e) corresponding Fourier transform of a vortex lattice $t_\mathrm{hold} = 200$ ms after loading the rotating BEC into a hybrid trap ($R_\mathrm{r} : R_\mathrm{z} \sim 4 : 1$). (c) Faraday image and (f) corresponding Fourier transform of a vortex lattice $t_\mathrm{hold} = 500$ ms after loading the rotating BEC into a hybrid trap ($R_\mathrm{r} : R_\mathrm{z} \sim 4 : 1$). Faraday imaging parameters: $\Delta = 2\Gamma$ from $|F = 2\rangle \rightarrow |F' = 3\rangle$, $P_\mathrm{BEC} \sim 300$ $\mu$W (probe), and $P_\mathrm{BEC} \sim 112$ $\mu$W (repump)

while images taken after 10-20 s of hold time show a relatively pure BEC, indicating further evaporation and subsequent atom loss, over the course of spinning and crystallization. In addition, BECs containing a lattice have a measurable change in aspect ratio as determined from the phase-contrast images taken along the $x$-axis, with $(R_\mathrm{r}, R_\mathrm{z}) \sim (40, 15)$ $\mu$m after spinning compared to $(R_\mathrm{r}, R_\mathrm{z}) \sim (35, 19)$ $\mu$m without spinning. We suspect that a loss of atoms, combined with the increase in the radial extent of the cloud due to its rotation, may result in a decrease in overall BEC density and subsequent increase in healing length and vortex core radius.

The bulk BEC healing length $\xi$ depends on the peak BEC density $n_0$,

$$\xi = \frac{1}{\sqrt{8\pi n_0 a_s}}, \tag{9.1}$$

where $a_s$ is the scattering length. In the 3D Thomas-Fermi limit, the ground-state peak BEC density is

$$n_0 = \frac{15N}{8\pi R_{\rm r}^2 R_{\rm z}}, \tag{9.2}$$

where $N$ is the number of atoms in the BEC, and $R_{\rm r}$ and $R_{\rm z}$ are the radial and axial Thomas-Fermi radii respectively. If we consider a constant atom number of $N = 1.8 \times 10^6$ we find $\xi = 400$ nm for $(R_{\rm r}, R_{\rm z}) = (35, 19)$ $\mu$m, and a just slightly larger $\xi = 410$ nm for $(R_{\rm r}, R_{\rm z}) = (40, 15)$ $\mu$m. However, if we conservatively estimate that the BEC loses about half of its atoms over 10-20 s of spin and an additional 10-20 s hold period after spinning, we find that $\xi = 580$ nm for $(R_{\rm r}, R_{\rm z}) = (40, 15)$ $\mu$m. If we go further and estimate that three-quarters of the atoms are lost prior to imaging, our estimate for $\xi$ increases to $\xi = 820$ nm, twice the original value. With this in mind, it seems probable that our ability to observe a vortex lattice in bright-field as well as dark-field is due in part to atom loss and subsequent increase in vortex core size.

When considering the destructiveness of the multi-shot images we calculate the number of photons scattered per atom per image, $N_{\rm ph}$. For minimally-destructive images we require $N_{\rm ph} << 1$. Based on the imaging parameters used for the set of four dark-field images shown in Fig. 9.1, reported in the image caption, we estimate that with linearly polarized light and a rotating magnetic bias field, $N_{\rm ph} \sim 1.4$. This estimate is clearly too high since we observe four frames with good bulk BEC signal and identifiable vortex cores. This overestimate could be due to the beam power being lower for the 100-$\mu$s exposures used for the images, than for the steady-state conditions when we measured the beam power. In addition, our measurement of the probe $1/e^2$ beam radius may be off, with the actual beam radius being larger than the reported $w_0 \sim 2$ mm.

Lastly we introduced a defect into the lattice with a pulse of resonant laser light and observed the rotation of the defect to go clockwise or counterclockwise depending on the

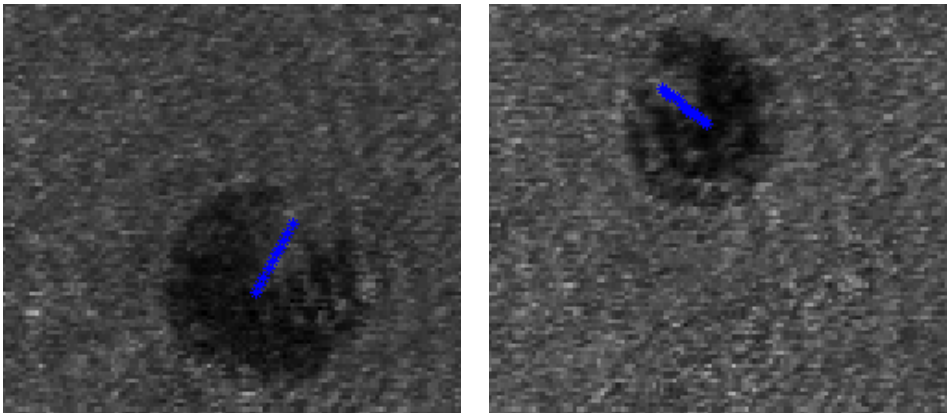

(a) Frame 1 (b) Frame 2

Figure 9.7: Multiple *in situ* transmission images of a single BEC containing a vortex lattice, taken with bright-field absorption imaging. The lattice is spun up with $\omega_{\mathrm{mod}} = 2\pi \times 3988$ Hz ($\omega_{\mathrm{TOP}} = 2\pi \times 4000$ Hz), resulting in counter-clockwise rotation. A hole is blasted into the BEC with a pulse of focused, resonant laser light. The blue lines show the angular progression of this defect, with frames separated in time by 32 ms. The measured precession rate of the defect is $\Omega \sim 2\pi \times 7$ Hz. Note the significant slosh.

rotation of the trap as shown in Figs. 9.7 and 9.8. The precession rate of the defect was measured to be $\Omega \sim 2\pi \times 7$ Hz, fast compared to the estimates of the lattice rotation frequency based on the number of vortex cores and the measured Thomas-Fermi radii. Our observation of a precessing defect is similar to the precessing giant vortex cores observed by Engels *et al.* as part of the sequence of formative vortex lattice experiments done at JILA between 2001 and 2006 [87, 88, 89, 90, 91, 92, 93, 94]. In their experiment, Engels *et al.* observed what they identified as long-lived giant vortex cores that formed when they applied a pulse of focused resonant laser light to the center of the lattice, causing a localized depletion of BEC atom density [87]. They postulate that the Coriolis effect in the rapidly rotating BEC (their lattice contained 200-300 vortices) prevents the depleted area from refilling. As part of this study they moved the pulse off-center and observed the precession of the giant vortices, similar to our precessing defect.

As an extension to our *in situ* observation of a lattice of vortex cores, we consider

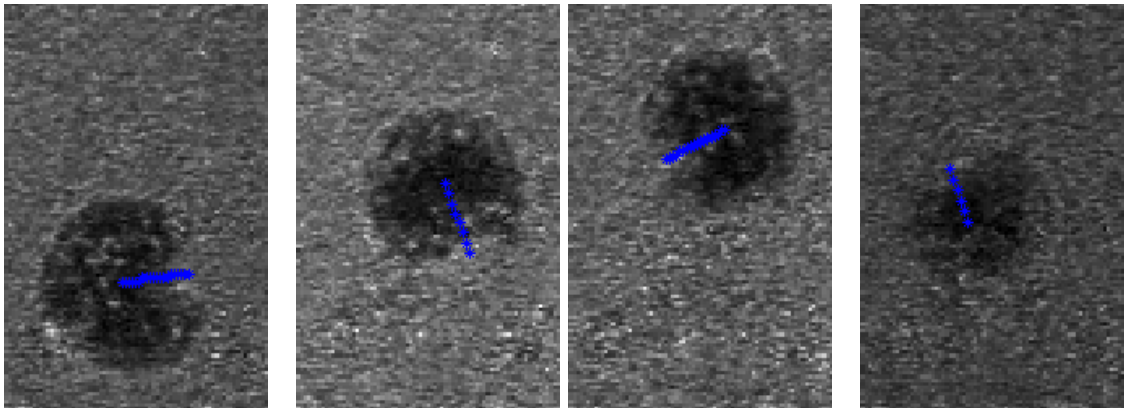

(a) Frame 1 (b) Frame 2 (c) Frame 3 (d) Frame 4

Figure 9.8: Multiple *in situ* transmission images of a single BEC containing a vortex lattice, taken with bright-field absorption imaging. The lattice is spun up with $\omega_{\mathrm{mod}} = 2\pi \times 4012$ Hz ($\omega_{\mathrm{TOP}} = 2\pi \times 4000$ Hz), resulting in clockwise rotation. A hole is blasted into the BEC with a pulse of focused, resonant laser light. The blue lines show the angular progression of this defect, with frames separated in time by 32 ms. The measured precession rate of the defect is $\Omega \sim 2\pi \times 7$ Hz. Note that the direction of the defect rotation depends on the sign of $\omega_{\mathrm{TOP}} - \omega_{\mathrm{mod}}$, as well as the significant slosh.

ramping on a blue-detuned potential in the center of the vortex lattice, and observing the effect that changing the BEC geometry has on the vortex distribution. In the rotating frame, a vortex lattice is the ground state of a BEC confined in a harmonic trap, but this is most likely not the case in a toroidal trap, and the subsequent reconfiguration of vortex cores could result in turbulent fluid flow. However, the significant slosh observed in the images shown in Fig. 9.8 would need to be eliminated prior to exploring this scenario with our experimental apparatus.

## 9.2 Soliton trains

While we have had success observing a vortex lattice *in situ* in the TOP trap, as discussed in the preceding section, we have been largely unable to observe vortices *in situ* in the highly oblate BECs formed in the hybrid trap. The numerics discussed in Chapter 7 suggest that focus might be the problem since the vortex signal falls to about half of the maximum for

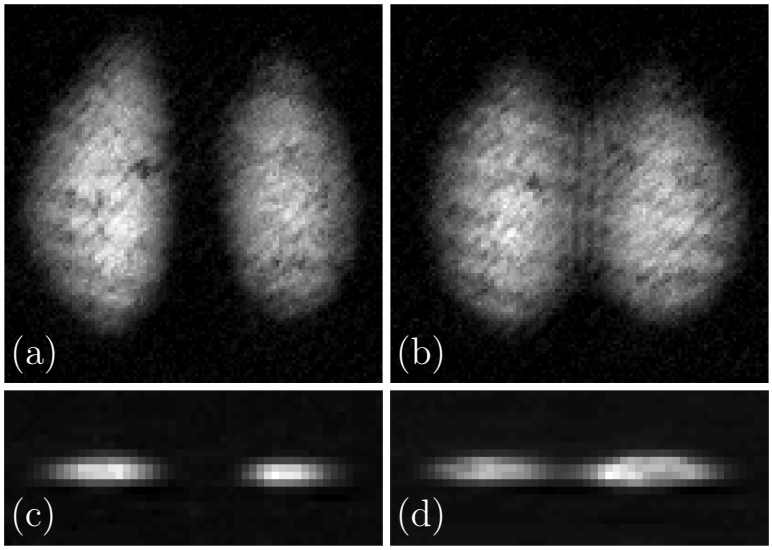


Figure 9.9: Merging BECs following the timing sequence shown in Fig. 9.10. (a) and (b) $130 \times 130$-$\mu$m *in situ* bright-field absorption images taken along the vertical imaging axis ($M = 11.7$) with (a) the 660-nm beam on at $U_0 \sim 1.2\mu_0$ ($V_{660} = 3$ V) prior to the ramp, and (b) the 660-nm beam on at $U_\mathrm{f} \sim 0.9\mu_0$ ($V_{660} = 1.9$ V) after the 20-ms ramp and a 20-ms hold. (c) and (d) $130 \times 50$-$\mu$m *in situ* phase-contrast images taken along the horizontal imaging axis ($M = 5.15$) with (c) the 660-nm beam on at $U_0 \sim 1.2\mu_0$ ($V_{660} = 3$ V) prior to the ramp, and (d) the 660-nm beam on at $U_\mathrm{f} \sim 0.9\mu_0$ ($V_{660} = 1.9$ V) after the 20-ms ramp and a 19-ms hold.

a shift of $\Delta f = \pm 10$ $\mu$m from the best-focus position as shown in Fig. 7.8. However, in our efforts to locate the best-focus position based on the vortex signal in the *in situ* lattice images discussed in Sec. 9.1, we found the vortex signal remained relatively the same over a range much larger than the DOF $= \pm 5$ $\mu$m predicted by Zemax and measured with the offline mockup of the QVM2. In order to rule out any effect of imaging an object that exceeds the DOF of the imaging system, as is the case with the TOP trap BECs where $R_\mathrm{z} \sim 15$ $\mu$m for a BEC containing a lattice, we searched for methods of creating a regular test target in a highly oblate BEC confined in the hybrid trap. It is possible to introduce vortex cores into an oblate BEC by rotating the trapping potential as discussed in Sec. 4.3, but vortex lattice crystallization times in a highly oblate BEC are predicted to be longer

than our BEC lifetimes [59], and we suspect that part of our success with *in situ* imaging of a vortex lattice was due to the regularity in the vortex distribution.

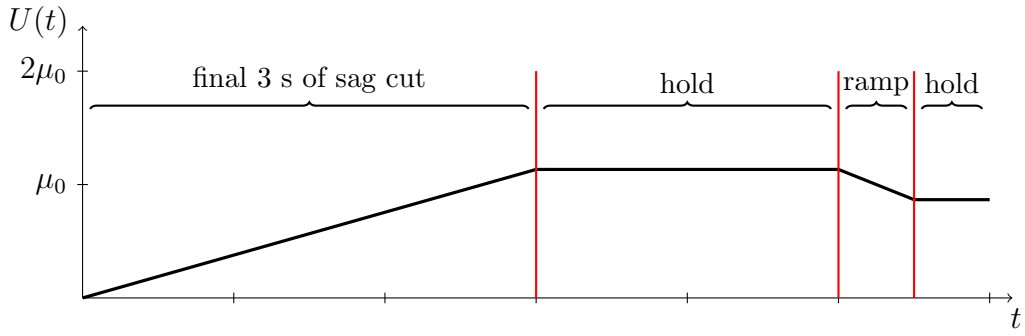


Figure 9.10: 660 beam power timing sequence for forming two independent BECs that are then allowed to collide in the central region (not to scale). The 660-nm beam is ramped on to $U_0 \sim 1.2\mu_0$ over 3 s at the end of the sag cut and the beam power is held constant at $U_0$ for 2 s. The 660-nm beam is then ramped down to a variable value $U_\mathrm{f}$ over $t_\mathrm{ramp} = 20$ ms, and then held for a variable time $t_\mathrm{hold}$.

With this mind we generated an array of solitons in the highly oblate BEC. Our method for soliton formation involved adding an axial 660-nm repulsive potential to the hybrid trap, such that we formed two BECs separated with a barrier of height $U_0 > \mu_0$ as shown in Figs. 9.9(a) and (c). The asymmetrical barrier beam, with focused $1/e^2$ beam radii of $(w_\mathrm{x}, w_\mathrm{y}) \sim (21, 75)$ $\mu$m, was directed upwards through the BEC cell using the low NA beam path shown in Fig. 8.19. The barrier was then ramped down to $U_\mathrm{f}$ just below $\mu_0$ resulting in the creation of a set of dark solitons, or fringes, in the low density region between the BECs as they merged together as shown in Figs. 9.9(b) and (d). The solitons are clearly observed in the bright-field absorption image taken along the vertical imaging axis shown in Fig. 9.9(b). These fringes are distinct from the matter wave interference patterns observed by Andrews *et al* [67], in that the merging of the two BECs occurs well within the nonlinear regime, rather than after a period of expansion. The nonlinear interaction results in the eventual breakdown of the solitons into vortices, a point of interest from a physics perspective, in addition to the utility of the soliton train as an imaging test

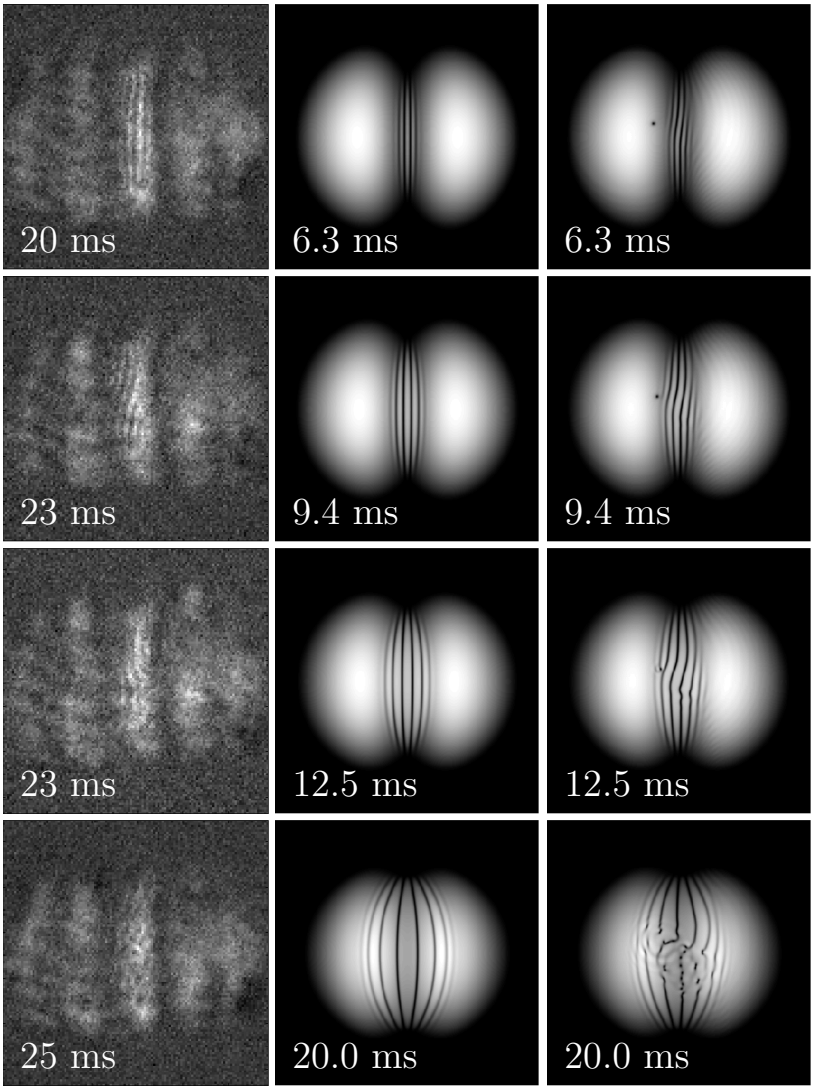


Figure 9.11: $130 \times 130$-$\mu$m images of the BEC after the two halves are allowed to merge. Images were taken at varying hold times shown on each image. (a) Experimental dark-field *in situ* images taken after ramping the 660-nm barrier from $U_0 \sim 1.2\mu_0$ to $U_\mathrm{f} \sim 0.9\mu_0$ and holding. Dark-field imaging parameters are $\Delta = 2\Gamma$ from $|F = 2\rangle \rightarrow |F' = 3\rangle$, using a $D = 690$ $\mu$m wire mask aligned parallel to the solitons. (b) and (c) Frames from a GPE simulation showing the BEC density profile after ramping from $U_0 = 1.6\mu_0$ to $U_\mathrm{f} = 0.8\mu_0$ and holding. A vortex was intentionally added in the simulation shown in (c).

target.

The merging process follows the timing sequence shown in Fig. 9.10. The 660-nm beam is ramped on to $U_0 \sim 1.2\mu_0$ over the final 3 s of the sag cut. After a 2 s hold at $U_0$, the 660-nm beam is ramped down to a variable final potential $U_\mathrm{f}$ over $t_\mathrm{ramp} = 20$ ms, and then held for a variable time $t_\mathrm{hold}$ ranging between 15-25 ms. As we increase $t_\mathrm{hold}$, we expect to observe the fringes breaking down into a mess of vortices.

Figure 9.11 shows experimental dark-field images of a set of solitons in the merging region between two BECs, with complementary images from numerics employing split-step GPE propagation. For the set of experimental images shown in Fig. 9.11(a), the barrier height was ramped from $U_0 \sim 1.2\mu_0$ to $U_\mathrm{f} \sim 0.9\mu_0$ and held for varying time $t_\mathrm{hold}$ shown on each image. Figures 9.11(b) and (c) show BEC images from GPE simulations for similar system parameters, with the barrier height ramping from $U_0 = 1.6\mu_0$ to $U_\mathrm{f} = 0.8\mu_0$. The 660-nm beam used for the barrier in the simulations had focused $1/e^2$ beam radii of $(w_\mathrm{x}, w_\mathrm{y}) = (25, 75)$ $\mu$m, whereas the 660-nm beam in the experiment had focused $1/e^2$ beam radii of $(w_\mathrm{x}, w_\mathrm{y}) \sim (21, 75)$ $\mu$m. In the simulation used to generate the images for Fig. 9.11(c), a vortex was added into one of the BECs, which appears to seed the soliton breakdown. While the hold time needed to observe solitons differs between experiment and simulation, the overall behavior appears to be similar. Experimentally, for $t_\mathrm{hold} = 20$ ms, we observe the solitons as a set of straight fringes, similar to the numerics with $t_\mathrm{hold} = 6.3$ ms. However, for longer hold times the pattern starts to break down. In particular, in the second image in Fig. 9.11(a) corresponding to $t_\mathrm{hold} = 23$ ms, the fringes appear curved in a manner similar to the second image in Fig. 9.11(c) with $t_\mathrm{hold} = 9.4$ ms. By $t_\mathrm{hold} = 25$ ms in the experiment, the fringes appear to have dissolved, although we see no clear evidence of vortex cores. We note that this process seems to be fairly sensitive regarding 660-nm beam power and BEC quality, and we include two back-to-back images for $t_\mathrm{hold} = 23$ ms to show the variability in the experimental process. In the numerics we observe a distinct difference in the soliton pattern due to the presence of a vortex core in one of the merging

BECs, which leads us to suspect that the curvature of the fringes noted in the second image of Fig. 9.11(a) is due to a spontaneous vortex core [95] appearing in one of the BECs prior to merging, although there is no clear evidence for a vortex visible in the image. We also note that in the numerics the presence of the vortex core seems to seed the breakdown of the solitons and shorten the timescale over which the solitons dissolve into vortex dipoles.

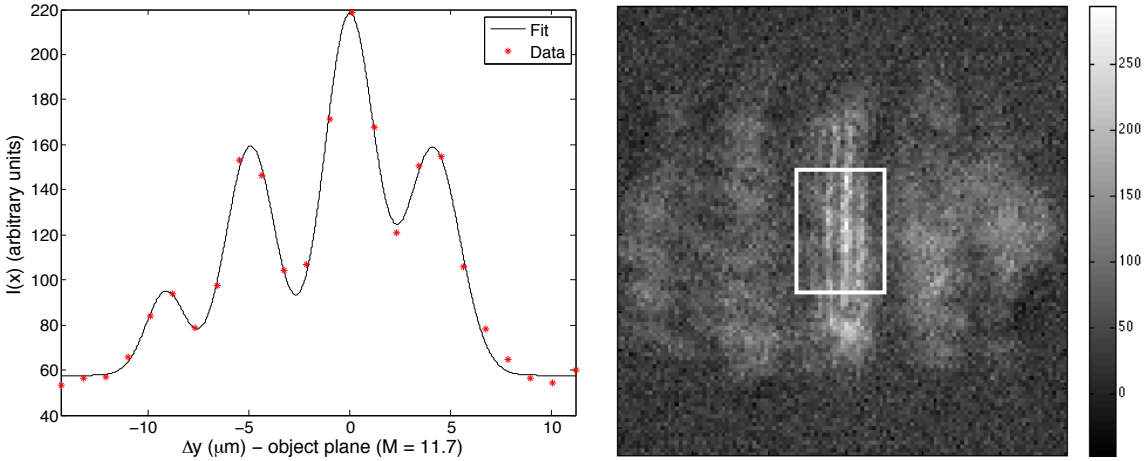


Figure 9.12: Fit to an average cross section from a dark-field *in situ* image taken with the Pixis CCD camera ($M = 11.7$). The plot on the left is the best fit of four gaussians to four peaks in the average of the set of 31 horizontal cross sections enclosed in the white rectangle shown on the dark-field image on the right. The vertical scale is proportional to image intensity per pixel; the horizontal plot axis shows the distance $\Delta y$ away from the central soliton, with the scale corresponding to real distances at the object plane. From left to right the FWHM of each Gaussian is 2.3 $\mu$m, 2.9 $\mu$m, 3.0 $\mu$m, and 3.1 $\mu$m. Fringe centers are separated by 4.2 $\mu$m, 5.0 $\mu$m, and 4.1 $\mu$m.

Perhaps the best measure of the resolution of our imaging system was obtained through fitting a set of four Gaussians to the soliton fringe pattern shown in the dark-field image in Fig. 9.12. Based on this fit, we estimate the FWHMs of the observed solitons are approximately 3 $\mu$m with soliton centers separated by 4-5 $\mu$m. The reported soliton FWHMs and separations are given for the object plane, using $M = 11.7$ for images taken with the Pixis CCD camera. Based on our GPE numerics, we estimate that the solitons should have a FWHM of approximately 1.1 $\mu$m, similar in size to a vortex core. Again our ability to

observe such small features in bright-field is unexpected, and we can move the objective over an axial range $\Delta z = 10 - 20$ $\mu$m and still observe the soliton fringe pattern in the bright-field image.

## 9.3 Best focus

One of the most puzzling aspects of our search for good imaging parameters to use for *in situ* imaging of vortex cores has been the difference in vortex signal for vortices in BECs confined in the TOP trap and vortices in the highly oblate BECs confined in the hybrid trap. As shown in Fig. 9.2, we observe good vortex core signal when imaging a vortex lattice with dark-field, bright-field and Faraday imaging techniques. However, vortex core signal drops significantly in the tight hybrid trap ($R_{\rm r} : R_{\rm z} \sim 10 : 1$) to the point where singly-charged vortex cores are no longer observable with the QVM2. Figure 9.13 shows the series of Faraday images used to locate the best-focus position of the Cascade EMCCD camera. In order to generate a vortex distribution for this focus test, BECs were formed in a weak hybrid trap ($R_{\rm r} : R_{\rm z} \sim 3 : 1$) using a 1090-nm beam power of approximately 50 mW. The BEC was then spun in the manner described in Secs. 2.2 and 4.3, with $B_\epsilon \sim 0.16 B_0$, spin time $t_{\rm s} = 2$ s, and hold time $t_{\rm h} = 3$ s. While the core contrast is still poor, we observe a clear lack of core signal on the far edge of the range of camera positions ($\Delta F = \pm 4$ mm) allowing us to bracket the range of camera positions over which vortex cores are discernible. Based on the images in Fig. 9.13, we estimate the range of in-focus camera positions to be $\Delta Z \sim 5$ mm. Given that axial magnification scales as $M^2$, we are able to back out a DOF $\sim \pm 20$ $\mu$m for the QVM2. This DOF is about a factor of 4 larger than the predicted DOF $\sim \pm 5$ $\mu$m but could be overestimated due to the finite size of the vortices.

After determining the best-focus position for the Cascade camera when imaging *in situ*, we briefly returned to dark-field imaging to image vortex cores generated by spinning in the weak hybrid trap, using spin and hold times similar to those used for the Faraday focus test. While signal-to-noise is still lower than ideal, vortex cores are clearly visible in the

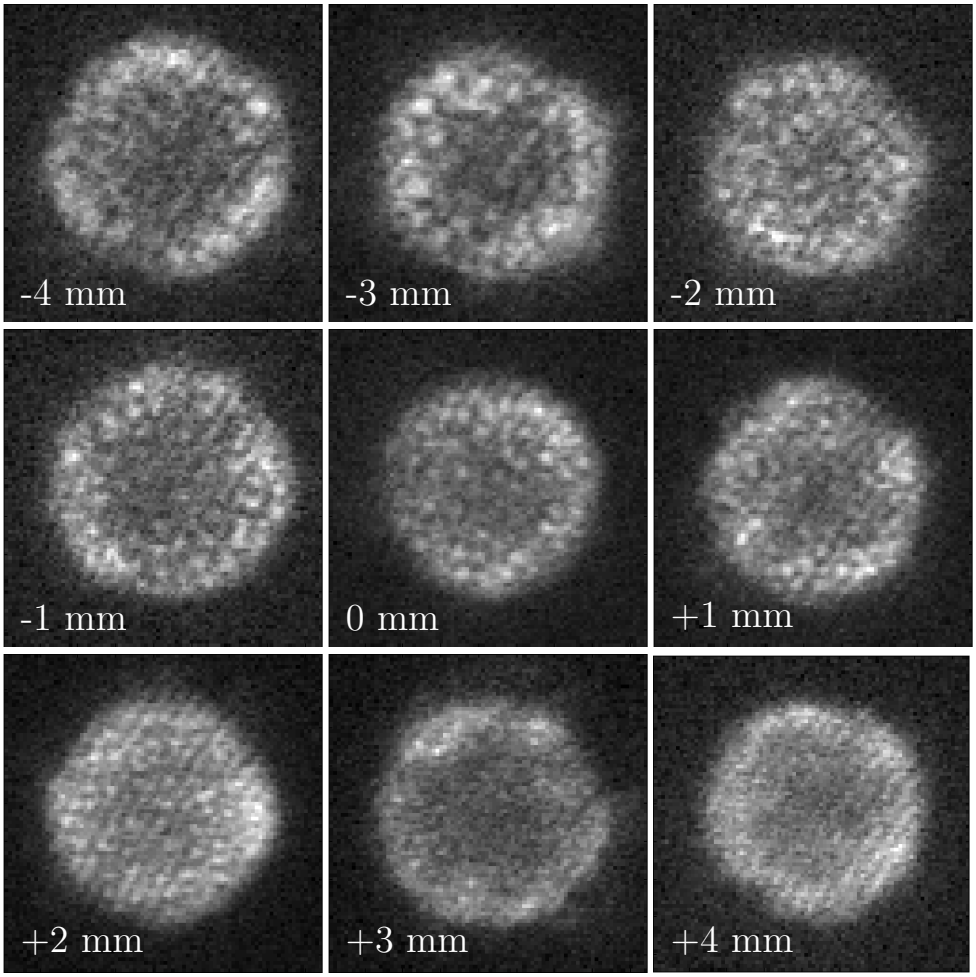


Figure 9.13: 120×120-$\mu$m Faraday *in situ* images of the BEC after spinning for $t_{\rm s} = 2$ s, and holding for $t_{\rm h} = 3$ s in a weak hybrid trap with $P_{1090} \sim 50$ mW. Images were taken with the Cascade EMCCD camera with imaging parameters: $\Delta = +2\Gamma$ from $|F = 2\rangle \rightarrow |F' = 3\rangle$, $t_{\rm exp} = 60$ $\mu$s, $P_{\rm BEC} \sim 190$ $\mu$W (probe), and $P_{\rm BEC} \sim 230$ $\mu$W (optical pumping). Images were taken at varying camera positions indicated by $\Delta F$ shown on each image. Here $\Delta F$ is the axial distance the camera has been moved with $\Delta F = 0$ mm representing the best-focus camera position inferred from these images. As of June 2015, the Cascade camera is located at $\Delta F = +1$ mm corresponding to 11 mm on the axial Cascade micrometer. The objective micrometer is set at 3.38 mm, and the *in situ* vertical BEC position when imaged along the horizontal imaging axis onto the Pixis CCD camera is Vpix $\sim$ 582, with the vertical micrometer for the Pixis set at 12.0 mm.

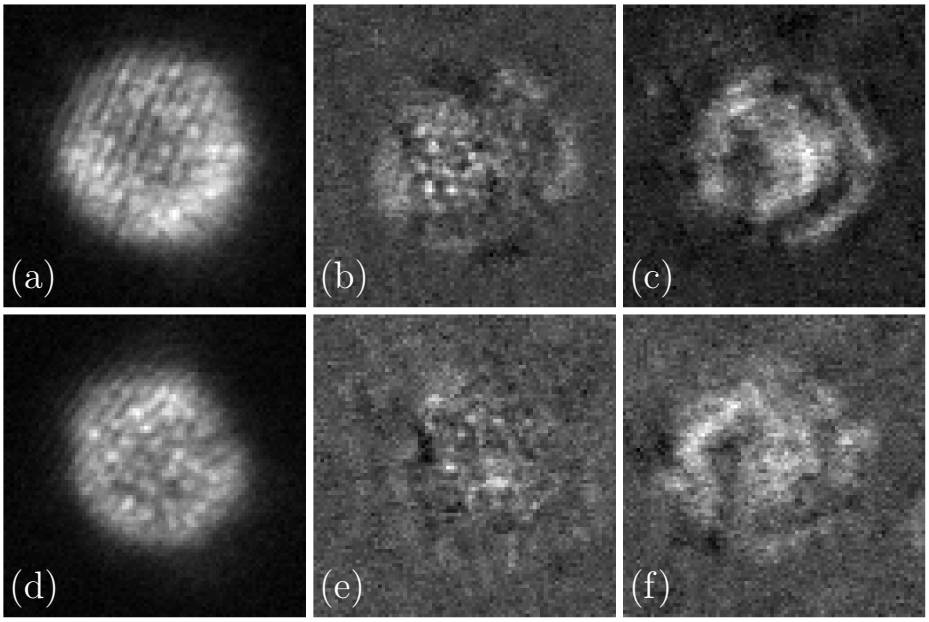


Figure 9.14: (a) $120 \times 120$-$\mu$m *in situ* images of vortex cores after spinning for $t_{\rm s} = 3 - 4$ s and holding for $t_{\rm h} = 3$ s. (a) Faraday and (b) dark-field images of a vortex lattice in a rotating BEC spun in the standard TOP trap ($R_{\rm r} : R_{\rm z} \sim 2 : 1$). (c) Dark-field image of a BEC in the standard TOP trap with no spin. (d) Faraday and (e) dark-field images of a vortex lattice in a rotating BEC spun in a weak hybrid trap ($R_{\rm r} : R_{\rm z} \sim 3 : 1$). (f) Dark-field image of a BEC in the weak hybrid trap with no spin. Faraday imaging parameters: $\Delta = 2\Gamma$ from $|F = 2\rangle \rightarrow |F' = 3\rangle$. Dark-field imaging parameters: $D_{\rm mask} = 800$ $\mu$m, $\Delta = 17$ MHz from $|F = 1\rangle \rightarrow |F' = 2\rangle$, (b)-(c) $P_{\rm BEC} \sim 28$ $\mu$W, $t_{\rm exp} \sim 100 - 200$ $\mu$s, (e)-(f) $P_{\rm BEC} \sim 15$ $\mu$W, $t_{\rm exp} = 200$ $\mu$s.

dark-field images shown in Fig. 9.14(b) corresponding to a BEC spun in a standard TOP trap ($R_{\rm r} : R_{\rm z} \sim 2 : 1$), and Fig. 9.14(e) corresponding to a BEC spun in a weak hybrid trap ($R_{\rm r} : R_{\rm z} \sim 3 : 1$) .

While the images shown in Fig. 9.13 seem to clearly pinpoint a best-focus position for the Cascade camera, we have made several confusing and potentially contradictory observations regarding the best-focus position of the Cascade camera. As shown in Fig. 9.15, the camera position that allowed for imaging soliton trains with the Cascade was $\Delta F = +8.5$ mm corresponding to $\Delta f \sim 70$ $\mu$m with respect to best-focus in the object plane, and well

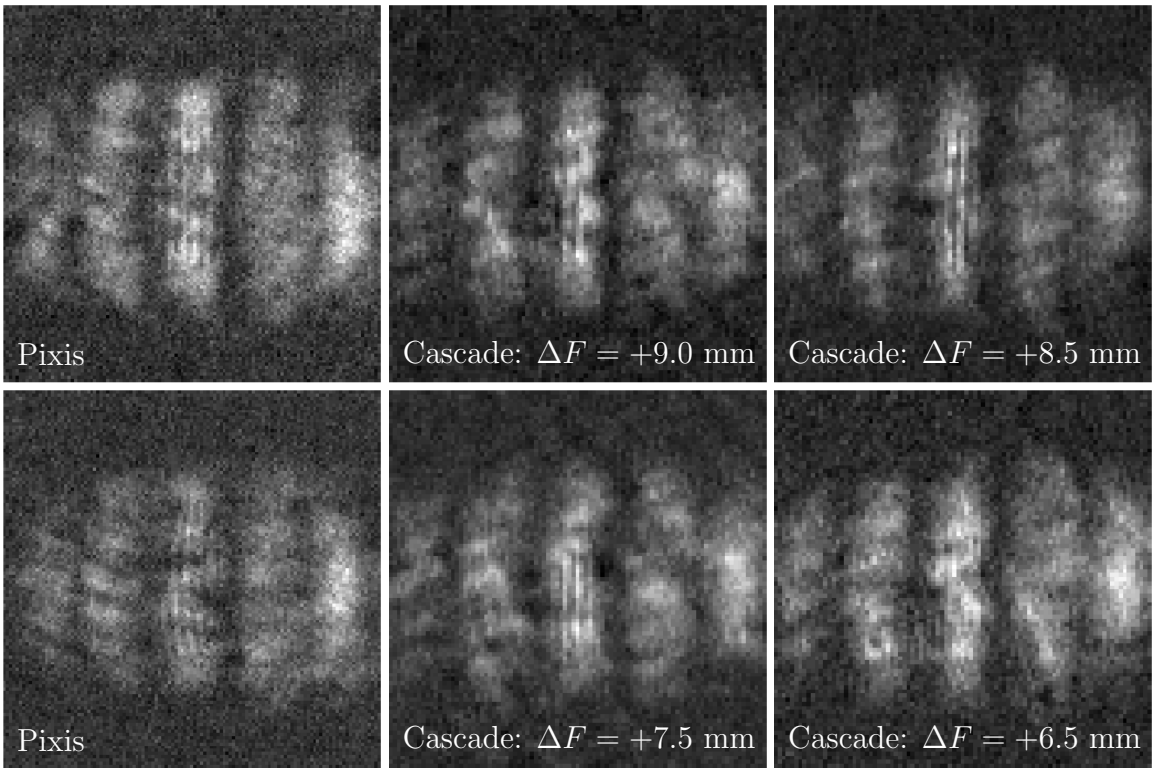


Figure 9.15: $130 \times 130$-$\mu$m dark-field *in situ* images of the central soliton train formed as two BECs are allowed to merge, as described in Sec. 9.2. Dark-field imaging parameters are $\Delta = 4\Gamma$ from $|F = 2\rangle \rightarrow |F' = 3\rangle$, using a $D = 710$ $\mu$m wire mask aligned parallel to the solitons. The leftmost column shows reference images taken with the Pixis CCD camera; note the overall decrease in contrast from the Pixis images shown in Fig. 9.11. The two rightmost columns show images with the Cascade EMCCD camera at varying positions relative to the best-focus image plane, $\Delta F$ shown on each image. Note that the soliton train is resolvable even for images with $\Delta F = +8.5$ mm from the best-focus position for the Cascade.

outside of the DOF of the imaging system. With this in mind, it is surprising that we were able to observe any soliton signatures with the Cascade camera. We also note that currently the imaging system is being used for Faraday imaging after a period of expansion, and in order to see crisp vortex cores after a period of tens of ms of expansion, the BEC needs to be located at a vertical position as much as $30 - 40$ $\mu$m below the vertical BEC position used for the *in situ* Faraday focus test shown in Fig. 9.13. As an additional ob-

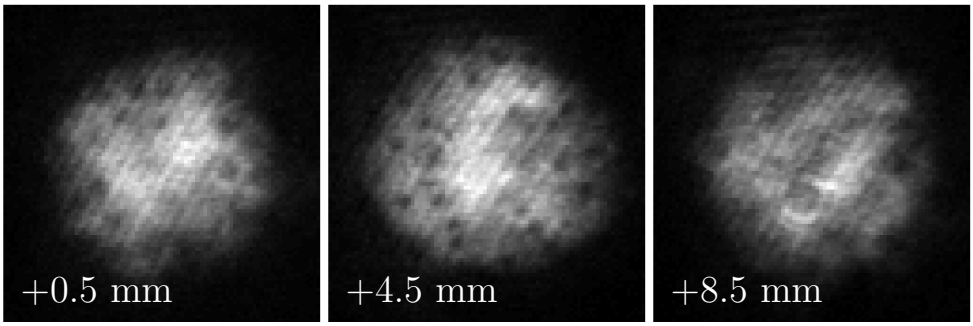


Figure 9.16: $120 \times 120$-$\mu$m Faraday images of the BEC after spinning for $t_{\rm s} = 2$ s and holding for $t_{\rm h} = 2$ s in a hybrid trap with $P_{1090} \sim 170$ mW, and then expanding for 12 ms. Images were taken with the Cascade EMCCD camera with imaging parameters: $\Delta = +2\Gamma$ from $|F = 2\rangle \rightarrow |F' = 3\rangle$, $t_{\rm exp} = 60$ $\mu$s. Images were taken at varying camera positions indicated by $\Delta F$ shown on each image, where $\Delta F$ denotes the relative axial Cascade position from the best-focus position inferred from the images shown in Fig. 9.13.

servation, the images shown in Fig. 9.16 seem to indicate that when imaging vortices after a period of 12 ms of expansion, the best-focus position for the Cascade EMCCD camera is actually at $\Delta F = 4.5$ mm.

At this point the discrepancy in the optimal focus position of the Cascade camera remains an open question. We suspect that some of the discrepancy may be accounted for by lensing effects that depend on the optical depth of the BEC as well as the detuning of the imaging light; these effects can be particularly prevalent near-resonance. In addition, feature size, and the axial extent of the BEC, may factor into the observation of a larger than expected DOF.

## 9.4 Superfluid dynamics: multiply-charged vortex dipoles

As part of our search for a reliable test target in the highly oblate BECs, we imaged vortex dipoles nucleated by swiping a 660-nm focused laser beam through the BEC in the manner described by Neely *et al.* [3]. Of particular note, we used Faraday imaging to take multiple *in situ* images of what we believe are multiply-charged vortex dipoles in a highly oblate BEC, nucleated by swiping a repulsive obstacle through the BEC at speeds above

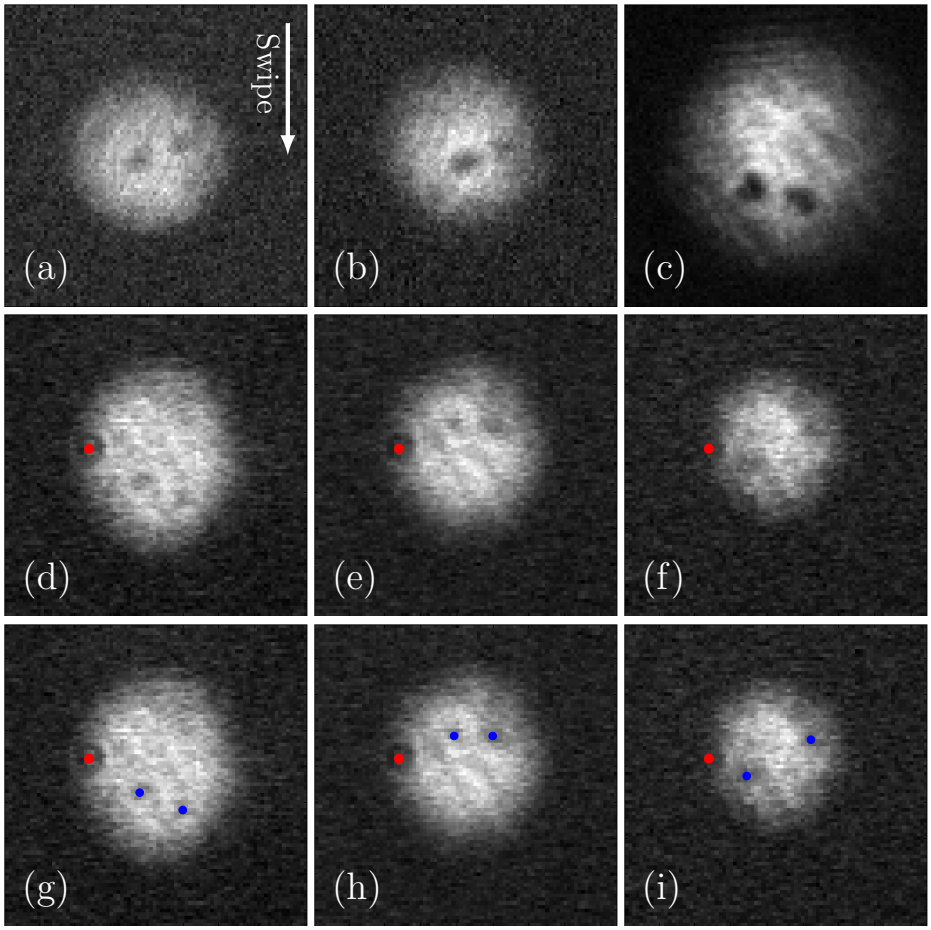


Figure 9.17: $120 \times 120$-$\mu$m Faraday images of a multiply-charged vortex dipole nucleated by swiping with a blue-detuned laser beam in a highly oblate BEC. (a)-(b) *In situ* Faraday images taken $t_{\mathrm{hold}} = 20$ ms (a) and $t_{\mathrm{hold}} = 35$ ms (b) after swipe. Imaging parameters: $\Delta/2\pi = -80$ MHz from $|F = 1\rangle \rightarrow |F' = 2\rangle$, $t_{\mathrm{exp}} = 10$ $\mu$s. (c) Expansion Faraday image after swipe and hold for $t_{\mathrm{hold}} = 35$ ms, then a 15 ms period of expansion. Imaging parameters: $\Delta/2\pi = -240$ MHz from $|F = 1\rangle \rightarrow |F' = 2\rangle$, $t_{\mathrm{exp}} = 10$ $\mu$s. (d)-(f) Set of three *in situ* Faraday images of a multiply-charged dipole in a single BEC. Imaging parameters: $\Delta/2\pi = -80$ MHz from $|F = 1\rangle \rightarrow |F' = 2\rangle$, $t_{\mathrm{exp}} = 10$, 20, and 30 $\mu$s for images (d), (e) and (f), respectively. The feature marked with the red dot is an imaging artifact and not a superfluid density feature. (g)-(i) Same set of three Faraday images with the loci of vorticity marked with blue dots. We clearly obtain three frames with good signal, although there is noticeable atom loss by the third frame.

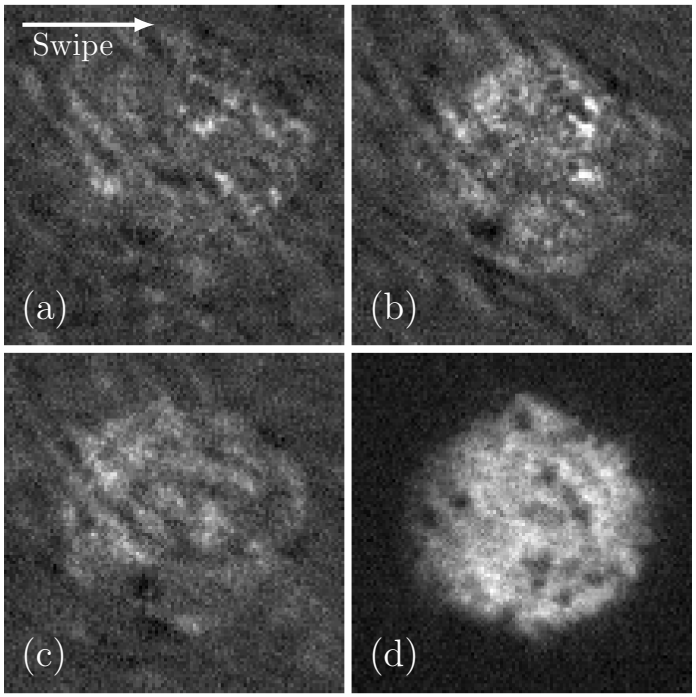


Figure 9.18: $120 \times 120$-$\mu$m dark-field images of a multiply-charged vortex dipole nucleated by swiping with a blue-detuned laser beam in a highly oblate BEC. (a)-(b) *In situ* dark-field images taken $t_{\rm hold} = 50$ ms after the swipe. (c) *In situ* dark-field image taken with no swipe for comparison. Dark-field imaging parameters: $D_{\rm mask} = 1.1$ mm, $\Delta = -6\Gamma$ from $|F = 2\rangle \rightarrow |F' = 3\rangle$, $t_{\rm exp} \sim 10$ $\mu$s. (d) Expansion Faraday image after swipe and hold for $t_{\rm hold} \sim 50$ ms, then a period of expansion. Imaging parameters: $\Delta = 3.5\Gamma$ from $|F = 2\rangle \rightarrow |F' = 3\rangle$, $t_{\rm exp} \sim 10$ $\mu$s.

the critical velocity reported by Neely *et al.* As with the *in situ* Faraday vortex lattice images discussed in Section 9.1, we suspect that these multiply-charged vortex dipoles are visible due to an increase in feature size. To obtain a back-of-the-envelope estimate of this feature size, we estimate that each loci of vorticity corresponds to a cluster of like-signed cores containing on the order of 2-3 vortices, which seems reasonable given the expansion image shown in Fig. 9.17(c). We estimate that the cores are at the corners of an equilateral triangle with legs of length $b \sim 3$ $\mu$m, giving us a density feature with a diameter on the order of 2-3 $\mu$m, sufficiently large to observe *in situ*. The observed poor core contrast is

consistent with several small features whose separation $b$ is less than the resolution of the imaging system.

Figures 9.18(a) and (b) show dark-field images for a similar swiping scenario. Although the signal-to-noise for the dark-field images is less than desirable, there is a clear difference between Figs. 9.18(a) and (b), and the reference dark-field image shown in Fig. 9.18(c) where the swipe was disabled. Figure 9.18(d) shows a representative Faraday image taken after a period of expansion but for similar swiping parameters.

## 9.5 Superfluid dynamics: shockwaves and solitons

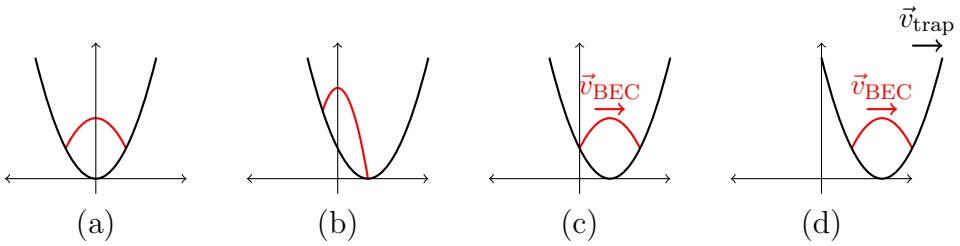


Figure 9.19: Trap timing sequence for pushing the BEC past a repulsive obstacle at speeds $v_{\rm BEC} > c_{\rm s}$. (a) $t < t_0$: BEC and harmonic trapping potential are centered at $y = 0$. (b) $t = t_0$: Center of trapping potential is shifted instantaneously by a distance $d$. (c) $t_0 < t \leq t_0 + \pi/2\omega_{\rm r}$: Trap position is held constant, while the BEC moves back to the center of the trap. After holding for one quarter of the radial trapping frequency $\omega_{\rm r} = 2\pi \times 8$ Hz, the BEC has reached maximum speed $v_{\rm BEC}(t_0 + \pi/2\omega_{\rm r}) = \omega_{\rm r} d$. (d) $t > t_0 + \pi/2\omega_{\rm r}$: Trap and BEC move together at a constant speed $v_{\rm trap} = v_{\rm BEC} = \omega_{\rm r} d$.

In this section we return to the search for the oblique dark solitons introduced in Sec. 4.5. As discussed in our previous treatment, we expect oblique dark solitons to form in the wake of an obstacle moving at speeds greater than the speed of sound. However, these oblique dark solitons quickly dissolve into vortex cores over timescales shorter than that required to ramp the 660-nm stirring beam off, expand the BEC, and image. To that end, the QVM2 offers several improvements that might aid in the soliton search. First, a 660-nm stirring beam can be directed downwards through the high-NA beam path shown

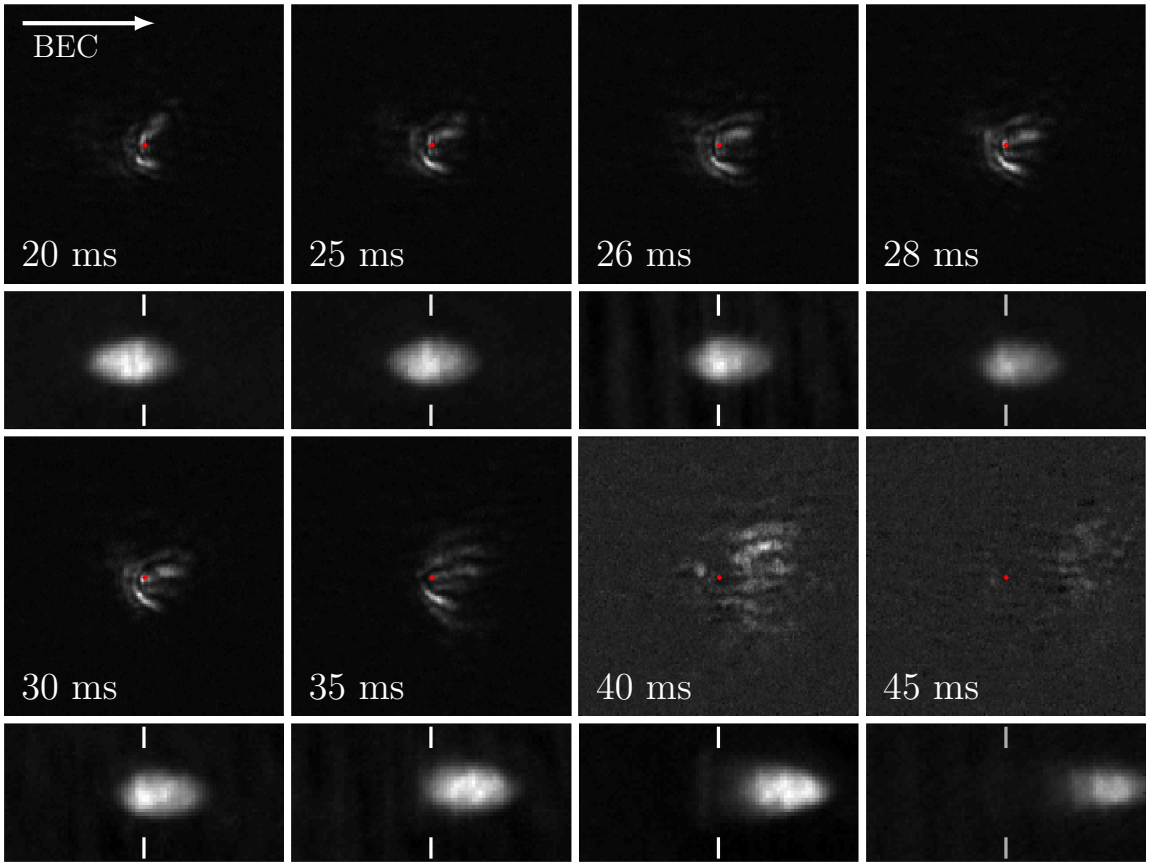


Figure 9.20: $200 \times 200$-$\mu$m *in situ* dark-field images taken along the vertical imaging axis, and corresponding $200 \times 100$-$\mu$m *in situ* phase-contrast images taken along the horizontal imaging axis, of a BEC confined in the TOP trap, moving past a 660-nm focused laser beam. The 660-nm potential is on the order of 2-3$\mu_0$ and held constant for the entire push coil ramp. The BEC moves past the 660-nm beam with a speed $v_{\mathrm{BEC}} \sim 2c_{\mathrm{s}}$, and all images were taken mid-ramp so as to avoid any shockwaves due to abruptly stopping the BEC. The red dot in the top-view, dark-field images and the vertical white lines in the side-view, phase-contrast images mark the approximate 660-nm beam position. Dark-field imaging parameters were: $D_{mask} = 1.5$ mm, $\Delta/2\pi = +40$ MHz from $|F = 1\rangle \rightarrow |F' = 2\rangle$, $t_{\mathrm{exp}} = 150$ $\mu$s, and $P_{\mathrm{BEC}} \sim 25$ $\mu$W.

in Fig. 8.19, allowing for a narrow obstacle with a focused $1/e^2$ beam radius $w_0 \sim$ 3-5 $\mu$m in the plane of the BEC. The 660-nm stirring beam propagates in the opposite direction as the imaging probe, and therefore the 660-nm beam is not incident on the camera and

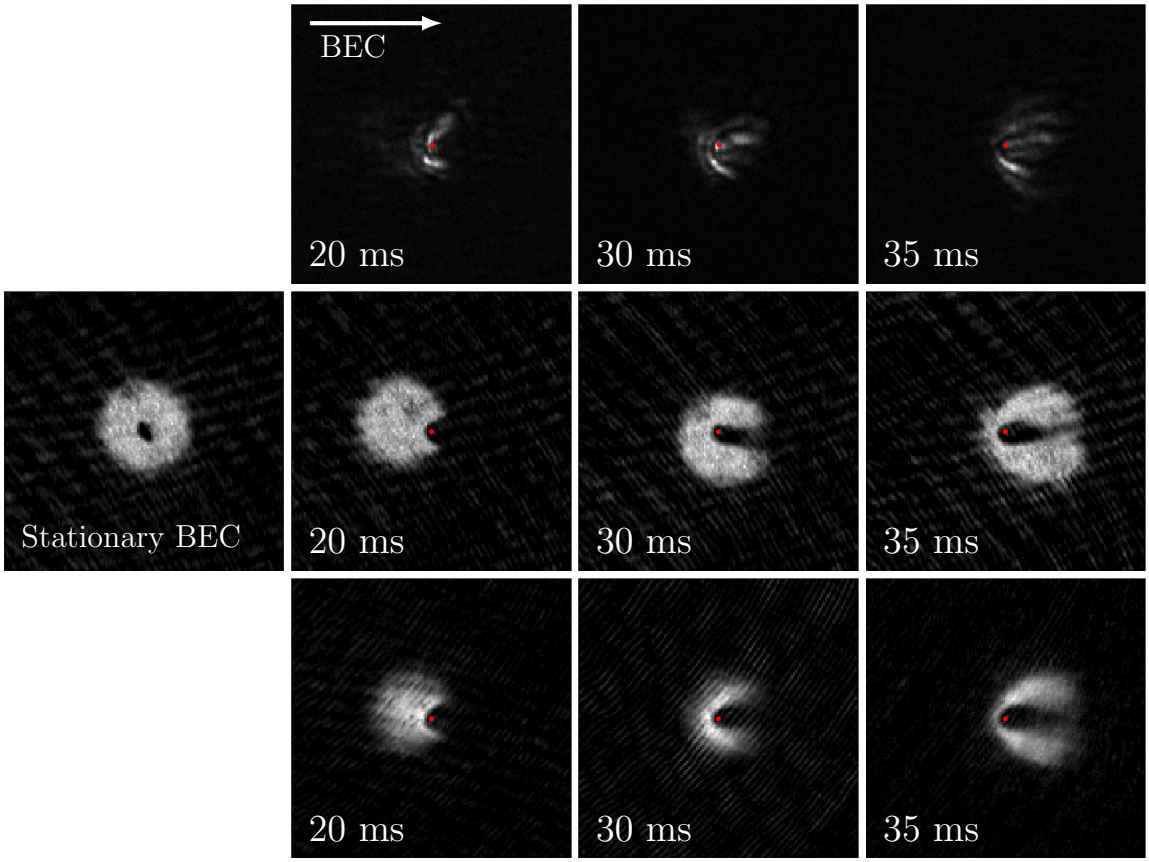


Figure 9.21: $200 \times 200$-$\mu$m *in situ* images showing a BEC in the $R_\mathrm{r} : R_\mathrm{z} = 2 : 1$ TOP trap moving past a 660-nm impenetrable obstacle at supersonic speeds. The 660-nm beam height is held constant at $U_0 \sim 2 - 3\mu_0$ through the entire push coil ramp, and located at the position marked with a red dot on the images. All images were taken mid-ramp so as to avoid any shockwaves due to abruptly stopping the BEC. Top row: Dark-field images taken using $D_\mathrm{mask} = 1.5$ mm, $\Delta/2\pi = 40$ MHz from $|F = 1\rangle \rightarrow |F' = 2\rangle$, $t_\mathrm{exp} = 150$ $\mu$s, $P_\mathrm{BEC} \sim 25$ $\mu$W ($P_\mathrm{fiber} = 100$ $\mu$W). Middle row: Bright-field images taken using the imaging parameters $\Delta/2\pi = 0$ MHz from $|F = 1\rangle \rightarrow |F' = 2\rangle$, $t_\mathrm{exp} = 100$ $\mu$s, $P_\mathrm{BEC}$ not known. Bottom row: Bright-field images taken using the imaging parameters $\Delta/2\pi = 0$ MHz from $|F = 1\rangle \rightarrow |F' = 2\rangle$, $t_\mathrm{exp} = 80$ $\mu$s, $P_\mathrm{BEC} \sim 375$ $\mu$W ($P_\mathrm{fiber} = 1.5$ mW).

can be left on during the image. Secondly, the improved resolution of the imaging system, combined with the dark-field imaging technique should enable us to observe density features such as dark solitons *in situ*. These two improvements combined should allow us to image

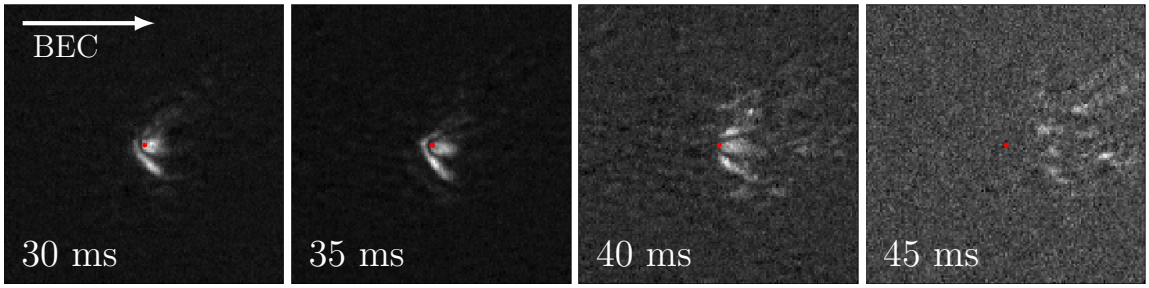


Figure 9.22: $200 \times 200$-$\mu$m *in situ* dark-field images of a highly oblate BEC moving past a 660-nm impenetrable obstacle at $v_{\mathrm{BEC}} \sim 2c_{\mathrm{s}}$. Imaging parameters: $D_{\mathrm{mask}} = 1.1$ mm, $\Delta/2\pi = 40$ MHz from $|F = 1\rangle \rightarrow |F' = 2\rangle$, $t_{\mathrm{exp}} = 100$ $\mu$s, $P_{\mathrm{BEC}} \sim 23$ $\mu$W. The 660-nm beam height is held constant through the entire push coil ramp, and located at the position marked with a red dot on the images. All images are mid-ramp so as to avoid any shockwaves due to abruptly stopping the BEC.

Table 9.1: Imaging parameters for Figs. 9.23 and 9.24 with feature widths $\sigma$ reported from the fits included in Fig. 9.24.

| Figure | Mask Size (diameter) | $\Delta/2\pi$ ($\|F = 1\rangle \rightarrow \|F' = 2\rangle$) | $t_{\mathrm{exp}}$ | $P_{\mathrm{BEC}}$ | $\sigma$ ($1/e^2$ radius) (left to right) |
|---|---|---|---|---|---|
| 9.23(a) 9.24(a) | 1.1 mm | 80 MHz | 20 $\mu$s | $\sim 50$ $\mu$W | 7.3 $\mu$m, 8.5 $\mu$m, 7.8 $\mu$m, 7.1 $\mu$m, 6.0 $\mu$m |
| 9.23(b) 9.24(b) | 1.1 mm | 40 MHz | 100 $\mu$s | $\sim 23$ $\mu$W | 2.8 $\mu$m, 5.0 $\mu$m, 3.4 $\mu$m, 4.8 $\mu$m, 7.4 $\mu$m, 2.9 $\mu$m |
| 9.23(c) 9.24(c) | 1.5 mm | 40 MHz | 150 $\mu$s | $\sim 25$ $\mu$W | 6.8 $\mu$m, 7.9 $\mu$m, 4.5 $\mu$m, 3.6 $\mu$m, 5.6 $\mu$m, 5.9 $\mu$m |
| 9.23(d) 9.24(d)* | 2.1 mm | 40 MHz | 100 $\mu$s | $\sim 25$ $\mu$W | 3.3 $\mu$m, 2.2 $\mu$m, 2.7 $\mu$m, 3.8 $\mu$m, 4.3 $\mu$m, 6.4 $\mu$m |
| * 2nd image from left Fig. 9.23(d) | 2.1 mm | 30 MHz | 100 $\mu$s | $\sim 25$ $\mu$W | |

density features that follow in the wake of the obstacle created by the 660-nm beam.

We used a magnetic push coil to move the BEC rapidly past the 660-nm barrier at speeds $v_{\mathrm{BEC}} \sim 2c_{\mathrm{s}}$, where $c_{\mathrm{s}} = 1700$ $\mu$m/s is the speed of sound for our system parameters

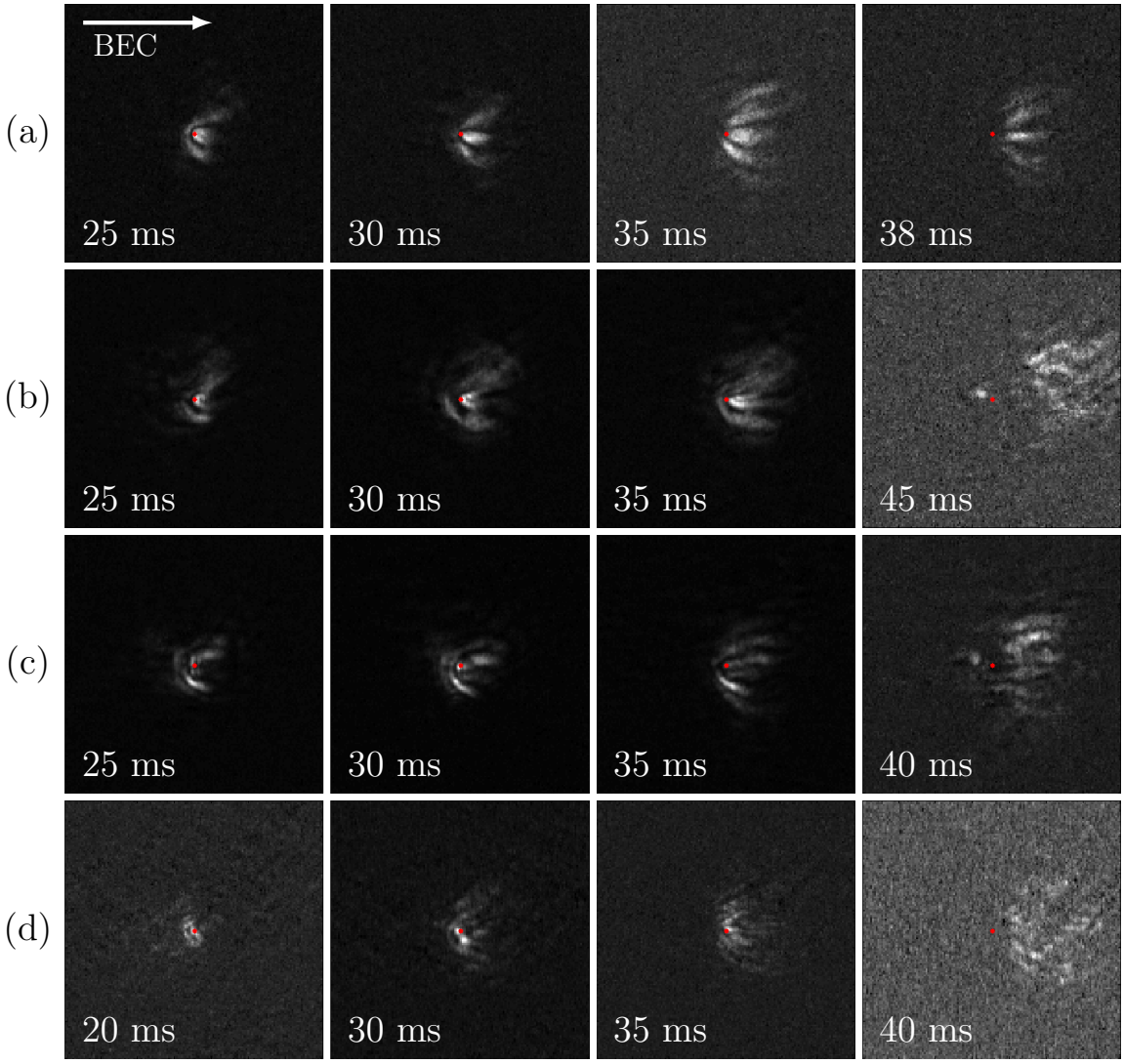


Figure 9.23: $200 \times 200$-$\mu$m *in situ* dark-field images showing a BEC in the $R_r : R_z = 2 : 1$ TOP trap moving past a 660-nm impenetrable obstacle at $v_{BEC} \sim 2c_s$ for varying mask size $D_{mask} \sim 1.4$ mm (a) and (b), 1.6 mm (c), and 2 mm (d). Imaging parameters are reported in Table 9.1. The 660-nm beam height is held constant through the entire push coil ramp, and located at the position marked with a red dot on the images. All images are mid-ramp so as to avoid any shockwaves due to abruptly stopping the BEC.

[3]. Here the BEC moves linearly past the barrier, with the initial and final position of the 660-nm beam outside of the BEC. In order to avoid generating density features in the BEC

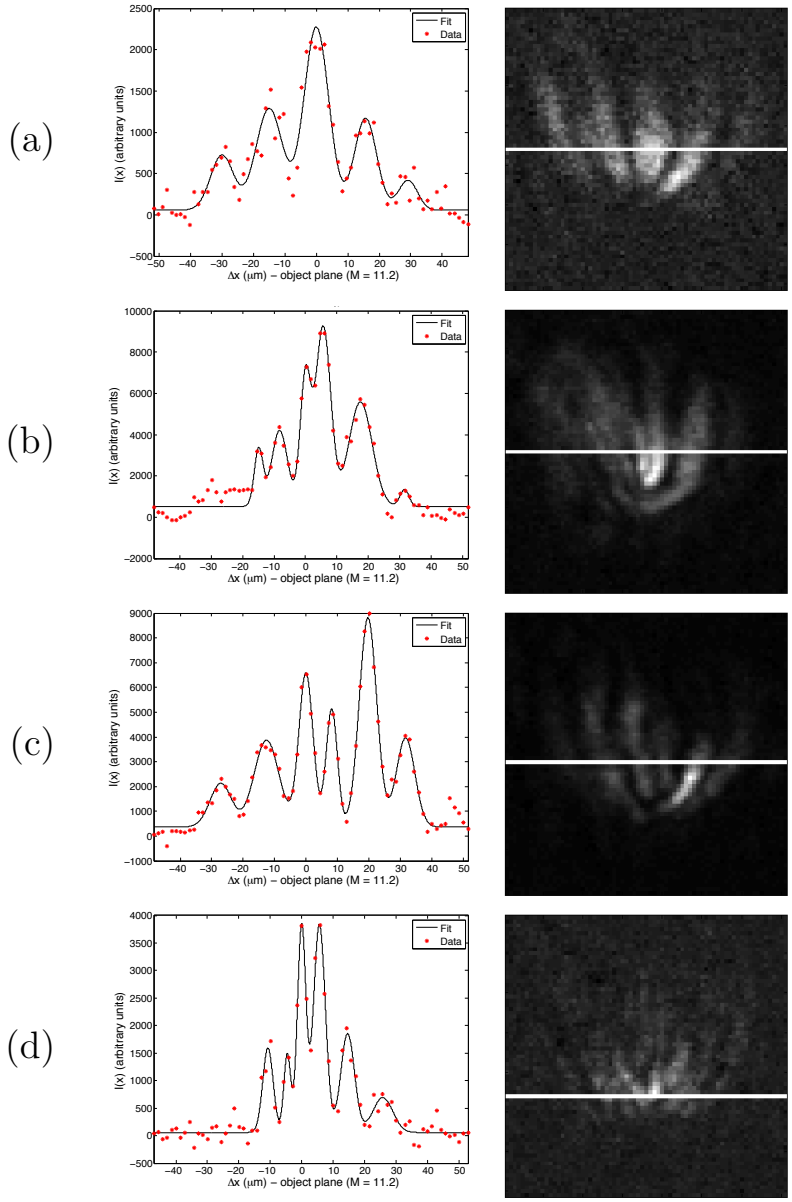


Figure 9.24: Fit to shockwave cross sections from *in situ* dark-field images taken with varying mask sizes and detunings. The plot on the left is the best fit of five (a) or six (b)-(d) Gaussians to the density features shown in the dark-field image on the right. The images were taken 35 ms into the linear push with $v_{\mathrm{BEC}} \sim 2c_{\mathrm{s}}$. Imaging parameters and $1/e^2$ half widths for each Gaussian in the fit are reported in Table 9.1.

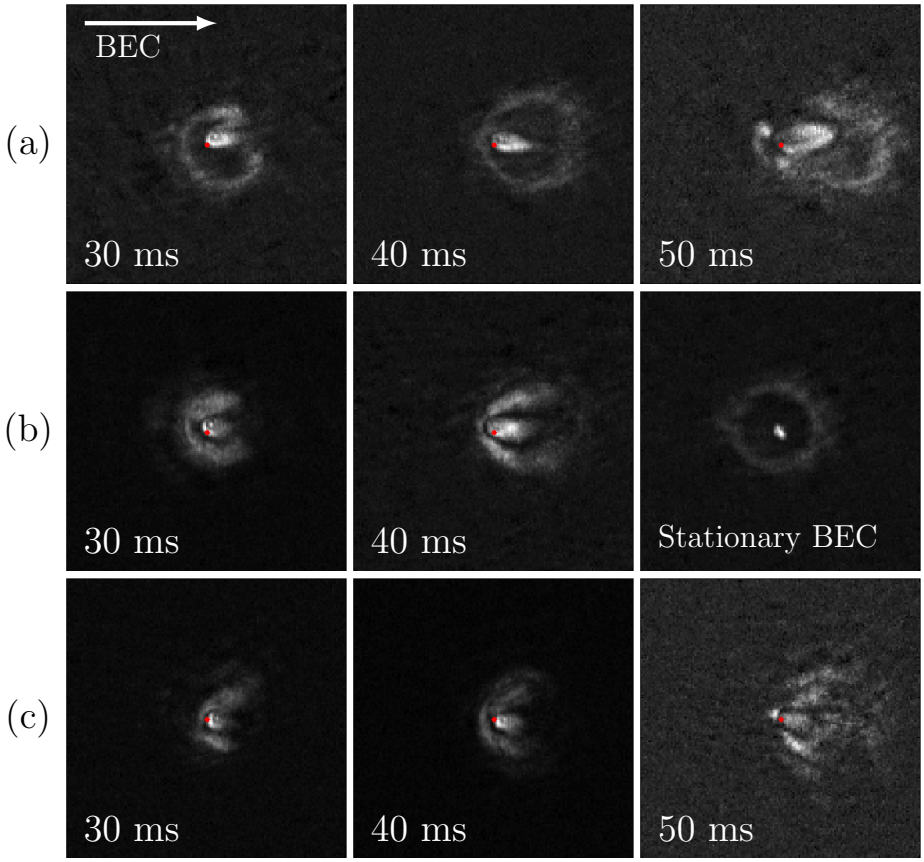


Figure 9.25: $200 \times 200$-$\mu$m *in situ* dark-field images showing a BEC in the $R_r : R_z = 2 : 1$ TOP trap moving past a 660-nm impenetrable obstacle at $v_{BEC} \sim c_s$. The 660-nm beam height is held constant through the entire push coil ramp, and located at the position marked with a red dot on the images. All images are mid-ramp so as to avoid any shockwaves due to abruptly stopping the BEC. (a) Images taken using $D_{mask} = 800$ $\mu$m, $\Delta = 0$ MHz, $P_{BEC} \sim 110$ $\mu$W ($P_{fiber} = 450$ $\mu$W), and $t_{exp} = 20$ $\mu$s. (b) The two leftmost images were taken using $D_{mask} = 800$ $\mu$m, $\Delta/2\pi = 40$ MHz, $t_{exp} = 20$ $\mu$s, $P_{BEC} \sim 45$ $\mu$W ($P_{fiber} = 180$ $\mu$W). The rightmost image is of a stationary BEC with the 660-nm beam on and approximately centered in the BEC, taken with the same parameters as those used in (a). (c) Images were taken using $D_{mask} = 1.1$ mm, $\Delta/2\pi = 40$ MHz, $t_{exp} = 20$ $\mu$s, $P_{BEC} \sim 45$ $\mu$W ($P_{fiber} = 180$ $\mu$W).

due to the acceleration involved at the beginning and end of the push coil ramp, we took advantage of the harmonic confining potential as shown in Fig. 9.19. Initially the BEC is held in either the TOP or the hybrid trap as shown in Fig. 9.19(a). At the beginning of

the push coil timing sequence, the push coil current is jumped to some initial value such that the trap is displaced a distance $d$ as shown in Fig. 9.19(b). After waiting a quarter of the period of the harmonic trap, the BEC now has a speed of $v_{\mathrm{BEC}} = \omega_{\mathrm{r}} d$, where $\omega_{\mathrm{r}}$ is the radial frequency of the harmonic trap as shown in Fig. 9.19(c). At this point the push coil current is increased linearly such that $v_{\mathrm{trap}} = v_{\mathrm{BEC}}$. We make sure to image the BEC prior to the end of the push coil ramp in order to avoid deceleration effects.

Figure 9.20 shows a sequence of dark-field images taking along the vertical imaging axis, and corresponding phase-contrast images taken along the horizontal imaging axis ($x$-axis). Each pair of dark-field and phase-contrast images are from the same BEC, with the dark-field image taken with the Cascade 512B EMCCD camera ($M = 11.2$) and the phase-contrast image taken with the Pixis 1024 BR CCD camera ($M = 5.15$). The images were taken at varying times during the push coil ramp with all times measured with respect to the start of the linear ramp portion of the push coil timing sequence. The stationary 660-nm beam position is denoted with a red dot in the dark-field images and with a white vertical line in the phase-contrast images. In the frame of the BEC, the 660-nm obstacle moves through the BEC at supersonic speeds, and we observe a buildup of density on the leading edge of the beam. Eventually we observe density features trailing the beam as shown in the dark-field images taken at 35 ms and 40 ms.

The dark-field images are somewhat difficult to interpret, so we provide corresponding bright-field images in Fig. 9.21. We note that while there is a build-up of density on the left side of the 660-nm repulsive obstacle as shown in the bottom two rows of Fig. 9.21, there are extra density features that show up only in the dark-field images. In particular, the dark-field image in the top row of Fig. 9.21, corresponding to $t = 35$ ms into the push coil ramp, shows six distinct density features trailing the beam, whereas from the bright-field image we would expect to see two or at most four density features. We suggest that the density features observed in the dark-field images are due to small, sharp density features within the BEC such as shockwaves [96], that are not readily observable in bright-field.

In any case, the dark-field imaging accentuates the regions of the BEC associated with rapid changes in density. We note that the sag trap is not ideal for observations of dark solitons given that the $R_{\rm r} : R_{\rm z} = 2 : 1$ geometry is more conducive to generating 3D density features such as vortex rings in the wake of the obstacle, which as we discuss in Chapter 5, complicate matters since our imaging techniques integrate the BEC density along the imaging axis. Our primary reason for searching for oblique dark solitons in the TOP trap was that the signal due to density features was observed to be much higher for BECs confined in the TOP trap than for the highly oblate BECs confined in the hybrid trap, shown in Fig. 9.22.

As part of our search for oblique dark solitons we varied mask size, detuning and speed. Figure 9.23 shows dark-field images for varying mask size, and Fig. 9.24 shows the best fit of a series of Gaussians to a cross section across the density features trailing the 660-nm beam for the set of images from Fig. 9.23 corresponding to 35 ms into the push coil ramp. Lastly, Fig. 9.25 shows dark-field images for a BEC moving past a 660-nm beam at a speed $v_{\rm BEC} \sim c_{\rm s}$ with varying mask size and detuning. In particular, note the difference between the first two images in Fig. 9.25(a) corresponding to $\Delta/2\pi = 0$ MHz and those of Fig. 9.25(b) with $\Delta/2\pi = 40$ MHz. The images in Fig. 9.25(a) show the edge of the BEC, whereas the ones in Fig. 9.25(b) do not.

## 9.6 Conclusions and limitations

Table 9.2 lists the sizes of the features observed with the QVM2 and provides an estimate of the actual size of the features. We note from our numerics that we can expect an increase of roughly a factor of two between the $\mathrm{FWHM}_{\rm obj}$ of a vortex core and the observed dark-field vortex signal, reported as $\mathrm{FWHM}_{\rm img}/M$, where $\mathrm{FWHM}_{\rm obj}$ and $\mathrm{FWHM}_{\rm img}$ are the FWHM in the object and image planes respectively. While the relative size of a vortex (image/object) appears to be greater than that observed for the 1-$\mu$m-radius pinhole, we are dealing with two very different scenarios in that the pinhole is essentially a binary

amplitude mask, whereas dark-field imaging looks at the phase imprinted on the probe beam when passing through a BEC, such that the BEC is phase mask.

Table 9.2: Summary of FWHM from dark-field images.

| **Object** | **Object Size** | **FWHM from Image ($\mathbf{FWHM_{img}/M}$)** | **Mask Diameter** |
|---|---|---|---|
| Nanofiber | $D \sim 500$ nm (estimated) | 1.4 $\mu$m | 370 $\mu$m (28 AWG mag. wire) |
| Vortex (Numerics) | FWHM = 780 nm | 2.03 $\mu$m | 1.04 mm |
| Pinhole (Numerics) | $D = 1$ $\mu$m | 1.56 $\mu$m | N/A |
| Pinhole (Numerics) | $D = 2$ $\mu$m | 1.63 $\mu$m | N/A |
| Pinhole (Experiment) | $D = 2$ $\mu$m | 1.9 $\mu$m | N/A |
| Solitons (Experiment) | FWHM $\sim 1.1$ $\mu$m (estimated) | 2.3 $\mu$m - 3.1 $\mu$m | 690 $\mu$m (22 AWG mag. wire) |
| Vortex (Experiment) | | 3.4 $\mu$m - 3.8 $\mu$m | NA - Faraday |
| Vortex (Experiment) | | 5.7 $\mu$m - 8.4 $\mu$m | NA - Bright-field |
| Vortex (Experiment) | | 3.5 $\mu$m - 7.3 $\mu$m | 800 $\mu$m |
| Shockwave (Experiment) (See Fig. 9.24(c)) | | 4.2 $\mu$m - 9.3 $\mu$m | 1.5 mm |

In general, we observe the QVM2 to be capable of imaging density features with theoretical $\mathrm{FWHM_{obj}}$ on the order of 1 $\mu$m when these features are arranged in some regular pattern, such as a lattice of vortex cores and an array of solitons which have $\mathrm{FWHM_{obj}}$ on the order of 1 $\mu$m. However, despite advances in *in situ* imaging of vortices with BECs confined in weak hybrid traps, we have not been able to observe individual vortex cores *in situ* in highly oblate BECs, which is highly desired for our studies of 2DQT, as vortex distributions associated with 2DQT are by definition disordered. Based on the images of

the dark soliton array shown in Figs. 9.11 and 9.12, we are relatively confident that the imaging system is capable of resolving vortex cores, and we suspect that the problem lies in achieving a sufficient signal-to-noise ratio. While more tweaking of mask size, probe detuning and focus should help improve signal-to-noise, we suspect that the primary limitation is the quality of the probe beam. Given that we are dealing with very low signals, the approximately 1% of the probe beam power that makes it past the dark-field mask adds a significant amount of background noise to the image and makes the EMCCD camera less effective at boosting the dark-field vortex signal. The leakage of the probe beam past the mask may be due to light scattered off dust fused to the BEC cell, or to the probe beam profile deviating from a smooth Gaussian.

New measurements of the best-focus position shown in Fig. 9.13 indicate that, for the BEC parameters tested to date, the system does not actually have the capability of imaging vortices in a BEC with tight axial confinement; core signal is indistinguishable from noise for BEC aspect ratios above $R_{\mathrm{r}} : R_{\mathrm{z}} \sim 3 : 1$. We suspect that this limitation is due in part to the decrease of healing length with increased axial confinement; see Sec. 9.1 for a discussion of BEC parameters affecting healing length and vortex core size. When designing the QVM2, we chose a microscope objective with NA $\sim 0.25$ because we wanted to resolve two vortex cores separated by approximately 2 $\mu$m, rather than resolve the submicron structure of the vortex core. Thus, we let the vortex core separation set the lower limit on the resolution required for the QVM2. However, based on our subsequent online QVM2 tests, we suspect that the NA of the microscope objective fails to collect sufficient high-angle signal diffracted by the smallest vortex cores, resulting in a loss of valuable vortex core signal. The vortex lattice images discussed in Sec. 9.1 show high vortex core signal which suggests that above some threshold feature size, the QVM2 collects plenty of vortex core signal. Unfortunately, vortex cores in the highly oblate BECs that we currently routinely create for studies of 2DQT may be below that threshold.

At the same time, we note that, for a given atom number, the decrease in healing length

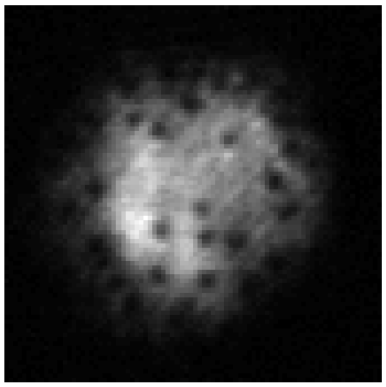

Figure 9.26: $120 \times 120$-$\mu$m Faraday image of a BEC after 20 ms of 2D expansion (1090-nm beam remains on during expansion) from a weak hybrid trap ($P_{1090} \sim 90$ mW). Image was taken with the Cascade EMCCD camera with imaging parameters: $\Delta = +2\Gamma$ from $|F = 2\rangle \rightarrow |F' = 3\rangle$, $t_{\rm exp} = 100$ $\mu$s, $P_{\rm BEC} \sim 250$ $\mu$W (probe). The BEC vertical position is $V_{\rm pix} \sim 593$ pixels, measured with the Pixis CCD camera.

between a trap with $\omega_{\rm z} \sim 2\pi \times 16$ Hz and a trap with $\omega_{\rm z} \sim 2\pi \times 70$ Hz is only $\sim 25\%$ which suggests that the dramatic drop in vortex core signal when switching from the TOP trap to a tight hybrid trap may be more complicated than simply a decrease in feature size. Both dark-field and our implementation of Faraday imaging rely on the phase shift of light as it passes through the BEC, which depends on the integrated atom density along the imaging axis $\tilde{n}(x, y)$, as discussed in Chapter 3. If we assume the same number of atoms in the weak ($R_{\rm r} : R_{\rm z} \sim 3 : 1$) and the tight ($R_{\rm r} : R_{\rm z} \sim 10 : 1$) hybrid traps, then a BEC confined in the weak hybrid trap will have larger $\tilde{n}(x, y)$ and should therefore impose a larger phase shift on the imaging probe, resulting in a higher vortex signal. Alternatively, the mask size and detuning chosen to optimize signal from the weak hybrid trap might not be optimal for the tight hybrid trap, especially when imaging close to resonance where phase-winding is prevalent.

At this juncture, the QVM2 is probably best utilized for single-shot imaging of vortex cores after a period of expansion. We include a representative expansion image in Fig. 9.26 as proof that, even without *in situ* imaging, the QVM2 is still capable of capturing quality

images with clear vortex cores. In particular, the image shown in Fig. 9.26 demonstrates 2D expansion where the entire expansion takes place within the 1090-nm beam. This type of expansion is enabled by the increased magnification and resolution of the QVM2.

## 9.7 Quantum vortex microscope mark III

The QVM2 images presented in this chapter provide further proof that imaging tiny transmission features *in situ* in a BEC is indeed possible. Extension of the imaging techniques presented in this dissertation beyond proof-of-principle and into the realm of useful scientific tools is limited as always by signal-to-noise. At this point, we suggest several routes to improving the signal-to-noise and leave it to a certain long-suffering advisor and future graduate students to decide which combination, if any, to pursue.

First, regardless of the imaging techniques pursued with the QVM3, trap design will need to be taken into consideration. Based on the vortex lattice images presented in Sec. 9.1, we estimate that a factor of two increase in healing length would be sufficient to reliably image vortex cores *in situ*. With that in mind, the biggest gains in vortex core signal may come from designing a trap with weaker radial confinement. At the same time, a DC trap where the net magnetic field is aligned along the imaging access would allow access to cycling transitions and simplify the search for good imaging parameters, especially for Faraday imaging. Lastly, a flat-bottomed trap would allow for a more consistent healing length across the BEC.

Second, proper focusing of the imaging system is crucial both for obtaining good signal-to-noise and for accurately interpreting the images. To that end, we will need to come up with a reproducible test target that can be used to efficiently find focus and optimal alignment of the imaging system. Such a test target needs to have an axial extent that lies within the DOF of the QVM3 and density features of a similar size and shape to a vortex core. Ideally the size of these density features would be able to be smoothly tuned as we narrow in on focus. An optical lattice superimposed on a highly oblate BEC could

fulfill these criteria. Spinning in a weak hybrid trap has recently shown promise as a test target, although it is unclear how consistently vortex cores are generated as the axial trap strength is increased.

Third, the QVM3 will most likely need a higher NA objective than the one used for the QVM2. While we do not need sufficient NA to observe the sub-micron structure of the vortex core, we suspect that part of the limitation on the size of the observable density features was due to the relatively low NA of our microscope objective. Smaller features diffract light into higher angles, and the NA $\sim 0.25$ of the QVM2 may have cut off too much of the vortex core signal. While choosing a higher NA objective for the QVM3 will lower its DOF, our vortex lattice images indicate that vortices can be observed even when the axial extent of the BEC exceeds the DOF of the imaging system. There will always be a tradeoff between NA and DOF but our observations with the QVM2 suggest that we should sacrifice DOF before NA.

Lastly, we consider the choice between dark-field imaging and Faraday imaging. Based on the multi-shot images of vortex lattices, dark-field imaging is probably the least destructive technique. In theory, with the appropriate choice of mask-size and detuning, dark-field imaging should be able to entirely remove both the unrefracted component of the probe beam, and the bulk BEC background, with just the light associated with vortex cores reaching the camera. In practice, we found that weakly-scattered probe light contributed significantly to increasing the noise in the image. Further progress with *in situ* imaging of vortex cores using dark-field imaging will require careful shaping of the probe intensity profile to minimize probe power transmission past the dark-field mask; removal of dust and other potential scatters from the BEC vacuum cell; manufacture of a set of circular masks with diameters ranging from about 500 $\mu$m to 2 mm, with open apertures of $r = 12$ mm, and printed on thin, AR-coated coverslips; and an extensive search of imaging parameters.

With Faraday imaging the probe beam quality is no longer an issue. Improvements would involve purchasing high-quality wave plates; working in a DC trap with a well-defined

magnetic field along the imaging axis; and an extensive search of imaging parameters, although mask size is no longer included in the parameter space. The bulk BEC signal is not blocked in Faraday imaging, so distinguishing tiny density features in the bright background of the bulk BEC may end up being a limitation. However, Faraday imaging in conjunction with a trap that has been designed for BECs with a larger healing length may circumvent this problem.

# Chapter 10
# Conclusion

We experimentally explored a number of vortex nucleation techniques with the goal of generating an initial vortex distribution in a highly oblate BEC that exhibits robust signatures of turbulence. These techniques included spinning the BEC in the hybrid trap, modulating the power of a stationary 660-nm laser beam directed through the BEC, and circular stirring with a 660-nm beam at varying speeds and beam powers. We found that it is relatively straightforward to nucleate vortex distributions that exhibit phenomenological aspects of turbulence, i.e. large disordered distributions with a range of inter-vortex separations. Many of these states are long-lived which is ideal for studies of 2DQT, however heating, injection of acoustic energy, and bulk BEC oscillations are still areas of concern. Lastly, we present a technique for the controlled injection of an arbitrary number of vortex clusters consisting of several like-signed vortex cores. We anticipate that this type of cluster generation may be particularly useful for generating the vortex distributions with large point-vortex energies desirable for observation of Onsager's negative temperature states.

Lastly, these vortex techniques were largely developed prior to the imaging gains made with the QVM2, and we anticipate that when *in situ* vortex imaging is successfully extended to highly oblate BECs we will be able to better characterize and fine-tune these vortex nucleation mechanisms. As we try to keep pace with the current theoretical progress in 2DQT, we anticipate moving to trapping configurations that enable larger and more uniform BECs confined in novel trapping potentials. With the exception of spinning the BEC, the vortex nucleation techniques presented in this dissertation should be extendable to these new BEC geometries.

We demonstrated single-shot *in situ* imaging of a lattice of vortex cores in a BEC with the QVM1, and extended our imaging capabilities to take multiple *in situ* images of a

vortex lattice within a *single* BEC with the QVM2. These results represent the first *in situ* observations of bare vortex cores in dilute-gas single-component BECs, and the current state-of-the-art of *in situ* imaging of vortex distributions; together with the development of the QVM2, they represent the contribution of this dissertation towards progress in imaging 2DQT and vortex dynamics in BECs. In addition to multi-shot *in situ* imaging of a vortex lattice, we used the QVM2 to image shockwaves in a BEC confined to the TOP trap, and to image arrays of dark solitons formed by merging two BECs in the hybrid trap. While our attempts at imaging single vortex cores within the highly oblate BECs formed in the hybrid trap were largely unsuccessful, our *in situ* observation of dark solitons demonstrates that the QVM2 can resolve fine density features of approximately the same size and shape as a vortex core.

The observation of dark solitons with the QVM2 leads us to suspect that our inability to image vortices in the highly oblate BECs is largely due to low signal-to-noise rather than the resolution of the imaging system, although the two are ultimately coupled. In particular, when imaging in dark-field, weakly scattered probe light results in significant background noise compared to the weak signal due to a single vortex core, and limits the effectiveness of an EMCCD camera in boosting the vortex signal. While improving signal-to-noise in the dark-field images has proven to be much more difficult than initially anticipated, we believe the current signal-to-noise issues are largely technical, rather than an ultimate limit of *in situ* vortex imaging or the dark-field imaging technique. We anticipate that the next iteration of the quantum vortex microscope, the QVM3, designed based on the information acquired regarding the limitations of the QVM2, will enable *in situ* imaging of arbitrary vortex distributions in a highly oblate BEC, whether through improved imaging or careful trap design to increase the vortex core size.

*In situ* imaging of vortex distributions has the potential to revolutionize the study of BEC vortex dynamics. Single-shot *in situ* imaging would enable studies of vortex distributions in toroidal or flat-bottomed potentials, where the lack of self-similar expansion means

that expansion-dependent vortex imaging techniques are not sufficient. In addition, single-shot *in situ* imaging allows for immediate observation of the state of the BEC and should enable observation of short lived density features such as oblique dark solitons formed in the wake of a rapidly moving impenetrable obstacle. The acquisition of two images of a vortex distribution from a single BEC would enable the study of vortex decay rates and studies of the rate at which vortices detach from a pinning potential. Two *in situ* images of a single vortex distribution would allow us to directly link final and initial vortex states, allowing us to avoid some of the uncertainty due to shot-to-shot fluctuations in the initial vortex distribution, and lessening our dependence on measurements of vortex number statistics. Lastly, the rapid acquisition of many, on the order of ten or more, images of a single vortex distribution would give unprecedented access to vortex dynamics, potentially enabling the identification of the circulation of individual vortex cores, as well as direct tests of the point-vortex model.

While implementation of all of these vortex detection goals is a formidable challenge, the realization of even a few of these goals could revolutionize the study of 2DQT in atomic gases, and eventually help answer some of the most intriguing, difficult, and long-standing questions about turbulence. This dissertation represents the first efforts dedicated to eventual realization of these goals, and serves as a foundation for future work in this direction.

# Appendix A

# Reprint: Experimental Methods for Generating Two-Dimensional Quantum Turbulence in Bose-Einstein Condensates

The following manuscript was prepared as an article for the Annual Review of Cold Atoms and Molecules, and the draft reproduced here can be found on arXiv (arXiv:1303.4764). A selection of the results presented in this manuscript are discussed in Chapter 4. The final version of the manuscript was published in the Annual Review of Cold Atoms and Molecules, Vol. 1. Reference: K. E. Wilson, E. C. Samson, Z. L. Newman, T. W. Neely, and B. P. Anderson, *Experimental Methods for Generating Two-Dimensional Quantum Turbulence in Bose-Einstein Condensates*, Annual Review of Cold Atoms and Molecules, Vol. 1, Chpt. 7, pages 261-298 (2013). Copyright (2013) by World Scientific Publishing.

# Experimental Methods for Generating Two-Dimensional Quantum Turbulence in Bose-Einstein Condensates

K. E. Wilson, E. C. Samson*, Z. L. Newman, T. W. Neely†, and B. P. Anderson

*College of Optical Sciences, University of Arizona,*
*1630 E. University Blvd., Tucson, Arizona 85711, USA*

Bose-Einstein condensates of dilute gases are well-suited for investigations of vortex dynamics and turbulence in quantum fluids, yet there has been little experimental research into the approaches that may be most promising for generating states of two-dimensional turbulence in these systems. Here we give an overview of techniques for generating the large and disordered vortex distributions associated with two-dimensional quantum turbulence. We focus on describing methods explored in our Bose-Einstein condensation laboratory, and discuss the suitability of these methods for studying various aspects of two-dimensional quantum turbulence. We also summarize some of the open questions regarding our own understanding of these mechanisms of two-dimensional quantum turbulence generation in condensates. We find that while these disordered distributions of vortices can be generated by a variety of techniques, further investigation is needed to identify methods for obtaining quasi-steady-state quantum turbulence in condensates.

## 1. Introduction

Dilute-gas Bose-Einstein condensates (BECs) present unique opportunities for studying quantum fluid dynamics due to the wide range of experimental tools available for probing and manipulating condensates, and the quantitative accuracy available with theoretical and numerical approaches [1]. Experimentally, magnetic and laser fields can be arranged to create a wide variety of trapping configurations and geometries. Superfluidity hallmarks such as persistent currents and quantized vortices [2; 3] may be precisely generated and their dynamics probed, and numerous measurement techniques allow for observations of density and quantum phase distributions. Regarding simulations of superfluid dynamics in BECs, common numerical approaches utilize the Gross-Pitaevskii equation (GPE), a nonlinear Schrödinger equation that incorporates a mean-field approximation to represent the BEC with an order parameter, the familiar macroscopic condensate wavefunction [4]. Numerous variants of the GPE such as those that model finite-temperature environments extend the predictive accuracy of simulations [5]. Taken together, these features allow for highly synergetic experimental, numerical, and theoretical explorations of superfluid dynamics.

In this respect, Bose-Einstein condensates may be ideally suited for investigating quantum turbulence and the dynamics of interacting quantized vortices in compressible quantum fluids; for recent reviews of this subject see Refs. [6] and [7] and the references therein. In superfluids, vorticity appears in the form of superfluid-free vortex cores about which there is quantized flow circulation [2]. Whether in superfluid helium or trapped BECs, quantum turbulence is often phenomenologically

*Current address: School of Physics, Georgia Institute of Technology, Atlanta, Georgia 30332, USA.
†Current address: School of Mathematics and Physics, University of Queensland, Qld 4072, Australia.

described as a tangled distribution of these quantized vortices throughout the fluid [8; 9], and recent work with superfluid helium provides fascinating visual evidence for these vortex distributions [10; 11].

In BECs, quantum turbulence is relevant to early investigations on the formation of large vortex lattices [12] and routes to vortex nucleation by dynamical instabilities [13; 14], and has been experimentally observed and explicitly addressed in these contexts [15; 16; 17; 18]. More recent experiments have been principally dedicated to the study of quantum turbulence phenomena and the related vortex distributions [19; 20; 21; 22]. Images of vortex tangles in BECs have also been experimentally obtained [17; 19]. Yet while BECs readily permit vortex observations, other aspects of turbulence remain significant experimental challenges within the BEC field. Notably, direct measurement of kinetic energy spectra is an open problem, whereas such measurements of liquid helium have allowed direct comparison of classical and quantum fluid turbulent energy spectra [23]. The different approaches and systems for studying quantum turbulence are therefore complementary, with BEC research playing a potentially important role in understanding the broad subject of turbulence, particularly in the context of compressible quantum fluids.

More specifically, BECs are now beginning to contribute to the development of an understanding of *two-dimensional* (2D) turbulence [24; 25; 26] in compressible quantum fluids. In the basic manifestation of 2D classical turbulence (2DCT), energy and enstrophy[a] are injected into a fluid at a small length scale, and patches of vorticity merge and lead to the development of large-length-scale flow. This is opposite to the dynamics of the familiar energy cascade of three-dimensional (3D) turbulence in a classical fluid, in which large-scale flows continuously decay to smaller-scale flows that are eventually dissipated by viscous damping. This *inverse* energy cascade of 2DCT has been studied for decades and numerous excellent reviews exist on 2DCT [27; 28; 29].

### 1.1. *Experimental study of two-dimensional quantum turbulence in BECs*

In order to study two-dimensional *quantum* turbulence (2DQT) in a BEC, one might envision subjecting the BEC to continuous injection of energy and vorticity. Dissipation of energy may also exist, perhaps by thermal damping that could induce vortices to exit the BEC at its boundary, or perhaps due to vortex-antivortex annihilation. A balance between forcing and dissipation can be envisioned to lead to a statistically steady degree of turbulence in a BEC. We might picture such a state as an approximately constant mean number of vortices in the BEC, since enstrophy in a quantum fluid is proportional to the number of vortices [30; 31]. With the likelihood of future experimental methods for observing vortex dynamics and measuring energy spectra, we further imagine a scenario in which 2DQT can be experimentally and numerically studied, linked with new analytical approaches, and compared with 2DCT phenomena. The prospects for the development of a new understanding of at least this one aspect of the exceptionally challenging topic of turbulence are tantalizing motivations for pursuit of 2DQT research.

Unfortunately there are a number of experimental challenges that must first be overcome. Significantly, an isolated, trapped BEC subjected to continuous injection of energy would eventually become depleted of atoms as the system rethermalized. It appears that a BEC experimentalist's primary hope in this respect is to develop methods for studying 2DQT that are quasi-steady, where

[a] Over a 2D surface $S$, the enstrophy $\Omega = \int_S dS\,|\omega|^2$ is a measure of the vorticity $\omega = [\nabla \times \vec{v}]_z$ about the $z$ axis, where $\vec{v}$ is the fluid velocity in the plane normal to $z$.

steady forcing and dissipation rates are balanced over finite timescales during which the BEC is not significantly depleted of atoms. Experimentally, the path to studying decaying 2DQT is perhaps much simpler, since this topic is more concerned with the dynamics of a BEC after forcing has stopped.

While it should not be surprising that disordered vortex distributions in a highly oblate BEC are relatively simple to obtain by a variety of experimental techniques, as we discuss in this article, how best to obtain a quasi-steady state of forced 2DQT remains an open problem. We have begun to empirically tackle only the forcing aspect of this problem, although simulations are also beginning to address this issue [22; 31; 32; 33]. Several of our methods for driving large numbers of vortices into highly oblate BECs are described below. We generally associate these states with 2DQT in the sense that the disordered vortex distributions may be considered a 2D phenomenological equivalent of the vortex tangle that exists in 3D quantum turbulence. We do not provide any evidence that such disordered vortex distributions conform to particular kinetic energy spectra or display vortex dynamics that may be expected in fully developed 2DQT; discussions of links between vortex distributions, vortex dynamics and aggregates, and kinetic energy spectra in BEC 2DQT can be found elsewhere [22; 31; 33; 34; 35]. We also note that in the highly oblate trapping limit, BEC confinement in one spatial direction is much stronger than the trapping in the two orthogonal directions. This limit is not strictly necessary for studying 2DQT, but vortex excitations in the form of Kelvin waves are suppressed and vortices can be accurately approximated as having point-like dynamics in a plane within this limit [36].

In the following, we first describe some of the key phenomenological features of 2DCT, and summarize only a few of the theoretical advances in 2DQT, some of which have been aimed at uncovering the similarities and differences between the classical and quantum systems. This article is not intended as a review of the state of theoretical understanding of 2DQT in BECs; for discussions of theoretical aspects of 2DQT we direct the reader to Refs. [22; 30; 31; 33; 34; 35; 37] and the references contained therein. The study of 2DQT, particularly in compressible quantum fluids such as BECs, is still young and a full range of characteristics remains to be explored. Our aim is to give an overview of the types of observations that may be desirable in 2DQT BEC experiments, then to describe our experimental approach to creating and probing 2DQT in highly oblate BECs. We present a range of tools available for exciting the BEC using laser beams and magnetic fields. The bulk of the remainder of this article is devoted to describing various specific methods for driving vortices into a highly oblate BEC, and we show example images of BECs in such excited states. We conclude by briefly summarizing some of the open experimental challenges in generating and probing 2DQT in BECs.

## 2. Overview of Two-Dimensional Turbulence

From a phenomenological standpoint, Lesieur describes classical turbulence of continuum flows as having non-deterministic flow details, rapid mixing relative to molecular diffusion, and flow characteristics distributed among and interacting over a wide range of length scales [38]; see also Sommeria's similar characterization of turbulence [27]. Such a description encompasses 2D turbulence, where flow dynamics vary primarily over two spatial coordinates ($x$ and $y$); flow in a third direction ($z$) may exist uniformly throughout the $x$-$y$ plane or there may be negligible flow along $z$, hence a 3D fluid system may display 2D turbulence. Building from this general description, the further characteristics of 2D turbulence are markedly different from the characteristics of 3D turbulence. As

noted earlier, one such difference is the direction of energy flux between length scales: in 2D flows, small-scale forcing can lead to the development of large-scale flows.

### 2.1. *Key ideas of 2D turbulence*

Given their disordered and unpredictable nature, and challenges in discerning details of flow dynamics, turbulent flows are often characterized by the statistical properties of the system such as the kinetic energy density $E(k)$ over wavenumber $k$, which describes the distribution of kinetic energy among the length scales of the system. In 1967, Kraichnan [24] found the existence of two inertial ranges associated with distinct kinetic energy spectra power laws, joined by the wavenumber associated with energy and enstrophy forcing. The first range extends from the forcing length scale to larger length scales (or smaller wavenumbers), and displays a kinetic energy spectrum $E(k) \propto k^{-5/3}$. This spectral distribution has the same form discovered by Kolmogorov in 1941 [39] in the context of 3D fluids, but in 2D this spectrum corresponds to an inverse energy cascade. The second range extends from the forcing scale to smaller length scales (or larger wavenumbers) and the kinetic energy spectrum approximately corresponds to $E(k) \propto k^{-3}$.

This two-component spectrum is a classic feature of 2D turbulence, and is further described in reviews of 2D turbulence [27; 28; 29]. Physically the inverse energy cascade corresponds to the aggregation of vorticity such that small-scale forcing leads to the growth of large-scale vorticity until flows are of the order of the size of the system. At this scale dissipation of some form occurs, possibly due to frictional damping at the container's walls.

Prior to the development of 2D turbulence theory in the 1960s [24; 25; 26], Onsager [40; 41] approached turbulent flow in 2D inviscid fluids by focusing on the dynamics of point-like centers of vorticity, or point vortices. A collection of point vortices may be constructed to approximately represent classical continuum flows, or may quite accurately describe vortex distributions in superfluids. In fact, in the same conference proceeding in which Onsager described his theory of vortex states in 2D turbulent flows, he also first postulated the existence of quantized vorticity in superfluids, and implied that superfluids could be ideal testing grounds for his theoretical arguments of 2D turbulence [40]. Onsager argued that a system with a large number of vortices would maximize entropy when vortices of the same sense of circulation form aggregates, giving more room in a finite-volume phase space for the remainder of the vortex cores to distribute themselves and move with fewer constraints. Onsager's predictions, which were the first hints of the existence of an inverse energy cascade, have yet to be directly confirmed experimentally in a superfluid. However, numerical simulations of 2DQT involving forcing in BECs are indeed finding evidence for the existence of vortex aggregates that resemble Onsager's predictions [22; 31].

### 2.2. *Vortices and 2D Quantum Turbulence in BECs*

Based on the above descriptions of 2D turbulence, direct experimental challenges for the study of 2D turbulence in quantum fluids include: (i) reaching a quasi-steady state of forced 2DQT; (ii) observation of the aggregation of like-circulation quantized vortices in a superfluid in a state of forced 2DQT; and (iii) direct measurement of the kinetic energy spectra associated with such turbulent states. These challenges all depend on the existence of means to generate 2DQT, so we now turn to the subject of vortices in highly oblate BECs, and then focus on describing methods to nucleate large disordered distributions of vortices in these compressible quantum fluids.

A dilute-gas BEC is often adequately described in terms of an order parameter, or macroscopic wavefunction, of the form [1]

$$\psi(\vec{r},t) = \sqrt{n(\vec{r},t)}e^{i\phi(\vec{r},t)}, \tag{1}$$

where $n(\vec{r},t)$ is the atomic density distribution of the BEC and $\phi(\vec{r},t)$ is the quantum phase profile. The dynamics of the wavefunction $\psi$ are governed in the mean-field approximation by the Gross-Pitaevski equation (GPE)

$$i\hbar\frac{\partial\psi}{\partial t} = -\frac{\hbar^2}{2m}\nabla^2\psi + V(\vec{r},t)\psi + g|\psi|^2\psi \tag{2}$$

where $g = 4\pi\hbar^2 a/m$ characterizes the interaction strength between atoms, $a$ is the s-wave scattering length of interatomic interactions, $m$ is the atomic mass, and $V(\vec{r},t)$ is the potential due to the trap and other external perturbations.

From a hydrodynamic perspective, a dilute-gas BEC can behave as a tiny droplet of superfluid, where the local velocity of superfluid flow is proportional to the local gradient of the phase:

$$\vec{v} = \frac{\hbar}{m}\nabla\phi. \tag{3}$$

Consequently, the velocity field of a BEC is irrotational, $\nabla \times \vec{v} = 0$, except at singularities of the quantum phase $\phi$. These singularities are the superfluid-free cores of the vortices, about which fluid circulation is quantized [1]. A singly quantized vortex is associated with a $2\pi$-phase winding about the core, and vortex positions and circulations can therefore be experimentally determined using atom interferometry techniques [42; 43; 44], or by sequential images that reveal the dynamics of the vortices [45; 46; 47; 48]. Most single-shot images of BECs, however, only reveal the location of the vortices and not their circulation.

Vortex cores in a BEC have a diameter on the order of the healing length $\xi$ [1], which is typically sub-micron and much less than the wavelength of imaging light. Release of the BEC from the trap followed by ballistic expansion of the atom cloud enables the vortices to expand to diameters large enough to be optically resolvable, and this method is the standard approach to observing vortices in a BEC. In a 3D trap, vortices may also bend with respect to the imaging axis [49], making them even more difficult to observe. In two dimensions however, these Kelvin wave excitations are suppressed [36]. As an example of the clarity that can be obtained in vortex detection, vortices in a highly oblate BEC are shown in Fig. 1; the vortices are the circular dark regions within the BEC fluid, shown in grayscale with lightness of shade corresponding to integrated column density after ballistic expansion from the trap.

In addition to isolated vortex cores, vortex dipoles may be found in highly oblate or 2D quantum fluids. These structures consist of two vortex cores of opposite circulation in close proximity. Vortex aggregates, consisting of clusters of vortices of the same circulation, have also been experimentally observed in the form of multi-quantum vortex dipoles [46]. In the context of 2DQT in a BEC, however, to date only numerical simulations have observed vortex aggregates and their dynamics [22]. In BECs with a vector order parameter, other types of vortex structures may also be found; see Ref. [3] for a summary of vortex experiments in BECs from their initial study in 1999 through 2010, including vortices in degenerate Fermi gases and multi-component BECs.

In the hydrodynamic regime, where quantum pressure can be neglected, and with vortices that are spaced far enough apart from each other that their core shapes are only very weakly distorted, the GPE formalism can be formally linked to the Navier-Stokes equation that plays a key role in

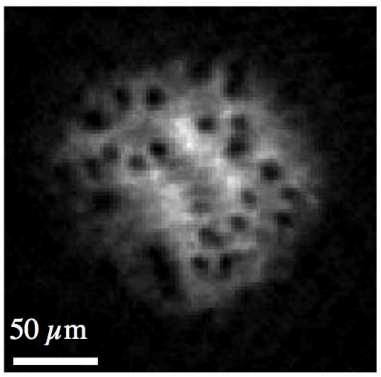


Fig. 1. A representative absorption image of an expanded oblate BEC with a resolvable disordered distribution of vortex cores. The column density of the expanded cloud is proportional to grayscale, with lighter shades representing higher densities. Vortices appear as the dark circular holes within the cloud.

classical fluid dynamics [38]. By incorporating into the GPE damping due to atomic scattering with thermal atoms, a Reynold's number can also be defined [31], although this has yet to be tested experimentally; see Ref. [31] for a discussion of the GPE – Navier-Stokes equation correspondence. Given this correspondence, it should not be surprising that the concepts of turbulence may be investigated using BECs and the variants of the GPE.

Much like the vortex tangle that characterizes quantum turbulence in three dimensions [8], we would like to similarly physically characterize a state of 2DQT in a BEC. We consider the simple picture of a disordered distribution of numerous vortex cores. Such a distribution would satisfy the phenomenological criteria of turbulence stated earlier. First, a large disordered distribution of vortices would have non-deterministic and chaotic flow dynamics [50]. Second, numerical simulations have shown that such distributions can rapidly distribute vorticity [22; 31] or particles [51], even if these are initially concentrated in a small region, thereby satisfying the rapid mixing criterion of turbulence. Finally, such a distribution of vortices can display a large range of inter-vortex separations with no characteristic length scale; in contrast, a vortex lattice has a well-defined length scale of the spacing of the vortices in the lattice [31]. We therefore interpret a disordered 2D distribution of numerous vortex cores as a phenomenological picture that corresponds to 2DQT. Such a picture can be made more quantitative, for example by invoking the methodology and results of Onsager [40] or vortex position statistics, as has been investigated numerically [31; 33; 52]. Nevertheless, our general experimental goal is to create states that consist of many vortices distributed throughout highly oblate BECs with no discernible or well-defined arrangement.

As noted above, a primary factor distinguishing 2D and 3D turbulence is the suppression of significant flow dynamics in one spatial direction, relative to the flow dynamics in the plane normal to that direction. In the case of quantum turbulence, this corresponds to the suppression of Kelvin waves [36]. It may then be possible to study 2DQT in 3D BECs, and it should be noted that quasi-2D BECs [53] or even highly oblate BECs are not strictly needed for studies of 2DQT. On the other hand, even in highly oblate BECs, vorticity can decay due to vortex-antivortex annihilation. It is therefore possible that enstrophy need not be conserved and that a direct energy cascade may

appear, as has been recently noted in numerical simulations of decaying 2DQT [30]. In a practical sense however, we expect that 2DQT is more readily achievable in highly oblate geometries. Our experimental focus is therefore on generating large disordered distributions of vortices in highly oblate BECs.

## 3. Experimental Setup

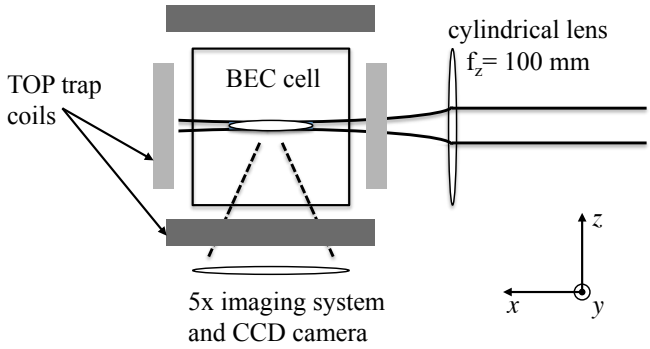


Fig. 2. Experimental configuration for the combined magnetic and optical harmonic trap. A cylindrical lens is used to focus a collimated beam of red-detuned laser light into a sheet with a vertical $1/e^2$ radius of 23 $\mu$m at the location of the BEC. The coils for the DC component of the TOP trap, represented as dark gray bars, are located above and below the BEC cell. The coils for the AC component, represented as light gray bars, are located on either side of the cell normal to the $x$-axis, and the $y$-axis (not shown). A lens below the cell collects light for the vertical imaging system.

To obtain the highly oblate $^{87}$Rb BECs desired for our studies of vortex and 2DQT generation methods, we use a conventional magnetic time-averaged orbiting potential (TOP) trap [54] overlaid with a 1090-nm red-detuned laser light sheet propagating along the $x$-axis as illustrated in Fig. 2 and Fig. 3(a). A cylindrical lens focuses the laser light in the $z$ direction only, with a waist at the position of the BEC such that the laser has horizontal and vertical $1/e^2$ radii of $(w_{0y}, w_{0z}) =$ (2000 $\mu$m, 23 $\mu$m). This red-detuned optical potential provides the additional axial ($z$) confinement needed to flatten the BEC while having a minimal effect on the radial ($r$) confinement.

We begin our experiments with evaporative cooling of atoms in the $|F = 1, \mathrm{m_F} = -1\rangle$ hyperfine state of $^{87}$Rb in the purely magnetic TOP trap. Prior to the final evaporation stage, we ramp on the trapping laser to a power of $\sim 1$ W over 4 s, and then cool the system below the BEC transition temperature $T_c \sim 100$ nK in the combined magnetic and optical potential. The potential well that confines the BEC is an axially symmetric harmonic trap with radial and axial trap frequencies of $(\omega_\mathrm{r}, \omega_\mathrm{z}) \sim 2\pi \times (8, 90)$ Hz.

The BECs formed in the combined magnetic and optical potential have up to $N \sim 2 \times 10^6$ atoms with a system temperature of $T \sim 50$ nK and Thomas-Fermi radii of $(R_\mathrm{r}, R_\mathrm{z}) \sim (52, 5)$ $\mu$m. The chemical potential is $\mu_0 \sim 8\hbar\omega_\mathrm{z}$, and our BECs are consequently far from the quasi-2D limit and well into the 3D regime. Nevertheless, the $R_\mathrm{r} : R_\mathrm{z} \sim 11 : 1$ aspect ratio generated by the tight axial confinement suppresses vortex bending and tilting, resulting in a system characterized by

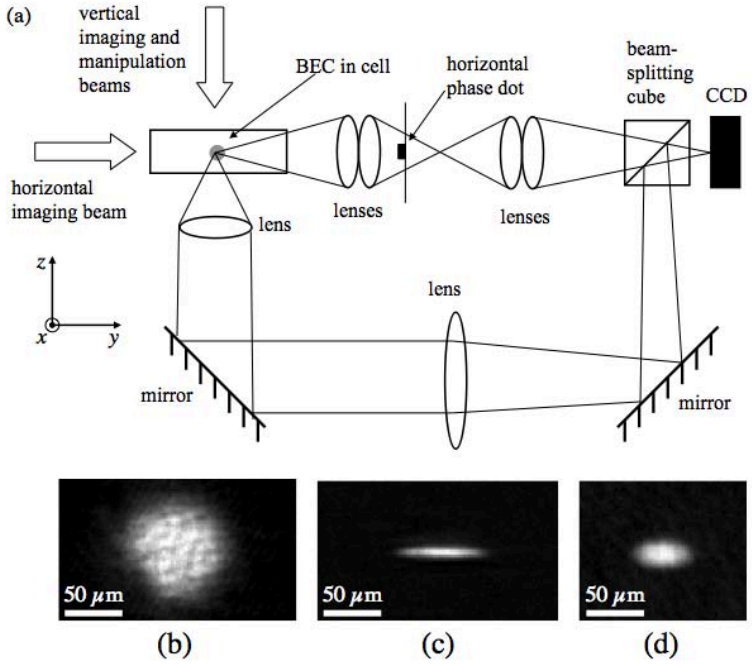


Fig. 3. BEC imaging. (a) illustration of the imaging layout. Both horizontal and vertical imaging systems have magnification M = 5. Side views of the BEC are obtained with phase contrast imaging along the horizontal imaging axis and top views are obtained with absorption imaging along the vertical. (b) a vertically directed absorption image of the BEC in the combined magnetic and optical trap immediately after removal of the trapping potential but prior to any expansion. (c) a corresponding *in situ* horizontal phase-contrast image of the BEC in the combined magnetic and optical trap. (d) *in situ* horizontal phase-contrast image of the BEC in the purely magnetic TOP trap for comparison, with an aspect ratio of Thomas-Fermi radii of $R_{\rm r} : R_{\rm z} = 2 : 1$.

approximately 2D fluid dynamics [36]. Figures 3(b) and 3(c) show images of a condensate held in the combined magnetic and optical trap. For comparison, Fig. 3(d) is an *in situ* image of the BEC in the purely magnetic TOP trap with an aspect ratio of $R_{\rm r} : R_{\rm z} = 2 : 1$. Side views of the BEC are obtained with phase contrast imaging along the horizontal ($y$) imaging axis and views along the vertical ($z$) direction are typically obtained with absorption imaging.

Vortex cores in our highly oblate BECs have a diameter on the order of the healing length, $\xi \sim 0.4\,\mu$m for our system. This is well below the resolution of our imaging system and it is currently beyond our ability to detect vortices with *in situ* images. In order to optically resolve the individual vortex cores of highly oblate BECs, we first turn off the TOP trap and allow the BEC to expand for 10 ms in the optical potential. The optical trapping potential is then removed, and the BEC freely expands for an additional 40 ms. During the entire expansion procedure, a separate magnetic field is applied with a gradient along the $z$ direction that cancels the downward gravitational force on the cloud. Figure 1 gives a representative absorption image after expansion, demonstrating that vortex cores are indeed resolved. In the remainder of this article, all images that

show vortices are absorption images taken with the vertical imaging system after a total of 50 ms of expansion.

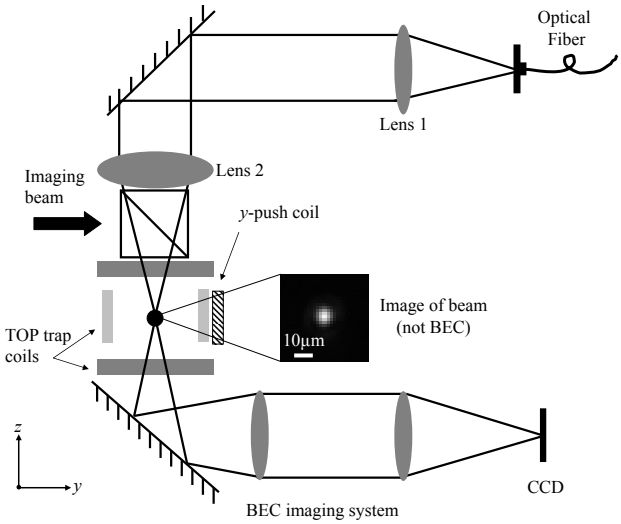


Fig. 4. Optical layout for the focused blue-detuned Gaussian beam directed axially through the BEC. An image of the laser beam can be acquired using the vertical imaging system; an example image is shown. The $y$ push coil (and a similar coil along $x$) can be used to manipulate the position of the center of the magnetic trap.

In many of the experiments described in the following sections, we make use of an additional, focused blue-detuned Gaussian laser beam with a variable power and $1/e^2$ beam radius, directed axially through the BEC as illustrated in Figure 4. This beam can be used to perturb and excite condensates through a variety of methods, which are described below.

We now turn to various experiments and tests of experimental methods, including relevant reviews of previous work in our lab on driving vortices into highly oblate BECs, and discussion of previously unpublished results on generation of 2DQT in highly oblate BECs.

## 4. Nucleation of Vortex Dipoles and Vortex Clusters

As described in Neely *et al* [46], our group observed the deterministic formation and dynamics of vortex dipoles in a BEC by slightly stirring the BEC with a laser beam. In this experiment, vortices were nucleated as the BEC was pushed around and past a blue-detuned laser beam that served as an impenetrable obstacle. In the frame of the moving BEC, the beam was swept through the middle of the BEC, and the vortex dipoles formed in the wake of the laser beam. A vortex dipole consists of a vortex and an antivortex – two vortices of opposite circulation – and tends to exist and move as a single excitation with linear momentum as long as the two vortices remain far from other

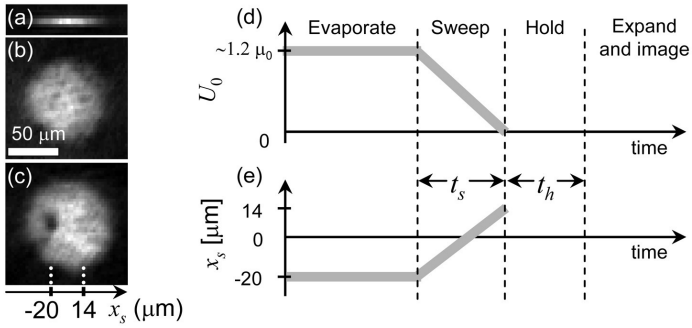


Fig. 5. The BEC initial state and experimental sequence. (a) Side-view phase-contrast image and (b) axial absorption image of a BEC in the highly oblate trap in the absence of the obstacle. Lighter shades indicate higher column densities integrated along the line of sight. Our axial and radial trapping frequencies are measured to be $\omega_z = 2\pi \times 90$ Hz and $\omega_r = 2\pi \times 8$ Hz, respectively. (c) BEC initial state with the obstacle located at $x_s = -20 \sim \mu$m relative to the BEC center. (d),(e) The maximum repulsive potential energy of the obstacle is $U_0 \approx 1.2\mu_0$ (where $\mu_0 \sim 8\hbar\omega_z$ is the BEC chemical potential) and is held constant during evaporative cooling. It is ramped down linearly as the trap translates; relative to the trap center, the beam moves from position $x_s = -20 \sim \mu$m to $x_s = 14 \sim \mu$m over a variable sweep time $t_s$. The BEC is then held in the harmonic trap for a variable time $t_h$ prior to expansion and imaging. Figure and caption from Ref. [46], T. W. Neely, E. C. Samson, A. S. Bradley, M. J. Davis, and B. P. Anderson, Phys. Rev. Lett. **104**, 160401 (2010). Copyright 2010 by the American Physical Society.

vortices or the boundaries of the superfluid. A vortex dipole can be generated from sound, hence a moving obstacle can excite a dipole in a compressible superfluid. Similarly the vortices of a dipole can recombine, annihilating one another and generating a pulse of acoustic energy; see Ref. [31] for a recent discussion of the role and consequences of compressibility in 2DQT.

### 4.1. *Overview of experiment*

In this experiment, the relative motion between the BEC and the blue-detuned laser beam occurred with a constant velocity, as illustrated in Fig. 5. BECs were created in a highly oblate harmonic trap as described above in Sec. 3 and shown in Figs. 5(a) and 5(b). The focused blue-detuned Gaussian laser beam with a $1/e^2$ radius of 10 $\mu$m was directed axially through the BEC 20 $\mu$m to the left of the BEC center as shown in Fig. 5(c). A magnetic bias field was used to translate the harmonic trap minimum horizontally along the $x$-axis at a constant velocity until the laser beam was located 14 $\mu$m to the right of the center of the BEC. At the same time the intensity of the beam was ramped linearly from a maximum of $U_0 \sim 1.2\mu_0$ down to $U_0 = 0$ as shown in Figs. 5(d) and 5(e). Here $\mu_0 \sim 8\hbar\omega_z$ is the chemical potential of the BEC in the highly oblate harmonic trap. At the end of the sweep, the BEC was held in the harmonic trap for varying hold times $t_\mathrm{h}$ before expanding and imaging.

Neely *et al* found a critical velocity necessary for observing vortex dipole nucleation of 170-190 $\mu$m/s. The repeatability and coherence of this process allowed the dynamics of the vortex dipole to be mapped using images of BECs from multiple experimental runs, with each image taken at increasing values of $t_\mathrm{h}$. As shown in Fig. 6, the vortex dipole orbited the BEC with a period of $\sim 1.2$ s. GPE simulations of the procedure provided visual and quantitative comparisons with the experimentally observed vortex dynamics; see Fig. 6(c). Hall's group at Amherst College has also observed a variety

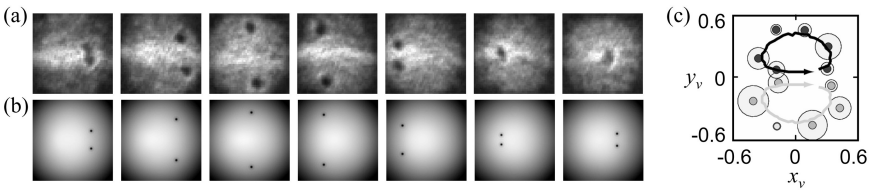


Fig. 6. Images showing the first orbit of vortex dipole dynamics. (a) Back-to-back expansion images from the experiment with 200 ms of successive hold time between the 180-$\mu$m-square images. (b) 62-$\mu$m-square images from numerical calculations of the GPE obtained for conditions similar to the data of sequence (a), but for a temperature of $T = 0$ (i.e., no damping was used). The orbital period is $\sim 1.2$ s, and the apparent vortex core size is smaller in the simulations because we show in-trap numerical data. (c) Black and dark gray small circles show average positions of the vortices $x_v$ and $y_v$ (as fractions of the BEC radius) of each of the two vortices from 5 sequences of experimental data identical to that of sequence (a). The larger circle around each average position point represents the standard deviation of the vortex positions at that specific hold time, and is calculated from the 5 images obtained at that time step. A continuous dipole trajectory from sequence (b) is rescaled to the Thomas-Fermi radius of the expanded experimental images, and superimposed as solid lines on the experimental data; no further adjustments are made for this comparison. Figure and caption adapted from Ref. [46], T. W. Neely, E. C. Samson, A. S. Bradley, M. J. Davis, and B. P. Anderson, Phys. Rev. Lett. **104**, 160401 (2010). Copyright 2010 by the American Physical Society.

of vortex dipole dynamics, using vortices spontaneously trapped in a BEC during the phase transition [55] and a detection method that permits multiple imaging of vortex positions in a single BEC [47; 48].

Sweeping the BEC past the barrier at velocities much faster than the first critical velocity generated multiply quantized vortex dipoles. At a coarse scale, multiply charged dipoles behave like pairs of highly charged vortices of opposite circulation. The loci of vorticity orbits the condensate just as in the case of a singly charged dipole, albeit with a shorter period indicative of faster fluid flow. A doubly charged vortex dipole, for example, orbited with a period of $\sim 0.8$ s. As shown in Fig. 7, at finer scales these loci of vorticity are actually aggregates of singly quantized vortices of the same circulation. Both singly and multiply charged dipoles exhibited lifetimes up to many seconds indicating that vortex-antivortex recombination may be suppressed and that vortex dipoles may be meta-stable in highly oblate BECs.

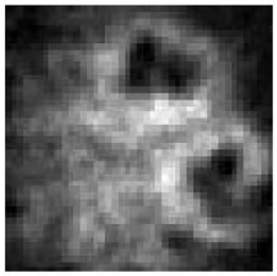

Fig. 7. An experimental image of a triply charged vortex dipole in a ballistically expanded BEC. Adapted from Ref. [46].

### 4.2. *Implications for the experimental study of 2DQT*

The generation of acoustic energy and the nucleation of vortex dipoles due to a moving obstacle are associated with injection of kinetic energy (both compressible and incompressible) into the condensate. The nucleation of vortices is also associated with the injection of enstrophy into the fluid, with the net enstrophy being proportional to the number of vortices [30; 31]. We may view this basic laser sweep mechanism as a possible tool for the generation of 2DQT in a BEC, however in the experiment described above, the deterministic dynamics of the vortex dipoles indicate that a state of 2DQT was not observed. The length scale associated with incompressible energy and enstrophy injection is most readily interpreted as the spatial separation between the vortices of the dipole at the instant of dipole nucleation; see Ref. [31] for further discussion of this point. With continuous laser stirring within the BEC, one may envision the generation of a 2DQT state, and indeed such a state has been observed as described in Sec. 7. See also the relevant simulations of Refs. [7] and [32] that involve an obstacle repeatedly sweeping through a BEC.

Whether or not a BEC with many vortices and antivortices would generally show traits associated with an inverse energy cascade or a direct energy cascade may strongly depend on specific experimental circumstances. In particular, vortex-antivortex recombination is one mechanism for dissipation of enstrophy in 2D fluid flow and might inhibit the formation of an inverse energy cascade, especially for decaying 2DQT [30]. The balance between vortex generation and vortex annihilation may influence observed characteristics of turbulence, such as energy spectra, kinetic energy flux, and aggregation of vorticity.

Finally, the vortex aggregates observed in this experiment are directly generated by the relative motion between the laser obstacle and the BEC, and we do not interpret their deterministic formation as a consequence of 2D turbulence as proposed by Onsager [40]. Nevertheless, their long lifetimes (at least one orbital period) and steady alignment with the tight ($z$) trapping axis may be taken as an indication that vortex aggregates in a highly oblate BEC can be long-lived, and vortex-antivortex annihilation rates may be slow enough to reach regimes of constant or increasing net enstrophy. In this sense, the observation of vortex aggregates in the experiment of Neely *et al* gives hope for future experimental observation of vortex aggregates in 2DQT BEC experiments.

## 5. Generating Turbulent States by Modulating the Magnetic Trapping Potential

Our TOP trap combines a DC quadrupole magnetic field having variable axial gradient $B'_{\rm z}$ with an AC bias field of magnitude $\rm B_0$ that rotates in the $x$-$y$ plane with frequency $\omega_{\rm TOP} = 2\pi \times 4$ kHz. The time-dependent bias field with $x$ and $y$ components

$$B_{\rm x} = B_0 \cos(\omega_{\rm TOP} t) \tag{4}$$

$$B_{\rm y} = B_0 \sin(\omega_{\rm TOP} t) \tag{5}$$

results in the minimum of the quadrupole field orbiting in a circle within the $x$-$y$ plane. For an atom with magnetic dipole moment $\mu$ and mass $m$, the time average of the combined magnetic fields

results in a harmonic potential with trap frequencies determined by

$$\omega_{\rm x} = \omega_{\rm y} = \left[\frac{\mu B_{\rm z}'^2}{8mB_0}(1+\eta^2)\sqrt{1-\eta^2}\right]^{1/2} \tag{6}$$

$$\omega_{\rm z} = \left[\frac{\mu B_{\rm z}'^2}{mB_0}(1-\eta^2)^{3/2}\right]^{1/2} \tag{7}$$

where the factors involving $\eta = mg/\mu B_{\rm z}'$ account for the vertical sag due to gravity (with acceleration $g$) of the TOP trap minimum from that of a static quadrupole field. Such traps are now in common use; see Ref. [56] for a detailed description of TOP traps. Modulations of the magnetic bias field and hence the shape of the trapping potential can excite various modes in the BEC. For example, by deforming the trapping potential and rotating the spatial deformation axis, surface waves can be excited that decay to numerous vortices [12; 15; 57]. In this section, we describe the vortex distributions and their lifetimes that result when highly oblate BECs are subjected to modulations of the magnetic component of the trapping field.

### 5.1. *Symmetric modulation: harmonic trap*

In this experiment, we modulated the amplitude of the magnetic bias field $B_0$ in Eqs. (4) and (5) by adding a small sinusoidal modulation to $B_0$ of the form

$$B_0(t) = B_0 + B_{\rm mod}\sin(\omega_{\rm mod}t). \tag{8}$$

Here $B_{\rm mod}$ is the amplitude of the bias field modulation and $\omega_{\rm mod}$ is the frequency of the modulation. This results in a small sinusoidal oscillation of the radial trap frequency $\omega_{\rm r}$ about the static value, but the trap remains axially symmetric. The axial trapping frequency $\omega_{\rm z}$ is primarily determined by the optical potential and therefore remains approximately constant. Our aim in this experiment was to determine if a weak symmetric modulation would drive vorticity into the BEC such that there was approximately no net angular momentum transfer, i.e., such that if any vortices were generated, approximately equal numbers of vortices of both circulations would be created.

In our procedure, we began with a highly oblate BEC in the combined magnetic and optical harmonic trap. We then modulated the amplitude of the rotating magnetic bias field at frequency $\omega_{\rm mod} = 2\pi \times 9$ Hz and amplitude $B_{\rm mod} \sim 0.05\,B_0$ for varying modulation time $t_{\rm mod}$. After the modulation we held the BEC in the static harmonic trap for varying hold times $t_{\rm h}$, then expanded and imaged, looking for the presence of vortices.

Figure 8(a) shows images taken at increasing modulation times from $t_{\rm mod} = 0.2$ s to 1.5 s. Vortex cores started to appear at $t_{\rm mod} = 0.4$ s and by $t_{\rm mod} = 0.6$ s we observed disordered vortex distributions. Vortex cores appear to be generated at the outer edge of the condensate and make their way into the center. In the next step of the experiment, we modulated the trap as described for $t_{\rm mod}$= 1.5 s before removing the modulation and returning the BEC to the unmodulated harmonic trap. We added increasing post-modulation hold times $t_h$ and then expanded and imaged the BEC. As shown in Fig. 8(b) the vortex distribution became better resolved with increasing $t_h$ and decayed to states with only a few cores remaining after $t_{\rm h} = 2$ s. By $t_{\rm h} = 8$ s no vortex cores remained. The condensate was completely destroyed for $t_{\rm mod} = 10$ s.

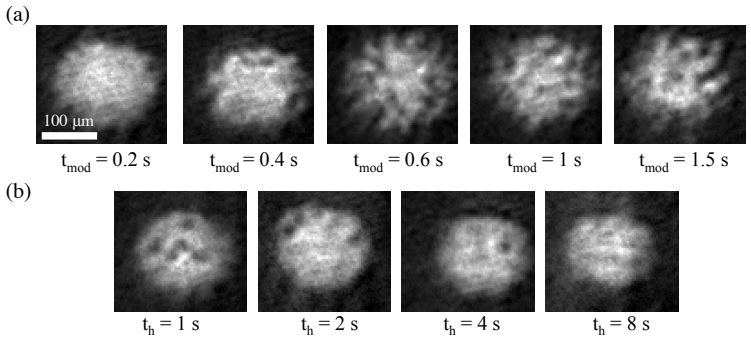


Fig. 8. Vortex distributions after varying modulation and hold times. (a) images taken at increasing modulation times from $t_{\rm mod} = 0.2$ s to 1.5 s. Vortex cores start to appear at $t_{\rm mod} = 0.4$ s and and by $t_{\rm mod} = 0.6$ s we see a disordered vortex distribution. (b) images taken for increasing hold times after modulating for $t_{\rm mod} = 1.5$ s.

### 5.2. *Symmetric modulation: annular trap*

In a similar experiment, we modulated the trapping potential of a highly oblate annular trap. To do this, we modulated the strength of the rotating bias field of the TOP trap in the same manner as described in Sec. 5.1. We added to the harmonic trap a focused blue-detuned Gaussian laser beam, directed axially through the BEC in the configuration shown in Fig. 4. Example images of such a BEC are shown in Figs. 9(a) and 9(b). Prior to imaging, the blue-detuned laser barrier was ramped off slowly enough to avoid significantly perturbing the condensate, allowing the BEC to expand from a harmonic trap for imaging. With $\omega_{\rm mod} = 2\pi \times 6.5$ Hz and $B_{\rm mod} \sim 0.1 B_0$, numerous vortices were quickly nucleated over just a few ms, a significant change from the harmonic trap. As shown in Fig. 9(c) vortex cores were observed to be distributed throughout the BEC, with the first cores appearing at least an order of magnitude earlier than in the purely harmonic trap. Compared to the results of Sec. 5.1, many more cores were visible using this modulation technique in the annular BEC, and the cores have higher contrast. We speculate that the presence of the blue-detuned barrier acted as a vortex dipole nucleation site located within the BEC, and that the vortex dipoles quickly dissociated and formed a state of 2DQT. Again, the modulation process was designed to be axially symmetric apart from experimental errors in beam positioning and trap roundness, and should have nominally added no net angular momentum to the condensate.

With additional modulation time, the BEC was driven into a state of high excitation in which individual vortex cores were not easily resolvable or countable. Such a state is shown in the rightmost image of Fig. 9(c). This process shows that too much modulation drives the BEC into a highly excited far-from-equilibrium state, a signature that it may be possible to identify a weaker modulation strength such that vortex nucleation rates and vortex decay rates due to annihilation and thermal damping at the system boundary would be balanced for a given temperature. Finding this optimum balance is a goal of future research.

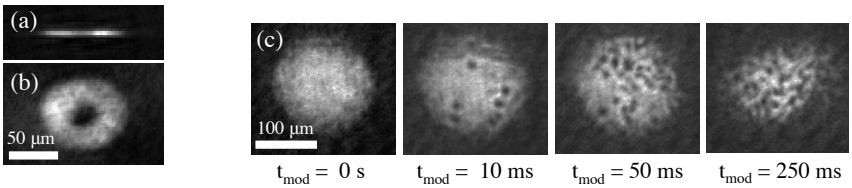


Fig. 9. Modulating the radial trapping frequency for a BEC in an annular trapping geometry. (a) side view of an annular BEC imaged using *in situ* phase contrast imaging. (b) top-down view of an annular BEC imaged using absorption imaging immediately after turning off the trapping potential. For these two images, the blue-detuned beam provides a barrier of height well above the chemical potential, confining the atoms to an annular trap. The annular trap used for the sequence of images in (c) had a narrower, weaker central barrier. (c) images taken at increasing modulation times with no hold after modulation. The first image shows the expanded BEC for $t_{\rm mod} = 0$ s to show that the hole created by the blue-detuned beam has completely filled between beam ramp down and imaging. For the annular trapping geometry vortices appear after much shorter modulation times than for the harmonic trapping case.

### 5.3. *Rotation of an elliptical magnetic trapping potential*

The straightforward experimental method of expansion imaging used in our experiments does not easily permit measurement of the circulation of vortices. While the interferometric or dynamic methods mentioned above can be used for this purpose, these have not yet been applied to turbulent states of BECs. In order to look for the clustering of vortex cores of like-circulation, an alternative is to examine statistics of vortex distributions containing only large numbers of cores of identical circulation. One possible approach to generate such distributions is by rotating the trapping potential, as has been utilized in numerous experiments of BECs with different aspect ratios, such as Refs. [12; 15; 57]; see also Ref. [3] for an overview of numerous other experiments that utilized this technique. Our approach follows such previous work, and is implemented by squeezing and rotating the magnetic trapping field as first implemented by Hodby *et al*[57].

In order to rotate and add angular momentum to the atomic cloud it is necessary to break the symmetry of the trapping potential. In our case this is done by adding an additional bias field to the one described by Eqs. (4) and (5) so that now

$$B_{\rm x} = B_0 \cos(\omega_{\rm TOP} t) + B_\epsilon \cos(\omega_{\rm mod} t) \tag{9}$$

$$B_{\rm y} = B_0 \sin(\omega_{\rm TOP} t) - B_\epsilon \sin(\omega_{\rm mod} t) \tag{10}$$

where $B_\epsilon \sim 0.1\, B_0$, and $\omega_{\rm mod}$ is the frequency of the modulating bias field. If $\omega_{\rm mod} = \omega_{\rm TOP}$ the bias field causes the time-averaged trap to have stationary ellipsoidal potential energy surfaces in the $x$-$y$ plane with the ratio of the minor and major axes determined by $B_\epsilon$ and $B_0$; for our case this ratio is $\sim 0.8$. Increasing $B_\epsilon$ with respect to $B_0$ increases this ellipticity. If $\omega_{\rm mod} \neq \omega_{\rm TOP}$ the ellipse rotates in the $x$-$y$ plane with frequency $\omega_{\rm s} = |\omega_{\rm mod} - \omega_{\rm TOP}|/2$. In the TOP trap, choosing $\omega_{\rm s} \sim 0.7\omega_{\rm r}$ excites the quadrupole mode which decays to a collection of quantized vortex cores of the same circulation. The minimum energy configuration of the rotating BEC consists of a large regular lattice of vortices [12]. A representative vortex lattice formed by spinning the BEC in our purely magnetic TOP trap (i.e., without the red-detuned trapping potential) is shown in Fig. 10.

Our investigations of highly oblate BECs subjected to trap deformation and rotation started with a BEC in the combined magnetic and optical harmonic trap. We then applied the magnetic field

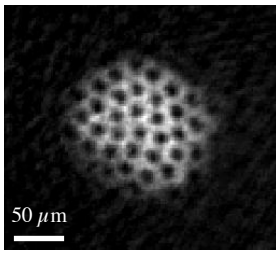


Fig. 10. An image of a slightly irregular vortex lattice in a rotating BEC released from our TOP trap.

ellipticity and spun in the highly oblate harmonic trap for time $t_{\rm s}$ at frequency $\omega_{\rm s}$ with ellipticity $B_\epsilon$. After spinning we returned to the symmetric harmonic trap and held for time $t_{\rm h}$ while the BEC shape deformations damped out. Finally, we let the condensate expand and we imaged the cloud.

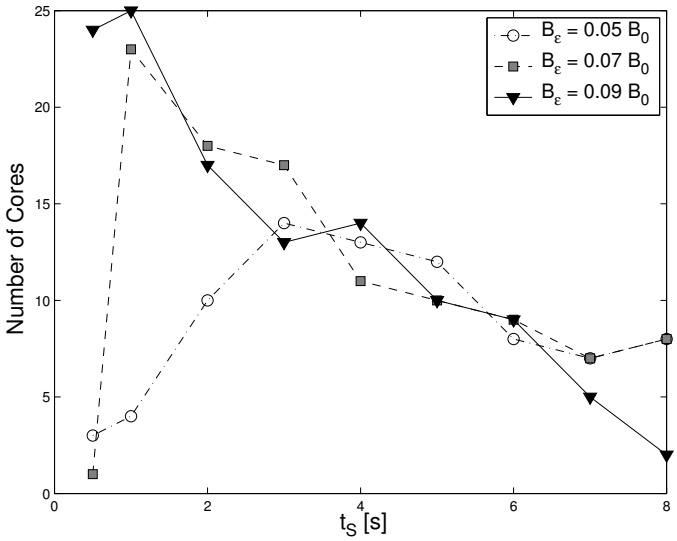


Fig. 11. Comparison of number of vortex cores versus spin time for different ellipticities. All data points were generated by spinning at $\omega_{\rm s} = 2\pi \times 6$ Hz for a variable spin time $t_{\rm s}$ and then holding for 2.5 s after the spin prior to expansion. Open circles represent a single set of data taken with $B_\epsilon = 0.05\,B_0$, gray squares represent $B_\epsilon = 0.07\,B_0$, and black triangles represent $B_\epsilon = 0.09\,B_0$. Both the peak number of vortex cores and $t_{\rm s}$ corresponding to the peak number of vortex cores seem to be dependent on ellipticity but all three ellipticities show decreasing vortex number for longer spin times.

By varying spin frequencies, we found a resonance condition for generating large numbers of vortices at $\omega_{\rm s} = 2\pi \times 6$ Hz. Here $\omega_{\rm s} \sim 0.75\omega_{\rm r}$ is consistent with previous observations of exciting

the quadrupole mode in 3D harmonic traps at $\omega_s \sim 0.7\omega_r$ [16]. We measured the number of vortex cores versus spin time for different ellipticities at this resonance frequency. Figure 11 shows three sets of data corresponding to ellipticities of $B_\epsilon = 0.05\,B_0$, $0.07\,B_0$ and $0.09\,B_0$. All data points were generated by spinning for a variable spin time $t_s$ and then holding for $t_h = 2.5$ s after the spin and before expansion. Both the peak number of vortex cores and $t_s$ corresponding to the peak number of vortex cores appear to be dependent on ellipticity with peak vortex number occurring at a much shorter spin time for $B_\epsilon = 0.09\,B_0$ and $0.07\,B_0$ than for $B_\epsilon = 0.05\,B_0$. All three ellipticities show decreased vortex numbers for longer spin times on the order of $t_s$= 8 s indicating that vortex cores may be annihilating or leaving the system before crystalizing into a lattice.

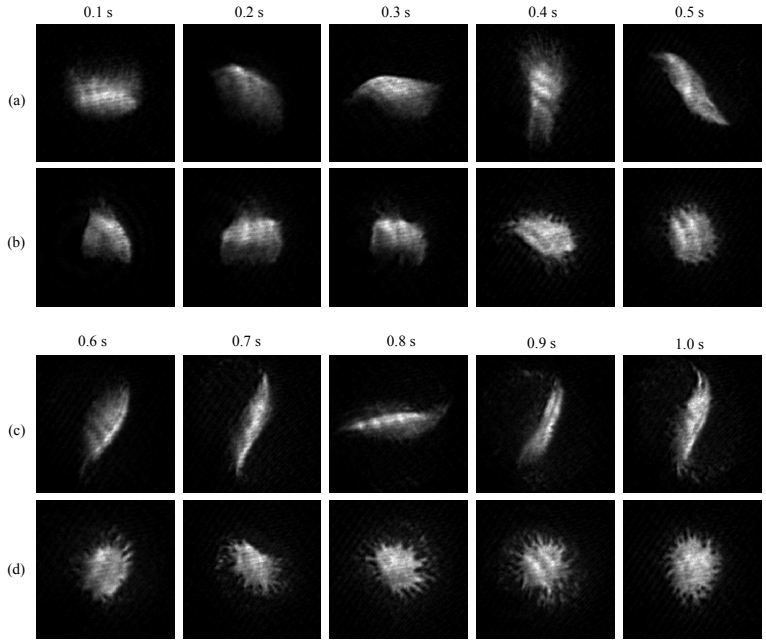


Fig. 12. 350-$\mu$m-square expansion images of an oblate BEC for varying $t_s$ (indicated above images) at increments of 100 ms. Spin frequency and ellipticity were held constant at $\omega_s = 2\pi \times 6$ Hz and $B_\epsilon = 0.07B_0$. (a) and (c) BECs were expanded and imaged directly after spinning, $t_h = 0$. (b) and (d) BECs were held for 400 ms after spinning, $t_h$ = 400 ms, then expanded and imaged.

Figure 12 visually tracks the evolution of the condensate during spinning. Figures 12(a) and 12(c) show successive images at 100 ms intervals for $t_s = 0.1$ to 1.0 s. The BECs were imaged directly after spinning with no hold in the axially symmetric harmonic trap ($B_\epsilon = 0$) prior to expansion. Figures 12(b) and 12(d) show successive images at 100 ms intervals for $t_s = 0.1$ to 1.0 s with an additional 400 ms hold time in the axially symmetric harmonic trap prior to expansion and imaging. The hold time in the symmetric harmonic trap seems important for the nucleation of vortices as vortex cores appear after $t_s = 400$ ms and $t_h = 400$ ms, but do not appear until $t_s = 1.0$ s for the

case of $t_{\rm h} = 0$.

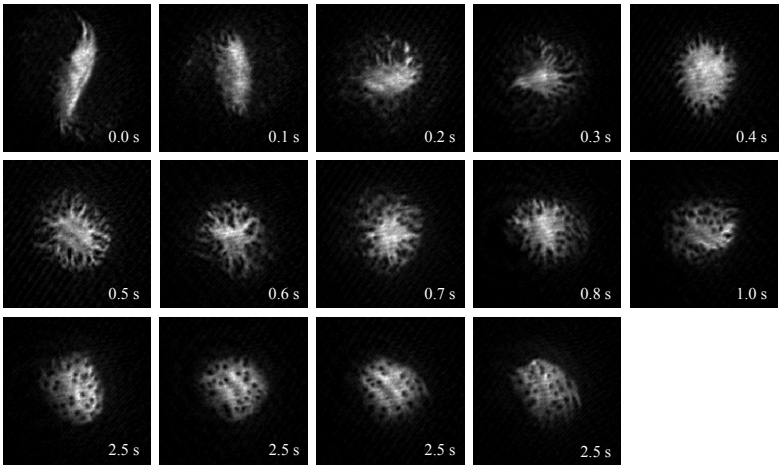


Fig. 13. 350-$\mu$m-square expansion images of vortex distributions in the highly oblate BEC for varying $t_{\rm h}$. Spin time, frequency, and ellipticity were held constant at $t_{\rm s} = 1.0$ s, $\omega_{\rm s} = 2\pi \times 6$ Hz and $B_\epsilon = 0.07 B_0$. Images were taken for variable $t_{\rm h}$ from 0 to 2.5 s. Multiple images for $t_{\rm h} = 2.5$ s are shown to give a representative sample of the variation in vortex distribution.

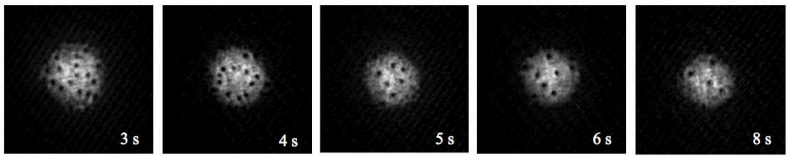


Fig. 14. 350-$\mu$m-square expansion images of vortex distributions in the highly oblate BEC for the varying hold times $t_{\rm h}$ shown from 3 to 8 s. By this time, BEC shape deformations have largely damped out. Spin time, frequency, and ellipticity were held constant at $t_{\rm s} = 1.0$ s, $\omega_{\rm s} = 2\pi \times 6$ Hz and $B_\epsilon = 0.07 B_0$.

Figures 13 and 14 show additional distributions of vortex cores nucleated by spinning and relaxing over subsequent hold times. Here $t_{\rm s} = 1.0$ s is held constant and the BECs are imaged after increasing values of $t_{\rm h}$. Vortices appear to be nucleated on the outer edge of the BEC. Presumably there is net angular momentum added to the condensate, so we expect the vortex cores to be predominately of the same circulation, at least once the system has relaxed to a meta-stable configuration. However, it may be the case that the net circulation is large, but that numerous vortices of the opposite circulation are also generated and present in these images, at least prior to the point at which a disordered distribution is uniformly distributed throughout the BEC. If vortices are indeed of the same circulation in images such as the ones in the bottom row of Fig. 13, then such states may be candidates for experimental measurement of vortex power-law distributions in a BEC, as has been analytically described for homogeneous BECs [31].

As observed, large, disordered vortex distributions can be generated by exciting collective modes of the BEC. The shape deformations damp more quickly than the number of vortex cores, leaving open the possibility of finding parameters where studies of decaying 2DQT could be performed before the system spins down to a state with no vortices. Spinning introduces a net angular momentum into the condensate and should result predominately in vortex cores of the same circulation, making this a possible system in which to observe vortex aggregates without time-resolved dynamics measurements. Nevertheless, this vortex excitation technique does not appear to satisfy the particular goal of continuous forcing, although it appears to be a candidate for studies of decaying 2DQT. It is interesting to note that even for long hold times we find no evidence of a vortex lattice in the highly oblate BEC. Thermalization times for a lattice in a highly oblate BEC may be beyond the lifetime of our BECs; see Ref. [58] for further discussion of this issue.

## 6. Generating Turbulent States with a Stationary Blue-Detuned Laser

In the experiments described in this section, we investigated the response of a BEC to time-dependent perturbations of the intensity of a focused blue-detuned laser beam that pierced the BEC. In all cases in this section, the relative position between the beam and the BEC was stationary. Our aim in these experiments was to locally excite the BEC as an empirical probe of the existence of thermal counterflow [59; 60] in a region where the BEC was locally depleted of atoms. While vortices were observed in all methods examined, the mechanisms for vortex nucleation remain unclear and merit further experimental and numerical investigation.

### 6.1. *Short pulse of blue-detuned laser light*

In this experiment we nucleated vortices by subjecting the BEC to a short pulse of blue-detuned laser light. We began by forming a highly oblate BEC in the purely harmonic trap. We then instantaneously turned on a blue-detuned Gaussian beam for a pulse time of 7 ms, short compared to the radial harmonic oscillator period of 125 ms. The focused blue-detuned Gaussian beam had a $1/e^2$ radius of 10 $\mu$m and was directed axially through the center of the condensate, as shown in Fig. 4. The power in the blue-detuned beam was chosen such that the optical potential generated by the beam was approximately equal to the chemical potential of the BEC. After the laser pulse we held the BEC in the harmonic trap for varying hold times $t_{\rm h}$ before expansion and imaging. Figure 15(a) shows an *in situ* absorption image of the BEC with the blue-detuned beam on, clearly penetrating the condensate.

The laser pulse generated a shock wave that can be observed as the central high density region in the first image in Fig. 15(b). Subsequent images show the condensate for longer hold times. Vortices appear to enter the condensate from the outer boundary as the shock wave propagates. Vortices eventually leave the system, most likely through vortex-antivortex recombination and thermal damping. Apart from the shock wave, this perturbation created vortices with little residual excitation of the BEC. Hoefer *et al* [61] performed experimental and numerical studies of the dispersive shockwaves generated when a BEC was subjected to a short pulse of laser light, however their experiments were performed with a prolate BEC and they do not report observations of vortex cores generated as a result of the laser pulse.

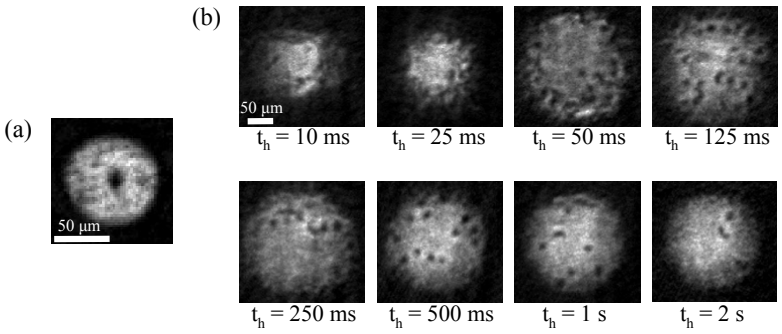


Fig. 15. Vortices generated by subjecting the BEC to a 7 ms pulse of blue-detuned laser light directed axially through the center of the condensate. (a) *in situ* absorption image of the BEC with the blue-detuned beam penetrating the center of the BEC. The beam intensity is chosen such that the beam potential is approximately equal to the condensate chemical potential. (b) Images show successive hold times after the 7ms laser pulse.

### 6.2. *Intensity modulation of a blue-detuned laser beam*

In this experiment we formed a highly oblate BEC in the purely harmonic trap, then turned on and sinusoidally modulated the intensity of a focused blue-detuned Gaussian beam for a varying time $t_{\rm mod}$. After the modulation we held the BEC in the purely harmonic trap for varying time $t_{\rm h}$, then expanded and imaged. The blue-detuned beam had a $1/e^2$ radius of 10 $\mu$m and was directed axially through the center of the condensate, as shown in Fig. 4. During the modulation time the optical potential $U(t)$ generated by the beam followed

$$U(t) = U_0 \sin^2(\omega_{\rm mod} t/2) \tag{11}$$

for $0 < t < t_{\rm mod}$, with maximum repulsive potential energy $U_0$, and frequency $\omega_{\rm mod}$. For all other times, the beam was turned completely off. We fixed the modulation time at integer multiples of the modulation period, $\tau_{\rm mod} = 2\pi/\omega_{\rm mod}$, such that the intensity of the blue-detuned beam always started and ended at zero, and we did not have to be concerned with ramping off the blue-detuned beam for imaging. As in the laser pulse technique, the blue-detuned beam acted as a perturbation to the confining potential. Figure 16 shows a sequence of images for varying values of $t_{\rm h}$ after modulating for $t_{\rm mod} = 187.5$ ms, with $U_0 \sim 0.3\mu_0$ (where $\mu_0 \sim 8\hbar\omega_{\rm z}$), and frequency $\omega_{\rm mod} = 2\pi \times 16$ Hz. This was approximately twice the radial trap frequency. An *in situ* image of the BEC in the harmonic trap with the blue-detuned beam aligned in the center is shown in the leftmost image of Fig. 17.

While this method generated a large number of vortex cores, we also observed large-scale breathing oscillations in the radial dimension of the condensate. The radius of the expanded cloud oscillated between $\sim 40$ $\mu$m and $\sim 180$ $\mu$m with a period of $\sim 70$ ms and eventually damped out with an exponential decay time constant $\tau_{\rm damp} \sim 500$ ms. As shown in Fig. 17, a disordered distribution of vortex cores remained in the condensate even after the bulk oscillations subsided, with $\sim 8$ cores remaining for $t_{\rm h} = 2$ s. It is not entirely surprising that we induced bulk fluid oscillations, given that we were forcing the BEC at a frequency that was twice the radial trapping frequency. However, further study is needed for positively identifying the vortex generation mechanism in this experiment.

In the sequence of images shown in Fig. 16, it is unclear where vortex nucleation occurs. To

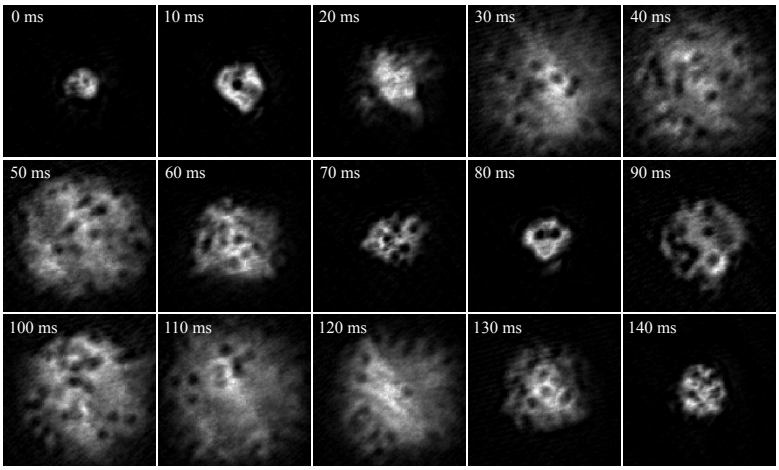


Fig. 16. 250-$\mu$m-square absorption images acquired after the hold times $t_{\rm h}$ indicated. The condensate undergoes large breathing oscillations in the trap, and this oscillation leads to a periodic variation in expanded BEC radius between $\sim 40\,\mu$m and $\sim 180\,\mu$m.

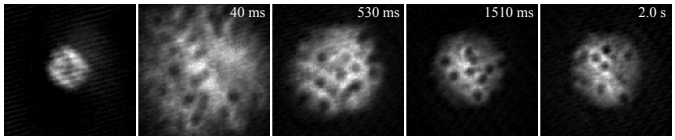


Fig. 17. 250-$\mu$m-square absorption images acquired after the hold times $t_{\rm h}$ indicated. The first image is an *in situ* image of the BEC in the harmonic trap with the blue-detuned beam partially penetrating the condensate; note that the optical potential strength is well below the BEC chemical potential.

further explore the nucleation mechanism, we aligned the blue-detuned beam near the edge of the BEC, and modulated for $t_{\rm mod} = 62.5$ ms, equivalent to one sinusoidal pulse of the laser light, with $U_0 \sim 0.3\mu_0$, and frequency $\omega_{\rm mod} = 2\pi \times 16$ Hz. After modulation, we held the BEC in the purely harmonic trap for $t_{\rm h} = 40$ ms, then expanded and imaged the BEC. As shown in Fig. 18, the vortex cores that resulted from the modulation appear to form near the location of the focused laser beam.

Lastly, we replaced the axially symmetric ($w_{0\rm x} = w_{0\rm y}$) focused blue-detuned Gaussian beam with a blue-detuned light sheet, focused along the $x$-axis with a $1/e^2$ radius $w_{0\rm x} = 10$ $\mu$m, spatially extended along the $y$ direction, and directed axially (along $z$) through the center of the BEC. The width of the beam along the $y$-axis was much larger than the diameter of the condensate so that beam extended beyond the edge of the condensate in the $y$-direction. Figure 19(a) is a vertical absorption image of the unexpanded highly oblate BEC with the elongated blue-detuned beam partially penetrating the condensate. We modulated at $\omega_{\rm mod} = 2\pi \times 16$ Hz for $t_{\rm mod} = 62.5$ ms and $U_0 \sim 0.3\mu_0$, held for $t_{\rm h}$, then expanded and imaged the BEC. Figures 19(b) and 19(c) were taken after $t_{\rm h} = 40$ ms. Here the vortices appear to be nucleated along the long axis of the elongated

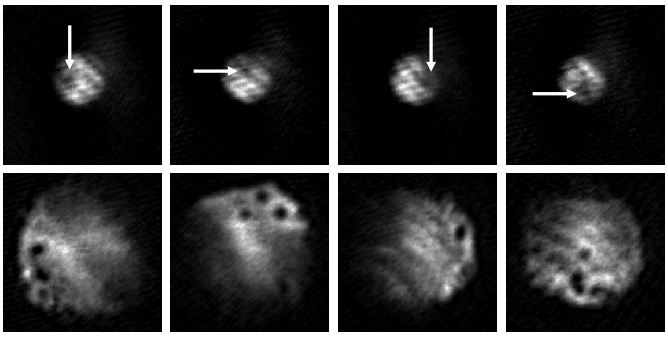

Fig. 18. Localization of vortex cores at the location of the blue-detuned beam. All images are 250-$\mu$m-square absorption images. The top row of images were taken with the BEC in the harmonic trap and the maximum height of the blue-detuned potential at $U_0 \sim 0.3\mu_0$. The locations of the laser beam correspond to the positions designated by the arrow. The bottom row of images were acquired after $t_{\rm h} = 40$ ms followed by the expansion procedure. Note the correlation between beam position and the position of the vortex cores in each vertical pair of images.

beam. The vortex cores shown in these images are not completely resolved but we suspect that the vortices are being nucleated as dipoles in a similar manner to the breakdown of a soliton due to the snake instability in a BEC[62; 63; 64]. Alternatively, these features may be acoustic precursors to vortex dipole formation [65].

As with the axially symmetric blue-detuned potential, we observed bulk excitations in the condensate. Figure 20 shows a sequence of images taken with $\omega_{\rm mod} = 2\pi \times 16$ Hz, $t_{\rm mod} = 62.5$ ms, and $U_0 \sim 0.5\mu_0$, for varying hold times $t_{\rm h}$. The oscillations in $x$ and $y$ are now out of phase by $\sim 90°$. Vortex cores appear to be generated at the location of the beam and move to the outer boundary. In particular the images corresponding to $t_{\rm h} < 40$ ms show vortices aligned with the long axis of the beam, but by $t_{\rm h} = 50$ ms the vortices are located along the outer boundary of the condensate

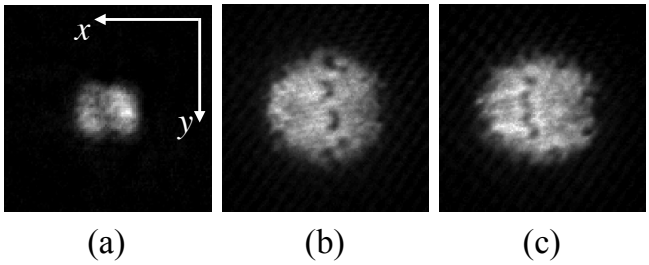


Fig. 19. Localization of vortex cores at the location of the blue-detuned beam. All images are 250-$\mu$m-square absorption images. (a) taken with the BEC in the harmonic trap and the blue-detuned potential on at a strength of $U_0 \sim 0.5\mu_0$. In (b) and (c), expansion images were taken after $t_{\rm h} = 40$ ms. For these images $U_0 \sim 0.3\mu_0$. Note that the vortex cores are localized along the long axis of the blue-detuned beam and that they appear to be nucleating in pairs.

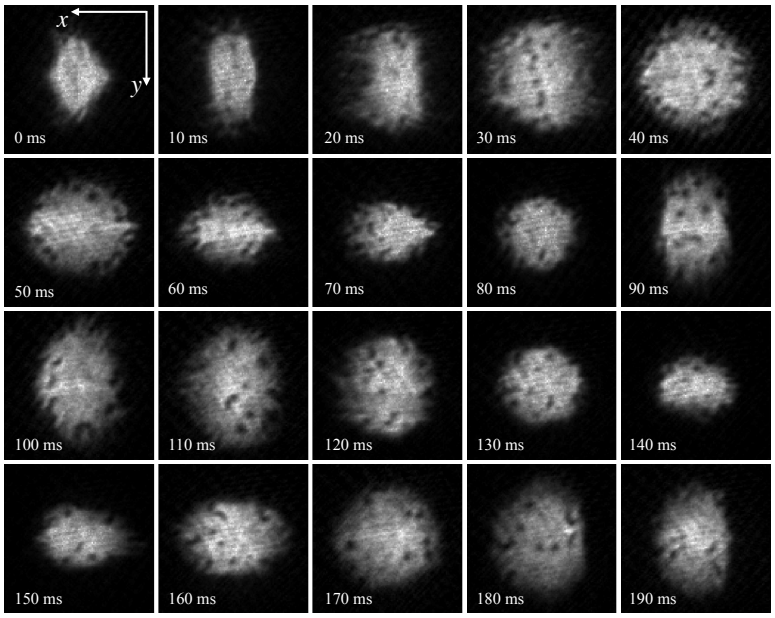


Fig. 20. 250-$\mu$m-square absorption images acquired after the hold times $t_{\rm h}$ indicated. The condensate undergoes bulk oscillations that are out of phase in $x$ and $y$. Vortex cores appear to nucleate at the location of the beam and then move throughout the BEC.

with no cores in the center. Later images show more disordered distributions of cores. Again, the mechanism for nucleation is not clear.

In all of these methods, intensity modulations of a blue-detuned laser beam were observed to be effective for nucleating vortices in a BEC. Although the mechanisms for vortex nucleation remain unclear, we observe correlations between the position of the laser beam and the site of vortex generation within the BEC. With careful parameter selection, it may be possible to use this method for controlled vortex generation rates. However, one must also be careful not to significantly excite shape oscillations, as these would make studies of 2DQT difficult. Perhaps with further adjustment of the modulation rates and times, shape oscillations could be minimized, and methods of this sort could be utilized for 2DQT studies.

## 7. Stirring with a Blue-Detuned Laser Beam

Rather than using intensity modulation of a blue-detuned laser beam, the experiment described in Neely *et al* [22] used small-scale stirring of the BEC with a blue-detuned Gaussian beam to generate disordered vortex distributions in a highly oblate annular trapping potential. It was also observed that vortices coalesced into large-scale flow in an annular trap, but here we review only the vortex distributions observed via stirring.

This experiment was performed with the BEC in an annular trap created with a focused blue-

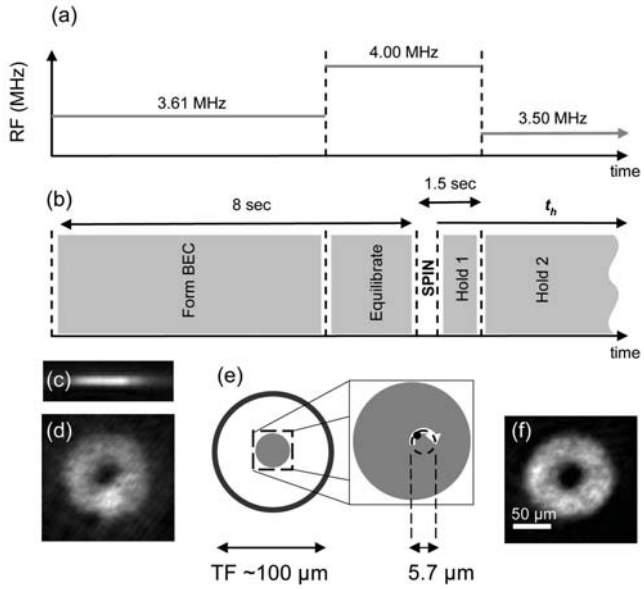


Fig. 21. Timing sequence used to study 2DQT. (a) and (b), experimental parameters vs. time. In (a), the radio frequency (RF) field is adjusted so that the RF value is jumped further away from cutting into the BEC while the BEC is stirred with the laser beam. After the stirring period and a 1.17-ms hold, the RF cuts into the cloud to lower the temperature of the system. (b) illustration of the sequence of events during BEC stirring. (c) and (d), experimental *in situ* column-density images of the BEC immediately prior to the stir, as viewed (c) in the plane of 2D trapping and (d) along the $z$ axis. Lighter grayscale shades indicate larger column densities. (e) illustration of stirring, the arrow shows the trajectory of the harmonic trap center relative to the larger fluid-free region created by the laser barrier. (f) *in situ* image of the BEC 10 s after stirring; vortices are not observable, necessitating an expansion stage to resolve them.

detuned Gaussian beam, with a $1/e^2$ radius of 23 $\mu$m, directed axially through the center of the BEC. As shown in Fig. 21 the blue-detuned beam penetrated the BEC with a barrier height of $U_0 \sim 1.5\mu_0$ where $\mu_0 \sim 8\hbar\omega_z$. Prior to stirring, the BEC was held at a temperature $T \sim 0.9T_C$, where $T_C \sim 116$ nK was the critical temperature for the BEC phase transition.

At $t = 0$ magnetic bias coils were used to move the center of the harmonic trap in a 5.7-$\mu$m-diameter, off-center circle about the stationary, blue-detuned barrier. At $t = 0.333$ s, at the end of the stirring motion, the center of the harmonic trap again coincided with the blue-detuned beam, and the BEC was held in this annular trap for varying hold times up to $t_h \sim 50$ s. At $t_h = 1.17$ s the temperature of the BEC was reduced to $\sim 0.6T_c$ to decrease thermal damping rates and vortex-antivortex recombination. At the end of the hold time the blue-detuned beam was ramped off over 250 ms and the BEC was expanded and imaged.

Experimental images acquired at varying hold times are shown in Fig. 22. Immediately after stirring, a large disordered distribution of vortex cores was observed. By $t_h = 0.33$ s, vortices had begun to coalesce on the central potential barrier, as indicated by the large-vorticity hole in the center of the images. Large-scale superflow developed over increasing hold times, as indicated by

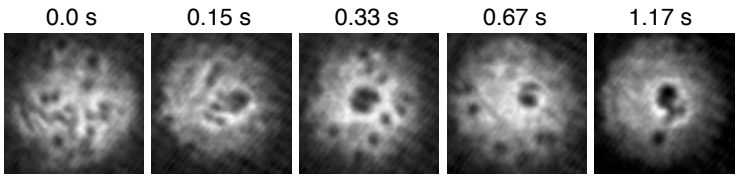


Fig. 22. 200-$\mu$m-square experimental column-density absorption images acquired at the hold times $t_{\rm h}$ indicated above the images. Each BEC undergoes ballistic expansion immediately after the central barrier ramp-down in order to resolve the vortex cores. Each image is acquired from a separate experimental run.

the growing large area of vorticity at the center of the BEC, and was observed to persist up to 50 s. The initial vortex distribution generated by the stirring varied significantly from shot to shot but consistently evolved into a large-scale flow.

The damped GPE was also used to numerically simulate the BEC stirring and subsequent dynamics; see Ref. [22] for details. In addition to the evolution of the large-scale flow observed in both experiment and numerics, analysis of the numerical simulations yielded two other results indicative of 2D turbulence. First, coherent vortex structures consisting of two cores of the same circulation intermittently formed and lasted for long timescales, tantalizing evidence for Onasger-type vortex aggregates. Second, analysis of the incompressible kinetic energy spectrum gave $E(k) \propto k^{-5/3}$ for $k < k_i$ and $E(k) \propto k^{-3}$ for $k > k_i$ where $k_i$ is the wavenumber associated with injection of kinetic energy into the BEC. In this case the injection mechanism was energy transfer between the sound field associated with the compressible component of the fluid excited by stirring, and the vorticity field associated with the incompressible component. Further relationships between stirring mechanisms and observed vortex distributions and dynamics are found in Refs. [22] and [31]. With the development of new experimental techniques, we hope that such information will soon also be experimentally discernible. As it stands, such small-scale stirring with a blue-detuned laser beam appears to be a promising mechanism for further studies of 2DQT, perhaps even with multiple beam sites or with longer stirring times.

## 8. Conclusions

We have found that it is relatively straightforward to nucleate large, disordered distributions of vortex cores in highly oblate BECs, that is, to generate 2DQT in a BEC. We interpret the disordered nature of these distributions as analogous to the vortex tangle characteristic of 3D quantum turbulence. Many of the vortex distributions that we have observed are long-lived, making them potentially useful for studies of 2DQT. However, methods such as modulating a blue-detuned beam in the center of the BEC excite bulk modes of the fluid where the entire condensate undergoes shape oscillations. In many cases, the vortex nucleation mechanisms are not completely clear. Possible mechanisms for vortex generation in the laser modulation experiments include counterflow between the thermal and superfluid components [9; 59; 60], vacuum bubble cavitation as described by Berloff and Barenghi [66], or perhaps other nonlinear fluid dynamics processes at the boundaries of the quantum fluid. While further numerical and experimental investigations are necessary to determine the origins of the vortices, we envision many of these highly disordered vortex distributions as starting points for further studies of 2DQT.

Although we have described a number of vortex generation mechanisms, a primary challenge for experimentalists is to characterize 2DQT in a BEC, and the characteristics observed may well depend on the vortex generation mechanism used. Experimental observation of an inverse energy cascade, vortex aggregation, and kinetic energy spectra are of primary interest. Such characteristics might or might not appear via the methods discussed in this article; this remains to be determined. Vortex dynamics and circulation measurements will likely prove to be among the most significant developments remaining to be developed for 2DQT studies in a BEC. Understanding the temperature dependence, and more generally the role of dissipation, are also of high importance. Finally, reaching a regime of quasi-steady-state 2DQT is a highly desired goal, one that may well be reached utilizing methods described in this article, presumably with a suitable balance of dissipation.

Although many of the methods we describe in this article represent only the beginnings of investigations into new methods for the study of 2DQT, we hope that the descriptions of our observations so far inspire the development of new experimental and numerical studies of vortex generation mechanisms. Further experimental and theoretical work in the field of 2DQT promises to provide an exciting new research direction for compressible quantum fluids.

We gratefully acknowledge the support of the US National Science Foundation grant PHY-0855467. KEW gratefully acknowledges support from the Department of Energy Office of Science Graduate Fellowship Program (DOE SCGF), made possible in part by the American Recovery and Reinvestment Act of 2009, administered by ORISE-ORAU under contract no. DE-AC05-06OR23100. We also thank Ashton Bradley and Ewan Wright for helpful discussions.

## References

1. C. Pethick and H. Smith, *Bose-Einstein Condensation in Dilute Gases*. Cambridge University Press, Cambridge, 2nd edn. (2008).
2. R. J. Donnelly, *Quantized Vortices in Helium II*. Cambridge University Press, Cambridge (1991).
3. B. P. Anderson, Resource Article: Experiments with Vortices in Superfluid Atomic Gases, *J. Low Temp. Phys.* **161**(5-6), 574 (2010).
4. L. Pitaevskii and S. Stringari, *Bose-Einstein Condensation*. Oxford Science Publications, Oxford (2003).
5. P. B. Blakie, A. S. Bradley, M. J. Davis, R. J. Ballagh, and C. W. Gardiner, Dynamics and Statistical Mechanics of Ultra-Cold Bose Gases Using C-Field Techniques, *Adv. in Phys.* **57**(5), 363 (2008).
6. M. Tsubota, Quantum Turbulence: From Superfluid Helium to Atomic Bose-Einstein Condensates, *J. Phys-Cond. Mat.* **21**(16), 164207 (2009).
7. M. Tsubota and K. Kasamatsu. Quantized Vortices and Quantum Turbulence. arXiv:1202.1863 (2012).
8. R. P. Feynman, Application of Quantum Mechanics to Liquid Helium, *Prog. Low Temp. Phys.* **1**, 17 (1955).
9. C. F. Barenghi, R. J. Donnelly, and W. F. Vinen, eds., *Quantized Vortex Dynamics and Superfluid Turbulence*. Springer, Berlin, New York (2001).
10. M. S. Paoletti, M. E. Fisher, K. R. Sreenivasan, and D. P. Lathrop, Velocity Statistics Distinguish Quantum Turbulence from Classical Turbulence, *Phys. Rev. Lett.* **101**(15), 154501 (2008).
11. M. S. Paoletti and D. P. Lathrop, Quantum Turbulence, *Ann. Rev. Cond. Matt. Phys.* **2**(1), 213 (2011).
12. J. R. Abo-Shaeer, C. Raman, J. M. Vogels, and W. Ketterle, Observation of Vortex Lattices in Bose-Einstein Condensates, *Science*. **292**(5516), 476 (2001).
13. K. Madison, F. Chevy, V. Bretin, and J. Dalibard, Stationary States of a Rotating Bose-Einstein Condensate: Routes to Vortex Nucleation, *Phys. Rev. Lett.* **86**(20), 4443 (2001).
14. S. Sinha and Y. Castin, Dynamic Instability of a Rotating Bose-Einstein Condensate, *Phys. Rev. Lett.* **87**(19), 190402 (2001).

15. K. W. Madison, F. Chevy, W. Wohlleben, and J. Dalibard, Vortex Formation in a Stirred Bose-Einstein Condensate, *Phys. Rev. Lett.* **84**(5), 806 (2000).
16. F. Chevy, K. W. Madison, and J. Dalibard, Measurement of the Angular Momentum of a Rotating Bose-Einstein Condensate, *Phys. Rev. Lett.* **85**(11), 2223 (2000).
17. C. Raman, J. R. Abo-Shaeer, J. M. Vogels, K. Xu, and W. Ketterle, Vortex Nucleation in a Stirred Bose-Einstein Condensate, *Phys. Rev. Lett.* **87**(21), 210402 (2001).
18. V. Schweikhard, I. Coddington, P. Engels, S. Tung, and E. A. Cornell, Vortex-Lattice Dynamics in Rotating Spinor Bose-Einstein Condensates, *Phys. Rev. Lett.* **93**(21), 210403 (2004).
19. E. A. L. Henn, J. A. Seman, G. Roati, K. M. F. Magalhães, and V. S. Bagnato, Emergence of Turbulence in an Oscillating Bose-Einstein Condensate, *Phys. Rev. Lett.* **103**(4), 045301 (2009).
20. J. A. Seman, E. A. L. Henn, R. F. Shiozaki, G. Roati, F. J. Poveda-Cuevas, K. M. F. Magalhães, V. I. Yukalov, M. Tsubota, M. Kobayashi, K. Kasamatsu, and V. S. Bagnato, Route to Turbulence in a Trapped Bose-Einstein Condensate, *Las. Phys. Lett.* **8**(9), 691 (2011).
21. M. Caracanhas, A. L. Fetter, S. R. Muniz, K. M. F. Magalhães, G. Roati, G. Bagnato, and V. S. Bagnato, Self-similar Expansion of the Density Profile in a Turbulent Bose-Einstein Condensate, *J. Low Temp. Phys.* **166**(1-2), 49 (2012).
22. T. W. Neely, A. S. Bradley, E. C. Samson, S. J. Rooney, E. M. Wright, K. J. H. Law, R. Carretero-Gonzlez, P. G. Kevrekidis, M. J. Davis, and B. P. Anderson. Characteristics of Two-Dimensional Quantum Turbulence in a Compressible Superfluid. arXiv:1204.1102 (2012).
23. J. Maurer and P. Tabeling, Local Investigation of Superfluid Turbulence, *Europhys. Lett.* **43**(1), 29 (1998).
24. R. Kraichnan, Inertial Ranges in Two-Dimensional Turbulence, *Phys. Fluids.* **10**(7), 1417 (1967).
25. C. Leith, Diffusion Approximation for Two-Dimensional Turbulence, *Phys. Fluids.* **11**(3), 671 (1968).
26. G. Batchelor, Computation of the Energy Spectrum in Homogeneous Two-Dimensional Turbulence, *Phys. Fluids.* **12**(12), II–233 (1969).
27. J. Sommeria, *Two-Dimensional Turbulence*, In eds. M. Lesieur, A. Yaglom, and F. David, *New trends in turbulence*, p. 385. Les Houches - Ecole d'Ete de Physique Theorique. EDP Sciences-Springer, Berlin (2001).
28. P. Tabeling, Two-Dimensional Turbulence: a Physicist Approach, *Phys. Rep.* **362**(1), 1 (2002).
29. G. Boffetta and R. E. Ecke, Two-Dimensional Turbulence, *Ann. Rev. Fluid Mech.* **44**(1), 427 (2012).
30. R. Numasato, M. Tsubota, and V. S. L'vov, Direct Energy Cascade in Two-Dimensional Compressible Quantum Turbulence, *Phys. Rev. A.* **81**(6), 063630 (2010).
31. A. S. Bradley and B. P. Anderson, Energy Spectra of Vortex Distributions in Two-Dimensional Quantum Turbulence, *Phys. Rev. X.* **2**(4), 041001 (2012).
32. K. Fujimoto and M. Tsubota, Nonlinear Dynamics in a Trapped Atomic Bose-Einstein Condensate Induced by an Oscillating Gaussian Potential, *Phys. Rev. A.* **83**(5), 053609 (2011).
33. A. C. White, C. F. Barenghi, and N. P. Proukakis, Creation and Characterization of Vortex Clusters in Atomic Bose-Einstein Condensates, *Phys. Rev. A.* **86**(1), 013635 (2012).
34. B. Nowak, J. Schole, D. Sexty, and T. Gasenzer, Nonthermal Fixed Points, Vortex Statistics, and Superfluid Turbulence in an Ultracold Bose Gas, *Phys. Rev. A.* **85**(4), 043627 (2012).
35. J. Schole, B. Nowak, and T. Gasenzer, Critical Dynamics of a Two-Dimensional Superfluid near a Non-Thermal Fixed Point, *Phys. Rev. A.* **86**(1), 013624 (2012).
36. S. J. Rooney, P. B. Blakie, B. P. Anderson, and A. S. Bradley, Suppression of Kelvon-Induced Decay of Quantized Vortices in Oblate Bose-Einstein Condensates, *Phys. Rev. A.* **84**(2), 023637 (2011).
37. B. Nowak, D. Sexty, and T. Gasenzer, Superfluid Turbulence: Nonthermal Fixed Point in an Ultracold Bose Gas, *Phys. Rev. B.* **84**(2), 020506(R) (2011).
38. M. Lesieur, *Turbulence in Fluids*, 4th edn. Kluwer Academic Publishers, Netherlands (1990).
39. A. N. Kolmogorov, The Local Structure of Turbulence in Incompressible Viscous Fluid for Very Large Reynolds Numbers, *Dokl. Akad. Nauk. SSSR.* **30**, 301 (1941). Reprinted and translated in: *Proc. R. Soc. London A* **434** (1890), 9, (1991).
40. L. Onsager, Statistical Hydrodynamics, *Il Nuovo Cimento.* **6 suppl 2**, 279 (1949).
41. G. Eyink and K. Sreenivasan, Onsager and the Theory of Hydrodynamic Turbulence, *Rev. Mod. Phys.* **78**(1), 87 (2006).

42. M. R. Matthews, B. P. Anderson, P. C. Haljan, D. S. Hall, C. E. Wieman, and E. A. Cornell, Vortices in a Bose-Einstein Condensate, *Phys. Rev. Lett.* **83**(13), 2498 (1999).
43. F. Chevy, K. W. Madison, V. Bretin, and J. Dalibard, Interferometric Detection of a Single Vortex in a Dilute Bose-Einstein Condensate, *Phys. Rev. A.* **64**(3), 031601(R) (2001).
44. S. Inouye, S. Gupta, T. Rosenband, A. P. Chikkatur, A. Görlitz, T. L. Gustavson, A. E. Leanhardt, D. E. Pritchard, and W. Ketterle, Observation of Vortex Phase Singularities in Bose-Einstein Condensates, *Phys. Rev. Lett.* **87**(8), 080402 (2001).
45. B. P. Anderson, P. C. Haljan, C. E. Wieman, and E. A. Cornell, Vortex Precession in Bose-Einstein Condensates: Observations with Filled and Empty Cores, *Phys. Rev. Lett.* **85**(14), 2857 (2000).
46. T. W. Neely, E. C. Samson, A. S. Bradley, M. J. Davis, and B. P. Anderson, Observation of Vortex Dipoles in an Oblate Bose-Einstein Condensate, *Phys. Rev. Lett.* **104**(16), 160401 (2010).
47. D. V. Freilich, D. M. Bianchi, A. M. Kaufman, T. K. Langin, and D. S. Hall, Real-Time Dynamics of Single Vortex Lines and Vortex Dipoles in a Bose-Einstein Condensate, *Science.* **329**(5996), 1182 (2010).
48. S. Middelkamp, P. J. Torres, P. G. Kevrekidis, D. J. Frantzeskakis, R. Carretero-González, P. Schmelcher, D. V. Freilich, and D. S. Hall, Guiding-Center Dynamics of Vortex Dipoles in Bose-Einstein Condensates, *Phys. Rev. A.* **84**(1), 011605(R) (2011).
49. V. Bretin, P. Rosenbusch, F. Chevy, G. V. Shlyapnikov, and J. Dalibard, Quadrupole Oscillation of a Single-Vortex Bose-Einstein Condensate: Evidence for Kelvin Modes, *Phys. Rev. Lett.* **90**(10), 100403 (2003).
50. H. Aref, Integrable, Chaotic, and Turbulent Vortex Motion in Two-Dimensional Flows, *Ann. Rev. Fluid Mech.* **15**(1), 345 (1983).
51. S. Wang, Y. A. Sergeev, C. F. Barenghi, and M. A. Harrison, Two-Particle Separation in the Point Vortex Gas Model of Superfluid Turbulence, *J. Low Temp. Phys.* **149**(1-2), 65 (2007).
52. E. A. Novikov, Dynamics and Statistics of a System of Vortices, *Zh. Eksp. Teor. Fiz.* **68**, 1868 (1975).
53. Z. Hadzibabic, P. Kruger, M. Cheneau, B. Battelier, and J. Dalibard, Berezinskii-Kosterlitz-Thouless Crossover in a Trapped Atomic Gas, *Nature.* **441**(7097), 1118 (2006).
54. W. Petrich, M. H. Anderson, J. R. Ensher, and E. A. Cornell, Stable, Tightly Confining Magnetic Trap for Evaporative Cooling of Neutral Atoms, *Phys. Rev. Lett.* **74**(17), 3352 (1995).
55. C. N. Weiler, T. W. Neely, D. R. Scherer, A. S. Bradley, M. J. Davis, and B. P. Anderson, Spontaneous Vortices in the Formation of Bose-Einstein Condensates, *Nature.* **455**(7215), 948 (2008).
56. J. R. Ensher. *The First Experiments with Bose-Einstein Condensation of* $^{87}$*Rb.* PhD thesis, University of Colorado (Boulder) (1998).
57. E. Hodby, G. Hechenblaikner, S. A. Hopkins, O. M. Maragò, and C. J. Foot, Vortex Nucleation in Bose-Einstein Condensates in an Oblate, Purely Magnetic Potential, *Phys. Rev. Lett.* **88**(1), 010405 (2001).
58. T. M. Wright, R. G. Ballagh, A. S. Bradley, P. B. Blakie, and C. W. Gardiner, Dynamical Thermalization and Vortex Formation in Stirred Two-Dimensional Bose-Einstein Condensates, *Phys. Rev. A.* **78**(6), 063601 (2008).
59. W. F. Vinen, Mutual Friction in a Heat Current in Liquid Helium-II. III. Theory of the Mutual Friction, *Proc. R. Soc. London A.* **242**, 493 (1957).
60. W. F. Vinen, Mutual Friction in a Heat Current in Liquid Helium-II. IV. Critical Heat Currents in Wide Channels, *Proc. R. Soc. London A.* **243**, 400 (1958).
61. M. A. Hoefer, M. J. Ablowitz, I. Coddington, E. A. Cornell, P. Engels, and V. Schweikhard, Dispersive and Classical Shock Waves in Bose-Einstein Condensates and Gas Dynamics, *Phys. Rev. A.* **74**(2), 023623 (2006).
62. D. L. Feder, M. S. Pindzola, L. A. Collins, B. I. Schneider, and C. W. Clark, Dark-Soliton States of Bose-Einstein Condensates in Anisotropic Traps, *Phys. Rev. A.* **62**(5), 053606 (2000).
63. B. P. Anderson, P. C. Haljan, C. A. Regal, D. L. Feder, L. A. Collins, C. W. Clark, and E. A. Cornell, Watching Dark Solitons Decay into Vortex Rings in a Bose-Einstein Condensate, *Phys. Rev. Lett.* **86** (14), 2926 (2001).
64. Z. Dutton, M. Budde, C. Slowe, and L. V. Hau, Observation of Quantum Shock Waves Created with Ultra-Compressed Slow Light Pulses in a Bose-Einstein Condensate, *Science.* **293**(5530), 663 (2001).

65. S. Nazarenko and M. Onorato, Freely Decaying Turbulence and Bose-Einstein Condensation in Gross-Pitaevski model, *J Low Temp Phys.* **146**(1-2), 31 (2007).
66. N. G. Berloff and C. F. Barenghi, Vortex Nucleation by Collapsing Bubbles in Bose-Einstein Condensates, *Phys. Rev. Lett.* **93**(9), 090401 (2004).

# Appendix B

# Lab notebook entry for sync circuit

In this appendix, we reproduce notes from lab notebook #44 (7/18/2013 and 7/26/2013). These notes pertain to using a sync circuit together with an adjustable phase-delay and duty-cycle circuit in order to time the imaging pulse to coincide with the $B_{\mathrm{y}}(t) = 0$ point of the bias field oscillation.

We note that syncing the image pulse to a particular point in the rotating bias field cycle is only effective when using the 1D TOP trap as described in Sec. 2.1.2. For the standard TOP trap described in Sec. 2.1.1, the net magnetic field vector subscribes a cone with an angle of $\theta \sim 60^{\circ}$ from the imaging axis.

108

7/18/13

dewpoint ~ 47°F?

2pm Temp = 73°F, RH = 36%

Old pulse sync circuit only syncs if TTL change occurs when SRS pulse sync signal is low. If SRS sync is high when TTL change occurs then the change registers immediately!!

So we were only syncing to the 4kHz signal HALF the time.

I rebuilt the pulse sync circuit using a D type positive edge triggered flip flop. Now any TTL change waits till the next rising edge of the SRS sync signal to register on the TTL output. See notes in Pulse-Sync folder.

Note: Now there are two separate TTL sync circuits that run off the same clock (the 4kHz SRS sync signal). I'm using one for the AC TOP VTTL and the other for the expansion coil TTL.

I don't know why I never noticed the problem w/ the old pulse sync circuit the last time that I tried to sync magnetic fields turn on/off to the 4kHz bias field. Maybe this is why I never noticed any improvement in BEC location consistency post expansion when I've synced in the past.

⟹ Recheck expansion location consistency using the NEW sync circuit.

128

Notes on using the sync circuit & pulse delay / duty cycle circuits for imaging.

1) The flip-flop sync circuit is clocked with a 4kHz signal meaning that the shortest possible TTL out from the sync circuit is 250 usec.
⇒ I think this explains the streaking I observed in some kinetics mode images.

2) The flipflop only changes output values on the rising clock edge so if the TTL input pulse is less than 250 usec it is possible for the pulse to never register.
⇒ I think this is why I kept having very low light levels when using the sync circuit.

3) ~~To do~~. If all I want is to sync a a rising or falling TTL event to the 4kHz clock then points 1 & 2 are not a problem

4) If instead we want to sync a very short TTL pulse $\Delta t_{pulse} < 250$ usec to the 4kHz clock we need to be more clever and use the adjustable duty cycle circuit.

⇒ Current sync / duty cycle configuration for imaging

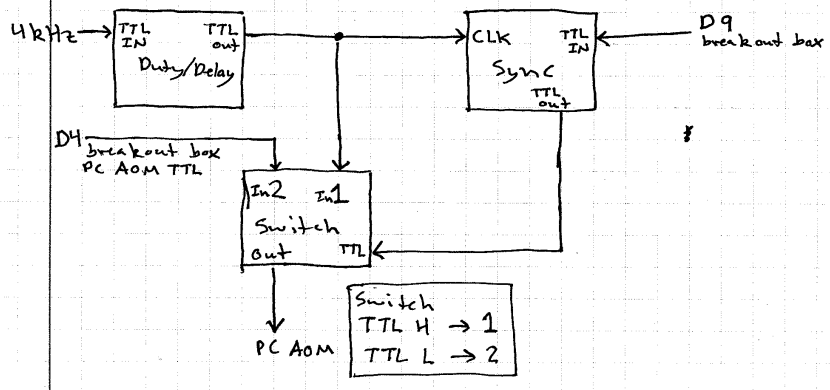

kinetics mode

For each ~~image~~ D9 goes high for 250 usec. A6 (cam trigger) goes high for 250 usec. The camera trigger is unsynced. setting the exposure time to 250 usec ensures that the image will register on the camera. Note: ~~##~~ to be sure of no streaking the camera trigger should also be synced but streaking seems to be minimal w/ the unsynced camera trigger.

For non kinetics mode images the camera can be triggered ~ 8 msec prior to the image as per usual (w/ exp time ~ 6 msec) without syncing the camera trigger

~~35~~
34-38 Kinetics mode. $t_{exp\,(cam)}$ = 250 usec
6 frames. $t_{cam\,trig}$ = 250 usec, cam trigger is not synced to the 4 kHz clock.
$t_{switch\,trig}$ (D9) = 250 usec.
$t_{PC\,pulse}$ = 10.4 usec with ~~##~~ ~~##~~ $\Delta t$ from 4 kHz = 22 usec

power = 0.25 mW post
~0.26 mW fiber

room lights off.
$\Delta PC$ = -320 MHz

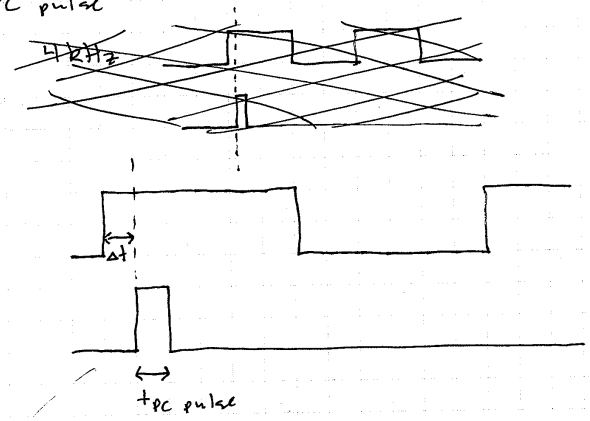


39 sync camera trigger to 4 kHz ~~##~~ CLK

40 relock PC. ⇒ better OD.
41 repeat. tripped.
42 repeat. ?
43 repeat. tripped.
44 repeat.

old Pulse Signal - TTL sync circuit

White → TTL (in)
Yellow → TTL out
Red → +5V
Black → GND
Gray → Pulse IN

---

Kali 7/17/13

New Pulse Sync Circuit

Use Dual D type Positive Edge Flip-Flop
Tie CLR & PRE set high. (5V) ^Triggered
$V_{cc}$ = +5V

SN74ALS74AN

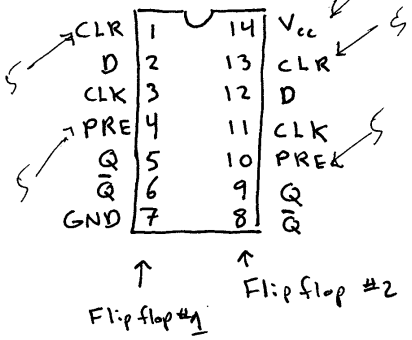


Truth Table (PRE & CLR = H)

| CLK | D | Q | Q̄ |
|---|---|---|---|
| ↑ | H | H | L |
| ↑ | L | L | H |
| L | X | $Q_0$ | $\bar{Q}_0$ |

D = Trigger In (TTL)
CLK = Pulse In (4kHz SRS Sync) → Used same input to run both CLKs
Q = Trigger Out (TTL synced to rising clock edge)

Note: This circuit may be glitchy ~~for fast changes to~~ under certain configurations
2. see Horowitz & Hill pg515-516 NAND gate + Flipflop.

## Pulse Signal - TTL Sync Circuit.

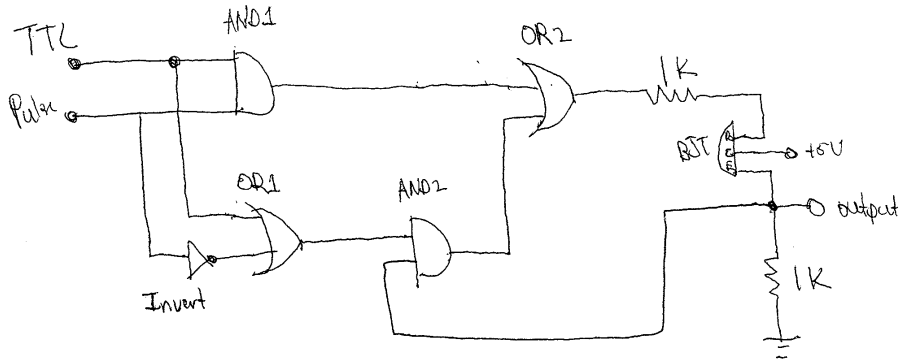


Signals:

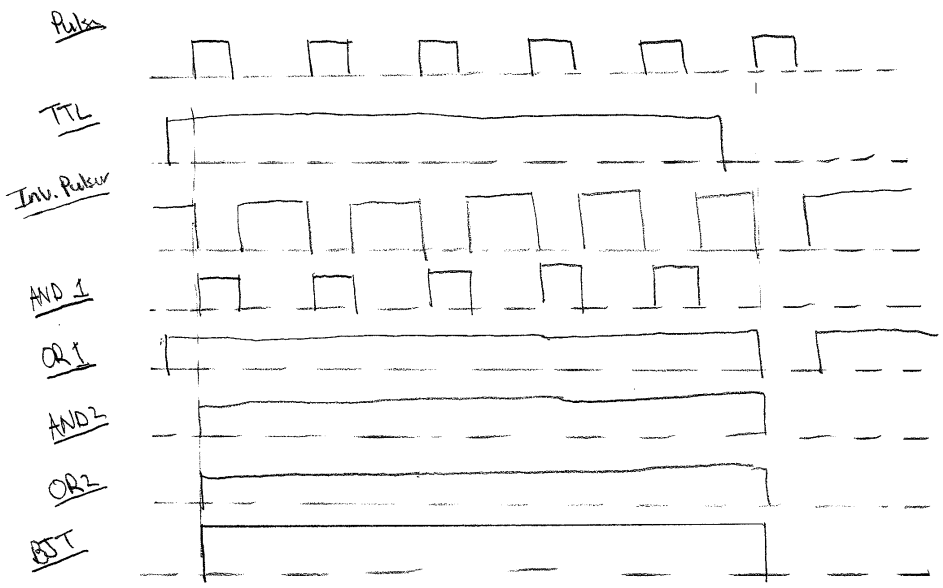


The idea of this circuit is to sync an arbitrary TTL signal to a pulsed signal. The output of the circuit does not turn on until both signals are high and does not turn off until the pulse hits again (regardless of TTL).

Essentially the BJT acts as a sort of "latch"

The behavior of the circuit is as follows:

① We flip TTL high.
- When Pulse goes high: (output Turn ON condition)
  - AND 1 high
  - OR 2 high
  - BJT conducts, output high.

② TTL still high but pulse low (we still want output high)
- AND 1 low
- OR 1 high (TTL is high)
- AND 2 high since BJT is conducting
- OR 2 high, keeping BJT going and output high.

} latch

③ We flip TTL off. (but must turn off with pulse!)
- AND 1 low.
- OR 1 is high until invert pulse goes low (Turn OFF cond.)
- When invert pulse goes low
  - OR 1 low
  - AND 2 low

  ⟶ OR 2 low, BJT turns off, output low.

Note: (Kali 7/17/13)
This circuit will sync TTL w/ pulse ~~edge~~ only if the pulse is low when TTL changes. Otherwise the TTL change is (if pulse high.)
~~not~~ observed @ the output immediately.
So not so useful for syncing Bfield turn off to 4kHz.

# Appendix C

# Lab notebook entry for repump AOM

In this appendix, we reproduce notes from lab notebook #40 (8/9/2012). These notes pertain to the AOM configuration for the MOT repump laser.

Tweaked up Ti:sapph Power to 1.33W
Power pre cooling fiber = 650 mW
$P_{fiber}$ = { ~400 mW / 240 mW
⇒ MOT = 2.48V wrt 720 mV

Repump temp. starting @ 15.55 kΩ
⇒ nice scan ~~wo~~ but starts to go multimode? near the transition I want.

went up to T=17.20 kΩ I = 133.8 mA

down to T=14.00 kΩ I = 114.3 mA

possible ~120 Hz noise on repump PD signal huh?

~~8/8/12~~ 8/9/12

~~Got a decent~~
Yesterday I got a decent MOT but I had to lock on the 1-2 crossover transition to do so rather than the F = 1 → F' = 2 transition (normal?)

~~Repump AOM lock:~~

On further investigation I noted that the AOM double pass was operating in a m = 0, m = +1 configuration ⇒ net ~80 MHz upshift of the probe light wrt the pump (and laser)
The ~~down~~ single pass AOM (post lock) was operating as normal in the m = -1 configuration
⇒ downshifts the laser light by ~80 MHz before the MOT.

In this configuration locking the laser on the 1-2' line in the sat abs ~~spectr~~ signal ∴ results in $V_{MOT}$ being 120 MHz below the desired freq (1-2' transition)
Perhaps I was actually making a small MOT using the 1-1' line for repumping and this is why locking the

84

laser on the high edge of the 1'-2' crossover dip gave a better MOT?

## Repump AOM lock

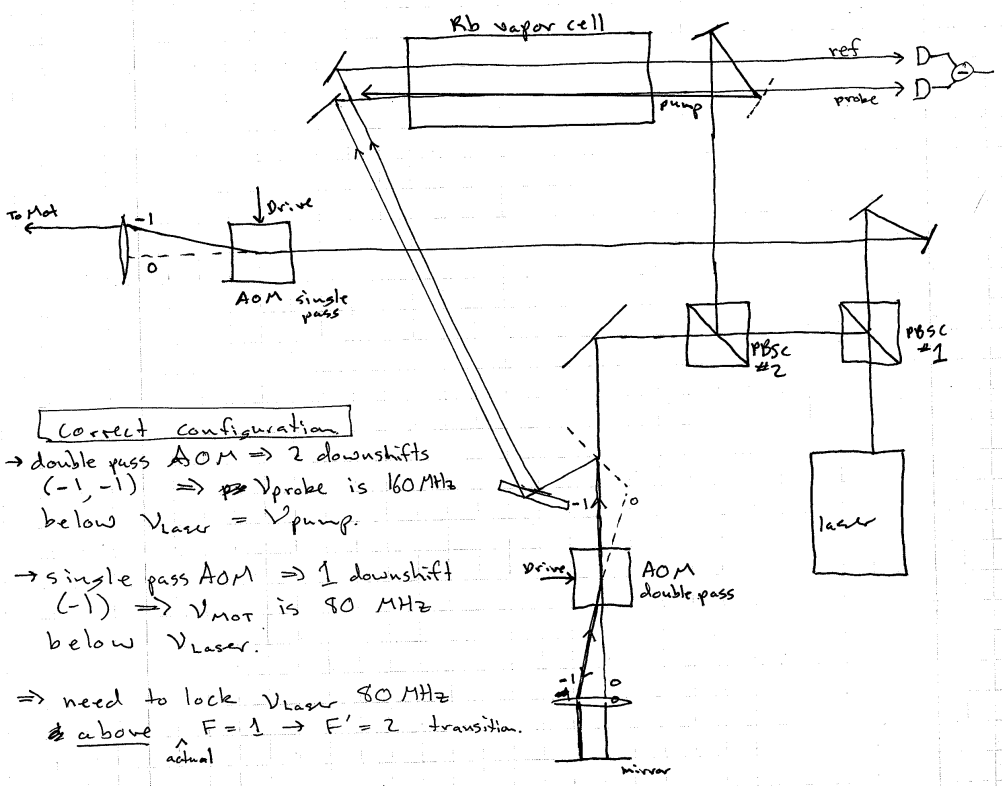


Correct configuration

→ double pass AOM ⇒ 2 downshifts (-1, -1) ⇒ $\nu_{probe}$ is 160 MHz below $\nu_{laser} = \nu_{pump}$.

→ single pass AOM ⇒ 1 downshift (-1) ⇒ $\nu_{MOT}$ is 80 MHz below $\nu_{Laser}$.

⇒ need to lock $\nu_{Laser}$ 80 MHz above actual F = 1 → F' = 2 transition.

Δ ≡ detuning from $\nu_{laser}$

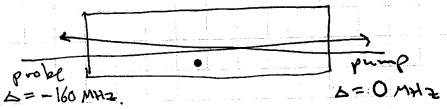


sat abs dip occurs when an atom sees the probe ~~down~~ upshifted by 80 MHz and the pump downshifted by 80 MHz ⇒ locking on the F = 1-2' line in the sat abs signal from this config actually locks the laser

85

90 MHz above the $F=1 \rightarrow F'=2$ transition which is what we want.

⇒ reset alignment to correct config. (downshifts all around)

Improved repump locking signal.

1) look @ $F=2 - F'=3$ $Rb^{87}$ line w/ just the single PD (no sub. or lock in) adjust pump alignment (overlap w/ probe) and relative pump & probe powers to maximize resolution of indiv dips. Also make sure doppler profile is gaussian if not probe power is too high.

2) adjust PD gains to set subtraction as close to perfect as possible. a small slope is probably unavoidable.

3) repeat # 1 w/ $F=1 - F'=2$ $Rb^{87}$ line.

4) adjust further looking @ subtraction signal. will be able to resolve at least 3 and maybe a 4th peak

5) look @ lock-in amp signal.
Things to adjust are.

lock in amp parameters
- → time constant
- → sensitivity
- → phase (offset by 90° & minimize signal then switch back)
- → amplitude (too little ⇒ noisy. too much ⇒ loose resolution)
- → lock in freq → made a big dif in signal strength. Why?

→ pump + probe powers.

signal is now ~ 300 $mV_{pp}$

laser still wants to go multimode right near desired transition.

# References


[1] R. J. Donnelly, *Quantized Vortices in Helium II* (Cambridge University Press, Cambridge, 1991).

[2] B. P. Anderson, J. Low Temp. Phys. **161**, 574 (2010).

[3] T. W. Neely, E. C. Samson, A. S. Bradley, M. J. Davis, and B. P. Anderson, Phys. Rev. Lett. **104**, 160401 (2010).

[4] K. E. Wilson, E. C. Samson, Z. L. Newman, T. W. Neely, and B. P. Anderson, *Experimental methods for generating two-dimensional quantum turbulence in Bose-Einstein condensates* (World Scientific, Singapore, 2013), vol. 1 of *Annual Review of Cold Atoms and Molecules*, chap. 7, p. 261.

[5] C. Pethick and H. Smith, *Bose-Einstein Condensation in Dilute Gases* (Cambridge University Press, Cambridge, 2nd edn., 2008).

[6] T. P. Billam, M. T. Reeves, B. P. Anderson, and A. S. Bradley, Phys. Rev. Lett. **112**, 145301 (2014).

[7] L. Onsager, Il Nuovo Cimento **6, Issue 2 supplement**, 279 (1949).

[8] R. Kraichnan, Phys. Fluids **10**, 1417 (1967).

[9] K. E. Wilson, Z. L. Newman, J. D. Lowney, and B. P. Anderson, Phys. Rev. A **91**, 023621 (2015).

[10] M. Lesieur, *Turbulence in Fluids* (Kluwer Academic Publishers, Netherlands, 1990), 4th ed.

[11] J. Sommeria, *Two-Dimensional Turbulence* (EDP Sciences-Springer, Berlin, 2001), p. 385, Les Houches - Ecole d'Ete de Physique Theorique.

[12] M. A. Rutgers, Phys. Rev. Lett. **81**, 2244 (1998).

[13] G. Eyink and K. Sreenivasan, Rev. Mod. Phys. **78**, 87 (2006).

[14] "And now you know how the little vortices arranged it so that most of them could play the way they wanted to. They just pushed the biggest vortices together until the big vortices had all the energy the little ones did not want, and then the little vortices played ring-around-the-rosy until you could not tell which was where," L. Onsager, Letter to L. Pauling (1945). See Ref. [13], pg. 120.

[15] R. P. Feynman, Prog. Low Temp. Phys. **1**, 17 (1955).

[16] M. R. Matthews, B. P. Anderson, P. C. Haljan, D. S. Hall, C. E. Wieman, and E. A. Cornell, Phys. Rev. Lett. **83**, 2498 (1999).

[17] S. J. Rooney, P. B. Blakie, B. P. Anderson, and A. S. Bradley, Phys. Rev. A **84**, 023637 (2011).

[18] C. F. Barenghi, R. J. Donnelly, and W. F. Vinen, eds., *Quantized Vortex Dynamics and Superfluid Turbulence* (Springer, Berlin, New York, 2001).

[19] C. F. Barenghi, L. Skrbek, and K. R. Sreenivasan, Proceedings of the National Academy of Sciences **111**, 4647 (2014).

[20] M. Tsubota, J. Phys-Cond. Mat. **21**, 164207 (2009).

[21] A. C. White, B. P. Anderson, and V. S. Bagnato, Proceedings of the National Academy of Sciences **111**, 4719 (2014).

[22] T. W. Neely, A. S. Bradley, E. C. Samson, S. J. Rooney, E. M. Wright, K. J. H. Law, R. Carretero-González, P. G. Kevrekidis, M. J. Davis, and B. P. Anderson, Phys. Rev. Lett. **111**, 235301 (2013).

[23] S. J. Rooney, T. W. Neely, B. P. Anderson, and A. S. Bradley, Phys. Rev. A **88**, 063620 (2013).

[24] W. J. Kwon, G. Moon, J.-Y. Choi, S. W. Seo, and Y.-I. Shin, Phys. Rev. A **90**, 063627 (2014).

[25] A. S. Bradley and B. P. Anderson, Phys. Rev. X **2**, 041001 (2012).

[26] M. T. Reeves, T. P. Billam, B. P. Anderson, and A. S. Bradley, Phys. Rev. A **89**, 053631 (2014).

[27] M. T. Reeves, B. P. Anderson, and A. S. Bradley, Phys. Rev. A **86**, 053621 (2012).

[28] M. T. Reeves, T. P. Billam, B. P. Anderson, and A. S. Bradley, Phys. Rev. Lett. **114**, 155302 (2015).

[29] A. L. Gaunt, T. F. Schmidutz, I. Gotlibovych, R. P. Smith, and Z. Hadzibabic, Phys. Rev. Lett. **110**, 200406 (2013).

[30] W. Petrich, M. H. Anderson, J. R. Ensher, and E. A. Cornell, Phys. Rev. Lett. **74**, 3352 (1995).

[31] D. R. Scherer, Ph.D. thesis, University of Arizona (2007).

[32] C. N. Weiler, Ph.D. thesis, University of Arizona (2008).

[33] T. W. Neely, Ph.D. thesis, University of Arizona (2010).

[34] E. C. Samson, Ph.D. thesis, University of Arizona (2012).

[35] J. R. Ensher, Ph.D. thesis, University of Colorado (Boulder) (1998).

[36] E. Hodby, G. Hechenblaikner, S. A. Hopkins, O. M. Maragò, and C. J. Foot, Phys. Rev. Lett. **88**, 010405 (2001).

[37] J. R. Abo-Shaeer, C. Raman, J. M. Vogels, and W. Ketterle, Science **292**, 476 (2001).

[38] K. L. Corwin, Z.-T. Lu, C. F. Hand, R. J. Epstein, and C. E. Wieman, Appl. Opt. **37**, 3295 (1998).

[39] D. A. Steck, *Rubidium 87 D line data*, available online at http://steck.us/alkalidata (revision 2.1.4, 23 December 2010).

[40] W. Ketterle, D. Durfee, and D. Stamper-Kurn, *Making, probing and understanding Bose-Einstein condensates* (IOS Press, Amsterdam, 1999), p. 67, Proc. Int. School of Physics "Enrico Fermi" vol CXL.

[41] H. J. Metcalf and P. van der Straten, *Laser Cooling and Trapping* (Springer-Verlag, New York, 1999), 1st ed.

[42] M. R. Matthews, D. S. Hall, D. S. Jin, J. R. Ensher, C. E. Wieman, E. A. Cornell, F. Dalfovo, C. Minniti, and S. Stringari, Phys. Rev. Lett. **81**, 243 (1998).

[43] D. V. Freilich, D. M. Bianchi, A. M. Kaufman, T. K. Langin, and D. S. Hall, Science **329**, 1182 (2010).

[44] M. R. Matthews, Ph.D. thesis, University of Colorado (Boulder) (1999).

[45] M. Gajdacz, P. L. Pedersen, T. Mørch, A. J. Hilliard, J. Arlt, and J. F. Sherson, Rev. Sci. Instrum. **84**, 083105 (2013).

[46] C. C. Bradley, C. A. Sackett, and R. G. Hulet, Phys. Rev. Lett. **78**, 985 (1997).

[47] M. R. Andrews, M.-O. Mewes, N. J. van Druten, D. S. Durfee, D. M. Kurn, and W. Ketterle, Science **273**, 84 (1996).

[48] A. Ramanathan, S. R. Muniz, K. C. Wright, R. P. Anderson, W. D. Phillips, K. Helmerson, and G. K. Campbell, Review of Scientific Instruments **83**, 083119 (2012).

[49] B. P. Anderson, P. C. Haljan, C. E. Wieman, and E. A. Cornell, Phys. Rev. Lett. **85**, 2857 (2000).

[50] F. Chevy, K. W. Madison, V. Bretin, and J. Dalibard, Phys. Rev. A **64**, 031601(R) (2001).

[51] S. Inouye, S. Gupta, T. Rosenband, A. P. Chikkatur, A. Görlitz, T. L. Gustavson, A. E. Leanhardt, D. E. Pritchard, and W. Ketterle, Phys. Rev. Lett. **87**, 080402 (2001).

[52] S. Donadello, S. Serafini, M. Tylutki, L. P. Pitaevskii, F. Dalfovo, G. Lamporesi, and G. Ferrari, Phys. Rev. Lett. **113**, 065302 (2014).

[53] S. Inouye, M. R. Andrews, J. Stenger, H.-J. Miesner, D. M. Stamper-Kurn, and W. Ketterle, Nature **392**, 151 (1998).

[54] C. Chin, R. Grimm, P. Julienne, and E. Tiesinga, Rev. Mod. Phys. **82**, 1225 (2010).

[55] S. Tung, G. Lamporesi, D. Lobser, L. Xia, and E. A. Cornell, Phys. Rev. Lett. **105**, 230408 (2010).

[56] A. T. Powis, S. J. Sammut, and T. P. Simula, Phys. Rev. Lett. **113**, 165303 (2014).

[57] K. W. Madison, F. Chevy, W. Wohlleben, and J. Dalibard, Phys. Rev. Lett. **84**, 806 (2000).

[58] F. Chevy, K. W. Madison, and J. Dalibard, Phys. Rev. Lett. **85**, 2223 (2000).

[59] T. M. Wright, R. G. Ballagh, A. S. Bradley, P. B. Blakie, and C. W. Gardiner, Phys. Rev. A **78**, 063601 (2008).

[60] W. F. Vinen, Proc. R. Soc. London A **242**, 493 (1957).

[61] W. F. Vinen, Proc. R. Soc. London A **243**, 400 (1958).

[62] D. L. Feder, M. S. Pindzola, L. A. Collins, B. I. Schneider, and C. W. Clark, Phys. Rev. A **62**, 053606 (2000).

[63] B. P. Anderson, P. C. Haljan, C. A. Regal, D. L. Feder, L. A. Collins, C. W. Clark, and E. A. Cornell, Phys. Rev. Lett. **86**, 2926 (2001).

[64] Z. Dutton, M. Budde, C. Slowe, and L. V. Hau, Science **293**, 663 (2001).

[65] S. Nazarenko and M. Onorato, J Low Temp Phys **146**, 31 (2007).

[66] N. S. Ginsberg, J. Brand, and L. V. Hau, Phys. Rev. Lett. **94**, 040403 (2005).

[67] M. R. Andrews, C. G. Townsend, H.-J. Miesner, D. S. Durfee, D. M. Kurn, and W. Ketterle, Science **275**, 637 (1997).

[68] M. J. Ku, W. Ji, B. Mukherjee, E. Guardado-Sanchez, L. W. Cheuk, T. Yefsah, and M. W. Zwierlein, Phys. Rev. Lett. **113**, 065301 (2014).

[69] S. Moulder, S. Beattie, R. P. Smith, N. Tammuz, and Z. Hadzibabic, Phys. Rev. A **86**, 013629 (2012).

[70] K. C. Wright, R. B. Blakestad, C. J. Lobb, W. D. Phillips, and G. K. Campbell, Phys. Rev. Lett. **110**, 025302 (2013).

[71] K. J. H. Law, T. W. Neely, P. G. Kevrekidis, B. P. Anderson, A. S. Bradley, and R. Carretero-González, Phys. Rev. A **89**, 053606 (2014).

[72] Z. Hadzibabic, P. Krüger, M. Cheneau, B. Battelier, and J. Dalibard, Nature **441**, 1118 (2006).

[73] R. Desbuquois, L. Chomaz, T. Yefsah, J. Léonard, J. Beugnon, C. Weitenberg, and J. Dalibard, Nature Physics **8**, 645 (2012).

[74] J. Choi, S. W. Seo, and Y. Shin, Phys. Rev. Lett. **110**, 175302 (2013).

[75] G. S. Settles, *Schlieren and Shadowgraph Techniques: Visualizing Phenomena in Transparent Media* (Springer-Verlag, Berlin, 2001).

[76] M. Pappa, P. C. Condylis, G. O. Konstantinidis, V. Bolpasi, A. Lazoudis, O. Morizot, D. Sahagun, M. Baker, and W. von Klitzing, New J. of Phys. **13**, 115012 (2011).

[77] The diffraction-limited resolution $R$ of the microscope objective is calculated using the Rayleigh criterion, $R = 0.61\lambda/NA$. While this criterion is defined for incoherent light it still provides a useful estimate of resolution when using coherent light.

[78] A. Stiebeiner, R. Garcia-Fernandez, and A. Rauschenbeutel, Opt. Express **18**, 22677 (2010).

[79] E. Vetsch, D. Reitz, G. Sague, R. Schmidt, S. Dawkins, and A. Rauschenbeutel, Phys. Rev. Lett. **104**, 203603 (2010).

[80] $RSR$ is the average of all the $RSR_{\text{cross}}$ values calculated for individual cross sections perpendicular to the nanofiber orientation. $RSR_{\text{cross}} = |I_{\text{sig}} - \bar{I}_{\text{BG}}|/\sigma_{\text{BG}}$, where $I_{\text{sig}}$ is the pixel value at the peak of the nanofiber signal, $\bar{I}_{\text{BG}}$ is the average pixel value, and $\sigma_{\text{BG}}$ is the standard deviation. When calculating $\bar{I}_{\text{BG}}$ and $\sigma_{\text{BG}}$, the 14 pixels on either side of the signal peak are not used.

[81] W. Alt, Optik **113**, 142 (2002).

[82] A. C. White, C. F. Barenghi, and N. P. Proukakis, Phys. Rev. A **86**, 013635 (2012).

[83] J. Goodman, *Introduction to Fourier Optics* (Roberts and Company, Greenwood Village, CO, 3rd edn., 2005).

[84] J. Greivenkamp, *Field Guide to Geometrical Optics* (SPIE-The International Society for Optical Engineering, Bellingham, WA, 2004).

[85] L. M. Bennie, P. T. Starkey, M. Jasperse, C. J. Billington, R. P. Anderson, and L. D. Turner, Opt. Express **21**, 9011 (2013).

[86] Lenses were purchased from LENS-Optics, www.lens-optics.de.

[87] P. Engels, I. Coddington, P. C. Haljan, V. Schweikhard, and E. A. Cornell, Phys. Rev. Lett. **90**, 170405 (2003).

[88] P. C. Haljan, I. Coddington, P. Engels, and E. A. Cornell, Phys. Rev. Lett. **87**, 210403 (2001).

[89] P. Engels, I. Coddington, P. C. Haljan, and E. A. Cornell, Phys. Rev. Lett. **89**, 100403 (2002).

[90] I. Coddington, P. Engels, V. Schweikhard, and E. A. Cornell, Phys. Rev. Lett. **91**, 100402 (2003).

[91] V. Schweikhard, I. Coddington, P. Engels, S. Tung, and E. A. Cornell, Phys. Rev. Lett. **93**, 210403 (2004).

[92] V. Schweikhard, I. Coddington, P. Engels, V. P. Mogendorff, and E. A. Cornell, Phys. Rev. Lett. **92**, 040404 (2004).

[93] I. Coddington, P. C. Haljan, P. Engels, V. Schweikhard, S. Tung, and E. A. Cornell, Phys. Rev. A **70**, 063607 (2004).

[94] S. Tung, V. Schweikhard, and E. A. Cornell, Phys. Rev. Lett. **97**, 240402 (2006).

[95] C. N. Weiler, T. W. Neely, D. R. Scherer, A. S. Bradley, M. J. Davis, and B. P. Anderson, Nature **455**, 948 (2008).

[96] M. A. Hoefer, M. J. Ablowitz, I. Coddington, E. A. Cornell, P. Engels, and V. Schweikhard, Phys. Rev. A **74**, 023623 (2006).